Mapping and modelling phreatic ballistic fields at tourism hotspots: a methodological assessment at Tongariro and Whakaari (White Island) Volcanoes, New Zealand.

A thesis
submitted in partial fulfilment
of the requirements
for the degree of
Master of Science in Geology
by

Stephanie Louise Gates

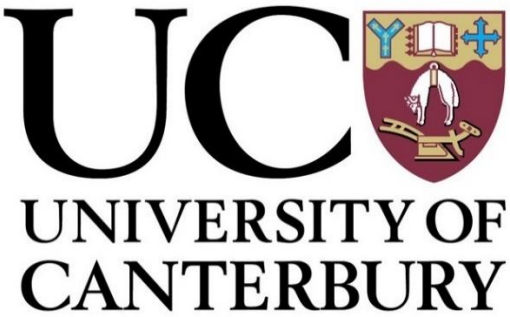

Department of Geological Sciences

University of Canterbury

New Zealand

2018

FRONTISPIECE

The Emerald Lakes, Tongariro

ABSTRACT

Ballistic projectiles ejected during explosive volcanic eruptions pose a significant hazard to people, infrastructure, buildings and the environment due to their high impact and sometimes heat energy, accounting for 40% of deaths within 5 km of volcanoes. Phreatic, steam-driven explosive eruptions, which often produce ballistics, are the most common eruption type on earth and can occur without warning. Active volcanoes with geothermal features such as bubbling crater lakes and fumaroles attract tourists, yet are most at risk of erupting phreatically. Recent mass casualties following hydrothermal or phreatic eruptions at Ontake Volcano, Japan in 2014, and a near miss at Tongariro, New Zealand in 2012, have highlighted the hazards posed by ballistics to tourists from relatively small but unheralded explosive eruptions. Ballistic hazard assessments are essential for informing risk management for these unexpected, ballistic-producing eruptions.

A ballistic hazard assessment seeks to determine the probability of eruptions which may eject ballistics, and to identify the areas or elements that ballistics may impact. A key part of this assessment is quantifying the area impacted and the intensity of the hazard within it, in metrics such as impact energy or number of blocks per area. However, current ballistic hazard assessments are limited by mapping methods which sample only a small proportion of a ballistic deposit, and guidance for field-appropriate methods is lacking. This thesis aims to advance ballistic hazard assessments by: (1) improving methods for mapping ballistic deposits through a comparative study; (2) using unique empirical data to improve input parameters for applying state-of-the-art 3D numerical modelling and; (3) creating a simple guide for future ballistic assessments that considers available resources, field time and state of the volcano. Two case-study tourist volcanic centres in New Zealand are the basis of these investigations, due to pressing need for their ballistic hazard to be assessed.

Current ballistic mapping approaches often inadequately describe the size distribution of erupted clasts, particularly small clast sizes, due to time and resource constraints of fieldwork and an under appreciation of their hazard. This constraint then limits the ability of numerical modelling to adequately describe the eruption dynamics and hazards. To investigate this, the most common mapping methods from the literature were applied to a complex phreatic block field at Red Crater, Tongariro and the results were compared to determine their efficiency, limitations and usefulness to risk assessments. Both a handheld photography or a newly-developed aerial imagery method was found to accurately determine the spatial density of ballistics, and, when combined with ground-

truthed field data, accurately and efficiently determined size and spatial distribution of blocks as small as 5 cm in diameter.

Using lessons learnt from this methodological comparison, and considering limited field time due to high risk of further eruptions, the handheld mapping method was applied at Whakaari/White Island. This provided a detailed spatial density and size distribution dataset to allow inverse, 3D multiparticle modelling to clarify the dynamics of an unwitnessed eruption. The modelled scenarios using both field and seismo-acoustic data indicate 3 highly directional eruptive bursts ejected blocks at speeds of 45 - 65 m/s at low angles of 30° from horizontal. 30% of the modelled mass did not exit the crater, and 8-21% of the tourist pathway was hit with blocks with sufficient kinetic injury energy to cause casualty. The addition of seismo-acoustic information also allowed the development of a 4D ballistic hazard scenario to analyse the ballistic hazard through time. The demonstration of a field to 4D ballistic hazard assessment approach and the development of a guide for future ballistic hazard assessments has supplied tools for increasing ballistic hazard assessment applicability to risk managers at volcano-tourism centres.

ACKNOWLEDGEMENTS

Firstly, to my amazing supervision team: Ben Kennedy, Tom Wilson and Jim Cole. Thank you for your time, wisdom and encouragement. Ben and Tom you've both been epic, providing a plethora of stories, beer and a series of amazing opportunities. Jim, you've been the glue that held this team together – for doing the hard yards and tackling the first iterations of my work I am so grateful.

To my field assistants, George, Matt, Elodie, Janina – the stories that were told on the 6 hour return hike, enthusiasm and amazing lack of complaints, despite the weather conditions, were great. To the tech savvy Dale and Alec, without your codes this work would not have been possible – thank you for being so generous with your skills and time. Ame McSporran and Janina Adolf – thank you for your help with the monotonous data crunching! Joshua Blackstock – thanks for approaching my poster at IAVCEI with such unrelenting enthusiasm and hatching the pixel-based identification plan.

Like raising a baby, a thesis takes a village, and I immensely thankful for to all the villagers who make up the UC geology department. To all the UC techies who have helped, in particular, Anekant Wandres, Matt Cockcroft, Grim, Rob Spiers, Sacha Baldwin-Cunningham, from building aluminium frames to being a mama bear – us post-grads would be lost without you all. For all the other staff who I have asked odd questions to and been patiently answered – thank you! Being a part of the CoUGARS and the Volc Group has made this past year so exceptional – learning from y'all and sharing the highs and lows of the thesis journey has been amazing. To my other Masters buddies, sharing this rollercoaster with you has been brilliant.

This project was supported by funding from the Mason Trust Fund, University of Canterbury Masters Scholarship & EQC Biennial Grant 16/727, without which this epic topic and fieldwork would not have been possible.

Finally, my friends and family, I am so lucky to have you all on my side – to my girl gang and mates – thanks for being into volcanoes, or at least faking it. To my family, thanks for being a consistent source of inspiration and wine; Mum, Dad, Briar, Meg, Jess, Becky & Pippa, Caro and Paul. Especially to Mutti for sharing your love of geology with dad who in turn passed it on to me – without you both I would not have appreciated this magnificent sphere we inhabit like I do today. And to my partner Callum – thank you for everything, for carrying a pack full of rocks for over 3 hours, for being there in times of celebration and commiseration, you have been amazing from start to finish.

GLOSSARY

Natural hazard - A natural hazard is defined as a natural event with the potential to cause loss of life or harm and damage to buildings, infrastructure and the environment (ISO, 2009).

Exposure – “the saturation of people, infrastructure, housing, production capacotes and other tangible human assets located in hazard prone areas” (UNISDR, 2017).

Risk – “The potential loss of life, injury, or destroyed or damaged assets which could occur to a system, society or community in a specific period of time, determined probabilistically as a function of hazard, exposure, vulnerability and capacity”. (UNISDR, 2017)

CONTENTS

LIST OF FIGURES

LIST OF TABLES

1. INTRODUCTION

1.1 Context of Study

Volcanic ballistics are a hazardous volcanic phenomenon which are a risk to people, infrastructure, buildings and the adjacent environment. Ballistics only account for only ~1% of total volcanic fatalities however, within distances of <5km, ballistic hazard accounts for 40% of deaths (Brown et al., 2017). The high impact and sometimes heat energy of ballistics can result in injury or death (Blong 1984, Baxter and Gresham 1997, Fitzgerald 2014, Oikawa et al., 2016), building damage through impact and ignition (Alatorre-Ibarguengoitia et al., 2006, Pisolesi et al., 2008, Wardman et al., 2012, Jenkins et al., 2014, Williams et al., 2017) and damage to the affected environment (Fitzgerald, 2017). In particular, ballistic hazards from unheralded phreatic eruptions have caused the greatest impacts and risk management challenges over the past decade (Barberi et al., 1992; Yamaoka et al., 2016; Baxter and Gresham, 1997; Fitzgerald et al., 2014). Additionally, the large growth in tourism on active volcanoes has substantially increased human exposure to these hazards (Taddeucci et al., 2017; Erfurt-Cooper, 2011, Stowell, 2017), whom with volcanologists and media personnel are the most commonly killed individuals by volcanic hazards (Brown et al., 2017). Complicating this, society has a decreasing acceptance of casualties in high-risk environments, such as active volcanoes, despite the increasing exposure through these higher visitor numbers. This has been observed globally, e.g. L'Aquilla Earthquake 2012 (Lauta 2014); Great Japanese Tsunami 2011 (Rich, 2017). This has required development of increasingly sophisticated risk management approaches. Whereas previously simple, coarse hazard or event exclusions zones were used for managing ballistic risk, now probabilistic risk assessment based approaches are increasingly being adopted (e.g. Biass et al., 2016).

The typical approach to risk management is the 'risk management process'. Figure 1 shows the standard practice framework for risk management used in New Zealand. First the parameters for study consideration are defined (Establish the Context), followed by identification, analysis and evaluation of the risk (Risk Assessment) before treatment options are implemented, for example reducing exposure through relocating walking tracks are considered (Risk Treatment). Communication and consultation with all stakeholders and review of the process should take place throughout each step of the process, to ensure the best possible risk assessment tools are being used, and the risk treatment options are useful and useable (AS/NZS, 2009; Section 1.2.3). This framework provides a structured and systematic approach for managing risk. Using this approach risk is calculated considering the hazard (natural event with the potential to cause loss of life or harm and damage to buildings, infrastructure and the environment (ISO, 2009)), the exposure of an element (person, building, asset)

and vulnerability (propensity to suffer impact) (Douglas, 2007). Simply expressed as; Risk = likelihood x (Hazard x Exposure x Vulnerability). There has been a number of challenges applying this for ballistic risk on active volcanoes, particularly in the risk assessment stage. The complex hazard of ballistics has been difficult to model, mostly through relatively poor understanding of the detailed physical process and the lack of substantive empirical data on the spatio-temporal distribution and intensity of ballistic impacts (Taddeucci et al., 2017). Secondly, assessing where people may be and how they may react when exposed to sudden ballistic hazards has also been a major challenge. The high impact velocities of >100m/s for ballistics from even small eruptions (Edwards et al., 2017) means humans and infrastructure are particularly vulnerable to ballistic impact, which studies are increasingly quantifying (Walker et al., 1971; Jenkins et al., 2014; Williams et al., 2017). The challenges of characterising ballistic hazard and exposure have led to a lack of understanding of ballistic risk compared to other volcanic hazards (Fitzgerald et al., 2017). Exposure assessments are complex and beyond the scope of this study, therefore the priority areas for improving ballistic risk assessment is hazard assessment, which this thesis focuses on.

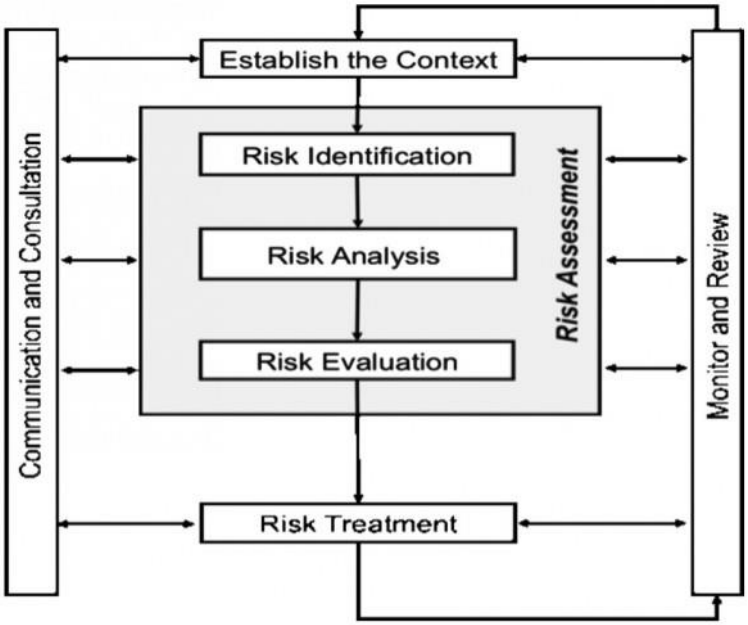

Figure 1.1 AS/NZS ISO 31000:2009 Framework for Risk Management. Retrieved from AS/NZS (2009)

Ballistic hazard assessments aim to determine the area impacted by ballistics, the intensity of ballistic impact (spatial density of ballistics and impact energy) and the frequency of the hazard, derived by a combination of field mapping and inverse numerical modelling (Fitzgerald et al., 2016). Recent eruptions and the frequency of casualties or near misses from phreatic eruptions in New Zealand (Table 1.1) have emphasized the need for ballistic hazard assessments for these eruptions. The Upper Te Maari eruption, Tongariro, in 2012 damaged the popular Tongariro Alpine Crossing track, but the timing and weather conditions of the eruption meant that there were no casualties (Fitzgerald et al.,

2014). In contrast, the Mt Ontake eruption in 2014, occurred during fine weather on a weekend killing 63 people (including missing persons), primarily from ballistic impact, and highlighted the hazard of 'small' phreatic eruptions (Kaneko et al., 2016; Shiroko, 2016). The Mt Ontake eruption also highlighted the danger of small clasts; with casualties from lapilli sized rock fragments (2-64mm diameter), much smaller than the cm-decimetre blocks (>64mm) usually considered in ballistic hazard assessments (Kaneko et al., 2016; Fitzgerald et al., 2014; Biass et al., 2016). Ballistic hazard assessments are currently limited by mapping approaches which are not systematic, frequently sample only a small fraction of the field and do not consider clasts < 20cm in diameter (e.g. Fitzgerald et al., 2014). Limited field data results in high uncertainty in modelling, and the subsequent resulting hazard metrics such as impact energy, which the model was employed to derive. As such, this thesis is focussed on developing structured, systematic approaches to mapping and modelling ballistic distributions for improved ballistic hazard assessments.

Table 1.1 Reported casualties or near miss eruptions in New Zealand, phreatic eruptions emboldened. Hydrothermal eruptions are considered a type of phreatic eruption in this study (see section 1.3). *signifies the area is a tourist attraction.

Date	Location	Phenomenon	Casualties/Fatalities	Reference
1846	Waihi (Lake Taupo)	Debris avalanche/mudflow from thermal area	~60 deaths	Civil Defence (1995)
1886	Tarawera	Magmatic eruption	>120	Cole (1970); Walker, Self & Wilson (1984); White & Chambefort, (2016)
1903	Waimangu (Tarawera)	**Hydrothermal eruption**	4	Civil Defence (1995)
1910	Waihi (Lake Taupo)	Debris avalanche	1	Civil Defence (1995)
1914	Whakaari	Debris avalanche/crater wall collapse	11 Sulphur miners killed	Nairn et al., (1996).
1917	Waimangu* (Tarawera)	**Hydrothermal explosion**	2	Civil Defence (1995), Migon & Pijet-Migon (2016)
1954	Ruapehu*	Lahar – destroyed rail bridge	151	Tephra, Civil Defence 1995
2001	Kuirau Park (Rotorua)*	**Hydrothermal eruption**	Near miss	Black (2006); White & Chambefort, (2016)
2003 November & October	Kairau Park *	**Hydrothermal eruption**	Near miss "park was filling with visitors"	"Eruptions at Kairau Park" (07/11/2003)
2005	Raoul Island	**Phreatic eruption**	1 DoC worker	Cole et al. (2006)
2006	Kuirau Park * (Rotorua)	**Hydrothermal eruption**	Near miss	Eriksen (2006)
2007	Ruapehu*	**Phreatic eruption**	2 injured, 1 severely, 1 near miss (snow groomer)	Kilgour et al. (2010)
2012	Te Maari (Tongariro)*	**Phreatic eruption**	Near miss	Fitzgerald et al., (2014) Bread et al., (2014)
2016, April & September	Whakaari*	**Phreatic eruption**	Near miss	Kilgour et al., (in review)
2018, July	Wai-O-Tapu*	**Hydrothermal mud eruption**	Near miss	Sparks (2017); Migon & Pijet-Migon (2016)

1.2 Aims and Objectives

The primary aim of this study is to improve ballistic hazard assessments through developing a guide for systematic hazard assessments which adequately define the spatial extent and intensity of the ballistic hazard. This will be achieved by using two New Zealand case study volcanoes, Red Crater, Tongariro and Whakaari (White Island). These volcanoes were targeted as they are prone to phreatic eruptions and attract >140,000 visitors annually (Jolley et al., 2014; Stowell, 2017; White Island Tours, 2018) yet lack ballistic hazard assessments. This thesis is concentrated on phreatic eruptions due to their hazard potential, relevance to New Zealand and their understudied status, however the lessons learnt are applicable to all ballistic hazard assessments.

The objectives of this thesis are as follows:

1. Review and analyse ballistic hazard mapping and modelling methods from the literature to discern current best methodological practice and knowledge gaps (Chapter 2).

2. Utilise and develop multiple ballistic mapping techniques at Red Crater, Tongariro Volcano to compare the effectiveness and efficiency of different mapping styles at a complex phreatic ballistic field (Chapter 3).

3. To improve mapping techniques of small clast sizes <5cm, for inclusion in ballistic hazard assessments (Chapters 3 and 4).

4. Apply an appropriate numerical model to inversely model a phreatic ballistic field, based on the mapping method utilised for the April 2016 eruption of Whakaari volcano, for informing both ballistic hazard and eruption dynamics (Chapter 4).

5. Develop a guide for location appropriate ballistic mapping techniques to assist future ballistic data collection for risk assessment or eruption dynamic studies (Chapter 5).

1.3 Thesis structure

To achieve the objectives stated above the thesis is structured as follows:

Chapter 1 introduces the thesis. Phreatic eruptions are defined and the specific hazardous characteristics which make them the study focus are explained. Ballistic hazard assessments are then addressed and placed within the risk management setting of New Zealand. Finally, the two case study field areas are introduced, including a brief geologic history.

Chapter 2 evaluates current ballistic hazard mapping techniques and their use within ballistic trajectory models, and the limitations of both mapping and modelling methods through a comprehensive literature review. How ballistic hazard assessments are applied within hazard maps internationally and in New Zealand is also reviewed.

Chapter 3 is a comparative study of mapping methods using Red Crater, Tongariro's phreatic ballistic field as a case study. Four different mapping methods are applied and assessed based on the area they cover and the accuracy of size and spatial distribution derived.

Chapter 4 uses the 27 April 2016 Whakaari eruption to demonstrate how intentional model choice, based on the mapped dataset type validated in Chapter 3, can successfully inversely model a complex phreatic eruption sequence. Use of a 3D trajectory model coupled with seismo-acoustic data allowed the development of a time varying ballistic hazard scenario with detailed spatio-temporal hazard intensities and extent.

Finally, Chapter 5 integrates the lessons from the Red Crater and Whakaari case studies into a simple ballistic hazard mapping and modelling methodology guide for future ballistic hazard assessments and concludes the thesis.

1.4 Phreatic and hydrothermal eruptions

Phreatic and hydrothermal eruptions are some of the most common, diverse and unpredictable types of volcanic activity on earth occuring frequently at volcanoes with volcano-hydrothermal systems (Barberi et al., 1992; Letham-Brake, 2013; Fitzgerald et al., 2014; Kato et al., 2015). The term 'phreatic eruption' has been used variably within the literature (Barberi et al., 1992; Browne & Lawless., 2001) to describe eruptions that are generated by either magmatic directly heating fluids, (Browne & Lawless, 2001) or by magmatic gases rising into a sealed or partially sealed hydrothermal system (Jolly et al., 2010). Phreatic eruptions are often difficult to distinguish from hydrothermal eruptions driven by shallow pressure changes in a hydrothermal system without the need for magmatic heat (Brown & Lawless, 2001). Here we do not distinguish between these eruption types and our use of "phreatic" also includes eruptions that may be referred to as hydrothermal by other authors.

Phreatic eruptions comprise different hazardous phenomena, including the eruption of rocks that follow approximate parabolic trajectories; which from here onwards we define as ballistics (Alatorre-Ibargüengoitia & Delgado-Granados, 2006). Phreatic eruptions eject country and conduit rocks following the expansion of liquid or gaseous water due to rapid decompression or heating of the system; as such initial particle velocity is higher on average for phreatic than magmatic eruptions (Mayer et al., 2015). Other phreatic phenomenon includes ash columns and crater formation (e.g. Inyo

Craters, California, Mastin 2001; Nisyros, Greece, Vougioukalakis & Fytikas, 2005), Surtseyan style activity (e.g. Ruapehu 2007; Kilgour et al., 2010), low temperature surges (Lube et al., 2014; Kilgour et al., in review) and smaller, bubble burst activity in crater lakes (Edwards et al., 2015). The ejected material consists of meter to ash sized particles of country rock, water when crater lakes are present (e.g. Kilgour et al., 2010), and notably an absence of any juvenile material. The greatest damage from phreatic eruptions is caused by ballistic impact and pyroclastic surges (e.g. Kaneko et al., 2016).

Phreatic eruptions are relatively small, poorly forecastable volcanic events. The lack of large volumes of shallow magma ascent reduces warning phenomena such a deformation, or distinctive evolving and shallowing earthquake swarms (Hurst et al., 2014). Barberi et al. (1992) reports that up to 38% of phreatic explosions had no precursory signals. However, many phreatic eruptions have seismic anomalies that are retrospectively identified as 'precursory signals' (Kilgour et al., 2010, Jolley et al., 2014, Walsh et al., in review; Chardot et al., 2016) but their subtle nature makes their pre-event identification rare. The small magnitude of phreatic eruptions also makes evidence of their occurrence scarce through poor preservation in the geological record (Strehlow et al., 2017). The lack of precursory eruption signals means that a phreatic eruption may leave little to no response time for persons proximal to the vent to take mitigative actions (Maeda et al., 2015; Strehlow et al., 2017). The lack of definitive precursors and mitigative options resulted in the deaths of six volcanologists in 1993 at Galeras Volcano, Colombia, and two volcanologists at Guangua Pichincha, Ecuador during phreatic events (Baxter & Gresham, 1997; Fink, 1995). These eruptions, plus the recent fatal phreatic eruption at Ontake (Kaneko et al., 2016) demonstrate how the most harmful ballistic-producing eruptions are often those which are relatively small and unexpected (Taddeucci et al., 2017).

Phreatic ballistics are one of New Zealand's most prominent volcanic hazards (Keys & Williams, 2013) as the eruptions are frequently unheralded (Barberi et al., 1992). Active volcanoes with geothermal features such as fumaroles and bubbling crater lakes often attract many visitors (Murphy et al., 2017) and worldwide volcano-tourism is a growing industry, including in New Zealand (Erfurt-Cooper, 2011, Stowell, 2017). Closure of attractions due to an eruption can severely impact individuals and community livelihood's (Leonard et al., 2014). This is especially true at our case studies of Tongariro and Whakaari, which attract >130,000 visitors per year combined (Jolley et al., 2014a; Stowell, 2017; White Island Tours, 2018).

1.5 Ballistic Hazard Assessment in a Risk Management Setting.

To contribute towards mitigating the impact of volcanic eruptions on society, hazard assessments are undertaken by volcanologists to evaluate the area impacted by a volcanic phenomena and the frequency of impact (Thouret et al., 2000, Alatorre-Iberguengoitia et al., 2006; 2012). The ultimate aim of hazard assessments is to help to reduce casualties from volcanic disasters (Burby & Wagner, 1996; Baxter & Gresham, 1997; Blong et al., 1984; Erfurt-Cooper, 2011). Ballistic hazard assessments seek to understand the frequency of previous eruptions to determine probability of future eruption and understand the extent and intensity of ballistic hazard. The extent and intensity is derived through mapping past eruption deposits and using numerical models to determine intensity metrics, such as impact velocity and number of blocks per m^2 (Fitzgerald et al., 2014). The frequency of the hazard can be determined using the eruptive history of a volcano, found through literature review (e.g. Scott & Potter, 2014) or fieldwork (e.g. Moebis et al., 2011). The spatio-temporal information gathered during a hazard assessment is then used as a basis for risk assessment where the likelihood of consequences (e.g serious injury or death, property and infrastructure damage, economic impact) from the hazard is determined (Blong 1996, Fitzgerald 2017). Increasingly, quantification of proximal volcanic hazards is required as tourism to active volcanoes around the world rises, and governments and stakeholders seek to protect life safety, and minimise economic and environmental impact (Erfurt-Cooper 2011).

For ballistic hazard assessment to produce high quality spatial extent and intensity data for risk assessments, detailed field mapping and probabilistic ballistic trajectory modelling is required. Currently a variety of ballistic mapping methods are applied around the world, with a range of time and technical resources required. Ballistic mapping varies in the level of detail sought, ranging from mapping only a few individual ballistics at maximum range (Alatorre-Ibarguengoitia et al., 2010, 2016; Biass et al., 2016; Bertin, 2017), to highly detailed field mapping with the number of particles, size of particles and spatial density per area mapped (Pistolesi et al. 2008; Guroli et al. 2013; Fitzgerald et al., 2014; Kaneko et al., 2016). As the detail of the mapping increases, so too does the length of time necessary to carry out fieldwork. Data collection may be largely direct with trained individuals in the field, requiring significant time to map (Swanson et al., 2012), or remote mapping through collection of ortho-imagery which may reduce field time demands, but limit the detail of data collected (Kaneko et al., 2016; Guroli et al., 2008; Fitzgerald, 2017). To translate the mapped ballistics into relatable hazard maps or obtain eruption conditions, numerical trajectory modelling is commonly applied, the nature of which is determined by the detail of the mapping. Highly detailed maps give a good indication of the hazard footprint and intensity and allow inverse modelling (Fitzgerald et al., 2014; Tsunematsu et al., 2016), while ballistic hazard studies based on a few ballistics or with high levels of

uncertainty require a probabilistic approach (Alatorre-Iberguenoitia et al., 2006, 2012, 2016; Biass et al., 2016; Bertin, 2017).

Currently, ballistic hazard assessments are limited by both the mapping and modelling methods used. Most ballistic mapping campaigns do not collect complete datasets, focussing on only the most distal clasts (Alatorre-Ibarguengoitia et al., 2012, 2016; Biass et al., 2016) or field outlines (Minakami, 1942). Whilst these mapping approaches determine the hazard footprint they do not adequately constrain the hazard intensity in terms of the spatial density of clasts, a crucial parameter for ballistic risk assessments (Fitzgerald et al., 2017). For ballistic modelling to be informative to eruptive processes, the input parameters must be as constrained as possible, using high quality, completely mapped ballistic fields. Presently the size distribution of clasts is often over simplified for modelling (Biass et al., 2016, Strehlow et al., 2017) despite the huge importance of particle size on transport dynamics (Self, 1980; Wilson, 1980; de' Michieli Vitturi et al., 2010). In some cases, complete ballistic datasets are not possible due to time since eruption or other barriers to preservation (e.g. Waitt et al., 1995, Swanson et al., 2012). However, in cases where data is available but not collected due to restricted field time or resource constraints (Fitzgerald et al., 2014; Kilgour et al., in review), more efficient mapping methods can create more complete ballistic datasets and consequently more accurate modelling.

This study will address the challenges and potential of ballistic mapping and ballistic modelling to inform hazard managers using two New Zealand case studies. Red Crater, Tongariro Volcano has a composite phreatic ballistic field emplaced by multiple eruptions within the last 500 years through which the highly popular (>140,000 visitors per annum) Tongariro Alpine Crossing track traverses. Here four mapping techniques are applied and their effectiveness and efficiency compared. Whakaari is one of New Zealand's other highly popular tourist destinations with ~18,000 visitors per year (White Island Tours, 2018). Whakaari was chosen as the second case study after an unheralded phreatic eruption in 2016, which was rapidly mapped using a handheld photography method, due to risk of further eruption. The dataset collected was then used to inversely model the eruption for insights into eruption dynamics and ballistic hazard. As such, Whakaari is used to illustrate an appropriate model choice for ballistic hazard assessment based on the specific mapping techniques undertaken in a high-risk environment.

1.6 Geological Setting

1.6.1 New Zealand volcanism

Active volcanism, and most of New Zealand's geology, is driven by the oblique convergence of the Pacific and Australian plates (Cole et al., 2000). Subduction of the Pacific plate westward beneath the Australian Plate occurs at ~42-50mm/yr beneath the North Island forming the Taupo-Hikurangi arc-trench system (Bibby et al., 1995). The Taupo-Hikurangi arc-trench system is contiguous with the northern Tonga-Kermadec arc system, extending northward ~2800km (Cole et al., 2000). The southernmost expression of this arc and back-arc basin system is the Taupo Volcanic Zone (TVZ) (Figure 1). 22 Ma of continental volcanism in the North Island is now concentrated in the modern TVZ, with volcanism ongoing from the Late Pliocene (~2Ma) to contemporary times (Cole, 1990; Wilson et al. 1995). The TVZ consists of a ~300km long NNE-SSW trending zone, 60km wide at its maximum, extending from Ohakune in the south to the edge of the continental shelf ~100km offshore of the Bay of Plenty coast (Cole et al., 1990; Wilson et al., 1995). Extension is asymmetrical with extension rates of ~15mm/y in the Bay of Plenty reducing to <5mm/y at the southern end (Wallace et al., 2004; Reyners, 2010).

The TVZ is divided into approximately three sections, a central zone dominated by rhyolitic volcanism, with minor eruptions of high Al basalt (Cole, 1990), bordered by two zones of largely andesitic volcanism (Graham et al., 1995) (Figure 1.2). The southern andesite region is represented by the Tongariro Volcanic Complex, while 300km north Whakaari (White island) emerges above sea level in the Bay of Plenty andesitic region, marking the northernmost surficial expression of the TVZ (Bibby et al., 1005; Cole et al., 1990, Figure 1). Tongariro and Whakaari Volcanoes are both andesitic stratovolcanoes with large volcano-hydrothermal systems (Giggenbach et al., 2003). The presence of hydrothermal systems consequently leads to eruption styles varying from phreatic to phreato-magmatic to purely magmatic (Mongillo & Wood, 1995; Miller & William-Jones, 2016).

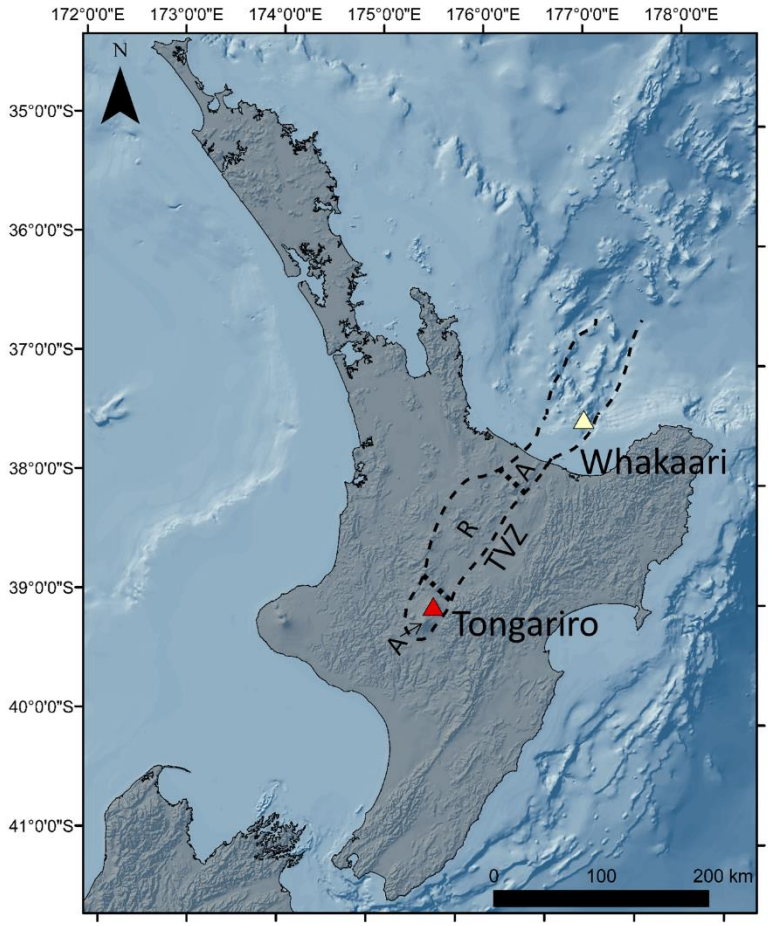

Figure 1.2 Location map of Whakaari and Tongariro within the Taupo Volcanic Zone (TVZ), showing approximate borded between the central Rhyolitic zone (R) and northern and southern Andesitic zones (A) drawn from Bibby et al., 1995.

1.6.2 Tongariro Volcanic Complex (TgVC)

The Tongariro Volcanic Complex (TgVC) is ~55km long and comprised of four large andesite edifices, Kakaramea, Pihanga, Tongariro and Ruapehu, three smaller cones; Maungakatote, Pukeonake and Huahungatahi and four explosion craters near Ohakune (Cole et al., 1990, Figure 1.3A). Although volcanism is largely calc-alkaline medium K andesites, minor basalt and dacite is present (Cole et al., 1986; Graham & Hackett, 1987). Compositional variation and frequent, small eruptions has led various authors to suggest that magma in the TgVC is erupted from a series of interconnected small magma bodies, dykes and sills, in the crust and upper mantle (Gamble et al., 1999, Hobden et al., 1999; Price et al., 2005; Kilgour et al., 2013).

Volcanism in the TgVC is at least 300ka (Flemming, 1953) based on pebbles of Mt Ruapehu Andesite found in Lower Pleistocene conglomerates, and likely ~350ka based on ring-plain volcaniclastic deposits (Gamble et al., 2003). Two volcanic chains have been identified within the TgVC; an older NW- SE chain which erupted >26ka; and the younger, currently active NE-SW chain (Figure 1.3B) (Cole,

1978; Topping 1974; Cole et al., 1986; Graham and Hackett 1987). The NE-SW alignment is parallel to the current subduction interface and evidence of the complex interplay between subduction related tectonism and volcanism in the TgVC (Gregg, 1961; Matthews, 1967; Cole, 1978; Shane et al., 2017).

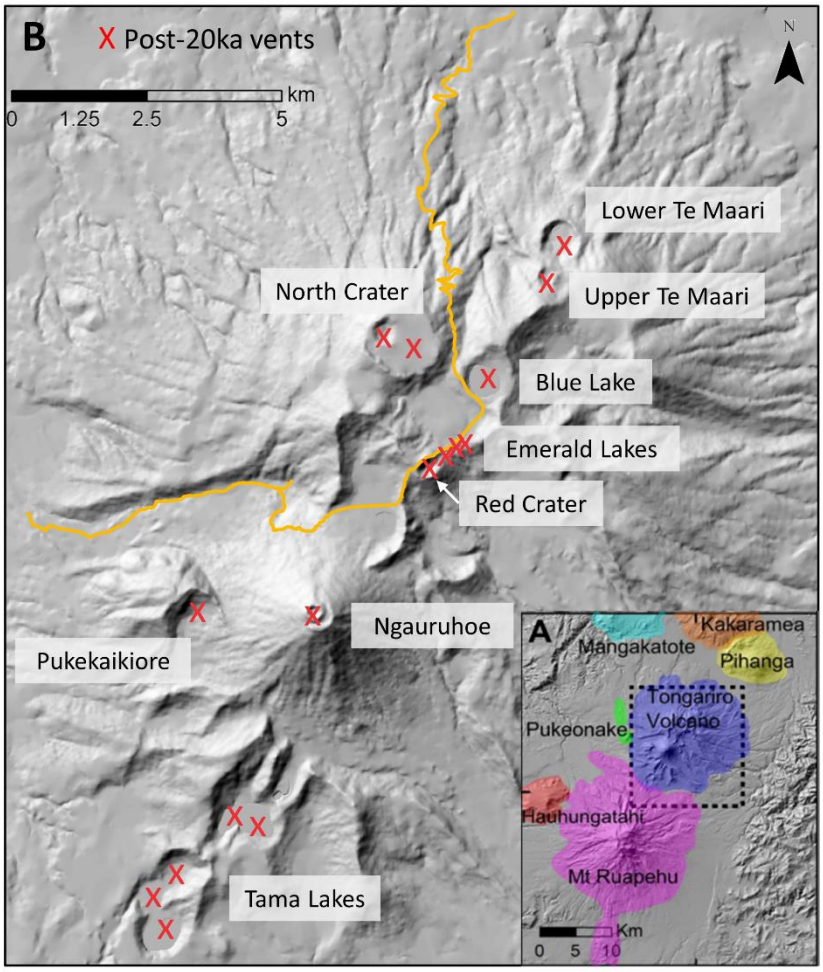

Figure 1.3 Location map of A) Tongariro Volcanic Centre (TgVC) (from Fitzgerald et al., 2014) and B) Young eruptive vents of TVC <20ka (following Shane et al., 2017). (DEM NZSoSDEMv1.0 09 Taumaranui 15m)

Tongariro Volcano Complex (TVC) is a massif ~60km^3 in volume made up of at least 17 coalescing composite volcanic cones, with individual volumes of ~0.3 - 12km^3 (Hobden, 1999; Shane et al., 2017). Volcanic activity has occurred along the NE-SW chain within a 13km by 5km vent zone with no spatio-temporal trends and some cone building overlapping in time (Hobden, 1999). Tongariro has been active since 275ka based on dating of lavas, however stratigraphic evidence suggests Tongariro has been active since at least 340ka (Cole, 1978; Topping, 1974). Activity has been clustered in time with peaks at 210-200ka, 130-70ka and 25ka – present day (Hobden et al., 1996). Ketetahi hot springs on the northern aspect of Tongariro and fumeroles at Red Crater and the Emerald Lakes are the surficial expression of a steam-dominated geothermal system (Moore & Brock, 1981). The potential for

eruptions from this system were recently demonstrated by the hydrothermal eruption at Upper Te Maari Crater in 2012 (Fitzgerald et al., 2014; Lube et al., 2014).

1.5.2.1 Red Crater

While the Tongariro Volcanic Complex (TVC) is dominated by andesitic volcanism, at its centre is Red Crater, a basaltic-andesite scoria cone (~0.3km^3) (Hobden, 1999). Red Crater has been active since ~3.4ka, erupting at least 11 lava flows (Topping, 1973, 1974, Shane et al., 2017). Late stage Strombolian style activity created the modern scoria cone, constructed upon the older Tongariro Trig andesite lavas (65-110ka) which outcrop at the base of the inner crater walls (Hobden et al., 1996; Bardsley, 2004; Wadsworth et al., 2015). The scoria cone was subsequently dissected along a NNE-SSW fissure during a final, undated, hydrothermal eruptive phase (Topping, 1973; Cole et al., 1986; Hobden, 2000; Wadsworth et al., 2015). At the top of the scoria cone are coarser andesite clast rich layers alternating with similar composition finer-grained ash-rich layers. The lithic rich coarser layers are interpreted by Bardsley (2004) to be a result of the late stage phreatic eruption with finer layers related to outwash from Tongariro summit. Following the NNE-SSW lineament along a poorly defined fault are a series of explosion craters considered part of Red Crater formed by phreatic and phreatomagmatic eruptive activity, the Emerald Lakes (Simons, 2014; Bardsley, 2004; Shane et al., 2017). The Emerald Lakes age are estimated at ~1.3ka based on tephra deposition (Topping, 1974) however the presence of ballistics on the adjacent Central Crater Lava flow, dated at 500-200 YBP (Greve et al., 2016) suggests recent activity is possible.

1.5.2.1. Recent eruptive history of Red Crater

Red Crater is the most historically active TVC vent following Ngauruhoe with active fumarolic activity for the entire history of recorded observations until the present day (Cole & Nairn, 1975; Scott & Potter, 2014). The eruptive history of Red Crater is relatively unconstrained with most of the historical eruptions known from distal observations of ash plumes or observations of new craters (Scott & Potter, 2014).

Scott and Potter (2014) complied historical data from newspaper collections, unpublished scientific reports, published research, parliamentary reports and New Zealand literature on eruptions from Mt Tongariro. They found that Red Crater likely erupted in 1855, 1886, March and August 1897, 1926 and likely 1927 (Table 1.2). In 1934 new craters appeared by Red Crater, presumably due to a phreatic or phreato-magmatic eruption, however no description of an eruption was found; this was followed by "high levels of unrest" in 1935 (Scott and Potter, 2014). Little detail on the style and duration of the eruptions was included in historical records, as many were noted based on distant observations of plumes. The short-term recurrence interval from historical observation suggests a minimum of 7

historically observed eruptions from 1855-2018, a recurrence interval of ~23 years. Moebis et al. (2011) used tephra stratigraphy to discern that Red Crater has erupted magmatically at least 16 times during the last ~300 years, a recurrence interval of ~18.75 years. The recurrence interval of Red Crater, based on historical and geological records is therefore between 18.75-23.57 years (Moebis et al., 2011; Scott & Potter, 2014).

Table 1.2 Historical activity at Red Crater (Modified from Scott and Potter, additional activity from Gregg 1961b).

Date	Description of Activity
January 1855	Ash eruption
1859	Steam Eruption
June 1886	Possible eruptive activity. Collapse and disappearance of 'chimney like cone, which stood near the verge of Red Crater' (Gregg, 1961b) Possible clouds of black smoke seen and visible changes to Red Crater
1887	Vigorous Steaming
1888	Small lava-stream inside crater
1891	Violent steaming, suffocating sulphur fumes
1893	Western side very active
2nd March 1897	Ash eruption
17 September 1897	"Eruptions" occurred at Red Crater and Te Maari (unknown if ash or steam)
1908	Vigorous steaming, very noisy
1911	Activity rapidly decreasing
1926	Vigorous Steaming
1926	Eruption black smoke from a 'new vent' - Emerald Lakes (?)
1927	Eruption likely from Red Crater
1934	New Craters by Red Crater - likely Emerald Lakes

1.6.3 Whakaari (White Island)

Whakaari is of similar size to Tongariro with a total volume of ~78 km^3 located 50km offshore of the Bay of Plenty coast (Figure 1.4, Cole et al., 2000). Most of the massif is underwater and rises from the continental shelf to emerge a maximum elevation above sea level of 321m, occupying an area of ~3.3km^2 (Nishi et al., 1996; Cole et al., 2000; Werner et al., 2008). Whakaari is comprised of two overlapping composite andesitic-dacitic cones, the extinct Ngatoro Cone to the northwest and the superimposed younger Central Cone to the Southeast (Duncan 1970, Figure 1.4). The horseshoe shaped main crater is elongated in the NW-SE direction (1.2km x 0.4km) and consists of three overlapping prehistoric craters that are filled with historical eruption deposits (Houghton & Nairn 1991). Historical volcanism has been concentrated in the western subcrater which is periodically filled with a hot (30-50^{oC}) acidic (-1-0 pH) crater lake (Houghton & Nairn 1991; Werner et al., 2008; Cole et al., 2000). A sector collapse(s) of the eastern side of the edifice has created the present horseshoe shape and breached the crater to the sea in three south-eastern locations (Cole et al., 2000). The modern crater floor is <30m above sea level and covered in hummocks from a debris avalanche in 1914 caused by the collapse of the south-eastern main crater wall in which 11 sulphur miners were killed (Nairn et al., 1996; Cole et al., 2000).

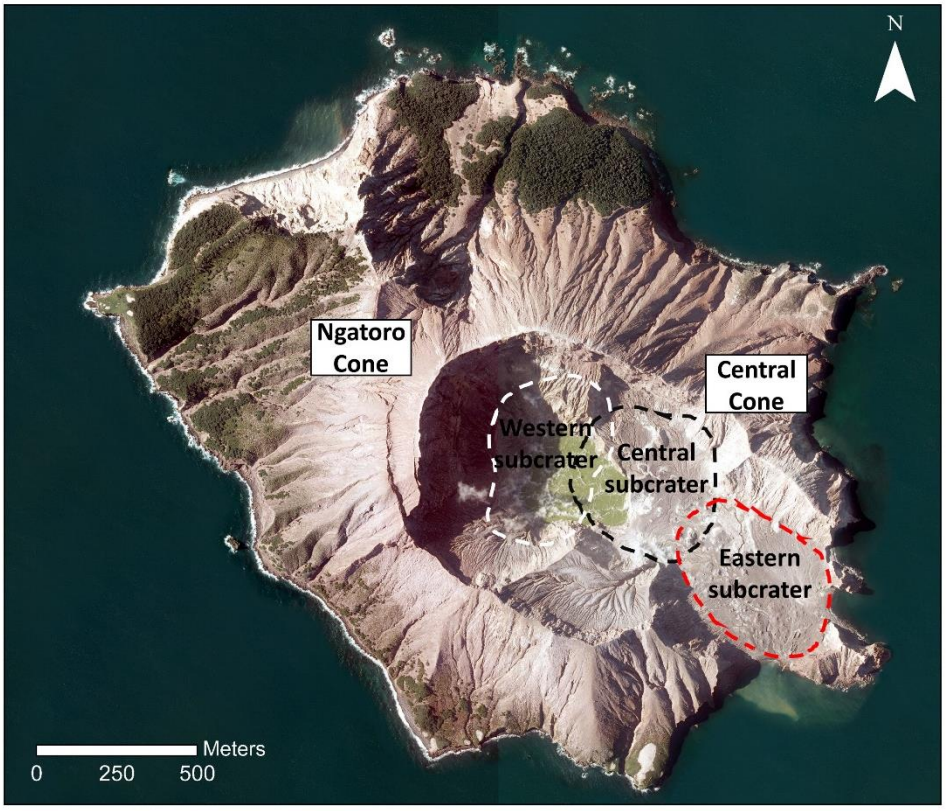

Figure 1.4 Whakaari Volcano. Craters are drawn from Moon et al. (2005), image shows extent of crater lake in 2011

Volcanism at Whakaari commenced subaqueously at ~150ka with earliest accessible lavas dated at ~22ka (±0.5ka) (Hamilton & Baumgart, 1959; Cole et al., 2000; Letham-Brake 2013). Magma periodically resides at shallow depths <500m, sourced from deeper magma chambers at ~1-2km and 2-7km depth (Cole et al., 2000). These shallow magma chambers drive Whakaari's characteristic strong outgassing and active fumuroles (100-800°C) and hotsprings (Giggenbach et al., 2003).

1.6.3.1 Recent eruptive history of Whakaari

Whakaari is New Zealand's most frequently active volcano over the last 150 years and has been in a near constant state of unrest since human settlement (Cole et al., 2000). Since 1826 Whakaari has had 27 documented phreatic eruptions (Mayer et al., 2015; Kilgour et al., in review) and has been continuously active since 1976 (Werner et al., 2008; Wood, 1994). Eruptive activity is characterised by phreatic and phreato-magmatic eruptions as well as infrequent strombolian events in historical times producing, in decreasing frequency, andesitic, dacitic and basaltic andesite eruption deposits (Cole & Nairn, 1975; Houghton & Nairn, 1991; Cole et al., 2000, Figure 1.4). The discharge of gases and hot springs onto the crater floor are the surface expression of the islands well developed volcano-hydrothermal system (Giggenbach et al., 1987; Christenson et al., 2017).

Several documented eruptions have emplaced volcanic material onto areas frequented by tourists. A phreatic, possibly phreatomagmatic, eruption occurred in October 1993, ejected blocks up to 20cm in diameter, although most were <10cm in diameter. Impact pits were spread an average of 1 m to 2 m apart with many blocks "skipping" up to 50cm across the surface from their original impact position. The blocks were primarily partially altered andesitic lava and clumps of poorly sorted breccia containing hydrothermally altered clastic material (Global Volcanism Program, 1993). A magmatic eruption in 2000 deposited juvenile pumice and tephra onto tourism pathways (Geonet, 2016). Whakaari has recently been in a heightened state of unrest with periodic explosive eruptions between 2012 and 2013 as well is the effusion of a small lava dome in late 2012 (Nairn et al., 1991; GeoNet, 2016). During the largest eruptions, 5 August 2012, 11 and 20 October 2013, ballistic ejecta and pyroclastic surge were generated which covered the crater floor as well steam and ash plumes (Chardot et al., 2015). Smaller phreatic/hydrothermal eruptions in 2012-2016 also erupted ballistics and mud, producing ballistic hazards to tourists (Edwards et al., 2017).

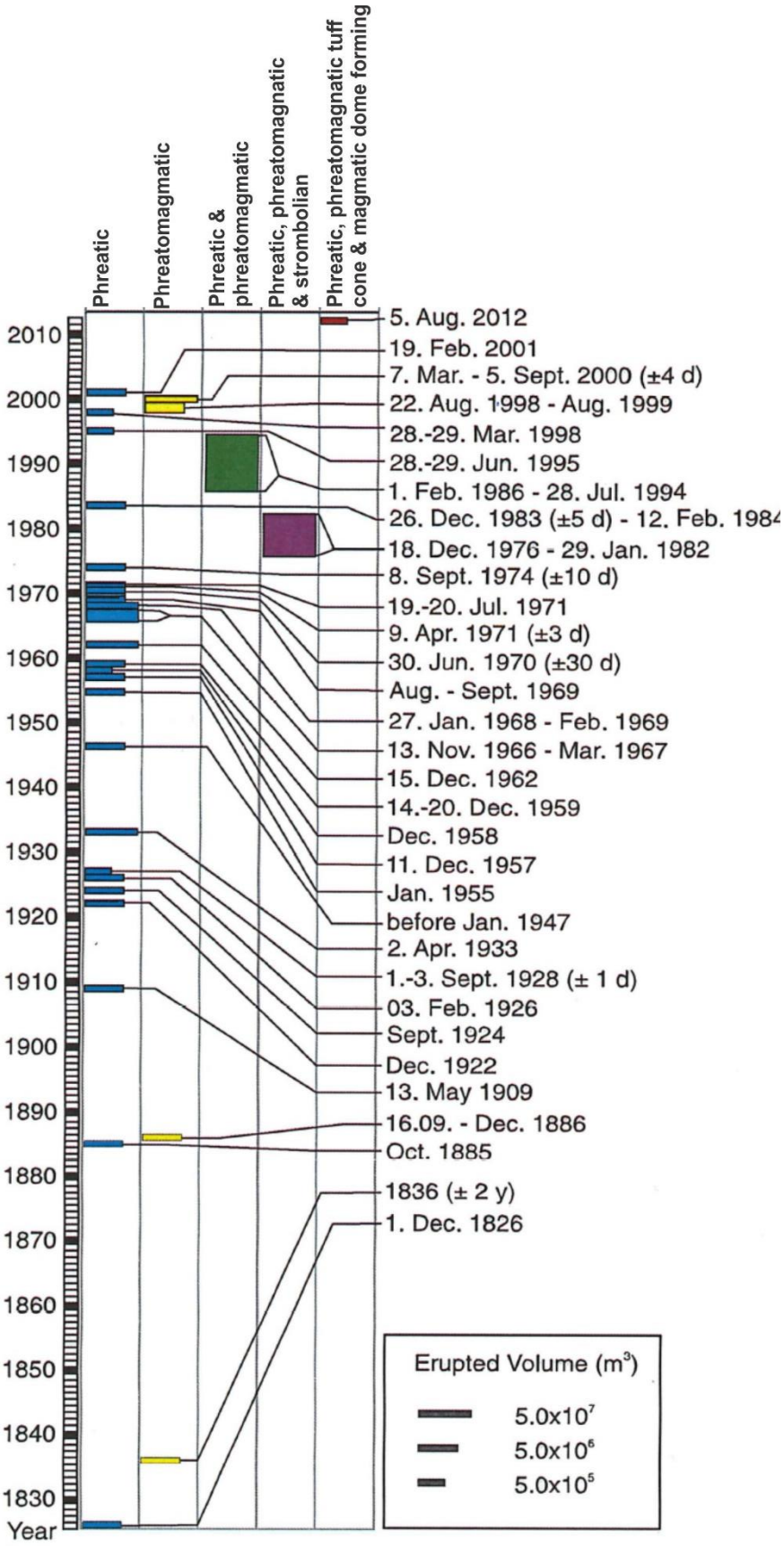

Figure 1.5 Historical eruptive history of Whakaari (Modified from Mayer et al., 2015).

2 LITERATURE REVIEW: BALLISTIC HAZARD MAPPING AND MODELLING APPROACHES.

2.1 Introduction

Ballistic hazard studies based on previous eruption deposits are the primary tool for hazard managers to assess how significant the hazard posed by phreatic ballistics is at any specific volcanic centre (Fitzgerald et al., 2017). For ballistic hazard assessments to be useful to risk assessors, hazard managers must provide information on the area likely to be impacted and the intensity of the hazard, as well as the frequency with which they occur (Fitzgerald et al., 2017). Ballistic hazard studies of phreatic eruptions are rare despite their hazard footprint being dominated by ballistic clasts, as well as pyroclastic surge and fallout of non-juvenile ash from steam plumes (Kilgour et al., in review; Kaneko et al., 2016). This is because the short lived, transient events are rarely witnesses or recorded and their small eruptive mass means their preservation potential in the geological record is low (Strehlow et al., 2017; Kilgour et al., in review). As such, this literature review largely draws on examples of the distribution of magmatic ballistics (bombs) which dominate the literature.

The methodology of ballistic field mapping is determined by (1) the purpose of the study, e.g., to determine the maximum ballistic hazard extent (e.g. Alatorre-Iberguenoitia et al., 2012, 2016); the zone with the highest probability of fatality hazard (Fitzgerald et al., 2014); using ballistics to infer eruption conditions (Tsunematsu et al., 2016). (2) The study site and situation e.g. crisis vs a quiescent volcano; remote vs accessible; time and financial resources available (Kilgour et al., in review; Leonard et al. 2014). Therefore, flexibility with the style of field approach is required. There is currently no guide as to what methods are appropriate when undertaking ballistic field mapping campaigns to inform hazard assessments, or how those methods should inform the choice of ballistic modelling software. This chapter serves to review the current state of ballistic mapping and modelling, and how these outputs are best used within a hazard management framework to address objective one of this thesis.

2.2 Ballistic Distribution Mapping Methods

Ballistic impact distribution maps are created after volcanic eruptions or when investigating the eruptive history of a volcano to show the form and extent of ballistic hazard (direction, distance from vent, size and shape of the field and variation of impact density) based on the spatial distribution of clasts. Ballistic distribution maps result from mapping a specific event ballistic field (Guiroli et al. 2013) or the cumulative ballistic field from several events (Swanson et al., 2012). While ballistic distribution

maps indicate the mapped area of ballistic hazard, they vary from hazard maps in terms of their purpose and use (Fitzgerald et al., 2017).

Ballistic distribution maps are used to infer eruptive conditions such as directivity and angle of eruption; the initial velocity of clasts; vent location (Swanson et al., 2012; Kaneko et al., 2016) and investigate vent development (Bread et al., 2014). Ballistic distribution maps show the area impacted by ballistics and are generally composed of the location of ballistics and/or their craters with some also indicating the size of clasts (e.g. Fitzgerald et al., 2014). In contrast, ballistic hazard maps can show the spatial extent and magnitude of ballistic hazard and/or likelihood of impact and maybe advise measures to reduce this hazard (Fitzgerald et al. 2017). The ballistic hazard map is therefore informed by the ballistic distribution mapping, literature and/or through application of a ballistic model. Ballistic hazard maps will be discussed later in the chapter; this section focuses on the methodology used to collect ballistic data and the creation of ballistic distribution maps.

There have been few studies that undertook detailed ballistic mapping and published maps are most often incomplete. Complete ballistic maps, in which the full ballistic field is mapped, are time intensive and require good preservation of deposits therefore 'incomplete' maps, in which only a portion or outline of a ballistic field is shown are more common (Minakami, 1942; Corbin & Foster, 1959; Lorenz, 1970; Fudali & Melson, 1971; Nairn & Self, 1978; Self et al., 1980). The lack of completeness of ballistic distribution maps could be due to (1) the risk of further volcanic activity limiting mapping time (Kilgour et al., 2010, in review), (2) poor preservation due to lithology impacted or subsequent deposition of volcanic material (e.g. Fudali & Melson, 1971; Self et al., 1980), (3) the large time resource and consequent cost of field mapping, (4) accessibility challenges due to remote field locations (Waitt et al., 1995) and (5) resolution or coverage limitations when mapping from aerial photography (e.g. Fitzgerald et al., 2014, Kaneko et al., 2016). Due to the above limitations complete ballistic maps are rare, however with technical advances, particularly the proliferation of aerial imagery from Unmanned Aerial Vehicles (UAV's), more complete maps are becoming common (Self et al. 1980; Pistolesi et al. 2008; Guroli et al. 2013; Fitzgerald et al., 2014; Kaneko et al., 2016).

2.2.1 Complete Maps

Complete maps that contain full size distributions can be used to understand both eruption dynamics and hazard. Following a detailed field campaign Self et al. (1980) produced a multi phenomenon deposit map that included the spatial extent of lithic blocks from the early phase of the 1977 eruption of Ukinrek Maars. They mapped impact craters (some were obscured due to ash fall), and the late

stage block and bomb aprons on the surface. They delineated the edge of the block field and undertook five transects for which they measured the dimensions, mass and assigned a shape factor to over 200 blocks of the late stage blocks and bombs. From this detailed mapping they found that the size distribution of blocks decreases in size away from the maar rim in the later eruption but increased with distance during the early stage. This comparison between size distributions allowed the authors to imply differing drag conditions and a varying role of water between the two eruptions.

Magmatic eruptions produce bombs and their distribution and total mass can be used to assess eruption energies and dynamics such as directivity. Pistolesi et al. (2008) mapped the 5 April 2003 eruption of Stromboli through a combination of impact crater mapping over multiple field seasons, and aerial photos taken before and a few days after the eruption. The aerial photos vary between the scale of 1:7000- 1:5000 with ground-truthing indicating that only blocks greater than 2 metres in diameter could be observed in aerial images. 37 impact craters were mapped covering an area of 0.3km^2 up to 2km from the vent with a maximum block size of 3.5m. The deposit was strongly asymmetrically distributed, concentrated in narrow lobes to the NE and WSW. Guiroli et al. (2008) mapped 780 bomb locations and sizes from the bomb field of the 21st January 2010 Stromboli eruption (Figure 2.1). They also used a combination of field mapping and aerial photos with the addition of a thermal camera which observed only one explosion directed towards the SSE-SW enabling them to map a deposit from a known eruptive burst. The bomb field extended to a maximum distance of 429 m with measured clast sizes ranging from 7cm – 459cm in diameter. These studies show the importance of complete and detailed ballistic mapping to assess eruption energy, directivity dynamics and to tie into monitoring data.

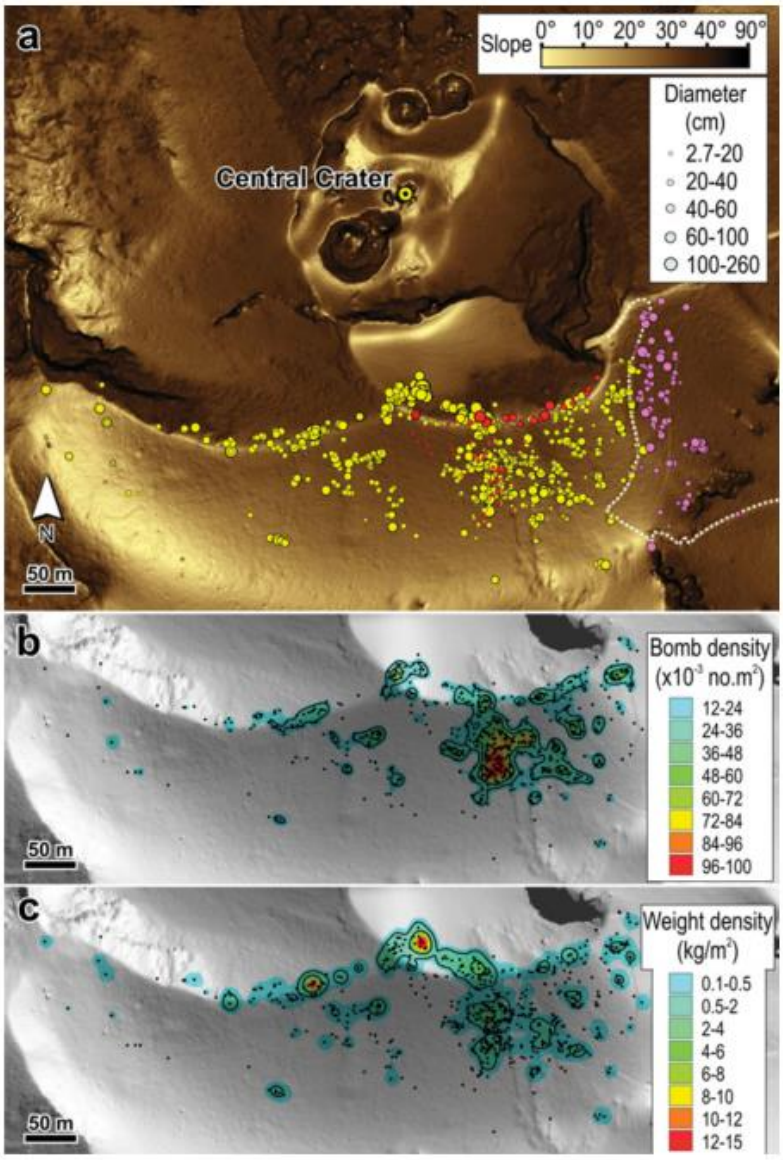

Figure 2.1 Published complete ballistic map of Stromboli volcano eruptions from Gurioli et al., (2013). a) Bomb locations mapped from thermal imagery by size. Purple circles from the 24 November 2009 eruption; Yellow 21 January 2010; Red field sampled bombs and dashed line shows tourism pathway. b) Spatial density of bombs from the 21 January event, c) weight density of bombs from January.

Monitoring data can also be coupled with ballistic mapping through eruption energies to give a fuller understanding of the eruption and its dynamics. The detailed ballistic map made following the phreatic eruptions of Te Maari volcano, Tongariro (Fitzgerald et al., 2014) was interpreted using seismo-acoustic data. By analysing more than 300 aerial photographs, orthophotographs with a 100m grid overlay Fitzgerald et al. (2014) found more than 3587 impact craters from the August 2012 hydrothermal eruption at Te Maari. The craters ranged from 0.3 to 10.8 m in diameter and fieldwork revealed an average ratio of 1 orthophoto detected crater to 4.5 field-mapped craters, indicating the need to combine fieldwork with remote mapping for accurate results. This mapping and seismo-acoustic interpretation allowed identification of low-angled, distinct eruption pulses.

A detailed spatial size distribution map also reveals important hazard considerations such as directionality and topographic shielding. Detailed mapping of the Tongairro 2012 ballistic field by Bread et al., (2014) found a high density section of the ballistic field. This information combined with application of a simple ballistic trajectory model (Eject! (Mastin, 2001)) indicated the eruption was highly directed. Kaneko et al., (2016) mapped the block field of the fatal 2014 Mount Ontake eruption, based on 350 photographs taken from a helicopter the day following the eruption. Extensive disruption of the field deposits following rescue efforts, restricted access, and rainfall meant photography and eyewitness testimony was the primary mapping input and ground truthing was limited. 5x5m areas were approximated on each photograph and the number, and size of the craters and ballistics recorded. Craters ranged from tens of centimetres to 1 m while ballistics ranged from 10 cm to a maximum of 1m. An isopleth style map was created with four zones based on the spatial density of craters with the number of ballistic per m^2 decreasing with distance from the vents. The deposit was slightly extended in a NNE direction due to the directionality of the eruption and/or the topographic barrier of the steep-sided, linear valley where the vent was located. Complete maps are therefore useful to understand both the spatial distribution of the hazard intensity and the dynamics of the eruption.

2.2.2. Incomplete Mapping Approaches

The limitations of mapping results in incomplete or partial maps recording only a section or the outer limits of the field and these can only be applied to obtain maximum travel distance for hazard or to answer specific eruptive condition studies. Minakami (1942) mapped the outer limits of the Vulcanian ballistic fields from the 20 April 1935, 16 April 1937 and 7 June 1938 eruptions of Asama volcano, Japan (Figure 2.2). The fields were mapped in the days following the eruptions. The maps show whole field outline, and the maximum distance and diameter of clasts greater than ~50cm. The 20 April 1935 ballistic field was approximately circular with clasts reaching 2.8km from the vent while the April 1937 and June 1938 had easterly distributed fields with clasts of 1-7.5m in diameter reaching up to ~3.4 and 4.5km from the vent respectively. Partial mapping of the field outline for June 1938, hampers the confidence in implications of directivity and maximum distance for this eruption and lacks an understanding of the severity of the hazard within the zone.

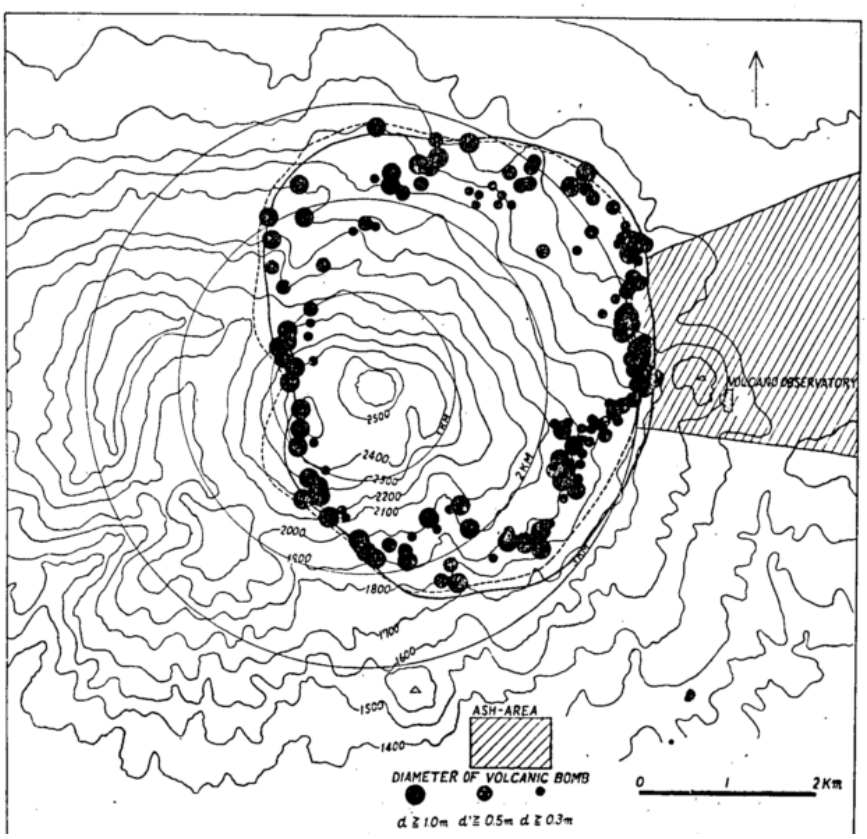

Figure 2.2 Mapped distribution of volcanic bombs at Asama volcano, Japan during the April 16, 1937 eruption from Minakami (1942). Diameter of bombs and their locations is mapped with a focus on the most distal samples for use in eruption parameter modelling.

Eruption dynamic studies require less complete ballistic distribution information than hazard maps intended to inform risk managers. Nairn and Self (1979) produced a map with the approximate range of ballistics from the 1975 eruption of Ngauruhoe, however the exact location of individual ballistics is not noted producing a large amount of uncertainty on the hazard. The map was created following fieldwork 3 days after the eruption and from witness testimony and excludes the eastern and southern sides of the volcano. The largest recorded bomb was up to 27m in diameter, landing within metres of the vent, and blocks were ejected to at least 2.8km, where a 0.8m block made an impact crater 2m diameter adjacent to the Tongariro Alpine Crossing path. Similarly, only the maximum distances and block sizes were reported for the 1988-89 Vulcanian eruption of Tokachidake (Yamagishi & Freebrey, 1994) and the Sub-Plinian 17 September 1966 Soufriere Hills eruption (Robertson et al., 1998). Despite the limitations of these ballistic datasets, it was sufficient for the authors to apply basic numerical models to and compare the eruptions to others documented in the literature. While this is useful for basic eruption dynamic investigations, it is very limited for interpretations of hazard magnitude.

Resolution limitations of aerial mapping can have significant ramifications for eruptive magnitude and hazard intensity/ footprint studies. Aerial photos on a 1:30,000 scale were used to complement field

mapping which was restricted by the remoteness of study area for investigating the 18 August 1992 eruption of Mount Spurr volcano (Waitt et al., 1995). Craters greater than 2m were visible on aerial photographs and extended to 8km km from the vent so this was used as a minimum ballistic field outline. Field studies showed the ballistic deposit was dominated by small clasts and the authors estimated the actual number of clasts as being at least an order of magnitude larger than mapped via photography due to the 2m resolution restriction. The 'complete' map from Fitzgerald et al. (2014) was similarly limited, with craters <2m in diameter difficult to identify from aerial photography and ground-truthing relationships used to estimate the number of small blocks missed and total number of erupted blocks. The minimum ballistic field outline found from these approaches is of limited use to hazard managers, with large uncertainties on the true hazard footprint.

Similar to resolution limitations reducing the certainty on ballistic hazard footprints, poor preservation of ballistic deposits is a common cause for partial ballistic maps, particularly when assessing pre-historic ballistic deposits. Lorenz (1970) mapped ballistic blocks at Big Hole Maar, Oregon which erupted ~20,000 YBP. Some of the ballistic apron is covered by lavas and thick pumice layers from more recent eruptions of nearby volcanoes. Despite exposure being restricted to the interior crater walls and to the northeast, they created an isopleth map, with clasts 30 cm in diameter erupted to 3km. The authors found clast size decreased with distance, which they attributed to the influence of a buoyant gas plume entraining smaller particles increasing their travel distance. Fudali and Melson (1971) encountered lush vegetation, ash deposition and several heavy rainfalls between eruption and mapping which obscured the complete outline of the Arenal Volcano 1968 Vulcanian eruption deposit. Blocks were mapped via aerial photography showing an asymmetric block field extended up to 5 km to the west. In the cases of partial datasets, due to preservation restrictions large uncertainties need to be placed on the data and its use.

Eruption dynamic studies focussed on vent locations may inform probabilistic ballistic hazard assessments and require detailed ballistic mapping combined with geochemical investigation. A portion of the thousands of lithic blocks ejected during phreatic and phreatomagmatic eruptions in ~1790 at Kīlauea Caldera were mapped by Swanson et al. (2012). They used the distribution and lithologies to infer how many ballistic lobes contributed to the block field and where previous vents were located. Three axes of each block were measured wherever possible (partial burial was a common barrier) for 1700 clasts, focusing on the largest or nearly the largest in a local area of a few tens of square metres. They found blocks were distributed asymmetrically around the caldera, however, extensive construction in the 20th century and brushy forests likely conceal some blocks

while lava flows in the inner wall of the caldera negated vent proximal mapping. The mapping focused on the largest blocks in any one area with no mention of the overall size distribution of clasts or the estimated proportion of the deposit mapped. This type of study provides specific data to answer questions such as vent locations but is limited in its application to hazard intensity however may contribute to a background ballistic hazard map.

Isopleth maps, with lines delineating areas of equal incidence of ballistic impact have been used due to their simplicity in conveying spatial information. Usually the location of individual ballistics and their size is not included in these maps (Kaneko et al., 2016, Kilgour et al.,2010). The isopleth mapping approach by Kilgour et al. (2010) allowed the total volume of ballistic mass ejected at Ruapehu during a Surtseyan-like phreatic eruption in 2007 to be calculated by using a scaling factor based on the percentage ground cover within each isopach. Their method combined aerial observations made the morning following the eruption, a field visit two days later and high resolution orthophotos taken three days after the eruption due to field mapping being restricted by further eruption risk. Separate isopleth maps, indicating the thickness of the deposit, were made for the ballistic apron and tephra fall from detailed mapping of the 19 March 2008 explosive eruption of Kilauea (Figure 2.3) (Houghton et al., 2011). This highlighted the relatively isolated area impacted by ballistics and the differing deposit direction to the wind-controlled tephra. The simplicity of isopleth maps makes for simple interpretations of eruption dynamics such as directivity and total erupted mass and also give some

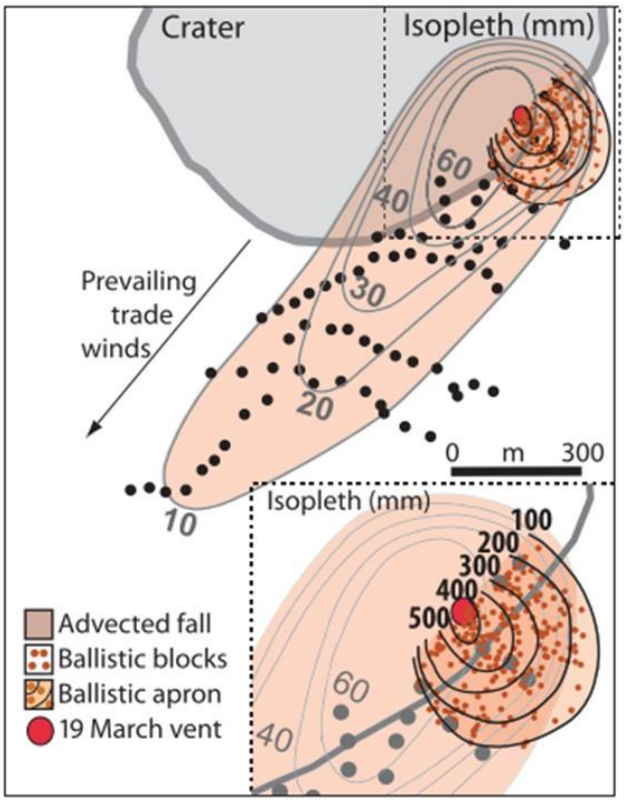

Figure 2.3 An example of a separated advective tephra fall and ballistic block isopleth map from Houghton et al., (2011)

indication of varying hazard intensity with distance, however their use has been cautioned against due to over simplification of deposits (Taddeucci et al., 2017).

Recent ballistic mapping for the purpose of hazard assessment has focused on finding the most distal ballistics from known eruptions to provide the basis for ballistic modelling (Alatorre-Iberguenoitia et al., 2006, 2012, 2016; Biass et al., 2016; Bertin, 2017). These authors have not produced ballistic distribution maps but use a restricted number of field locations, (e.g. 3 locations Biass et al., 2016) within a ballistic modelling framework to create ballistic hazard maps. This approach is discussed further in the following ballistic modelling section.

2.2.3. Summary of ballistic mapping review

Current approaches to ballistic mapping include detailed field mapping of individual blocks, transects of ballistic fields, aerial photography, mapping of sections of the field and creation of isopleth or isopach maps. Complete maps which show the spatial distribution of individual ballistics allow impact density to be calculated which is an important consideration in creating zones of variable hazard. However, complete maps generally require more resources such as aerial photography or thermal imagery as well as significant time in the field to collect ballistic attribute information. Barriers to complete ballistic distribution maps frequently include poor preservation of ballistic deposits due to burial or inaccessibility of inner craters and working under time constraints due to accessibility or risk of future eruptions. Incomplete maps often rely on non-ground-truthed aerial photography and basic fieldwork under time pressure. It is clear that aerial photographs with insufficient resolution frequently underestimate the total number of ejected particles (e.g. Waitt et al., 1995; Pistoli et al., 2008; Fitzgerald et al., 2014), however with the increasing affordability of UAV's to collect high resolution orthophotographs this approach is progressively being chosen. As such, an examination of the effectiveness of different methods, particularly focused on photographic mapping methods, is required to help inform hazard assessors of appropriate and efficient mapping approaches which Chapter 3 will address.

2.3 Ballistic Modelling methods

While mapping a ballistic field provides the spatial extent and density (method dependent) of a previous eruption's ballistic hazard, numerical modelling can shed light on the eruptive conditions and provide further useful hazard information (Wilson, 1972; Self et al., 1980). Ballistic models are a tool used within volcanic hazard assessments to quantify eruption parameters that were not observable or measurable and enable forward modelling for assessment of possible future scenarios and hazard zones (e.g. Fitzgerald et al., 2014; Alatorre-Ibarguengoitia et al., 2016). Ballistic modelling is most useful for hazard and risk managers when outputs include; the distance travelled, time in flight,

landing velocity, impact angle and landing energy of blocks (Tsunematsu et al., 2016; Taddeucci et al., 2017). This information can then be translated into probabilities of impact (Biass et al., 2016; Fitzgerald et al., 2014) and probability of infrastructure damage (Williams et al., 2017; Nurmawati & Konstantinou, 2018).

The clasts in volcanic ballistic models follow nearly parabolic, or ballistic trajectories. For a clast's motion to be truly parabolic it would need to be ejected into an atmosphere with no viscosity so the only force acting upon it is gravity. While this is evidently not the case in Earth's atmosphere, the term ballistic trajectory is used to describe the motion of an object ejected near the earth's surface travelling only under the force of gravity. Early workers on volcanic ballistics applied military ballistic calculations to volcanic particles and incorporated the density of earth's atmosphere and its variation with elevation to create a drag force on a clast and more realistic trajectory calculations (Minakami, 1942; Sherwood, 1967; Fudali & Melson, 1971).

Early workers used various mathematical assumptions to account for drag on particles. Minakami (1942) applied an analytical equation to determine the initial velocity of blocks ejected during the eruptions of Asama volcano, Japan, in 1935 and 1941. The equation related the initial velocity and angle to the distance travelled and included the effects of drag and wind speed. They calculated initial velocities based on the mapped outline of the field and sampled clasts with as spherical geometries as possible, as drag was calculated assuming spherical bodies. Sherwood (1967) derived equations for ballistic trajectories that were ejected during excavation type, crater producing explosions. Drag was calculated based on B, a dimensionless ballistic coefficient related to the ratio of initial drag force and gravitational force. They demonstrated the significant impact that drag has on the trajectory of particles.

Following Sherwood's examination of drag forces Wilson (1972) recalculated the initial velocities of clasts from the Arenal 1968 eruption based on a cylindrical shape as they found that the coefficient of drag (Cd) used by Fudali and Melson (1971) based on a sphere was too low. Wilson (1972) used a discrete numerical trajectory model, the first algorithm for volcanic ballistic transport which calculated trajectory using a rectangular coordinate system and 4th order Runge-Kutta method. The method accounted for gravity, drag force and the influence of elevation on atmospheric properties. The study examined the influence of size and density on the fall time of clasts from various heights and how initial velocity, density, size and the ejection angle of clasts influenced their range.

Ejection angle is another parameter recognised by early workers as crucial for calculating the distance a clast may reach. Lorenz (1970) used several blocks ejected from the ~20,000 YBP phreatomagmatic eruption at Big Hole Maar to calculate the initial velocity of blocks, maximum possible ejection distance and impact velocity. They assumed the most efficient angle of ejection was 45° and neglected the influence of air drag. Similarly, Fudali and Melson (1971) applied a mathematical model to the Vulcanian eruption of Arenal Volcano in 1968, also assuming an optimal ejection angle of 45°, but modelled a spherical particle to minimise the drag coefficient. Consequently, they calculated a minimal value for the maximum initial velocities. Steinberg and Lorenz (1983) recalculated initial velocities for Arenal (Fudali & Melson, 1971), Shiveluch (Steinberg, 1975) and Asama (Minakami, 1942) volcanoes. They proved that the assumption of 45° being the most efficient angle of ejection was not valid, as the angle is dependent on a derived ballistic coefficient calculated from the drag coefficient, size and density of an ejected particle. Calculations based on the most efficient angle of ejection provide useful information for both eruption dynamics with minimum maximum initial velocity found and also hazard footprint as they derive the maximum ejection distance.

2.3.1. Development of complex drag on particles

Pre-1990's workers had assumed that particles ejected during a volcanic eruption travelled through a still, ambient atmosphere from trajectory initiation. However, photographic evidence of the Ngauruhoe eruption of 1975 showed the presence of a gas slug at the beginning of the eruption, in which all particles were thought to be ejected at the same approximate speed before decoupling and travelling ballistically (Nairn & Self, 1979). Fagents & Wilson (1993) recognised the importance of large clasts initially being coupled with a body the air overlying the vent. They incorporate this effect by adding a model describing the explosion process whereby the ejected material acts as a coherent plug until it reaches a maximum velocity, from which the blocks are launched into the decelerating gas fluid (Figure 2.4). The concept of a decoupling gas and clast phase was continued by Bower and Woods (1996). In summary, the addition of a region of reduced drag showed how earlier modelling efforts had drag forces which were too high at the start of an eruption and consequently underestimated the final clast range and overestimated initial velocities.

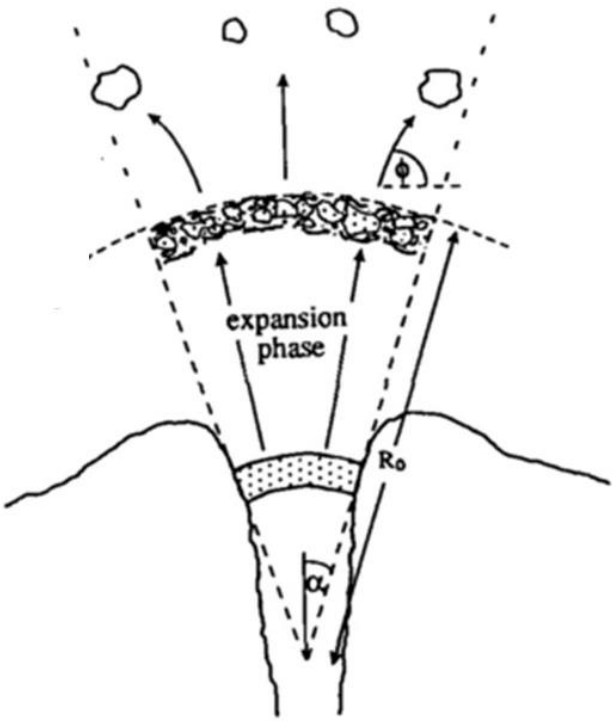

Figure 2.4 Schematic diagram from Fagents and Wilson (1993) showing the modelled initial expansion of gas/rock mixture out to the distance Ro where the maximum velocity of ejecta is reached. The fragmented caprock blocks are then launched into the gas flow field, the velocity of which decays over distance.

A simple accessible computer program was developed by Mastin (2001) which encompassed a region of reduced drag simply. Mastin (2001) created Eject! which is a computer program widely used for ballistic studies (e.g. Kilgour et al., 2010; Swanson et al., 2012; Bread et al., 2016) as it is free to download and has a simple graphical user interface which allows users to model scenarios themselves. Users can define the initial velocity, ballistic shape, particle density and diameter, atmospheric properties, drag coefficient, ejection angle and the height difference between ejection and deposition points. Following Fagents and Wilson (1993) a distance of reduced drag around the vent can also be specified. Particle trajectories are calculated using a rectangular coordinate system and Runge-Kutta approach as per Wilson (1972).

Modern laboratory experiments further developed drag coefficient using actual volcanic particles for more sophisticated ballistic hazard modelling. Following on from Waitt et al. (1995), who found that previous studies overestimated drag on blocks, Alatorre-Ibarguengoitia & Delgado-Granados (2006) performed wind tunnel experiments on pyroclastic particles from Popocatépetll volcano. They found that drag coefficients, within the Reynold number range applicable to volcanic pyroclasts, depend mainly on the shape and texture of the particle. Their description of the shape and texture of the volcanic particles measured and their corresponding Cd's ranging from 0.71-1.01, allows other workers to use drag values based on volcanic, not geometric, bodies thus allowing suitable choice

based on field characteristics. Alatorre-Ibarguengoitia et al. (2006) applied this clast specific Cd to their horizontal and vertical ballistic hazard assessment on Volcan de Fuego de Colima where they defined areas of high, medium and low ballistic impact risk.

Complex models have been used to provide insight into the relative importance of variables effecting ballistic motion. Saunderson (2008) expanded the simplified equations of motion that had been applied to volcanic ballistics in a theoretical study of the effect of variables such as drag and particle size on particle travel. Included in the computer model was centrifugal effects, lift, atmospheric stratification and changes in gravity due to altitude, including the primary forces acting on particles, following previous volcanic ballistic motion authors. They found recirculation of clasts within the jet plume, diverging particles from purely ballistic trajectories and that the combination of Coriolis and lift forces separated ejecta paths, but was of secondary importance on their own compared to other acceleratory forces. de' Michieli Vitturi et al. (2010) developed a complex 2D/3D Eulerian-Lagrangian model for Vulcanian ballistic clasts which included the initial acceleration of particles and interaction with a gas phase. They included a Eulerian multiphase flow code with a one-way coupling of the flow and particles where particles did not interact or have any impact on flow dynamics. The model describes the drag force that the multiphase flow has on large particles and confirms Fagents & Wilson's (1993) results, while showing the carrier flow has a more complex role than previously appreciated.

Visual observations using high speed video has allowed volcanic models to be calibrated with more accuracy than ever before, with parameters such as the ejection angle, average ballistic speed directly observable (Gaudin, 2014; Alatorre-Ibarguengoitia et al., 2012, Taddeucci et al., 2012; Taddeucci et al., 2015; Bernard et al., 2018). Following on from their 2006 work, Alatorre-Ibarguengoitia et al. (2012) used a ballistic model, in conjunction with an eruptive model, to create a hazard map for Popocatapetl volcano (Mexico) which is validated with video and field observations. The eruptive model considered caprock acceleration and energy consumed by fragmentation which allowed ballistic range to be correlated with initial pressure and gas content. Alatorre-Ibarguengoitia et al. (2016) applied the same approach to El Chichón volcano, Mexico. Similarly, Maeno (2013) combined an eruptive model with a ballistic model and used video observation of the expanding gas cloud of the February 2011 eruption of Shinmoedake volcano to estimate the distance gas and blocks are coupled to and used camera observations for block distribution. A thorough analysis of high speed imagery from various volcanoes allowed Taddeucci et al., (2017) to conclude that rotation and spinning of ballistics is ubiquitous in effecting travel paths, confirming previous invocations of the Magnus effect

(the deviation of a particle flight path due to spin) (Waitt et al., 1995). Not only is the Magnus effect confirmed through direct observation, collisions, deformation of ductile bombs, and fragmentation of clasts (in flight and on impact) is observed and the highly complex nature of ballistic flight and relative simplicity of ballistic models is shown (Taddeucci et al., 2017).

The advancement of volcanic ballistic models by expanding the variables considered, quantifying their relative importance and the development of probabilistic approaches has increased the presumed accuracy of ballistic models, however limitations in modelling capabilities remain. Taddeucci et al. (2017) observe that the complicated spatial distribution of pyroclasts and complex acceleration and deceleration of particles (Taddeucci et al., 2015) is related to other forces not currently modelled such as zoning between jet plumes or overlapping eruption lobes (e.g. Swanson et al., 2012). Atmospheric effects such as convecting clouds above volcanic vents, windshear (Fagents & Wilson, 1993), the Magnus effect (Waitt et al., 1995; Taddeucci et al. 2017), and the transition between air dominated and ballistic dominated regimes (Self et al., 1980) have been raised as requiring further investigation and integration into ballistic modelling. Ballistic models currently assume that mapped block landing distributions are in situ and can be used to inversely model block flight trajectories and consequently inform eruption parameters or forward modelling of ballistic hazards. However, it has been noted that ballistics can bounce out of their impact craters (e.g. Swanson et al., 2012; Fitzgerald et al., 2017), slide for 10's of meters (Pistolesi et al., 2008) and inclined volcanic slopes mean they may roll beyond their initial landing locations (Taddeucci et al. 2017).

2.3.2. Three Dimensional Considerations

Until recently, ballistic modelling was largely restricted to two dimensions, and only considered the motion of single particles. Ballistics are clearly launched in three dimensions and Vanderkluysen et al. (2012) demonstrated, based on thermal imagery and trajectory tracking, that 10-15% of particle trajectories observed at Stromboli deviated due to collisions, with ~12% increasing in range. As such, Tsunematsu et al. (2014) developed a 3D model to apply to Strombolian style eruptions which simulates the flight of multiple particles, which may be effected by particle collision, 'Ballista'. Importantly the particles final impact location is outputted as a 2D spatial distribution of ejected particles, allowing for direct comparison with ballistic impact maps. This work found that if collisions are dominant in an eruption, the distance between a mapped block or bomb and the eruption vent cannot necessarily be used to estimate eruption parameters such as initial velocity. The particle trajectories are calculated using a Discrete Event Simulation (DES) method. Ballista inputs include initial particle velocity, particle density and diameter, displacement of ejection points from the vents

centre, rotation and inclination angle (ejection angle and standard deviation), the number of particles ejected (per burst if multiple bursts are modelled), time between bursts, and the ejection direction. The first five parameters listed are defined and sampled from a chosen probability distribution to reflect their uncertainty, introducing a probabilistic element to the traditionally deterministic approach to ballistic modelling.

While designed originally for Strombolian eruptions, Ballista has been used to inversely model hydrothermal and phreatic ballistic distributions. Fitzgerald et al. (2014) applied Ballista to the 2012 Te Maari hydrothermal eruption to inversely model the mapped ballistic field. The effects of drag and the initial coupling of particles within a gas jet were incorporated into this version with wind speed variable available but not utilised in the study. Ballista was further developed when applied to the fatal Mt Ontake phreatic eruption in 2014 by including the effects of topography through use of a 10m Digital Elevation Model (DEM) in trajectory calculations (Tsunematsu et al., 2016). The successful inverse modelling of phreatic eruptions and hazard appropriate outputs of impact energy and spatial density of clasts means it has been used in Chapter 4 of this study to model Whakaari's phreatic ballistic distribution.

'Great Balls of Fire' (GBF) continues the development of 3D probabilistic ballistic modelling and accounts for drag and topography (Biass et al., 2016). Like Ballista, GBF samples the eruption source parameters for a ballistic stochastically and is constrained based on a probabilistic distribution. Unlike Ballista, it is a single particle model which allows a large number of events to be simulated but does not consider collisions. The purpose of GBF is to create probabilistic hazard and pre-event impact assessments which a post-processing function available on MatLab facilitates. As such, Biass et al. (2016) applied it to La Fossa volcano due to its tourism industry and permanent population using a generic Vulcanian eruption scenario, based on local stratigraphy, and found that the built environment is highly vulnerable to ballistic hazard.

Bertin (2017) suggests a 3D approach for modelling the dynamics of ballistic projectiles by focussing on ellipsoidal particles and considers both horizontal wind fields, virtual mass forces and drag forces subjected to variable shape dependent drag-coefficient. This study emphasised the importance of considering a horizontal wind-field and shape-dependent, variable drag-coefficients and the lack of influence that virtual mass forces have on ballistic trajectories. Each eruption parameter is defined through a Latin-hypercube sampling approach with a high number of simulations completed and the

probability of impact calculated. Bertins approach considers variable input parameters as random so that the bias introduced by highly explosive or directed eruptions on hazard zoning is reduced.

Since the first basic analytical equation was applied to Vulcanian eruptions by Minakami (1942) to calculate eruptive conditions, volcanic ballistic modelling has increased in complexity incorporating more of the forces that effect ballistic motion and is now an essential tool used within ballistic hazard assessment. 3D models such as Ballista that incorporate probabilistic approaches with outputs which show ballistic impact velocity, size and location at a study location, now allow inverse modelling of ballistic fields which have been mapped considering variable spatial density. 3D models not only produce outputs of importance for measuring hazard intensity (impact energy, spatial density) their probabilistic nature produces information that is useful for hazard managers and can be incorporated into ballistic hazard maps

2.4. Ballistic hazard information in hazard maps

When creating ballistic distribution datasets it is important to consider how this information will eventually be used. Hazard and risk maps are commonly used for natural hazard planning and communication (Haynes et al., 2007; Leonard et al., 2014). A ballistic hazard map should use the data derived from mapping and modelling to communicate the likely distribution, maximum range and spatial density of particles in various explosive scenarios. The level of hazard can be depicted through different hazards zones which allow local inhabitants and authorities to make mitigation plans to reduce risk from ballistic hazards (Alatorre-Ibarguengoitia et al., 2006).

The zonation of a ballistic hazard map may be based on maximum travel distance of particles (i.e. Alatorre-Ibarguengoitia et al., 2006, 2010, 2012; Biass et al., 2016, Bertin, 2017), number of ballistics per unit area (Guroli et al., 2013), the probability of ballistics of a specific size reaching a specific area (Artunduaga & Jimenez, 1997), or the probability of a specific consequence such as the injury or damage (Fitzgerald et al., 2014). Much work in volcanic hazard assessments has encompassed ballistic hazard within ‘all hazard’ or ‘multi-hazard maps’ (Neal et al., 2001; Hadisantono et al., 2002; Leonard et al., 2014) or not identified them as a hazard at all (e.g. El Chichón Volcano, Alatorre-Ibargüengoitia et al., 2016) depending on the purpose and end user of the map. Therefore, few specific ballistic hazard maps have been published, potentially leading to an under-appreciation of the risk posed by ballistic impact (Fitzgerald et al., 2017) which is concerning considering the increasing tourist population exposed and the prevalence of ballistic hazard proximal to volcanic craters.

A key distinction must be made between specific ballistic event distribution maps and background ballistic hazard maps for risk mitigation. The ballistic hazard maps produced from single event studies (e.g. Kaneko et al., 2016; Swanson et al., 2012; Fitzgerald et al., 2014; Kilgour, 2010) indicate the hazard intensity from the single studied eruption. Background ballistic hazard maps include the information derived from all previous events and minimise event specific parameter's, such as directionality, through applying the same maximum distance at all directions (e.g. Madea et al., 2015) or, more sophisticatedly, through probabilistic modelling approaches (Alatorre-Ibarguengoitia et al., 2006b; 2010, 201; Biass et al., 2016, Bertin et al., 2017).

Ballistic hazards maps and the assessments which feed into them vary depending on the state of the volcano and the requirements of the hazard map. Ballistic hazard maps should be created prior to volcanic unrest and updated during and after unrest (Leonard et al. 2014; Fitzgerald et al, 2017). Hazard assessments of a volcano in unrest may be limited by the availability of safe locations to survey, and risk management protocols of institutions involved which may limit the time hazard assessors can spend gathering data (Jolley & Taig, 2012; Kilgour et al., 2018). During a volcanic crisis exclusion zones are commonly created and distributed as maps for end users such as track managers to enforce but there is often little pre-event planning linking exclusion zones to hazard mapping (Leonard et al., 2014). The difference between background and crisis hazard maps is shown well by the 2012 eruptions at Upper Te Maari Crater, Tongariro volcano which wil be discussed in the following section.

Simplistic ballistic maps may be derived without intensive field mapping or ballistic modelling by using basic concentric hazard zones informed by the distance recent eruptions ejected clasts or by values taken from literature (e.g. Nurmawati & Konstantinou, 2018). Following the 1993 eruption sequence at Mayon Volcano, which began phreatically, without precursory signals and killed 77 people, the Philippines Institute of Volcanology and Seismology defined a permanent danger zone of 6km around the vent, even without activity signals (Maeda et al., 2015). Similarly, at Garioli Volcano Alaska, a detailed ballistic hazard assessment was not a priority as it is an uninhabited island, but a first order hazard assessment was needed. Therefore Coombs et al. (2008) use a basic eruptive history of the volcano. The distance of ballistic hazard is derived based on Blong's (1996) assessment that ballistics rarely travel beyond 5 km from the vent and that recent ballistic distributions reach no further than several hundred metres.

Alatorre-Ibarguengoitia and co-authors have developed a general methodology for assessing ballistic impact hazard using probabilistic modelling coupled with scenario development and applied it to three

high risk Mexican volcanoes; Volcán de Fuego de Colima, Popocatéptl and El Chichón (Alatorre-Ibarguengoitia et al., 2006, 2012, 2016). Fieldwork at each volcano found the maximum distance clasts from known eruptions impacted or used analogous volcanoes for large eruptions not documented in the field (Colima). The maximum distance of ballistic impact from previous eruptions and frequency of occurrence are used to define three eruption scenarios; High (low VEI as they are the most frequent), Intermediate and Low (high VEI as they impact a larger area but are less frequent). Vertical and horizontal hazard maps were created by the authors in order for authorities to make development and mitigation plans and to define exclusion zones during volcanic crises. Three horizontal zones were shown overlying a local map highlighting what population centres may be affected by ballistics (Figure 2.6A). The vertical hazard zones of each scenario was also developed to inform authorities with one or two profiles of vertical hazard depicted (Figure 2.6B). Each of these volcanoes have ejected ballistic projectiles during historical eruptions with evacuations of nearby villages and casualties, as in the case of the April 30, 1996 eruption from Popocatepetl where five climbers were killed from ballistic impact after ignoring official warnings. Despite these fatalities indicating a lack of understanding of the volcanic hazard presented, no currently published hazard maps were mentioned for Colima or Popocatepetl and the published multi-phenomenon hazard map at El Chichon by Macias et al. (2008) excludes ballistic hazard. The combination of fieldwork, scenario development and systematic numerical modelling produced ballistic hazard maps relevant for use by authorities and appropriate outputs for integration into multi-hazard maps.

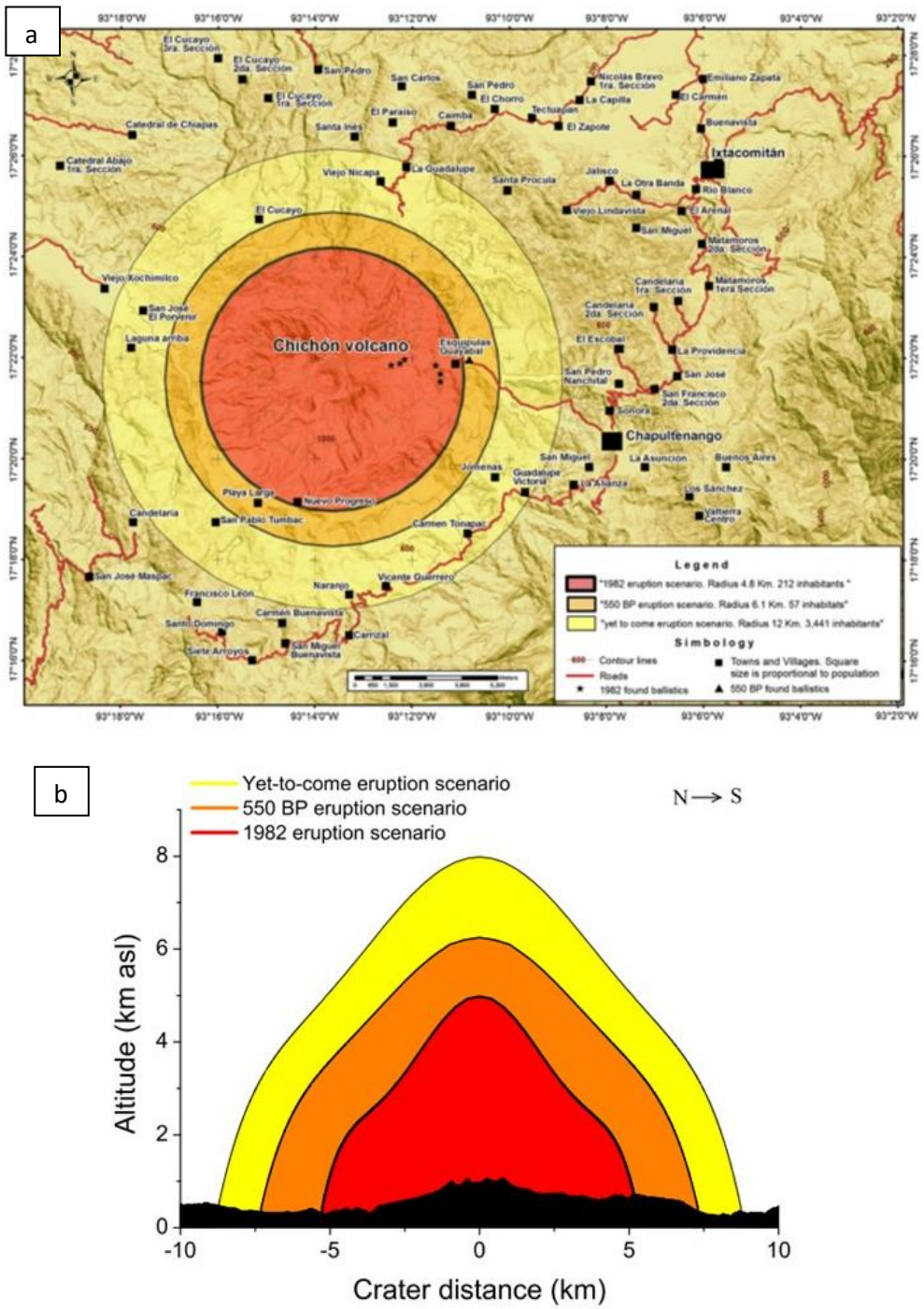

Figure 2.1 Ballistic hazard map for El Chichon Volcano from Alatorre-Ibarguengoitia et al., 2016. a) Horizontal ballistic hazard zones. Three hazard zones are shown based on probabilistic numerical modelling of three eruption scenarios. Importantly, population centres and the number of inhabitants within the hazard zones is included in the published map. b) complementary vertical hazard zones.

Nurmawati and Konstantinou (2018) undertook a basic ballistic hazard assessment for Mount Chihshin, Taiwan due to the thousands of recreational visitors and the lack of previous studies. They developed two scenarios; a hydrothermal eruption and a Vulcanian eruption. The initial velocities of clasts were found by solving eruption modelling equations from the literature. The maximum distances blocks of three sizes reached, 0.2 m, 1 m and 2 m in diameter, created zones of hazard

however the lack of integration of eruptive histories means the relative probability of impacts within these zones is not assessed. No fieldwork was undertaken to indicate the size or distance previous eruptions have ejected blocks to, but the study did show that projectiles could impact surrounding infrastructure including hiking trails and posed a threat to aircraft. As such the study serves to indicate that further detailed ballistic investigation is warranted for risk mitigation purposes but is not appropriate for use within a ballistic hazard map.

The deterministic approach necessitated when developing eruption scenarios is complimentary to probabilistic modelling when the probability of a future eruption tends towards one (Marzocchi et al., 2008). However Biass et al. (2016) argued that a deterministic approach was of limited application for long-term planning and risk reduction strategies. Biass et al. (2016) created a probabilistic ballistic impact hazard map for La Fossa volcano, Italy. The maps showed the probability of ballistic impact above certain energy thresholds and this hazard information was subsequently incorporated into a risk of ballistic impact damage assessment. While this map has the advantage of being purely probabilistic, it does not create the simple, easy to communicate hazard zones that end users are used to seeing and so needs work for integration into a hazard map suitable for a non-scientific end user.

Bertin (2017) applied their own probabilistic model to Lascar volcano, Chile for use by authorities in long-term planning. Using the most distal clast ejected in the 1984 to 1993 eruption sequence, they found the best fit for a range of reasonable parameters which could have ejected the clast. Using the range of each best fit parameter and stochastic sampling, the probability of ballistic impact or transit was modelled with 10^6 simulations. By including the probability of ballistic transport the use of only the most distal clast is justified by assuming all smaller ballistics would have impacted within the area the largest clasts transited. Like Alatorre-Ibarguengoitia (2006, 2012, 2016) the publication of vertical and horizontal hazard maps with three clear zones of hazard provides useful information to risk managers. However, intensity of hazard is very broadly defined and not fully calibrated.

2.5 Ballistic hazard assessments in New Zealand

The major contributor to volcanic hazard in New Zealand is ash sized tephra fall, ballistics are a significant and largely understudied hazard in New Zealand (Keys & Williams, 2013) . This was brought to light during the 2012 eruption of Te Maari, Tongariro Volcano, when blocks heavily impacted the Tongariro Alpine Crossing but a lack of previous studies made the creation of exclusion zone challenging (Leonard et al., 2014; Fitzgerald et al., 2014, Breard et al., 2014).

Disaster risk reduction and management is central to the New Zealand Civil Defence and Emergency Management Act (CDEM Act, 2002) which includes the mapping of natural hazards. GNS Science is the government research institute responsible for monitoring all of New Zealand's volcanoes through the GeoNet programme (Miller & Jolly, 2014). The primary communication tool to communicate the activity of New Zealand's volcanoes is the volcanic alert level system which range from 0 (low risk) to 5 (high risk). Within national parks mitigating the risk to visitor safety is a responsibility of the New Zealand Department of Conservation (DoC). The management of risk by DoC is informed by science (research, monitoring and interpretation/advice), response planning and risk assessments within the wider context of national park management and considering local communities, businesses and politicians (Jolly et al., 2014). While specific ballistic hazard maps do not exist for most New Zealand volcanoes, ballistic hazard is incorporated within multi-hazard maps at Tongariro, Ruapehu and White Island while publicly available hazard maps for other explosively erupting volcanoes such as Taranaki are difficult to find and do not include ballistic hazard (Neall & Alloway, 1993).

Volcanic multi-hazard maps are prominent within Tongariro National Park, with specific volcanic hazard maps for Tongariro (including Ngauruhoe) and Ruapehu created through collaboration between DoC and GNS Science. Both hazard maps have basic summit hazard zones of radial extent around active or recently active vents with gas and flying rocks identified as summit hazards, as well as pyroclastic flows lava flows and ashfall (Figure 2.5, 2.6A). Historical eruptive activity has informed the zonation of the summit hazard zones. At Tongariro two summit hazard zones are shown, reds

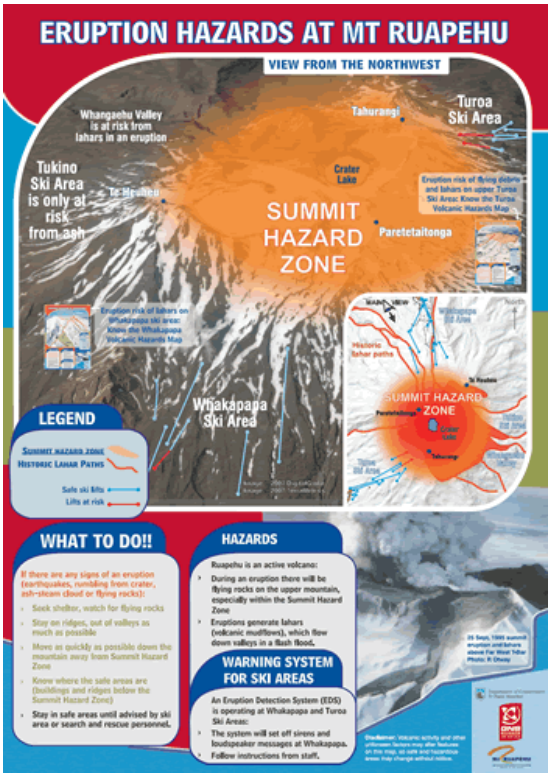

Figure 2.2 Volcanic Hazard map for Ruapehu volcano with ballistic hazard encompassed in "Summit Hazard Zone" GNS Science (compiler) 2008

zones around vents which have erupted in the last 150 years and are therefore high hazard, and orange zones around vents active in the last 27,000 years. Ruapehu has a single vent and therefore a single orange radial summit hazard zone, with the plan view inset map showing degradation of colours from the crater lake out to the edge of the summit hazard zone. Although there is some lack of consistency between the use colour between the two maps, the image of the hazardous areas is in both cases faded out to show that eruption hazards decrease gradually, not abruptly from the vent (Leonard et al., 2014).

The background hazard map for Tongariro Volcano (GNS Science (compiler), 2007) distinguishes between vents which have been historically active and those which have erupted in the last 27,000 years (Figure 2.6a). Only one hazard zone is displayed, 'a summit hazard zone' as per the Ruapehu background hazard map (Figure 2.6B). A crisis hazard map was developed following the initiation of anomalous seismic activity in 2012 near Te Maari, in order to provide concise representation of the hazards, their spatial extent, potential impacts, potential onset/warnings and correct response actions (Leonard et al., 2014). The crisis map 'summit hazard zone' comprised of surge and ballistic hazards was qualitatively judged by experts extrapolating from historic eruptions and geological data for T A riro National Park volcanoes, as well as obser B anges from the first eruption in August. The

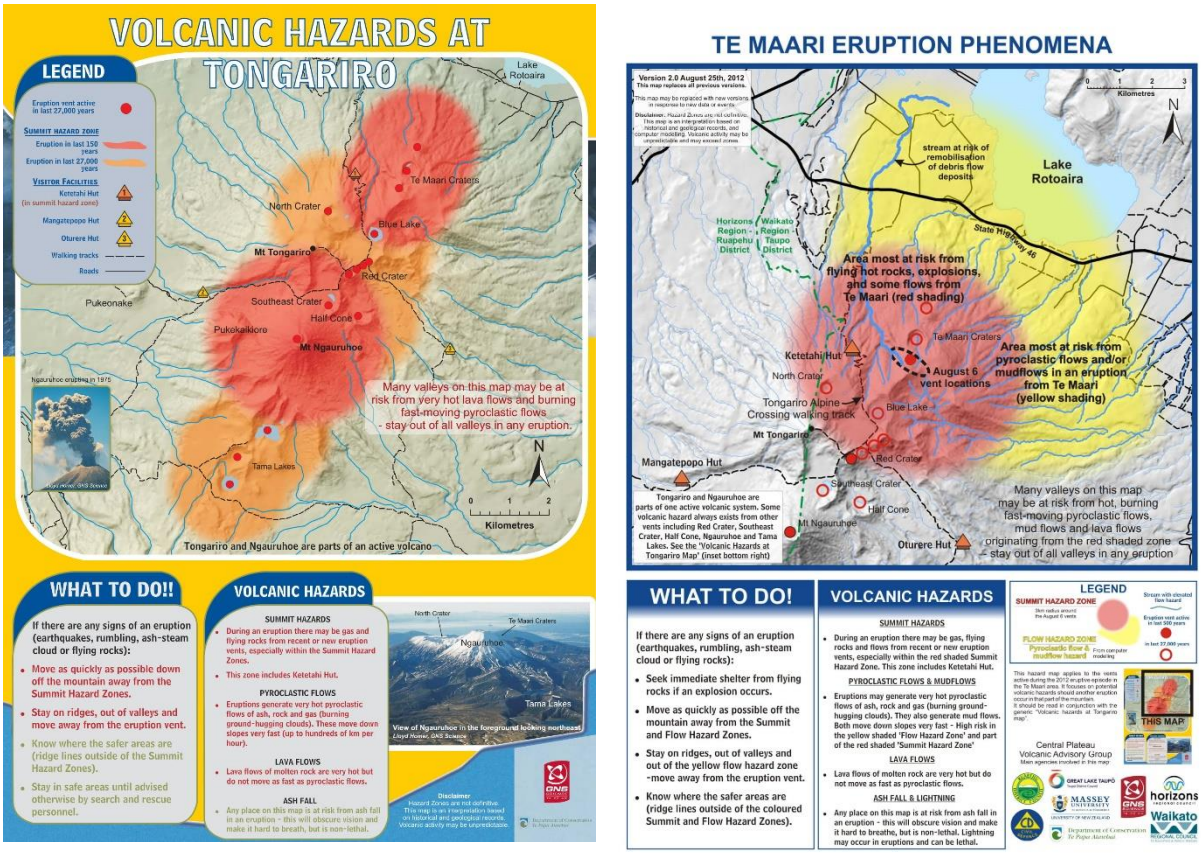

Figure 2.3 Volcanic hazard maps for Tongariro. A) Background volcanic hazard map (GNS Science (compiler) 2007) A) Crisis Te Maari eruption hazard map (GNS Science (compiler) 2012)

background hazard map, but slightly elongated as per the fissure vent geometry and topography (Figure 2.6b).

Whakaari volcano is a unique case as it is privately owned and so not government managed and no current hazard map available, however the volcano is heavily monitored by GNS Science. Volcanic Alert Bulletins produced by GNS Science inform tour companies decisions on whether to visit the island or not, based on their own risk management practices. The most recently published work showing hazard zones at Whakaari appears to be Cole et al. (1996) based largely on the 1976 -1982 magmatic eruption sequence. There are four hazard zones (Figure 2.7); a central zone at risk from multiple hazards; debris avalanches, pyroclastic flows and surges, including bomb or block falls on the main crater floor and slightly offshore. Beyond this an outer zone which is at risk from pyroclastic surges and a third zone at risk of impact from ballistic blocks up to 1 m in diameter which extends 4 km from the active vents. The largest zone of hazard is that for ashfall. It is noted that the crater shape restricts most ballistic fall to the east and all of the hazard zones are extended in an easterly direction.

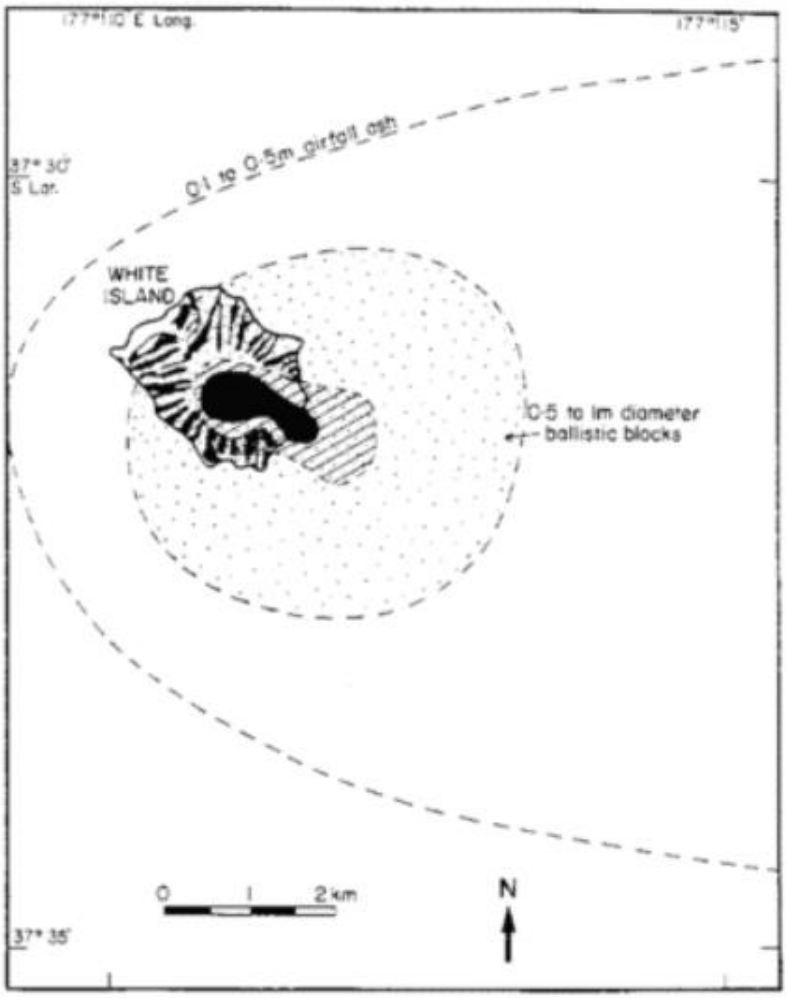

Figure 2.4 Hazard zones at Whakaari for typical eruptions with a yearly to century return period Inner multiple hazard zone in black, Pyroclastic flow zone in hatched, stippled area showing ballistic hazard zone and outermost hazard zone for ashfall. From Cole et al., 1996.

2.6 Summary and Research Gaps

A wide range of mapping methodologies are apparent in the literature with approach determined by site specific restrictions such as incomplete preservation, inaccessibility to some or all of the field area (Houghton et al., 2011; Kaneko et al., 2016) and restricted time in the field due to risk of further eruption (Kilgour et al., 2010, in review; Fitzgerald et al., 2014). Whilst all mapping methods provide varying levels of ballistic hazard information and require varying resources to achieve (Figure 2.8), the intended use of the data is the most important factor to consider when planning a field campaign. If the presence of a ballistic field and the maximum distance clasts reached is all that is required, simply mapping a field outline in as much detail as the study location allows may be sufficient. However, if the mapping is intended to be used to inform hazard zones or magnitude of the hazard, complete mapping or partial mapping complemented by modelling techniques are ideal. Similarly, reconstructing volcanic eruption parameters requires modelling for which appropriate field data is necessary. As such, a more complete mapping approach which is consistent with the chosen modelling approach will produce the best constrained parameters to constrain the eruption dynamics.

Ballistic hazard maps have traditionally been incorporated within multi-hazard maps, and largely remain so, in New Zealand and around the world. However, with advancements in ballistic modelling and clear methodologies to help apply modelling to the creation of hazard zones (Alatorre-Ibargüengoitia et al., 2016 and earlier work, Biass et al., 2016; Bertin, 2017) ballistic hazard maps are being increasingly published and may be relevant to emergency managers where ballistics are the primary hazard as in New Zealand (Keys & Williams, 2013).

Many models have been developed using input parameters from a wide range of ballistic producing eruptions (e.g. Tsunematsu et al., 2014). Realistically, different eruption styles and scales mean an equally wide range of processes control the motion of large pyroclasts (de' Michieli Vitturi et al., 2010). Therefore, clasts leaving a volcanic vent at a set velocity and angle may have very different flight trajectories depending on the eruption type (Taddeucci et al., 2017). This is shown by centimetre clasts being lofted within a convection cloud in Plinian eruptions but emplaced ballistically during smaller Strombolian style eruptions as well as Vulcanian, meter sized pyroclasts deviating from ballistic trajectories due to their interaction with the surrounding gas-ash mixture (de' Michieli Vitturi et al., 2010).

Finally, grain size distribution is important when considering eruption dynamics, and ballistic hazard studies are often limited by a lack of comprehensive total grain size distributions. Because of this there is commonly over-simplification of ballistic deposits (Biass et al., 2016; Strehlow et al., 2017). Mapping approaches which gain as much information such as the size of particles and their distribution, yet remain efficient in terms of time and money are crucial, and will be addressed in Chapter 3. Detailed spatial and size distribution field data has yet to be used in modelling to determine eruptive conditions, however the whole ballistic field, not simply the outline or individual clasts, would be expected to give greater accuracy of results. Chapter 4 of this study will demonstrate using a case study of Whakaari Volcano how detailed spatial mapping and complementary model choice can determine eruptive conditions and give hazard information appropriate for incorporation into ballistic hazard maps.

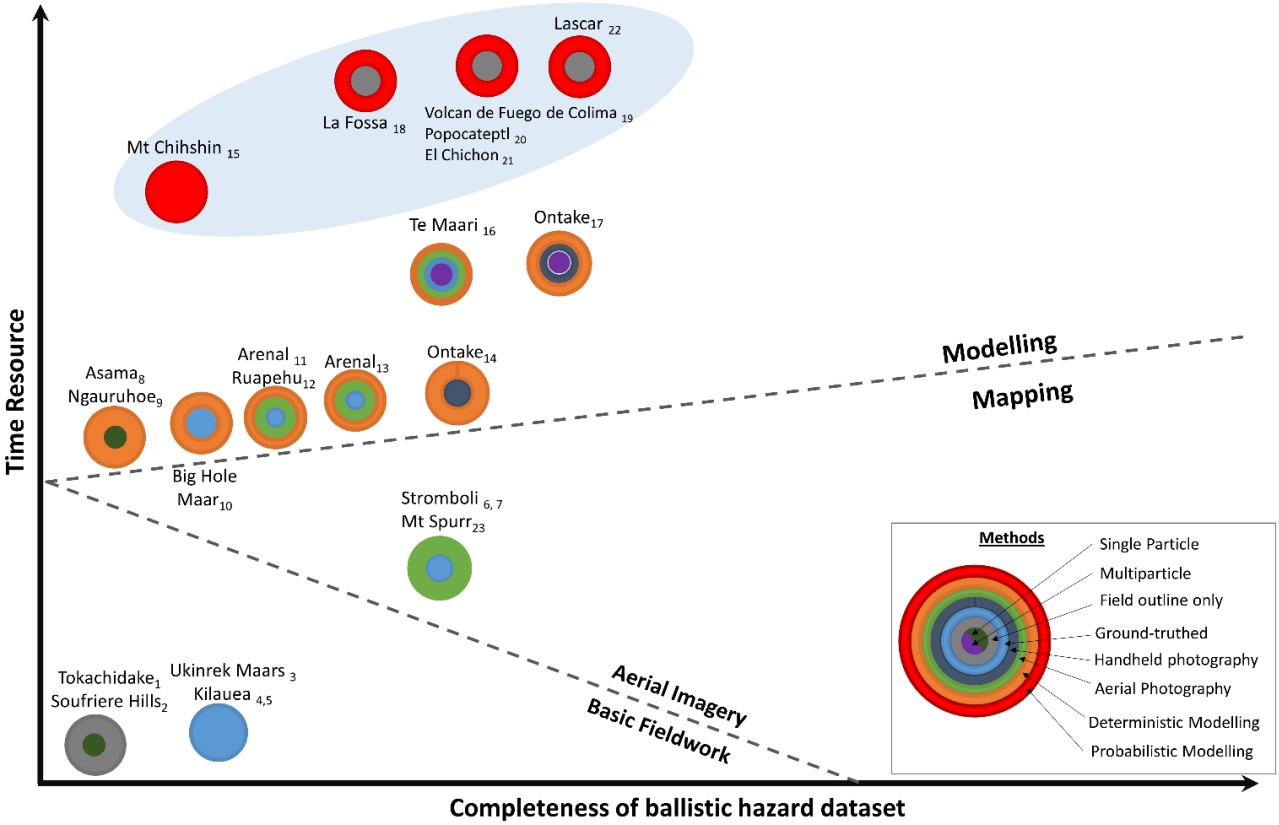

Figure 2.5 Conceptual summary diagram of ballistic mapping and modelling studies from the literature, with relative completeness of ballistic hazard dataset and estimated time requirements. *1 Yamagishi & FeeBrey (1994); 2 Robertson et al. (1998); 3 Self et al. (1980); 4 Houghton et al, (2011); 5 Swanson et al. (2012); 6 Pistolesi et al. (2008); 7 Guiroli et al. (2008); 8 Minakami (1942); 9 Nairn & Self (1979); 10 Lorenz (1970); 11 Fudali & Melson (1971); 12 Kilgour et al. (2010); 13 Wilson (1972);14 Kaneko et al. (2016); 15 Nurmawati & Konstantinou (2018); 16 Fitzgerald et al. (2014); 17 Tsunematsu et al. (2016); 18 Biass et al., (2016); 19, 20, 21 Alatorre-Iberguenoitia et al. (2006, 2012, 2016); 22 Bertin (2017); 23 Waitt et al. (1995).*

3 A COMPARATIVE STUDY OF BALLISTIC MAPPING METHODS AT THE PHREATIC BLOCK FIELD OF RED CRATER.

3.1. Introduction:

Complete ballistic hazard maps are crucial to management of ballistic hazards, yet a systematic examination of mapping approaches has not been conducted to date. Mapping is resource intensive and the choice of mapping approach determines the limitations and usefulness of a dataset. Detailed methods that consider spatial density and size distribution allow for comprehensive multiparticle modelling to be undertaken for use in both eruption dynamic studies and quantification of hazard intensity.

This chapter addresses aims two and three of this thesis by presenting the results of a comparative study of four ballistic mapping techniques using a phreatic block field at Red Crater, Tongariro, dominated by small clasts <10cm. The three most prevalent approaches from the literature review in Chapter 2, field measurements, handheld photography and aerial photography are compared, and a new remote method is developed.

3.1.1 Red Crater and the Emerald Lakes, Tongariro Volcanic Complex

Red Crater is an active volcanic vent, one of the youngest of Tongariro Volcano with a last known eruption in 1934 (Scott & Potter, 2014). It's status as a UNESCO world heritage site with famed views of active volcanism, accessible by the Tongariro Alpine Crossing (TAC) as a day walk, attracts >140, 000 visitors annually. Visitors walk over steaming ground and within meters of recently formed phreatic explosion craters (Scott & Potter, 2014). Red Crater is at the centre of the TAC track, where visitors stop to rest, eat and take photos, on top of blocks which were erupted in historic or recent times (Figure 3.1). Hydrothermal features such as fumaroles, hot ground and acidic lakes indicate the presence of an active volcano-hydrothermal system which has the potential to erupt phreatically, e.g. Te Maari 2012 (Fitzgerald et al., 2014). Despite the confluence of tourism and active volcanism, no mapping of the block field at Red Crater has occurred to date.

Best practice for creating complete ballistic maps has been to locate and characterise individual ballistic bombs or blocks in the field or through orthomapping to record the spatial distribution and size of clasts (Taddeucci et al., 2017). The ballistic field at Red Crater is phreatic and composite, made

Figure 3.1 Volcano-tourists at southern end of Red Crater, within block field. Photo is facing East, people for scale.

up of small blocks from multiple eruptions; creating a spatially dense field dominated by small blocks (<50cm diameter). Due to the time since eruption and subsequent erosion and deposition only two remnant sections of the field are sufficiently preserved for basic mapping (Figure 3.2). This leaves only a small portion ~0.3km^2 of a potentially much larger field from which to collect information.

Additional field variables include limited accessibility and a strong visual contrast between erupted blocks and the lithology they impacted. Access to the area is by foot, a 6 hour return hike, which combined with tumultuous weather restricted the field time from three weeks to 13 days. The blocks erupted from both Red Crater and the Emerald lakes were bimodal in appearance, darker vesicular lithologies and light grey and orange, hydrothermally altered lava blocks (Table 3.1). The lighter coloured blocks dominated the block field and contrasted the underlying lithology strongly, particularly on the Central Crater mafic lava flow.

The 2012 eruption of Te Maari highlighted ballistic hazard to users of the TAC and necessitated the study of ballistics at Red Crater, and Emerald Lake explosion craters. Therefore, considering the above key field variables of the field, we have sought to examine a range of mapping techniques that can be applied to small but complex, ballistic fields with large numbers of clasts to provide the maximum amount of information to hazard and risk assessors.

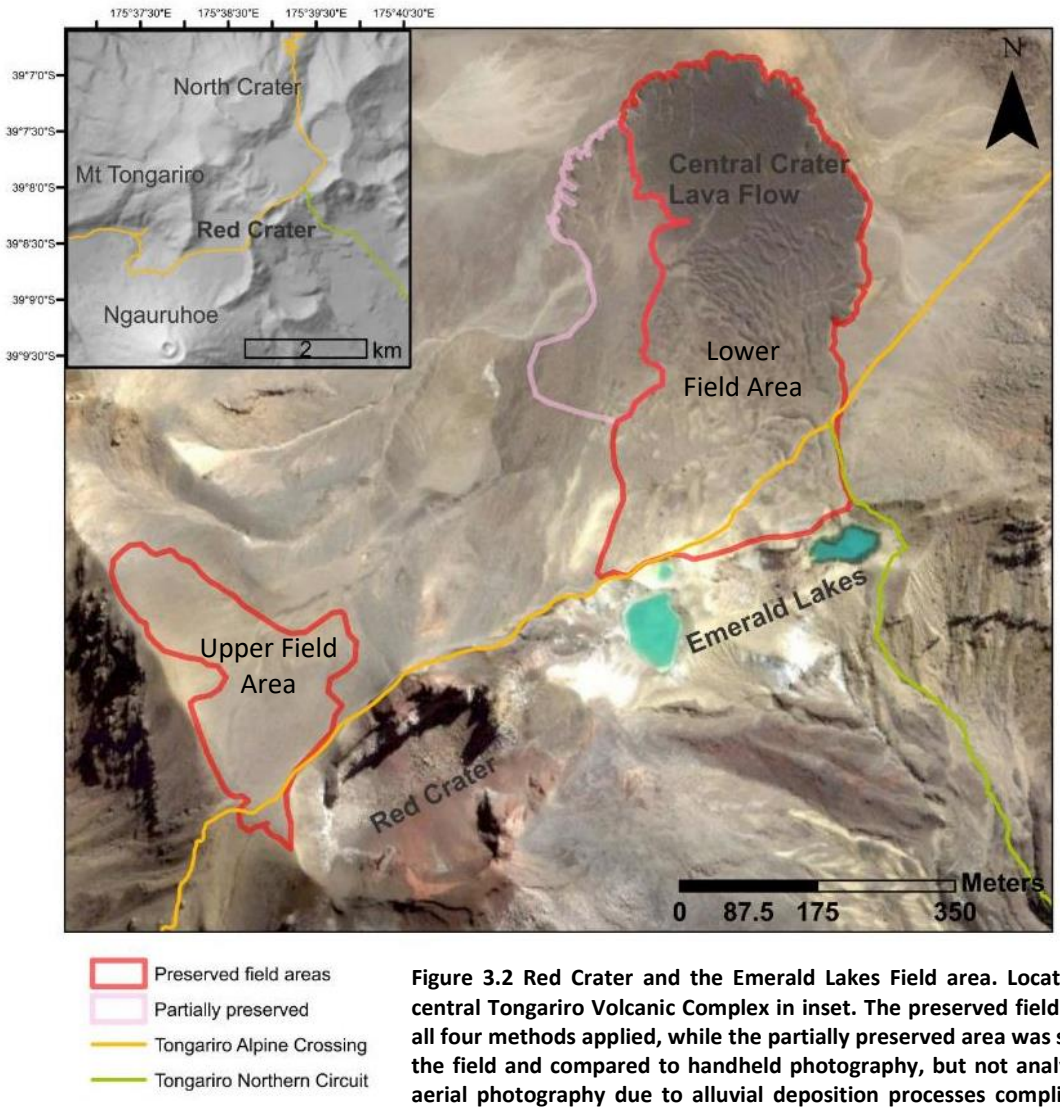

Figure 3.2 Red Crater and the Emerald Lakes Field area. Location within central Tongariro Volcanic Complex in inset. The preserved field areas had all four methods applied, while the partially preserved area was sampled in the field and compared to handheld photography, but not analysed using aerial photography due to alluvial deposition processes complicating the area, requiring high resolution for identification of clast origin – ballistic or gravitational.

3.2. Methodology

13 days of fieldwork in April 2017 focussed on mapping the spatial extent of blocks in the ballistic field of Red Crater and Emerald Lakes. The two preserved areas were mapped, a small (0.05km^2) flat plain to the NW of Red Crater and a larger area (0.25 km^2) to the NNW of the Emerald Lakes. Gullies, seasonal lacustrine sediments and steep volcanic slopes obscured sections of the assumed ballistic field. Steep slopes were not mapped as erosion and rock rolling and breaking evidence could be seen at the base of slopes.

The purpose of this study is to examine mapping techniques rather than eruption dynamics and therefore, only basic, colour emphasised, lithologic descriptions from hand samples and field observations are used to characterise blocks (Table 3.1). The upper field area to the north of Red Crater contained all four blocks types, black scoraceous, red scoraceous, and orange and grey

hydrothermally altered lava blocks (Table 3.1 and Figure 3.3 A-D). These were block types were also observed in the field outcropping in situ within Red Crater; the scoraceous material formed the scoria cone while the light grey and orange blocks were similar in appearance to the Tongariro Trig Andesite (65-110ka) outcropping within the Red Crater's centre (Bardsley, 2004; Wadsworth et al., 2015). The lower field area, beside the Emerald Lakes, contains all four lithologies proximal to the lakes. It is presumed that most blocks were ejected from the Emerald Lakes, however this is less constrained due to lack of outcrops within the craters. The lava blocks in this field section may be Tongariro Trig lavas, or as the Emerald Lakes are situated within craters in Toppings (1974) Red Crater lavas 4 and 5. For this mapped distribution to be used in a deterministic hazard model, an approach like Swanson et al. (2012) with geochemical sampling would be necessary to constrain both the lithology type, eruptive source and potential insight into the number of eruptive bursts.

The Central Crater lava flow (200-500 YBP, Greve et al., 2016) provides a strong visual contrast to the presumed hydrothermally altered lava blocks and a maximum age of emplacement. The hard lava flow surface reduces the potential for impact craters and the vesicular top of the flow is similar in appearance to the red and black scoraceous blocks. This makes identification of the scoareous blocks, which may have been ejected north during the blow out of the side of Red Crater scoria cone (Wadsworth et al., 2015), difficult in the field, and impossible using aerial imagery.

Table 3.1 Field lithology hand sample descriptions

Type	Hand sample description
Grey lava block (Figure 3A)	Medium grey-light grey, grey weathering rind, minor (<20%) orange weathering, vesicular ~1-2mm mode, up to 1cm, 5-10% vesicles. Porphyritic ~30%-10%, small 0.5mm white and black phenocrysts, aphyric groundmass. Weathering rind up to .5cm thick.
Orange lava block (Figure 3B)	Bright orange-yellow - rusty red weathering rind - pervasive rind ~2mm thick. Porphyritic, up to 60% phenocrysts, average ~40%, small 2-3mm white tabular phenocrysts, minor black phenocrysts, aphyric grey groundmass. Not vesicular.
Red Scoria (Figure 3C)	Rusty red-red brown, highly vesicular 70-80%, .1 – 2cm vesicle size, rounded, porphyritic ~5% white/grey tabular phenocrysts, glassy groundmass.
Black Scoria (Figure 3D)	Black, highly vesicular ~80-70%. Irregular size distribution of rounded vesicles, .1mm-1mm. Irregularly shaped, roundish, some have "breadcrust' like texture. Some porphyritic - up to 10% <1mm white tabular phenocrysts. Quenched rims – smaller vesicles on edge.

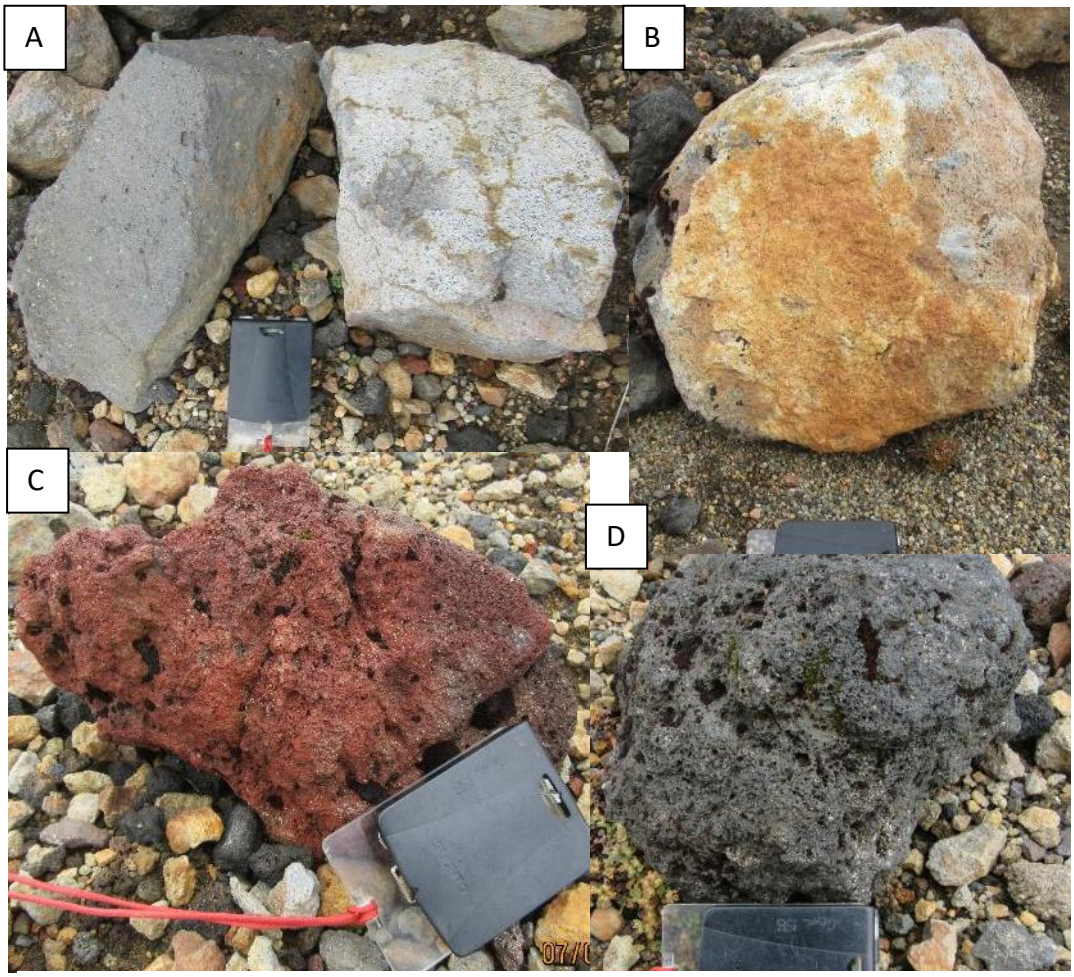

Figure 3.3 Field Lithologies: A) Grey lava block, B) Orange lava block, c) Red Scoria, D) Black scoria

Restricted field time encouraged a combined mapping approach of field measurements, handheld photography and Unmanned Aerial Vehicle (UAV) collected imagery (Figure 3.4). The contrast in block colour to the underlying lithology enabled this approach. Direct measurement in the field (ground-truthed method) and handheld photography (Handheld method) used a $1m^2$ metal frame as a set sample area within which the number and size distribution of clasts were mapped. UAV images were used to extend the limited field dataset. Visible clasts were measured within a $10m^2$ frame using a Geographic Information System (GIS) software (GIS Manual). A pixel-based reflectance method was also developed using the UAV imagery and GIS software to semi-automatically identify and measure block size and spatial distribution (GIS Reflectance).

Five transects at varying azimuths from the vents (N, NE, NW, SW) were conducted to investigate changes in the spatial distribution of clasts with varying distance and direction from the vent (Figure 3.5). Transects 1 and 5 traversed the small area NW of Red Crater where blocks have impacted a surface of lapilli and ash sized tephra and outwash from Tongariro summit (Bardsley, 2004). Blocks were

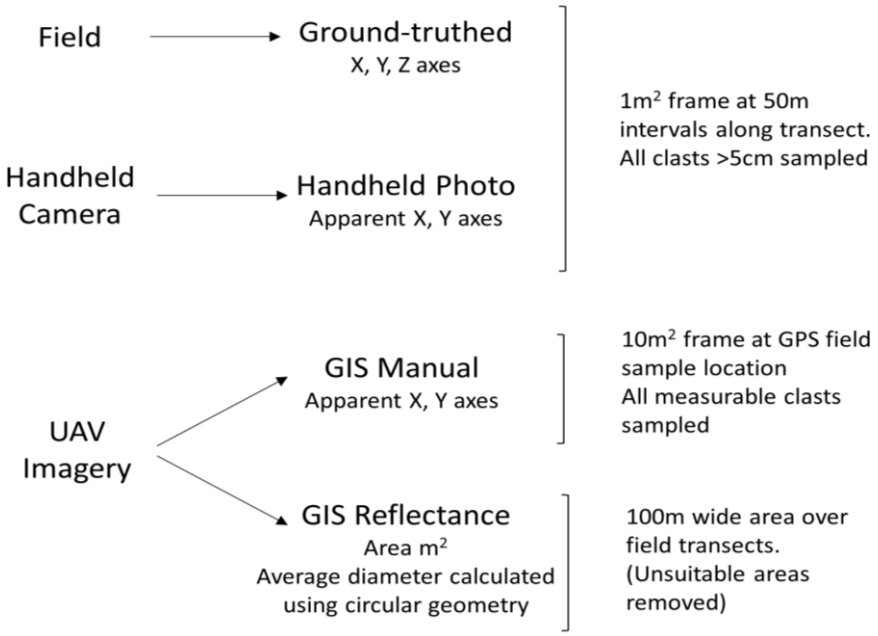

Figure 3.4 Ballistic mapping methodology schematic. Area covered by approach increases down the list.

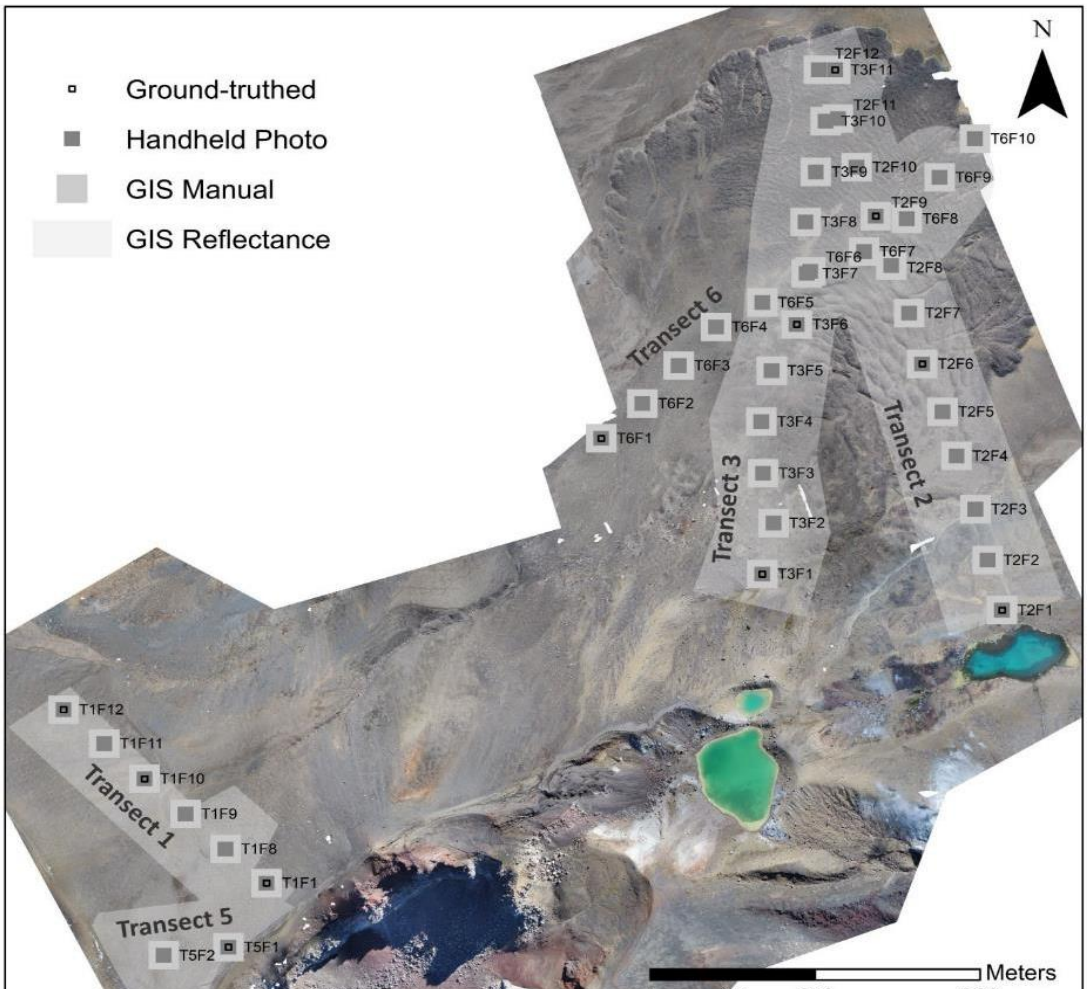

Figure 3.5 Transect and sampling locations, note only GIS Reflectance is to scale, ground-truthed and handheld photo are both 1m². Field image from UAV orthophotography

identified based on their outsized relationship to the underlying sediments and the lack of alternative transport mechanisms at the field site (e.g. no proximal cliffs for gravitational emplacement). Transects 2, 3 and 6 covered the larger section of the field by the Emerald Lakes (Figure 3.5). Due to at least 83 years since eruption (Scott & Potter, 2014), combined with the hard stratum of the lava flow, evidence such as shrapnel fields or craters to confirm ballistic emplacement is absent. However, the lack of other possible emplacement mechanisms and morphological evidence of phreatic activity (e.g. the Emerald Lakes) supported an assumption of ballistic emplacement.

3.2.1. Ground-truthed

Transects were mapped by placing a 1m² frame on the ground every 50m along a set azimuth (Figure 3.5). A 1m² frame was chosen to be compatible with the sampling style undertaken at Whakaari (Chapter 4) (Kilgour et al., in review) and combined with a transect approach to reduce bias. Every clast within the frame greater than 5cm in diameter had the X, Y and Z diameter measured. 5cm was an chosen as the size cut off, based on previous findings that clasts between 2 and 8cm in size may be emplaced with enough energy to be of risk to life and infrastructure (Waitt et al., 1995; Kaneko et al., 2016). However, <4cm was considered too small for the clasts motion to be dominated by ballistic forces (Self et al.. 1980). Sampling locations were recorded via GPS (NTZM 2000) and lithology of each clast, was noted. 11 transect locations were mapped in this manner.

3.2.2. Handheld Photo

All 41 transect locations were photographed for desktop analysis to extend the dataset in a time efficient manner. The $1m^2$ frame made image analysis simple as it provided a set scale for photo adjustment. Field photographs were imported into CorelDRAW, rectified to make the frame sides equant, and the outline of clasts traced (Figure 3.6). The traced image was then exported into ImageJ and the 1m² frame used to set a scale. The apparent X and Y axis of each clast was measured within ImageJ. Apparent X axis is measured as the maximum length or diameter of a clast and apparent Y axis is measured perpendicular to the apparent X axis. The 11 field locations were directly compared with the apparent block size using labelled field sketches to examine the error associated with photo-based size analysis (Figure 3.6).

3.2.3. GIS Manual

Three days were spent collecting orthogonal images of the field area using a DJI Phantom 4 quadcopter Unmanned Aerial Vehicle (UAV) with a 12 mega pixel camera. Flights were flown at 30m over transects to provide high quality images for desktop analysis of larger areas compared to the handheld photography. The field area presented many challenges to UAV use due to high winds and the propensity of clouds creating poor light conditions as well as permit restrictions around usage time and proximity to tourists. The low light and winds resulted in slow UAV speeds and high battery

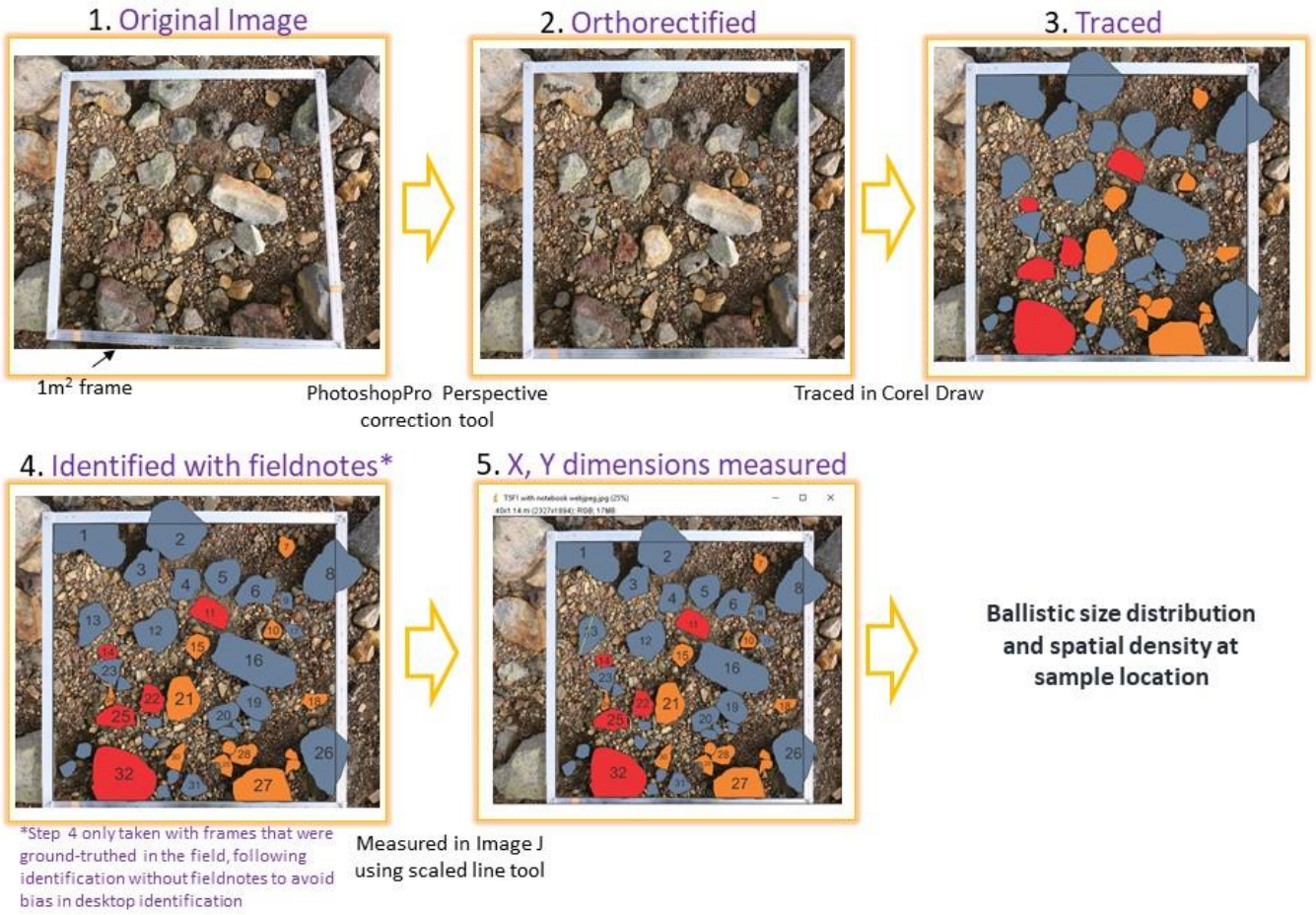

Figure 3.6 Photo ImageJ mapping workflow. Colour of block reflects the lithology and numbers reflect the numbering used in the field to allow direct comparison of field and ImageJ measurements

drainage. Therefore, an elevated flight height of 40 to 80m was required to cover the full field area. Images collected were modelled into a single mosaic image using Agisoft PhotoScan Professional V1.3.2.4205 by Anakant Wandres, University of Canterbury.

The UAV collected orthophotographs were used for two mapping methods, desktop identification within ArcGIS 10.3.1 and reflectance pixel reflectance-based mapping. For manual desktop mapping at Red Crater, a 10m² polygon was positioned over the UAV image at each GPS sampling location in ArcGIS. Individual clasts were identified and their X, Y dimensions and apparent lithology measured.

3.2.4. GIS Reflectance

Red Craters history of potentially multiple eruptions means the ballistic field is spatially dense and therefore time consuming to robustly sample throughout its preserved area. Therefore, a reflectance ballistic identification method was developed in collaboration with Joshua Blackstock from the United States Geological Survey, based on pixel reflectance values using the UAV images. Satellite and aerial remote sensing images have been used to study the distribution and deformation of volcanic eruption products such as lava flows, ash distribution, pyroclastic flows and surge deposits (James et al., 2012;

Pallister et al., 2013; Marzano et al., 2013; Ganci et al., 2018, Schaefer et al., 2016; Kereszturia et al., 2018). Previous imagery mapping includes thermal mapping using mid-infrared and thermal infrared (Ganci et al., 2018), radar intensity images (Schaefer et al., 2016) and microwaves (Pallister et al., 2013).

Schaefer et al. (2016) successfully mapped features at Pacaya volcano, Guatemala, using the intensity of each pixel in a radar image. The intensity of a pixel is related to the proportion of microwaves backscattered which is correlated to the type, shape, roughness, orientation and moisture content of the target area. Our approach is based on the same principle, however, we have used pixel reflectance within the visible wavelength as a simple approach utilising UAV collected colour images.

Visible light is only a very small portion of the electromagnetic spectrum, and so remote sensing studies tend to use to greater breadth of data available in the longer wavelengths collected by satellite and airborne surveys and applied ratio techniques to combine data from multiple wavelengths (Spinetti et al., 2009; Ganci et al., 2018; Schaefer et al., 2016). However, satellite or airborne data is restricted in resolution (pixel sizes of 0.5m – 7m in Schaefer et al., 2016) and the small size of the most ballistic projectiles, generally <1m in diameter, makes satellite data inappropriate for ballistic mapping.

Our GIS reflectance method was developed as an accessible approach which does not require sophisticated data processing tools (van der Meer et al., 2012) but uses simple functions within a GIS program. Mafic rocks are usually characterised by very low reflectance in the visible or near infrared spectral range due to the presence of large amounts of dark mafic minerals (Spinetti et al., 2009). Thus, the contrast between the black (mafic) Central Crater lava flow and the light grey, hydrothermally altered ballistic blocks in the collected imagery (Figure 3.7) led us to explore the feasibility of a reflectance-based mapping approach. The increasing prevalence of UAV's for image collection at volcanoes and the high resolution of images (<2cm pixel resolution) encourages investigation of a pixel-based reflectance approach. By using the visible spectrum only this method does not require the addition of broadband wavelength sensors to basic UAV's making it accessible to budget constrained studies.

The GIS Reflectance method has only been applied to the areas which contained ground-truthed locations for comparison. A 100m wide zone around the transect location was processed. Some sections of the image within the 100m zone were excluded as they went beyond the bounds of the preserved ballistic field, e.g. the inner wall of Red Crater (Figure 3.5 Transect 5). A single colour band image was created of the sampled field area, blue, and the reflectance spectrum of the whole image

compared with the reflectance spectrum of manually identified blocks. Using ArcGIS's Raster Calculator the image was then split into pixels greater than a user defined cut off value and transformed to a vector polygon layer, with individual blocks outlined. This final GIS layer contained the location and size, in area (m^2) of reflectance identified blocks. Full workflow is shown below (Figure 3.8).

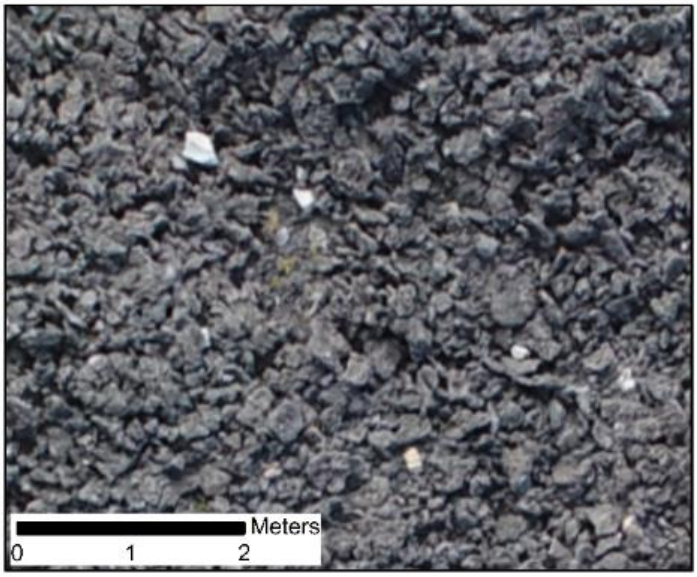

Figure 3.7 Light grey hydrothermally altered blocks on top of the black Central Crater lava flow visible in UAV imagery

This work aims to determine the feasibility of a semiautomated pixel-based approach to assess the distribution of volcanic blocks. As such, a statistical assessment of the difference in identification potential between imagery bands, Red, Blue and Green was not undertaken as focus was on developing the methodology. The blue band provided the clearest contrast between blocks and the underlying surface based on observation and hence was chosen for semiautomated image analysis.

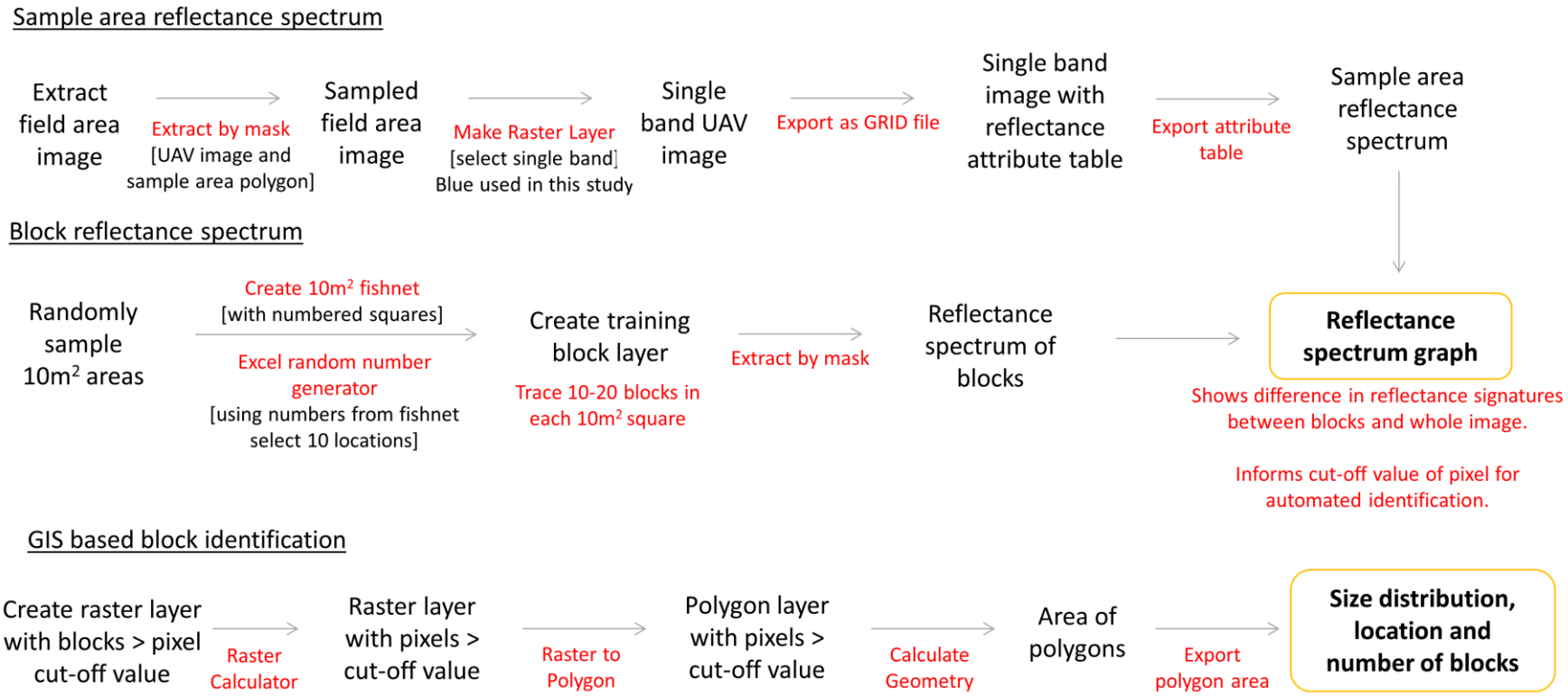

Figure 3.8 GIS Reflectance workflow schematic

The field area was split into two areas based on the range of reflectance values, the spectrum, of the lithology underlying the blocks; lava flow (lower field area) or tephra/alluvium (upper field area). To determine the pixel cut off value for each field area the reflectance values of 249 blocks were sampled and compared to the background reflectance spectrum (Figure 3.9). The recognition of a distinct peak of reflectance values for the blocks in contrast to the reflectance spectrum of the whole field area informed the pixel reflectance cut off values were tested.

Based on the reflectance spectrum of the whole image compared to the reflectance value of sampled blocks (Figure 3.9) three pixel cut off values were assessed for the smaller upper field area. Four cut off values were compared for the lower field area, largely atop the Central Crater lava flow. The extra pixel cut off for the lower area was due to greater scatter in the block reflectance values (Figure 3.9). All GIS Reflectance derived polygons <25cm^2 were excluded from analysis as they are below this studies definition of a block. 25cm^2 is equivalent to a block of 5cm in diameter when calculated using a square geometry or ~5.6cm average diameter using a circular geometry.

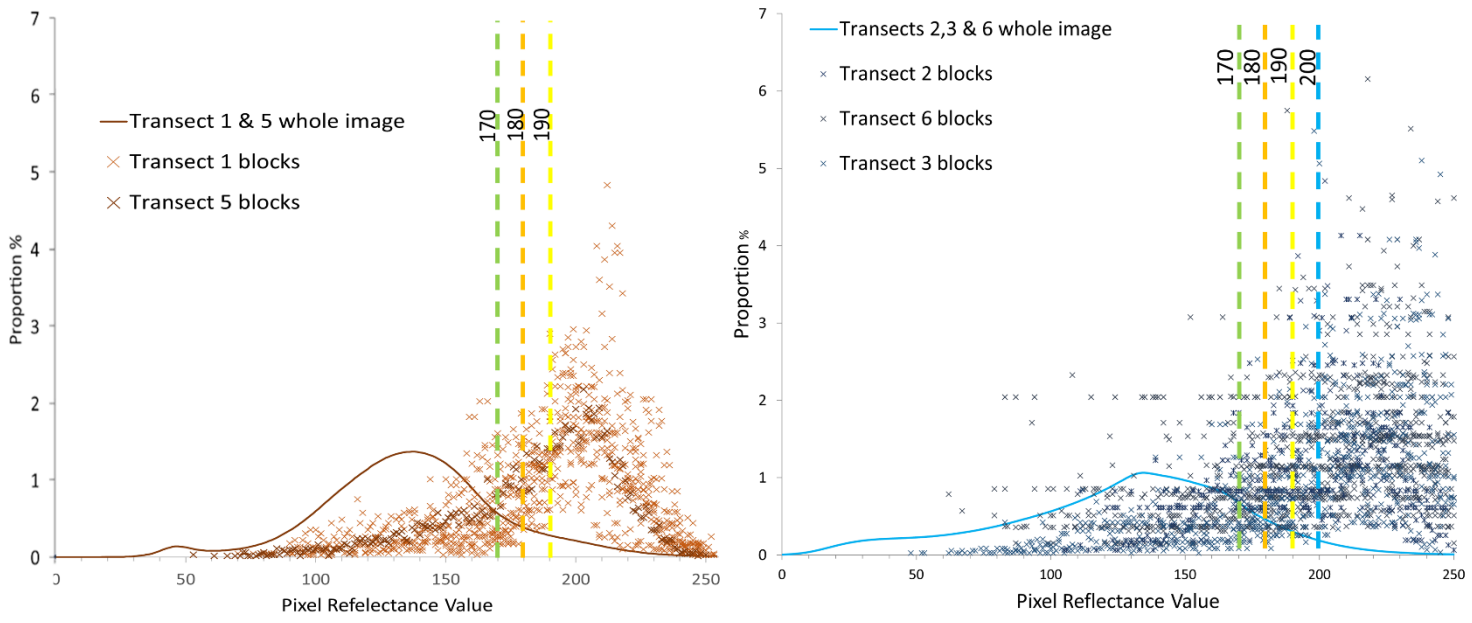

Figure 3.9 Reflectance spectrum for Transects 1 and 5. Dashed lines indicate reflectance values tested for identification of blocks (Figure 10). The reflectance values range from 0-255 and are dimensionless, the classes ArcGIS split the Blue band of the image into

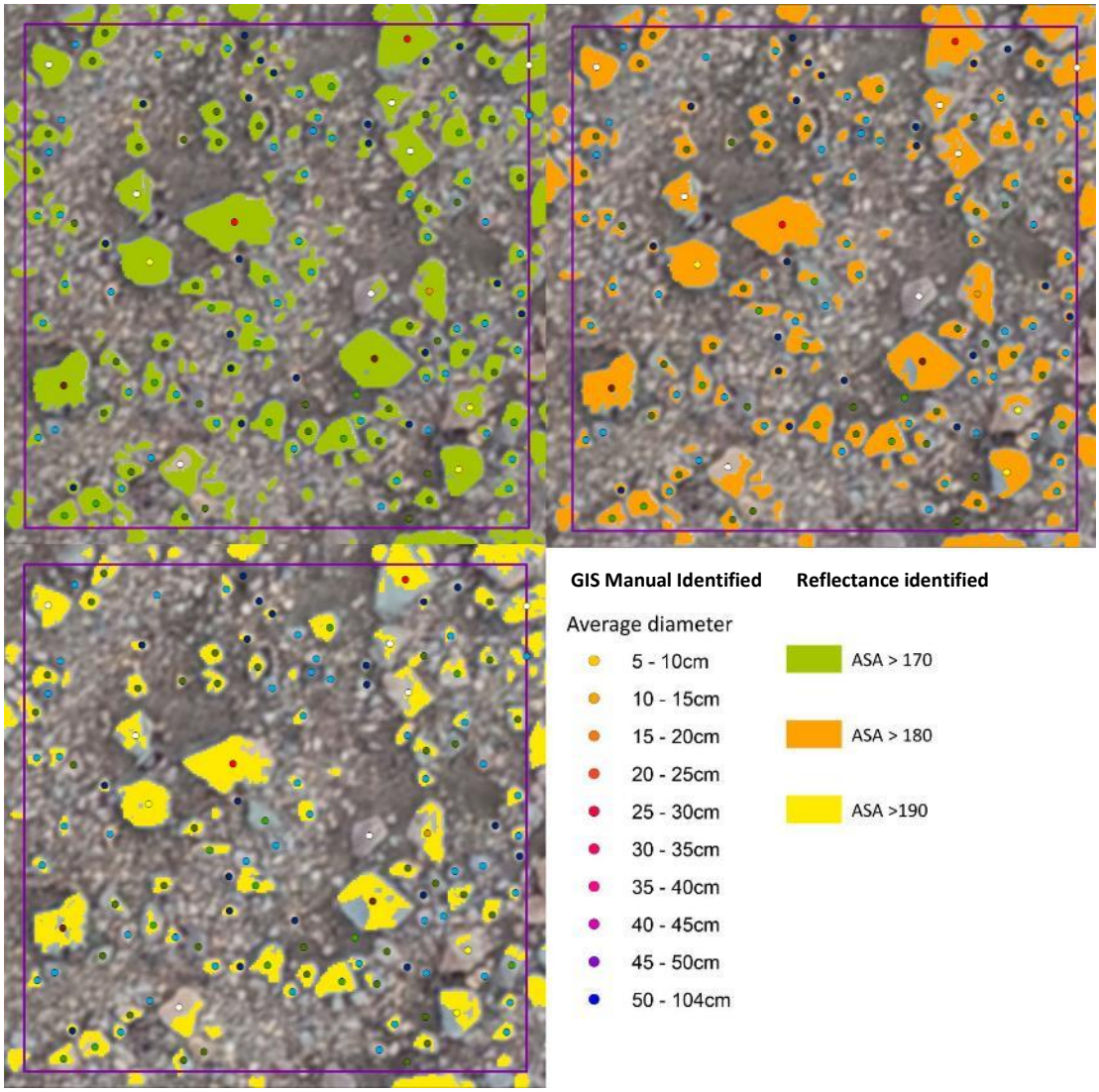

Figure 3.10 Example of identification success at site T5F2 (see figure 3.5) compared to GIS Manual using three reflectance value cut-offs, >170, >180 and >190. As reflectance value increases the portion of each block identified decreases while false positive and merging of blocks also decreases.

3.3. Results

Four methodologies were used to collect complementary datasets on the number, size and spatial distribution of blocks to extend the dataset collected in available field time and compare remote mapping accuracy. Ground-truthed spatial densities and block diameters were used to judge efficacy of a handheld photo approach. The larger dataset provided by the photographed locations was then used for comparison to GIS manual and GIS reflectance methodologies.

3.3.1. Ground-truthed mapping

11 locations were sampled in the field with a total of 213 clasts hand measured. Ground-truthed spatial densities decreased away from the Red Crater vents ranging from 39 to 1 b/m^2 (Figure 3.11).

The average block diameter is smaller when measurements are based on three axes compared to two axes. The average diameter was 9.2cm, compared to 10.5cm using only 2 axes and direct comparison of individual clast diameters found 2axes measurements were on average 15% greater (Table 3.2). The range of blocks was larger based on 2 axis measurements, from 3.9- 31.5 cm average diameter using 3 axes to 5 - 40.6cm based on a two axes measurement.

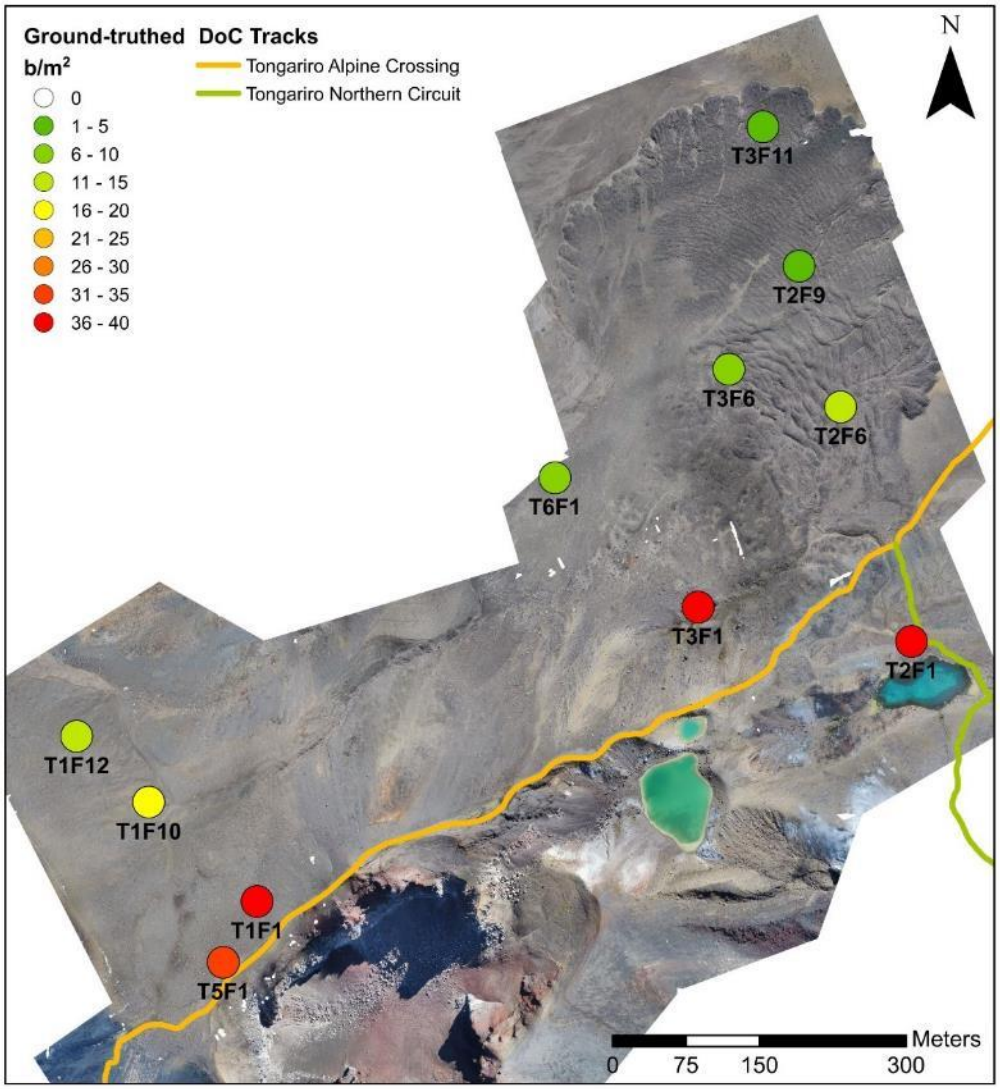

Figure 3.11 Ground-truthed spatial densities in blocks/m² (b/m²)

Table 3.2 Average size and spatial density from field measurements and handheld photography

	3 axes	*2axes*	*Handheld Photo (Ground-truthed sites)*	*Handheld Photo (all sites)*
Sample Area (m²)	11m²	11m²	11m²	41m²
Total no. sampled	213	213	209	425
Mean size (cm)	9.35	10.65	10.02	9.98
Average no. per m2	19.36	19.36	19.00	9.66

3.3.2. Handheld Photo

Field photography covered 41 sites, including the 11 ground-truthed locations, with the apparent X and Y axes of 425 clasts measured. The average clast diameter was 9.98cm and ranged from 3.5 to 47.5cm. The spatial density ranged from 0 b/m^2 to 39b/$m^2$with an average of 9.7 b/m^2 (Table 3.2). The average number of blocks/m^2 is less than for the ground-truthed locations, due to 4 out of 11 GT sites being proximal to the vent locations thereby increasing the spatial density average (Figure 3.12).

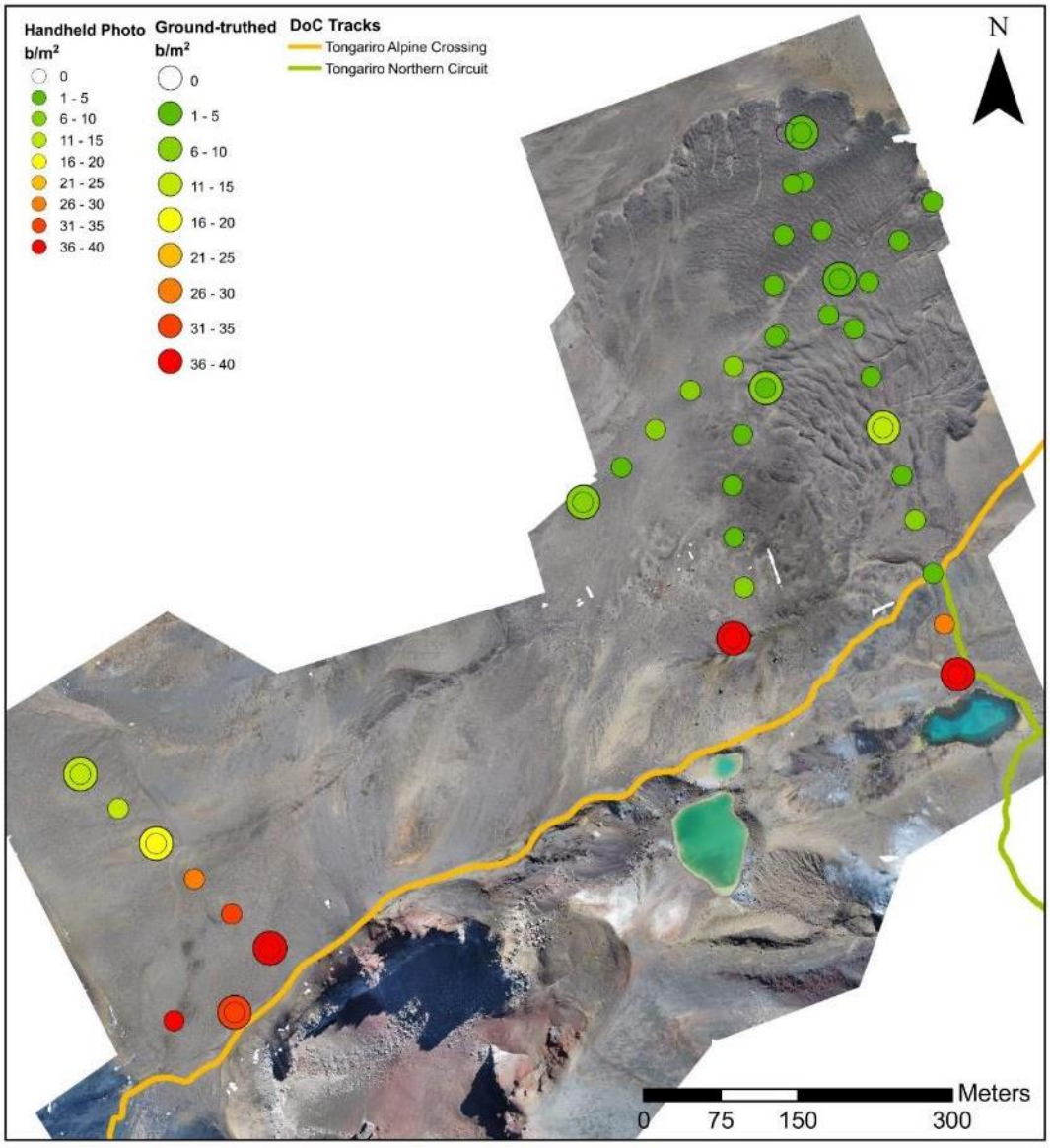

Figure 3.12 Spatial density mapped by Handheld photo method. Ground-truthed spatial densities shown as larger circles behind handheld photo, to demonstrate fit.

Handheld photo measurements matched the ground-truthed well (Figure 3.12). All 11 ground-truthed sites were directly compared to the handheld photos and 98.1% of clasts sampled in the field were identifiable and measured (Table 3.2). The average diameter of handheld photo was 10.02cm, between the 3 and 2 axes ground-truthed average diameters of 9.35 and 10.65cm respectively.

Handheld photo measurements overestimate the block size when compared to a three axes measurement by an average of 9%. This is because the z axes were commonly perpendicular to the ground surface in the field, with the larger two axes visible in the 2D photo plane. The minimum vertical axis may be related to the time since eruption and seasonal snow cover and melt adjusting the block positions over time. Conversely, hand photo analysis underestimates the block size when compared to the two axes in the field by approximately 5%. As the z axis isn't considered in the 2 axes method this discrepancy must be related to the difference in true and apparent axes measurements as well as ImageJ measurement errors.

3.3.2.1 Groundtruthed vs Handheld photo size distribution

The size distribution of the handheld photo dataset fits well to the ground-truthed field measurements. All datasets contain the majority of clasts within the smallest size bin, <10cm, with few clasts > 25cm measured as expected for phreatic size distributions (Kaneko et al., 2016; Kilgour et al., 2010, in review). The slightly smaller average block diameter of the 3 axes ground-truthed measurement skews its size distribution to the right slightly, however, there is no major difference between the 3, 2 and hand photo (11 sites) size distribution. The larger area sampled using handheld photo, 41m^2, shows a greater range in clast diameter (Figure 3.13).

The ~98% identification rate of ground-truthed blocks by the handheld photo method gives confidence in the results from hand photo as a baseline from which to compare UAV imagery methods to. The accuracy and greater coverage of the handheld photo method makes it the best dataset for comparing spatial densities, while the most accurate size distribution is from ground-truthed data.

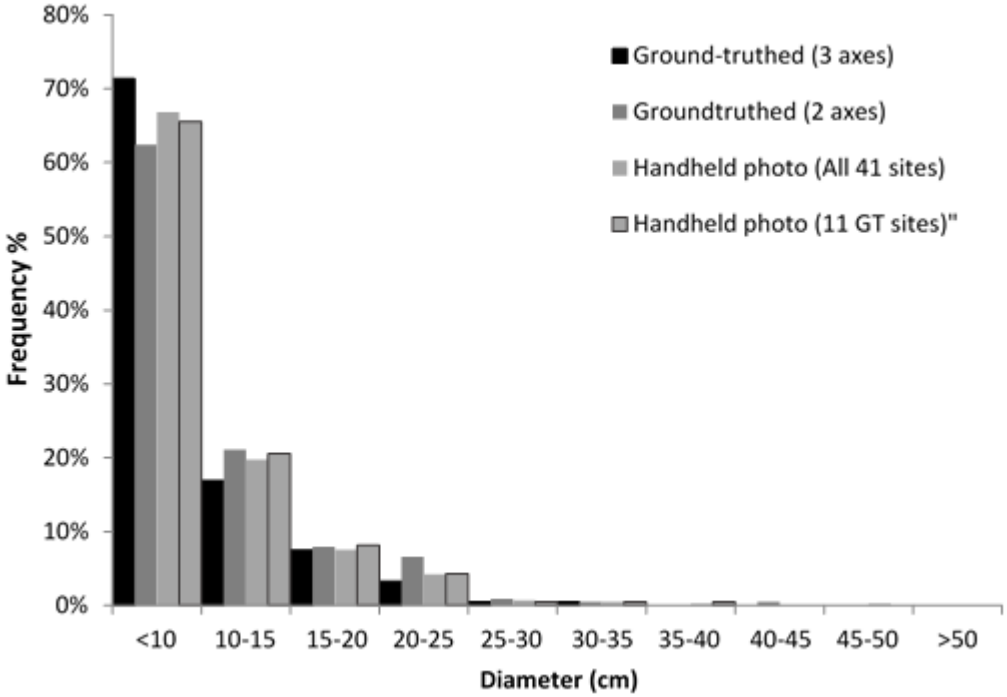

Figure 3.13 Size distribution of handheld and ground-truthed measurements

3.3.3. GIS Manual

The GIS Manual methodology sampled 407.5m^2 (2.5m^2 of T1F1 was excluded due to an error in the UAV photo merge) and identified a total of 1419 blocks. The average spatial density was much lower than via hand photo identification with an average of 3.24 b/m^2 and average clast diameter of 14.29cm (Table 3.3). The larger sample area covered by the GIS Manual approach, 10x that of the handheld photography and 900x bigger than ground-truthed, meant rarer large blocks were sampled increasing the maximum average block diameter to 104 cm.

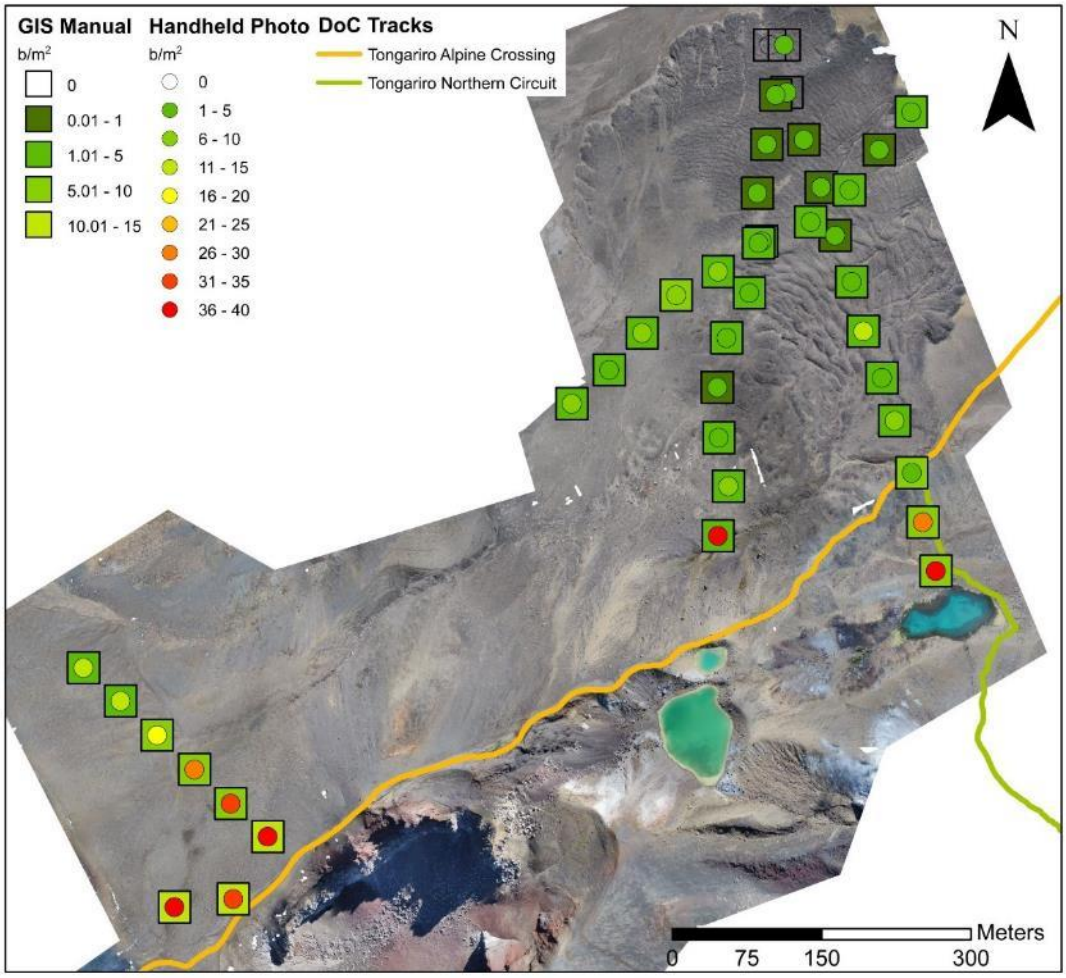

Figure 3.14 GIS Manual spatial density compared to handheld photography b/m².

The low flight heights of 30m over the targeted transect areas provided high resolution images, with pixels sizes of ~2cm allowing identification of clasts down to ~5cm in diameter. The resolution was variable depending on small scale fluctuations of UAV flight height and ~3-5% of the field were impacted by image merge errors and so were excluded from analysis. The impact of flight height was most pronounced at the Emerald Lakes end of Transect 2 (Figure 3.14), where flight heights were higher, ~60m, to reduce the UAV flight time to avoid flying above track users, a condition of permitting.

The resolution limitation of the ortho-imagery is evident in the size distribution, with a smaller proportion of small clasts (<10cm) identified by GIS Manual than ground-truthing or handheld photo

(Figure 3.15). The larger sample area does, however, increase the number of larger blocks measured providing a better estimate of maximum block size.

Table 3.3 GIS Manual compared to handheld photo ballistic data * 2.5m² of sample location T1F1 was lost due to an image merge error.

	Handheld Photo	*GIS Manual*
Sample Area (m^2)	41	407.5 *
Total no. sampled	425	1419
Mean size (cm)	9.97	14.29
Average no. per m2	9.66	3.48

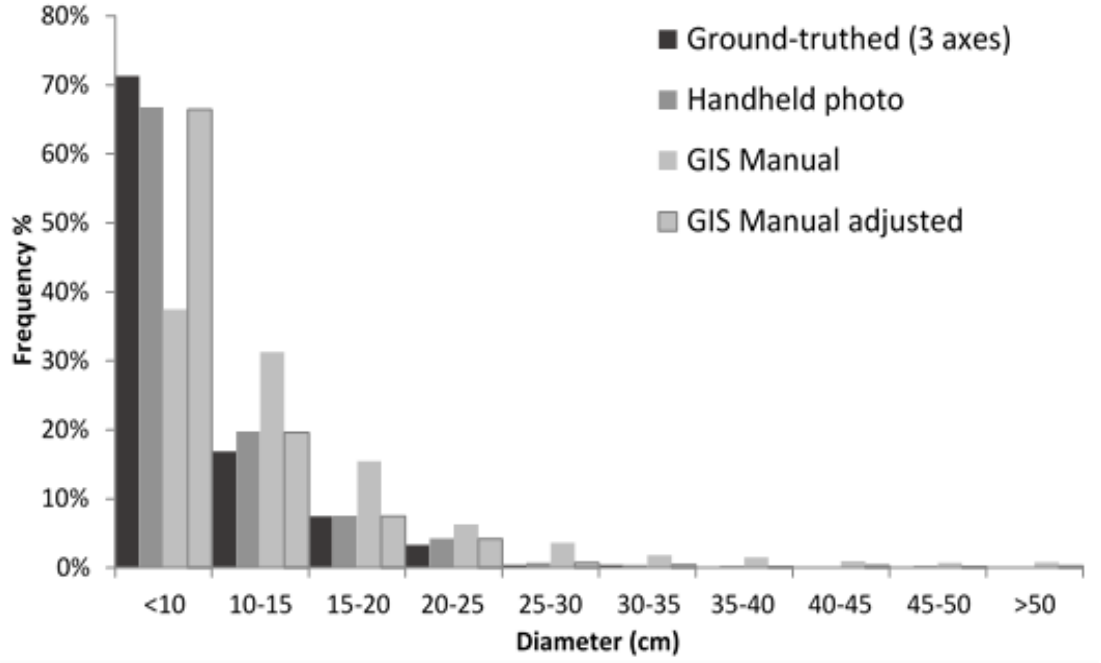

Figure 3.15 Size distribution of blocks from ground-truthed, handheld photo, GIS Manual and adjusted GIS manual methods

To estimate the total number of blocks within the area mapped by GIS Manual, including those below the resolution limitations, the number of blocks is adjusted to account for the missing blocks per m^2 (Figure 3.15, adjusted). The number of blocks per m^2 in each size bin was adjusted to equal the number found by handheld photo method (for full calculation see Appendix 1A). GIS manual greatly underestimates the number of clasts, particularly the smallest block size. Even when a size distribution based adjustment factor is applied, the spatial density still does not perfectly fit the handheld photo and ground-truthed data (Figure 3.16). Plotting the data indicates that the adjusted dataset is closer to the handheld photo spatial density (Figure 3.17), however the use of the adjustment factor meant that many of the low density field areas were overestimated, by up to 25b/m^2. Despite this, the size dependent adjustment factor does vastly improve the accuracy of the remote UAV imagery (Figure 3.17). The direct comparison also should provide a warning to be wary of the resolution limitations of

low resolution (12 megapixel) UAV imagery when identifying blocks of a few centimetres from heights of >30m.

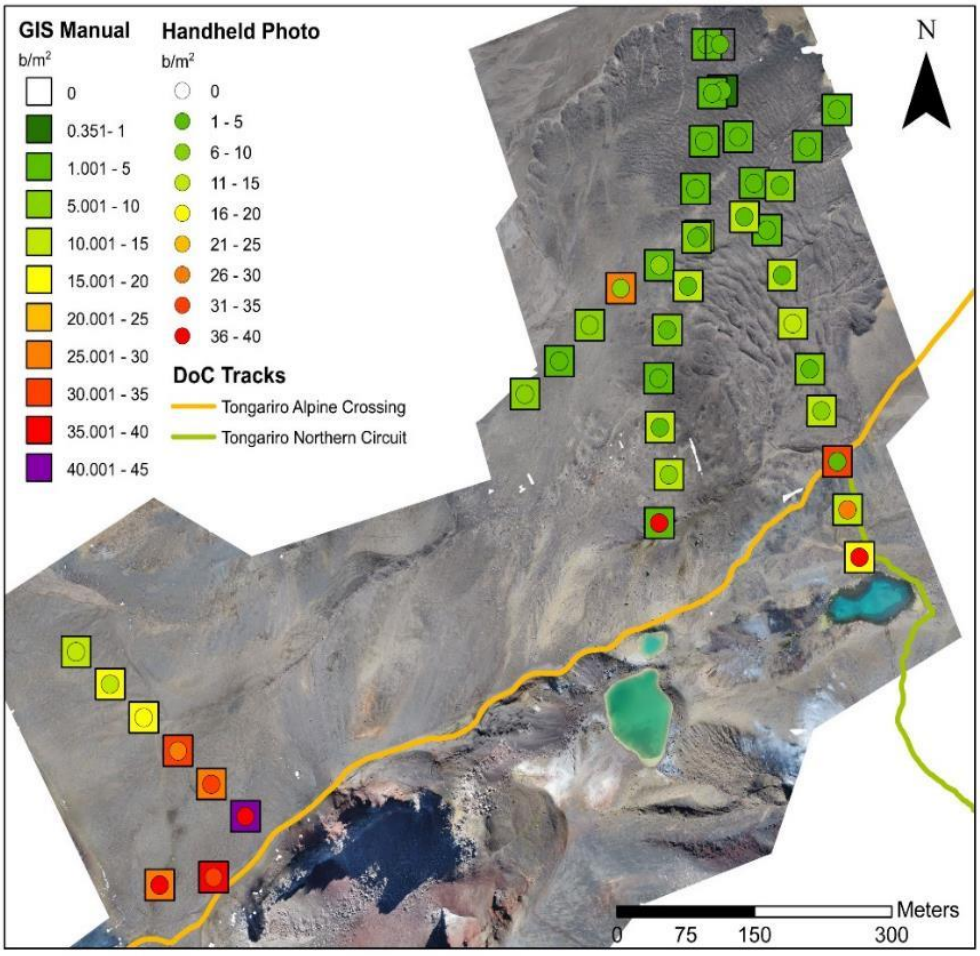

Figure 3.16 GIS Manual adjusted spatial distribution compared to handheld photo spatial density

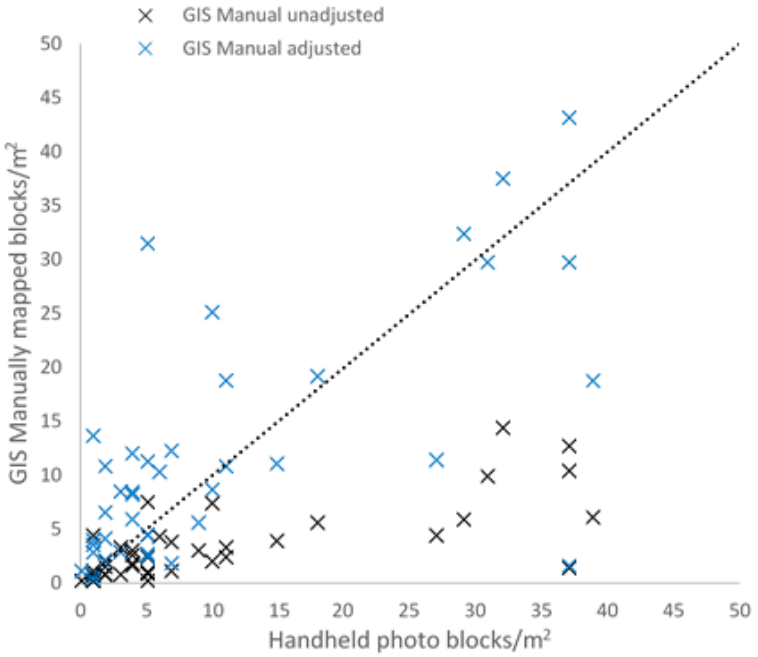

Figure 3.17 GIS manual fit to handheld photo dataset, dashed line is 1:1 relationship. Unadjusted GIS Manual underestimates the number of blocks, most significantly for sites with high spatial densities. Adjusting the dataset improves the fit of higher density location, however causes overestimation of lower density locations.

3.3.4. GIS Reflectance

A reflectance method using basic tools within ArcGIS and UAV collected imagery was developed as a method of mapping a large area with high block spatial density relatively quickly. Collection of ortho-imagery allowed manual identification and measurement of blocks in ArcGIS (GIS Manual), underestimating the number of blocks by 66.5% due to insufficient resolution and also required a very large amount of time. Crucially, the GIS Reflectance method covers a larger area and therefore better accounts for spatial density variation and size distribution variation. This is intended to provide a robust estimation of the preserved eruptive mass in a way that traditional isopach style approaches do not due to their simplistic categorisation of field areas (Tadeucci et al., 2017). Therefore, a method was developed where, using only a colour image, polygons are created in a GIS programme outlining blocks over a determined pixel brightness.

Two areas surrounding the field transects were sampled, 29617m^2 area at Red Crater and 105333m^2 at the field area by Emerald Lakes (Figure 3.4). Only half of Transect 6 was included as half of the transects underlying lithology was alluvium and not lava flow. While this section was included in previous methodologies with clast identified based on their outsized nature, the reflectance signature was too different for inclusion in this method therefore these 144 blocks are not used. The success of GIS reflectance block identification was compared to GIS Manual due to the large sample size of 1275 clasts. The greater accuracy of the ground-truthed or handheld photo measurements make them better comparative datasets for the small block sizes, however the small sample size of 1m^2 and subsequent difficulty in identifying frame locations exactly within the aerial photography did not allow this.

The accuracy of the area identified by the GIS Reflectance approach was assessed by comparing the area of 249 blocks randomly sampled and traced by hand to the GIS Reflectance polygon area (Table 3.4). The area of a block accurately identified was greatest at the lowest reflectance values, with darker edges of blocks being excluded from identification as the reflectance value increased resulting in a lower proportion of block identification.

Table 3.4 Percentage of area successfully identified by GIS Reflectance per reflectance value and transect location.

Reflectance Value	Transect 1 & 5	Transects 2,3,6
170	83% ±13	
180	70% ±30	86% ±36
190	71% ±11	74% ±47
200		60% ±30

The GIS Reflectance method was variably successful depending on the underlying lithology and average clast size (Figure 3.18, 3.19). The method worked well for Transects 1 and 5 identifying 51% of the total number of GIS Manual clasts at a reflectance value of 170, with a 4% false identification rate. Additionally, GIS Reflectance positively identified blocks missed in GIS Manual, which will be discussed later.

The method was not successful in identifying blocks in the second part of the field area, the Lava Flow. This was unexpected as the striking contrast between the light grey hydrothermally altered blocks and underlying mafic lava inspired this GIS Reflectance approach. The high misidentification rate on the lava flow was a result of the highly reflective wet lava block surfaces in some areas of the field (e.g. Figure 3.18 A vs B). Additionally, the size of the blocks was smaller on the lava flow with 77% of blocks <20cm in diameter as compared to 60% of the Red Crater field area (GIS Manual measured). As well as a high misidentification rate (Figure 3.18 B), the accuracy of each block area was lower than at RC with the most successful pixel cut off value of 200 identifying 60% of a clasts area with an error of ±30% (Table 3.4).

The time limitations of an MSc did not allow for further corrections, or refinement of imagery selection based on weather conditions at time of image collection, would potentially rectify the lava flow identification issue. However, the further work section 3.6 will address some potential solutions.

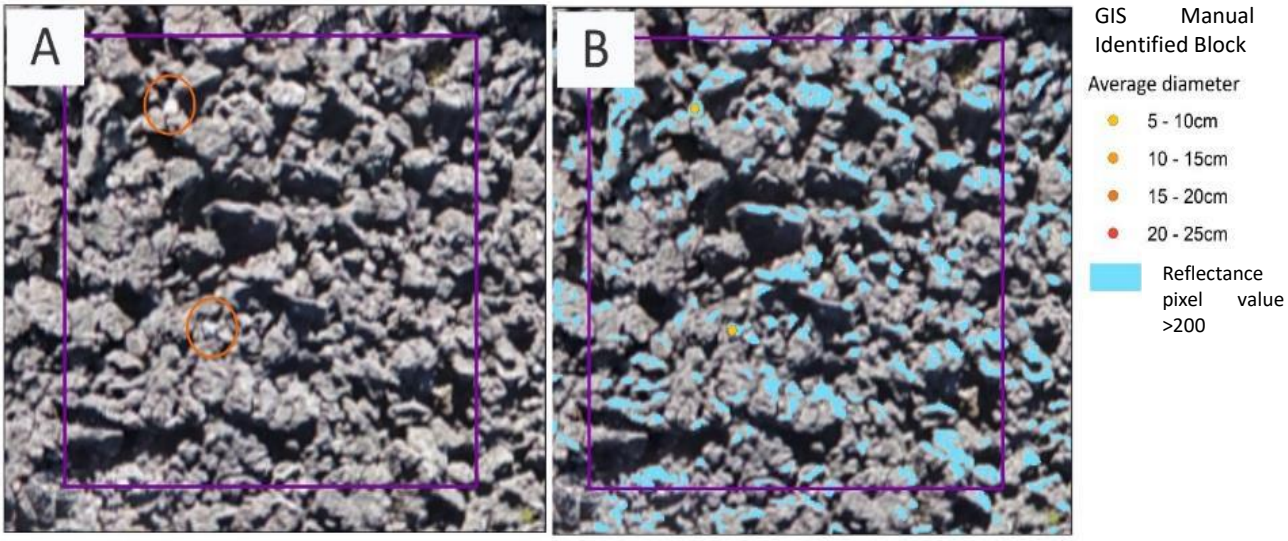

Figure 3.18 Example site 10m² sampling location at the end of the Central Crater Lava Flow. A) highlights the two small blocks mapped and B) shows the high proportion of lava flow blocks classified as blocks by the GIS Reflectance method.

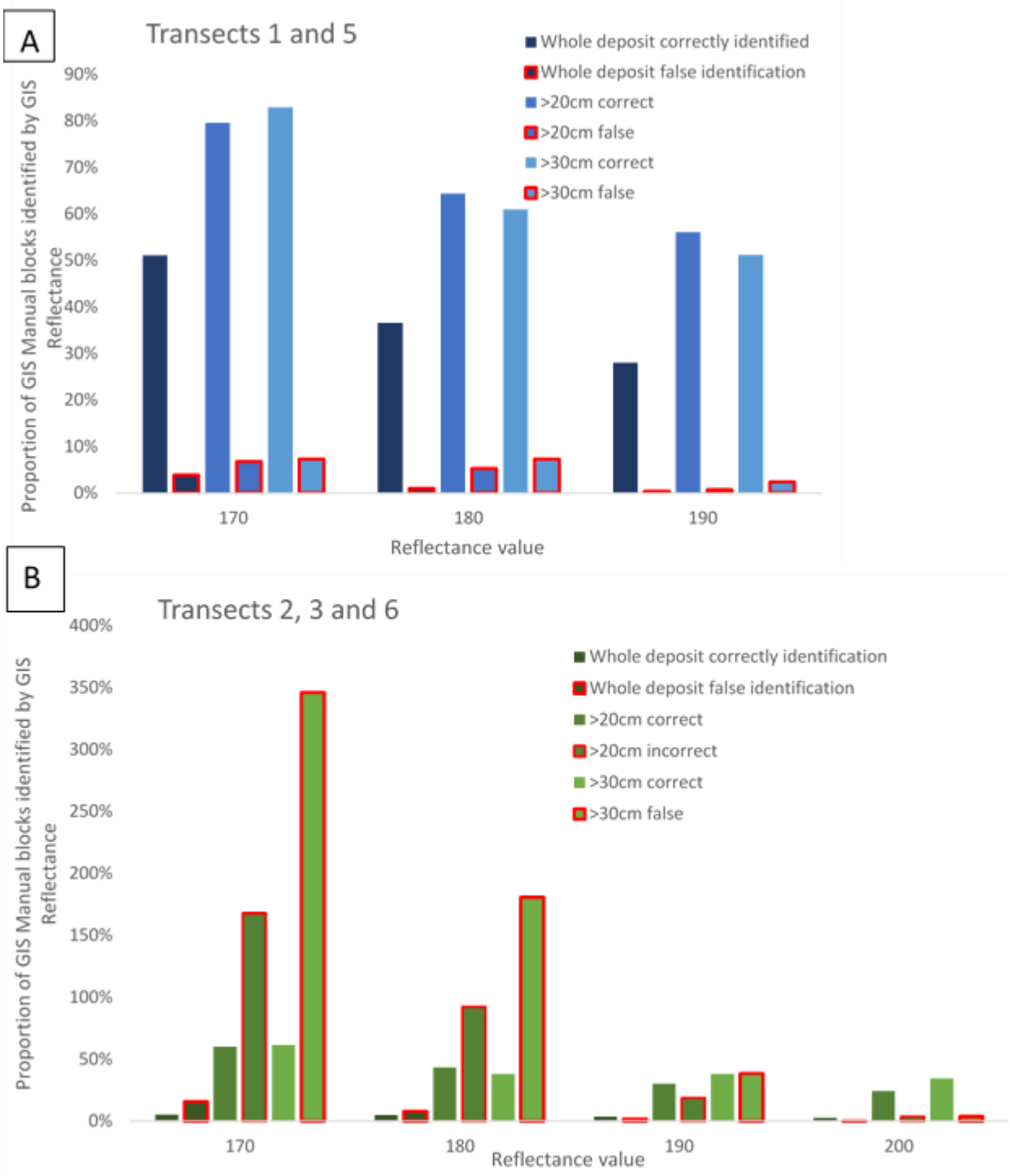

Figure 3.19 Identification rate of GIS Reflectance method compared to GIS Manual blocks. 77.5m2 compared for Transects 1 and 5, 290m2 for transects 2,3 and 6. Note the difference in Y axes scales. Bar colour lightens as block size increases and a smaller total pro portion of ballistic mass is considered. Red bordered bars indicate the proportion of clasts incorrectly identified within the size bin. For transects 1 and 5, positive identification is significantly greater than false identifications with a reflectance cut off value of 170 gaining the best results (A). In contrast, false identification of clasts outweighs the correct identification substantially for Transects 2,3 and 6 (B).

3.3.4.1. Size distribution of GIS Reflectance blocks

The GIS Reflectance method identified 340081 blocks within the 29617m^2 Red Crater field area sampled, an average spatial density of 11.5b/m^2. Compared to the average spatial density from Handheld Photo method, 20.5b/m^2, this suggests ~56% of the clasts have been identified. The size distribution of GIS Reflectance blocks at Red Crater fits the ground-truthed size distribution very well (Figure 3.20). While the ground-truthed dataset provides the most accurate size distribution, this is only true for the 4 locations which have been ground-truthed in this area. In this case two out of four sample location are close to the vent and would bias the any conversion factor towards spatial densities that are too high. Therefore, the handheld photo method is the best dataset available for comparison as it includes more distal sample locations. The relationship between handheld photo blocks per m^2 and GIS Reflectance blocks in each size bin was used to calculate a size bin-based conversion factor *L – See Appendix 1A for calculations.

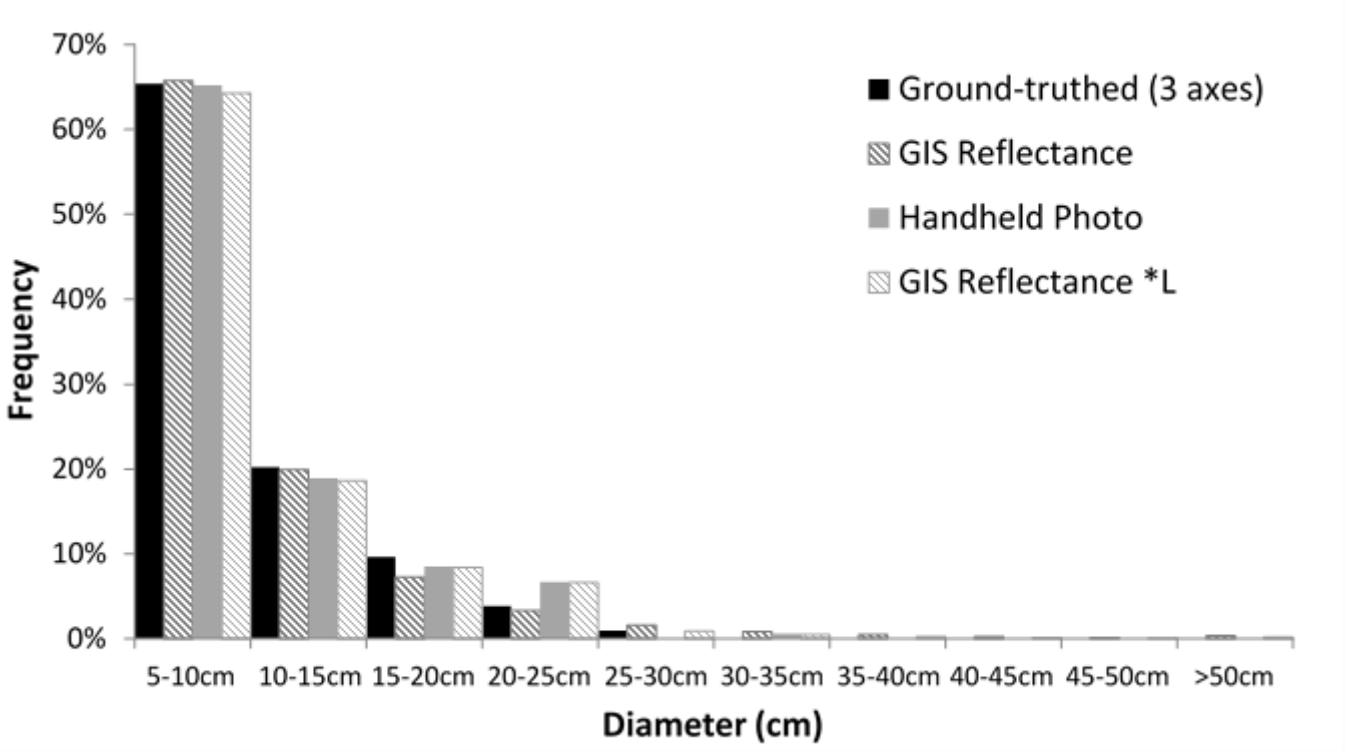

Figure 3.20 Size distribution of clasts identified with a reflectance value of 170 at upper field area/transects 1 and 5. Ground-truthed size distribution only from the upper field area, sample size of 104 clasts.

3.3.4.2. Spatial distribution of GIS Reflectance blocks

The spatial distribution of blocks found by GIS Reflectance underestimates the number of blocks per m^2 when compared to the handheld photo dataset (Figures 3.21A and 3.22). Therefore the conversion factor derived, *L, was applied to the mapped distribution to adjust the total number of blocks. Blocks

were weighted as per their size within ArcGIS and the kernel denisty function was used to derive the spatial denisty of blocks per m^2.

While the spatial density at each location is underestimated prior to adjustment, post adjustment GIS Reflectance data largely follows the 1:1 line with a small degree of underestimation. The highest

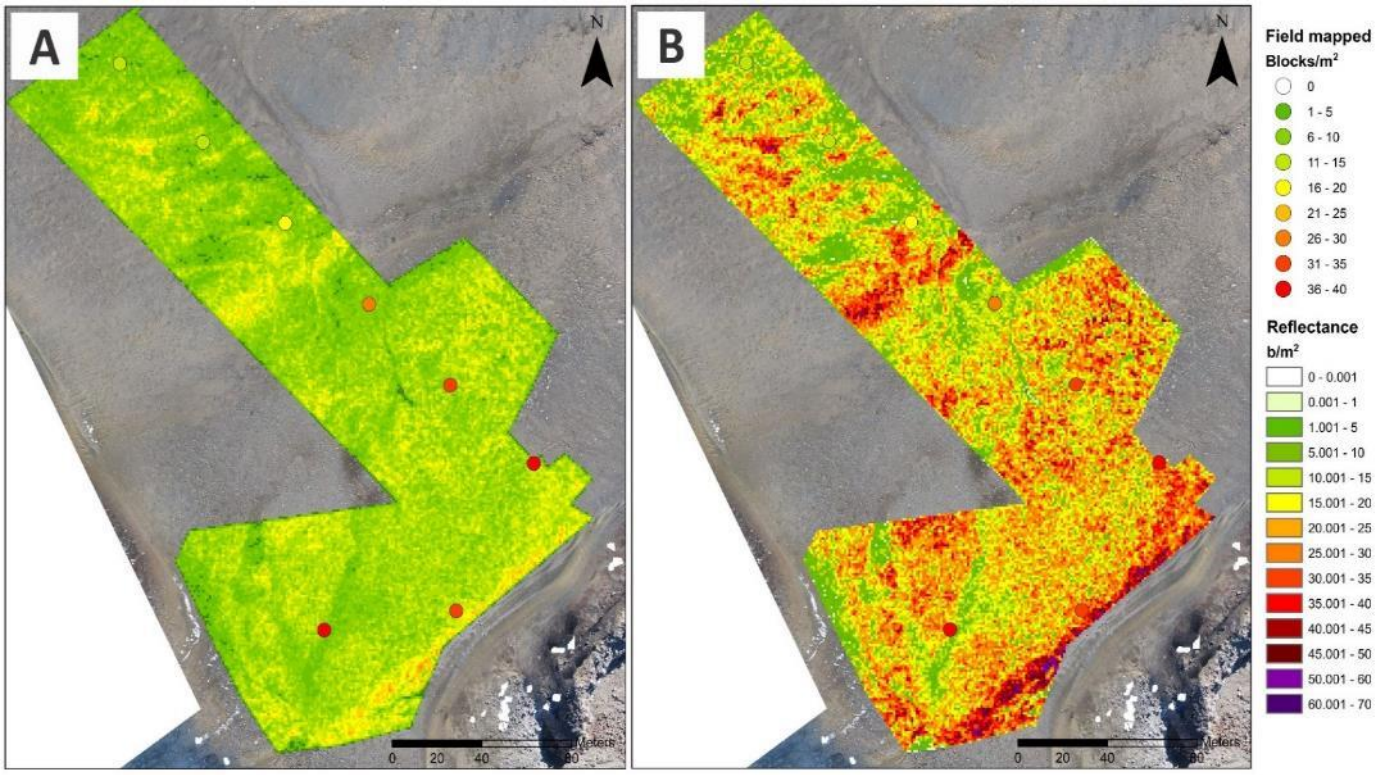

Figure 3.21 A) Raw GIS Reflectance spatial distribution of blocks/m2. B) GIS Reflectance converted based on size binned relationship to handheld photo spatial distribution *L

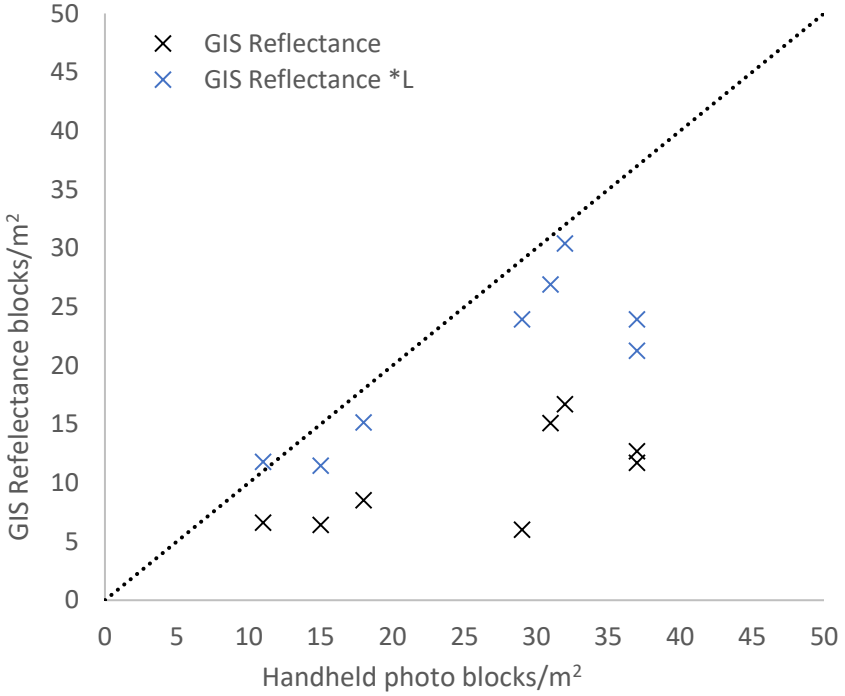

Figure 3.22 GIS Reflectance spatial density of blocks per m2 compared to handheld photo spatial density, raw and adjusted by factor *L. Dashed line indicates 1:1 relationship. The number of GIS Reflectance blocks within the 10m2 sample frame of GIS Manual is used to calculate block density per m^2.

density locations are the most significantly underestimated, by 16 and 13 b/m^2. (Figures 3.21B and 3.22).

Figure 3.23 demonstrates the high spatial variability of the field, with blocks/m^2 ranging from ~10-50 b/m^2 within only 10m^2. This highlights that the 1m^2 sampled in the field may not be representative and may therefore account for some of the difference between handheld photo and GIS reflectance spatial density. Unfortunately, the small handhald photo sample area of 8m^2, does not provide a large enough area for assessing the sources of identfication errors and so the amount of error due to spatial variability and that due to identfication differences cannot be known.

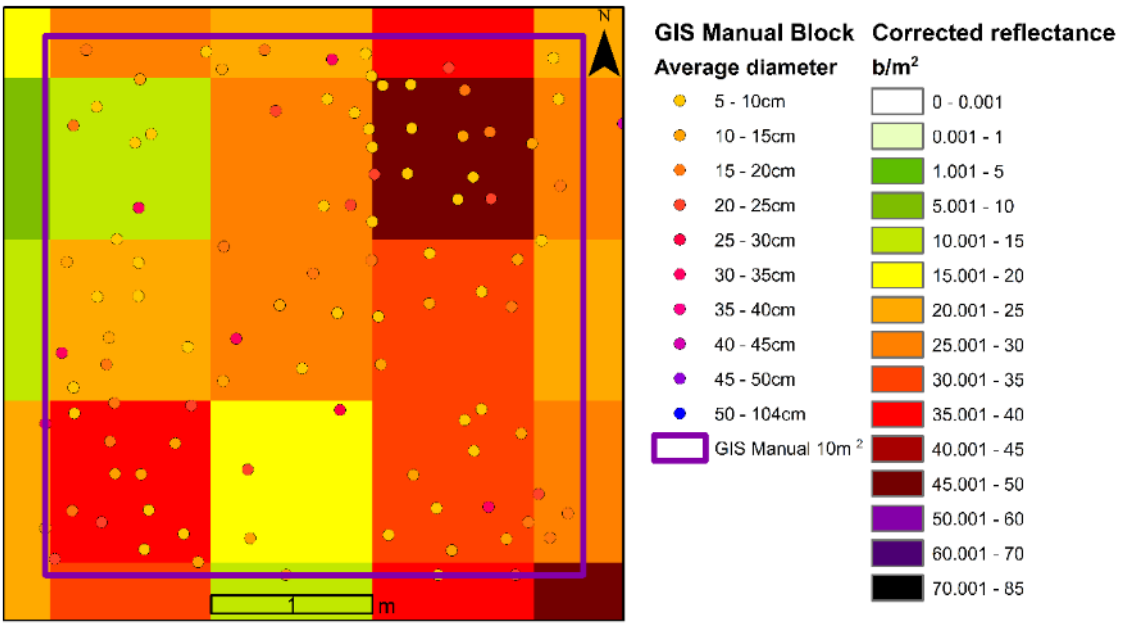

Figure 3.23 Transect 1 Frame 8 10m^2 sampling frame showing the high spatial variability within the small area from both GIS Manual and GIS Reflectance approach. Purple box is 10m^2 frame.

3.3.4.3. GIS Reflectance error calculation

674 GIS manual identified clasts were used to quantify the identification error of blocks based on clast size. Blocks were deemed successfully identified if a polygon was formed where a block had been manually identified. Identification errors occurred due to the merger of clasts, partial identification of segments and false identification of tussocks as blocks (Figure 3.24).

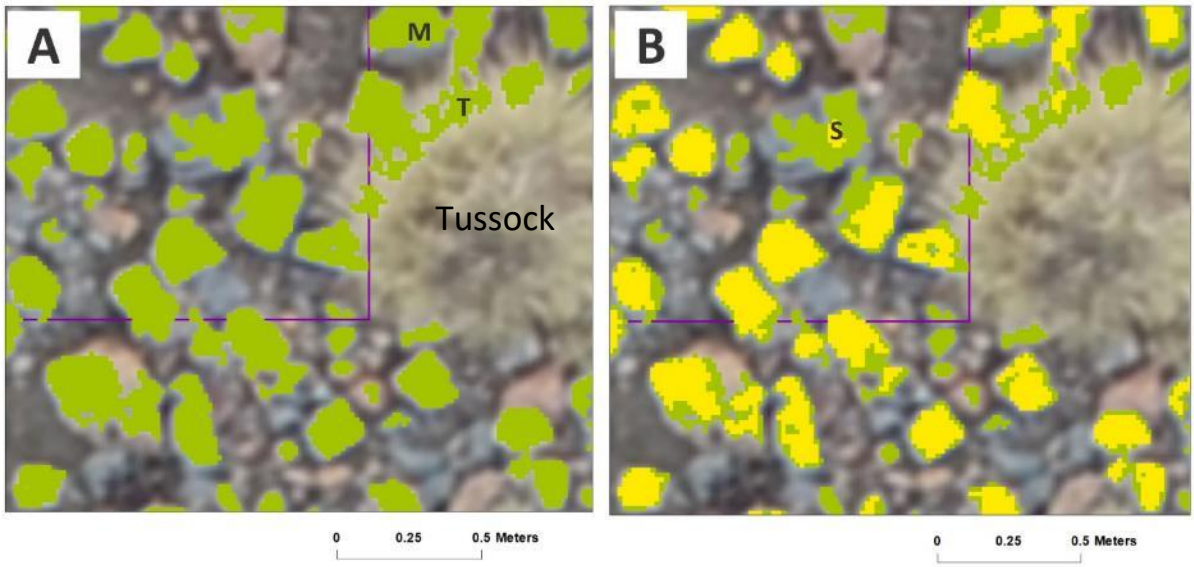

Figure 3.24 Error sources with GIS Reflectance method. Green polygons are indenitified at a reflectance value of 170 and yellow polygons at a value of 190. Merging of clasts into a single identified area (M) and incorrect identification of tussock (T) as a block shown in A. B shows the segmentation of a block (S) and how clasts merged at lower reflectance values become separated at a higher value.

Merging occurred where adjacent blocks were detected as a single, larger clast. The smallest size bins had the greatest addition of clasts counted while the 25-30cm size bins gained a small number of clasts in error (Figure 3.24). The larger size bins would be expected to gain clasts through the merging of smaller clasts but the smaller bins had many clasts bordering on the detection limit of ~5cm merge into larger clasts, but remain within the smallest two size bins creating a positive error. Negative merge errors, such as in size bins 15-20cm and 20-25cm, indicate the proportion of sampled clasts which were merged, and subsequently identified in another size bin.

The segment error classification indicates how many clasts are added or lost to each bin based on a clast being split into multiple segments. The smallest size bin gained clasts, 3% as larger blocks were split into multiple smaller blocks while the 25-30cm bin lost 3% through segmentation (Figure 3.25). The smallest two size bins also gained 5% and 1% of clasts respectively through false identification of tussocks as blocks.

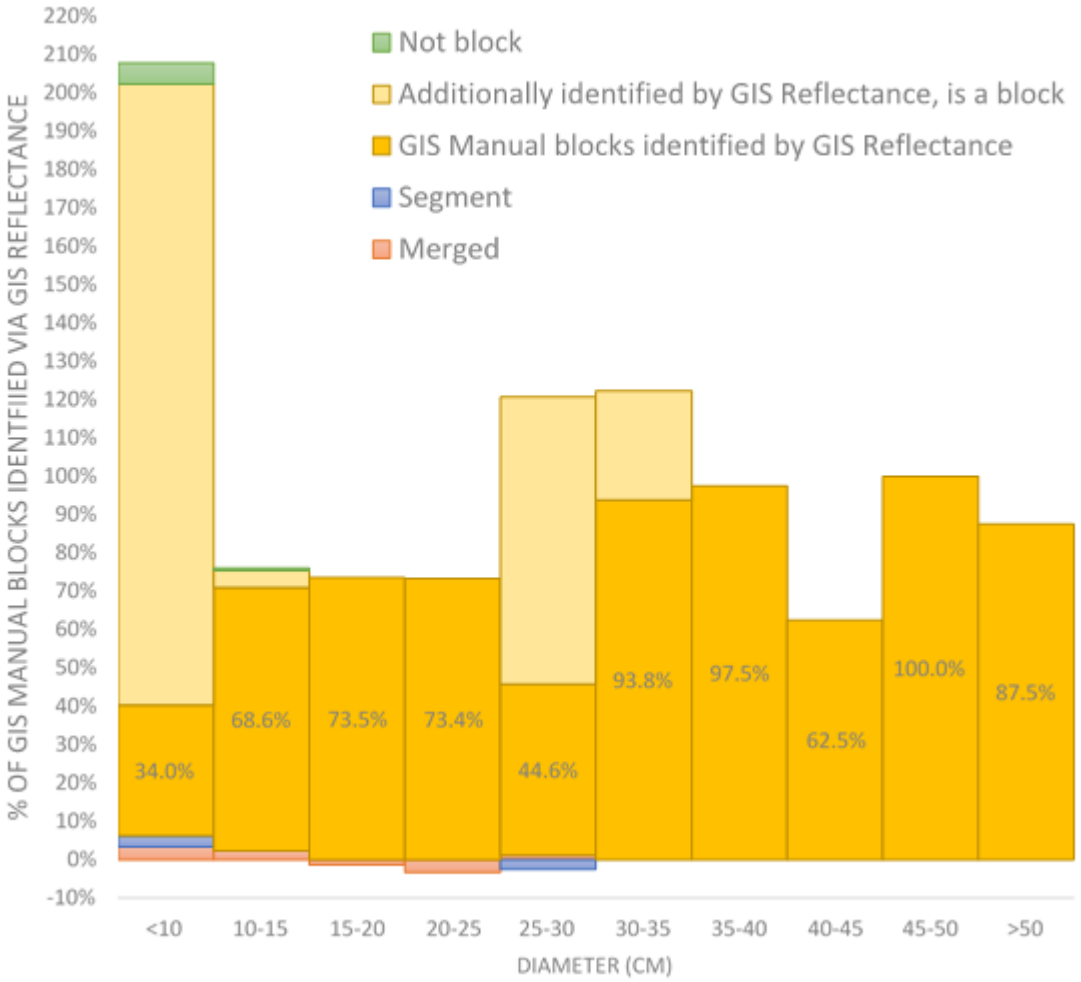

Figure 3.25 Error assessment of GIS Reflectance, relative to GIS Manual identification

The GIS reflectance method identified many blocks additional to that identified by GIS Manual. Within the 5-10cm bin, an additional 167% of identified GIS Manual blocks were counted and checked by eye to be actual blocks. These clasts could not be confidently identified and measured by via GIS Manual due to the image resolution limiting identification manually. GIS Reflectance could however identify pixels down to 2cm in diameter, which were excluded as they are below this studies definition of a block. The additional blocks within the 25-30cm and 30-35cm size bins could not be accounted for by human error. These extra blocks are therefore a likely result of GIS reflectance underestimating the size of clasts in the larger size bins. The under sizing of clasts may have resulted in a clast being manually categorised as a successfully identified clast in a larger bin, then double counted based on the polygons calculated diameter. A difference in error/success identification method occurred because the polygons created by GIS reflectance did not always overlap with the GIS Manual point, if the GIS Manual point was near the edge of the clast and the clast was slightly undersized by GIS Reflectance. As such an ArcGIS based success rate could not be determined based on the intersection between point (GIS Manual) and polygon (GIS reflectance). Incorrectly identified GIS reflectance

blocks/polygons were marked in ArcGIS, and the diameter from GIS Reflectance polygon, associated the error with the size bin.

This section of the thesis was focussed on developing and testing the feasibility for block identification to help aid field scale ballistic identification. The results highlight errors associated with this approach that are similar to those with manual identification from UAV imagery, however further work is required in the form of a full sensitivity analysis.

3.4. Limitations

The primary source of error in this methodological assessment is the difference in sampling areas between the ground-truthed and handheld photo methods and GIS based orthophoto methods. The $1m^2$ frame was chosen to be compatible with the mapping approach undertaken at Whakaari (Chapter 4) and to estimate the measurement error at Whakaari where ground-truthing was not undertaken. However, such a small sample area within a spatially variable block field means it is unlikely that a truly representative sample was obtained. The small frame location was also difficult or not possible to locate within aerial photos and provided a very small dataset for direct comparison. As such comparisons between techniques, instead of to ground-truthed data, was necessitated. Future work in which fewer locations but larger areas were ground-truthed would help to rectify this issue.

A limitation resides in the identified difference between 3-axes ground-truthed and image-based measurements. Both GIS Manual and GIS Reflectance data were compared to the handheld photo data to determine the degree of under-identification of UAV based methods. The total number of blocks for both GIS Manual and GIS Reflectance were then calculated. As handheld photo measurements overestimate block size by ~9%, this error is carried into the conversion factor between, and an unknown error is then added, the difference between handheld photo measurements and UAV image measurements. This error is unknown due to the sample size difference discussed above, were a direct comparison available this limitation would be avoided as the error could be calculated.

Another error related to sample size, the GPS location was assumed to be accurate within a meter or two and thus the $10m^2$ GIS Manual mapping frame was centred on the GPS data point as the actual identification of the $1m^2$ sample location was initially unsuccessful. However late stage, detailed examination showed the field frame locations, where they could be found, to be within 50cm of the $10m^2$ frame, but not contained within it.

Variable resolution of UAV imagery combined with a small number of image stitching errors limited the data which could be obtained from the GIS Manual and GIS Reflectance methods. Permitting restrictions meant the UAV could not be flown over others using the track, and that flight paths must limit proximity to others as much as possible. As such, imagery proximal to the Emerald Lakes is of lower resolution with flight heights of up to 60m which may have contributed to the GIS Manual methods poor performance at Red Crater.

Conversion factors for GIS Manual and GIS Reflectance are undefined in the larger size bins, as the small 1m^2 sampling area did not sample the rarer large blocks. With no comparison within the ground-truthed dataset the number of large blocks, >35cm in diameter, was unadjusted from that identified by UAV methods and the error for these size bins is undefined. Only 6% of GIS Manual clasts are >35cm in diameter therefore this does not impact most of the deposit by number, but the large volume of these clasts may be important when considering the total erupted mass.

3.5. Discussion

All fieldwork studies are a balance between the data required, the data available and what resources; financial, time and technology, a project has access to. This chapter has addressed aim two of this thesis, by exploring the benefits and limitations of four mapping methods for collection of ballistic distribution information at a complex phreatic block field. Four different mapping methodologies, including the development of a new reflectance-based technique have been applied to Red Crater's ballistic field. The case study shows how combined mapping approaches can provide detailed, extensive datasets depending on the time and technical resources available. The comparison of various techniques works towards thesis aim four by providing a useful reference for future workers when planning a ballistic mapping campaign, particularly for those focussed on phreatic eruptions.

Comprehensive ballistic grain size distributions are crucial for ballistic hazard, risk and eruption dynamic studies, however over-simplification of ballistic deposits due to mapping restrictions is common and small block sizes are often frequently ignored (Biass et al., 2016, Strehlow et al., 2017). The technologically simple ground-truthed transect and 1m^2 frame approach provided detailed size and spatial distribution information at Red Crater including the often-missed small blocks (thesis aim 3), but was spatially limited to 11m^2 of ~ 300,000m^2 (Table 3.5). Complimenting the ground-truthed approach with handheld photography reduces the field time required per measurement and extends the ground-truthed dataset in a simple manner, with only basic computer software and skills required (Table 3.5) and again includes the small blocks crucial to phreatic ballistic size distributions. However,

the proportion of the whole field covered is still small ~41m^2. The accuracy of the handheld photo method in identifying clasts validates it's use for spatial density mapping. The difference between ground-truthed and handheld photo measurements emphasises the importance of ground-truthed measurements for calculating errors in derived size distributions and total erupted mass.

The limited area covered in most studies by in-field measurement has encouraged the proliferation of aerial imagery mapping (Guroli et al., 2013; Fitzgerald et al., 2014; Kaneko et al., 2016) however GIS Manual was been shown to be the least effective method in terms of time and technology resource required, and data obtained (Table 5). GIS Manual has limited accuracy for small blocks and is very time consuming. Therefore, it's applicability for mapping phreatic ballistic fields, which are generally dominated by smaller clast sizes (e.g. Kaneko et al., 2016) and where the spatial density is high, is limited. In this study it did provide an avenue for estimating the error associated with the GIS reflectance method which the small field sampling approaches did not allow. However future work in which a larger, marked ground-truthed site is directly compared with a reflectance method, if applicable, could cut this time intensive step.

The development of an image-based, GIS reflectance method allows more complete ballistic mapping, where the spatial density variations and size distribution of a whole, or a significant part of, a deposit may be analysed. The GIS Reflectance method has proven to be applicable to some field areas, and capable of mapping a relatively large area in a time efficient manner. Additionally, a coversion factor can be applied to help represent the true number of blocks using the handeld photo mapped areas. Of all the methods applied to Red Crater it provided the largest dataset and covered the greatest area in the least amount of time (Table 3.5). At the upper field area, 60% of the field area was mapped via the reflectance method, vastly more than ground-truthed (0.0008%), handheld photography (0.002%) or GIS Manual (0.0215%).

Table 3.5 Comparison of each mapping method applied at Red Crater. Green to Red colour scheme indicates relative success of each method. Red to dark green colour scheme demonstrates relative efficacy or efficacy in each category. * indicates extra coverage by GIS Manual on lava flow that is not sampled by GIS Reflectance.

	Ground-truthed (GT)	GT + Handheld photo (HP)	GT + HP + GIS Manual	GT + GIS Manual	GT + HP + GIS Reflectance	GT + HP + GIS Manual + GIS Reflectance
Area Covered	11m^2	41m^2	407.5m^2	407.5m^2	~3000m^2 + 7m^2 *	~3000m^2 + 327.5m^2 *
Size Distribution (Accuracy)	Highly accurate down to 5cm within sample frame. Small sample size excludes large blocks	Samples blocks down to 5cm diameter. Photo overestimates block size by ~9%	Low accuracy of block identification, particularly small blocks <10cm. Includes large blocks.	Low accuracy of block identification, particularly small blocks <10cm. Includes large blocks.	Size distribution fits GT data well.	Size distribution fits ground-truthed data well.
Spatial Distribution Blocks/m^2	Within 1m^2 frame accurate, limited by frame size. High variability not well represented	Within 1m^2 frame accurate, limited by frame size. Local variability not sampled well.	Underestimates number of blocks by ~64%	Only 11/41 (27%) sites available for comparison.	Fit appears good, following conversion to GT, identification error unknown	Fits GT well, GIS Manual provides error estimates for each block size (binned).
Ability to calculate whole field block number	Small sample area – extrapolating to whole field creates high error margins with variable spatial densities not accounted for well.	Small sample area, but greater coverage of whole field than GT. High error margins.	Moderate sample size and general relationship to HP blocks allows estimate of number of blocks. Medium error margins	Larger sample size and general relationship to GT provides a loose estimate of number of blocks. High error margins	Spatial variation within field mapped, provides robust estimation for field areas where the technique is applicable. No error known	Spatial variation within field mapped, provides robust estimation for field areas where the technique is applicable. Error known.
Time Resource	Field time intensive ~ 1 week. Little work required to convert data into map. (~1.5 weeks total)	GT + Small amount of additional fieldwork ~1 day. 2 weeks desktop mapping (~3 weeks total)	3 weeks to map and measure individual blocks in GIS. + HP + GT UAV image collection 7 days (3 -4 flying + weather) (~8 weeks total)	3 weeks to map and measure individual blocks in GIS + GT + UAV image collection 7 days (3 -4 flying + weather). (~5 ½ weeks)	2 weeks in field for GT and UAV flight. 2 weeks HP mapping. 1 week defining reflectance spectrum. 1 week GIS processing and data analysis. (~6 weeks)	2 weeks in field for GT and UAV flight. 2 weeks desktop HP. 3 weeks GIS Manual. 1 week defining reflectance spectrum. 1 week GIS processing and data analysis. (~9 weeks)
Technology Resource	•GIS	•Corel Draw and ImageJ software (or equivalent) •GIS	•UAV flight + AgiSoft for image compilation •CorelDraw/ImageJ •GIS	•UAV flight + AgiSoft for image compilation •GIS	•UAV flight + AgiSoft for image compilation •GIS	•UAV flight + AgiSoft for image compilation •GIS

Ballistic mapping is often aided by desktop identification of craters and blocks or bombs from aerial imagery (Waitt et al., 1995; Guroli et al., 2013; Fitzgerald et al., 2014, Kaneko et al., 2016,). While relationships between the number of identified clasts and true field data have been estimated (Waitt et al., 1995) or quantified through ground-truthing (Fitzgerald et al., 2014), the impact of measurements from a 2D representation of the field area has not been detailed before. At Red Crater the ground-truthed three axes measurements were 15% smaller than when only 2 axes were considered. Subsequently, photo measurements overestimated the 3 axes block diameter by 9% and underestimated the 2 axes diameter by ~5%. A difference of this scale has important ramifications to eruptive energy when ballistic volume is extrapolated to a whole deposit. A basic calculation using the difference in average diameter for 3 vs 2 axes indicate that with 2 axes the total erupted volume would be ~1000m^3 compared to ~690m^3 for 3 axes. For larger ballistic fields mapped using only two dimensional methods (e.g. Fitzgerald et al., 2014; Kaneko et al., 2016), or a combination of field and photo (Pistolesi et al., 2008; Guiroli et al., 2013); quantifying the impact of the 2D mapping assumptions on average ballistic size is important for accurate erupted volume calculations.

Taddeucci et al., (2017) identified that even ballistic fields from a single eruption have complex distributions through jet streaming and overlapping eruptive burst lobes (e.g. Swanson et al., 2011). As such, isopach maps and other simple ballistic mass calculations based on average ballistic density are a poor tool for estimating the total ballistic mass. The reflectance method when combined with ground-truthed data can provide crucial information when seeking to estimate the erupted ballistic mass, number of blocks or bombs and energetics of the eruption. Simplistic methods in which small areas of sampled density is extrapolated to the whole area, or isopach maps (e.g. Kaneko et al., 2016; Kilgour et al., 2010) have been used to estimate erupted ballistic mass but will have large associated errors. A mapping method which can include the majority of a deposit,and be validated or adjusted to account for the small block sizes is step towards increasingly accurate representations of ballistic distributions.

3.5.2. Discussion of future work

The reflectance method was developed and undertaken to determine the feasibility of identifying relatively small blocks using the basic tools of UAV collected images and a geospatial information system. The success rate in areas where blocks have impacted a flat surface has proven this to be potentially applicable to other volcanoes around the world. Weather conditions had a large influence on the reflectance of the lava flow. At another field location, or at a time of year with less cloud cover, the approach has the potential to be more effective. As a component of a MSc thesis the full possibilities of this method have not been explored, for instance only one colour band was used. Field

photos were sectioned and analysed based on their relationship to ground-truthed transects. More sophisticated sectioning of the image, based on areas with different reflectance characteristics within a single lithology, i.e. images collected under similar light/weather conditions, would likely improve the output of the approach. Thus, with further development this approach should not be written off for lava flow's or other complex surfaces.

The hydrothermally altered and weathered surfaces of the blocks at Red Crater make them generally lighter than the underlying lithology and therefore the reflectance method identifies blocks based on their reflectance values above a certain threshold. At other volcanoes where fresh ballistics or blocks have impacted ash surfaces from the same eruption, the ballistics may not contrast in brightness due to their similar composition. Bocks may be significantly darker than the surface they impact (e.g Figure 3.26B). A reflectance approach may still be applicable in these cases to estimate the number of erupted clasts using shadows of blocks/bombs or fresh craters or selecting areas based on their relative lack of reflectance. Alternatively, infilling of craters by rainfall, such as at Arenal Volcano (Figure 3.26A) may provide the reflectance contrast needed for rapid collection of ballistic distribution information. Long-exposure images of glowing bombs ejected during magmatic eruptions have been used for ballistic trajectory studies and hazard assessment (Bernard et al., 2018) and could similarly be used for mapping the landing locations of bombs. Future work to develop the reflectance method should focus on quantifying the impact of various field characteristics such as lithologies, surface roughness, ballistic type (block or bomb), vegetation on identification accuracy.

For the information gathered in this comparative mapping study to be of use to hazard and risk managers, a complementary probabilistic ballistic modelling approach needs to be undertaken (Figure 3.27). Probabilistic modelling is required due to the high numbers of unknown variables; vent location, conduit geometries, ejection angle, number of bursts, blocks per burst. A geochemical sampling as per Swanson et al., (2012) may provide insight into variables such as the vent location and numbers of bursts which would need to be combined with the few literature examples of phreatic eruptions.
The GIS reflectance method, in combination with ground-truthing, has the potential to asist in rapid data collection at active volcanoes. It may be used to map ballistic fields from frequently erupting volcanoes, with only UAV flight accessibility required between eruptions, to study the ballistic mass of smaller eruptions/eruptive bursts. It may also be useful in aiding the rapid development of ballistic hazard zones following an unexpected eruption, like that required following the 2012 Te Maari eruption (Leonard et al., 2014).

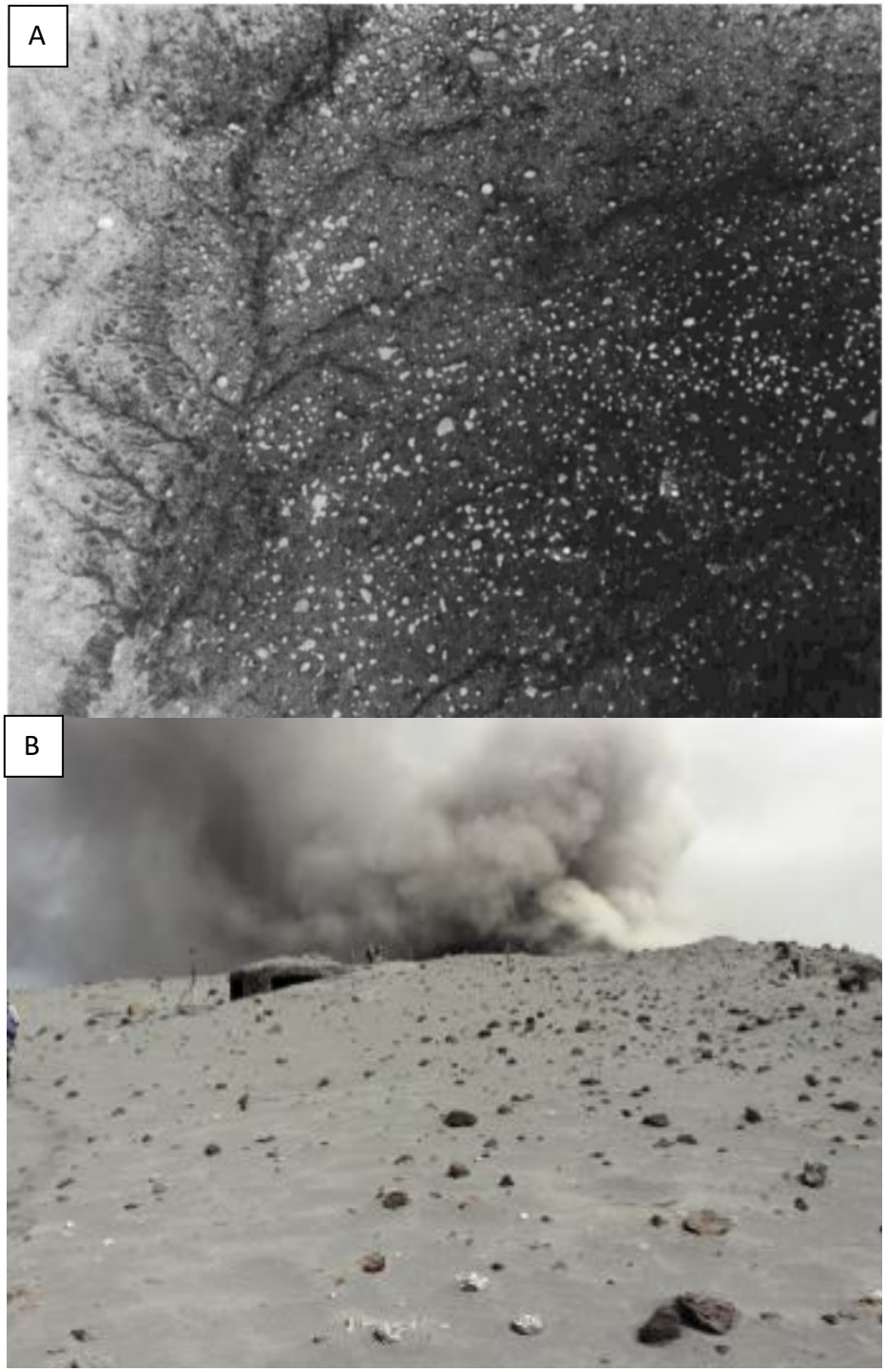

Figure 3.26 A) An intensely cratered area following the 1968 eruption of Arenal Volcano from Fudali and Melson (1971). Craters in this area have been partially filled with water making them more reflective than the impacted lithology. B) The phreatomagmatic ballistic field from the eruptions of Aso Volcano, Japan. Darker blocks on the simple ash surface show potential for the GIS Reflectance method. From Miyabushi et al., 2018.

3.6. Conclusions

This chapter has addressed the second objective of the thesis by examining four different ballistic mapping methods, including the development of an innovative and accessible mapping approach. It has also addressed thesis objective three by identifying the best methods for including small clast sizes in mapped distributions. The limitations and strengths of each method have been quantified wherever possible and a combined mapping approach has been found to be most effective in obtaining the maximum amount of information. The adjusted GIS Reflectance method has the potential to greatly improve the amount of ballistic hazard information gained from deposits (Figure 3.25) to provide well constrained data for hazard and risk managers. If the field area does not allow the reflectance method, then a combined mapping approach using handheld or UAV photography, directly compared to ground-truthed data can provide high quality datasets, aim four of this study (Figure 3.27).

The main conclusions of this chapter are:

1) Small clasts down to 5cm in diameter are mappable in a time efficient manner using handheld photography or GIS Reflectance methods (if applicable). When combined with ground-truthed field areas the difference between 2D and 3D measurements can be quantified.
2) Depending on field time available (crisis vs non-crisis, accessible vs inaccessible) and technology (aerial photography vs field data only) a range of mapping methods are available for high resolution spatial and size distribution ballistic data collection.
3) Mapping methods which most accurately measure size distribution, ground-truthed and handheld photography, are the most spatially restricted potentially leading to large errors when extrapolating data to whole field areas.
4) A multi-method approach taking advantage of an accurate size distribution method (ground-truthed or handheld photography) and large area coverage for spatial density variation (aerial imagery methods) is the most efficient way of obtaining complete ballistic datasets for use within detailed risk assessments.

A comparison of different methods was enabled due to Red Craters current low levels of activity but necessitated by it's potential for future eruptions and its popularity as a visitor attraction. The next chapter considers a phreatic eruption at Whakaari where field-time was significantly limited by eruption risk and a handheld photo mapping and a deterministic modelling approach imposed

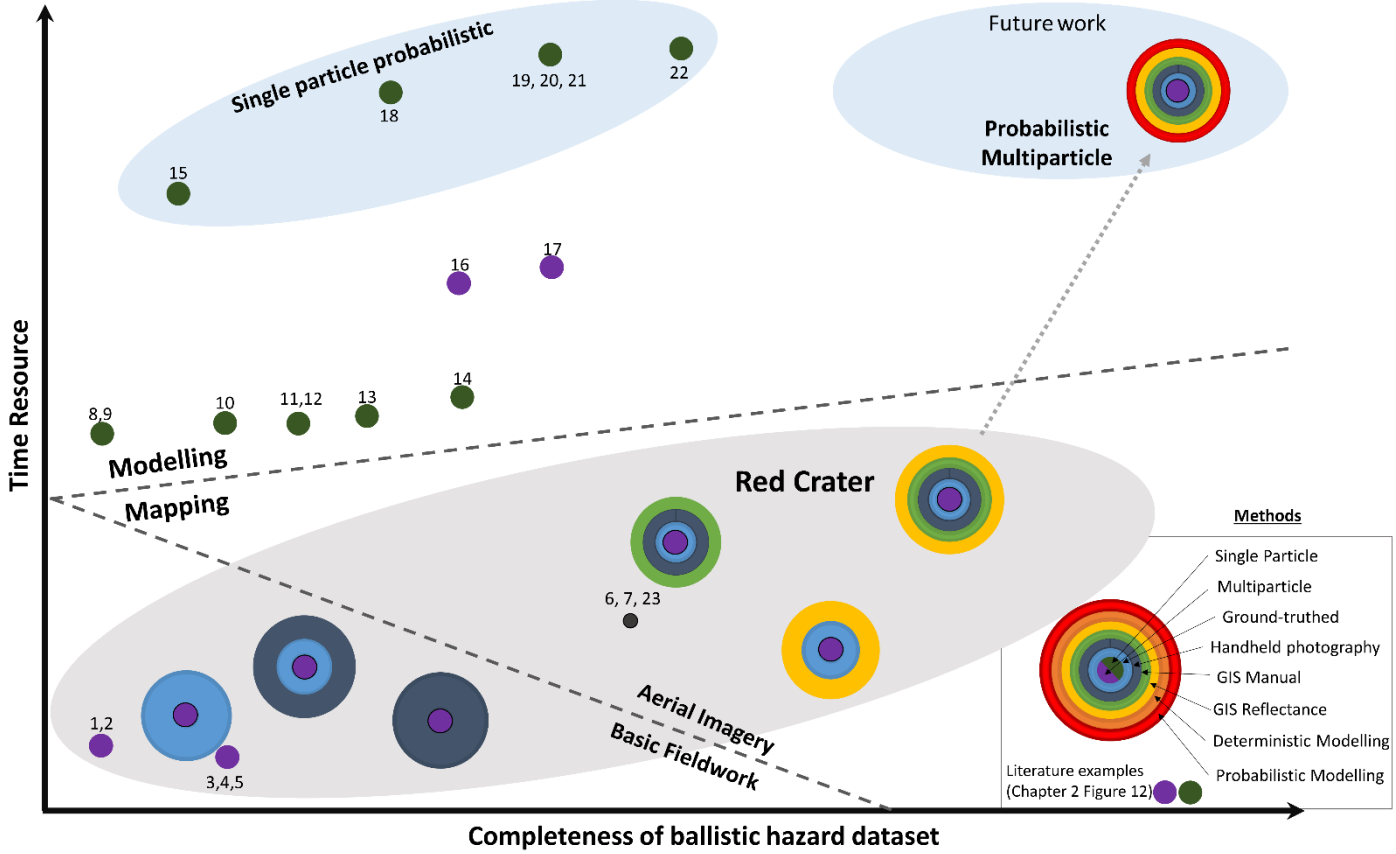

Figure 3.27 Updated conceptual figure from Chapter 2, Figure 12 showing how this work has developed combined methods which are able to collect more complete ballistic hazard data (number of blocks, size distribution, spatial distribution) than previous methods. The increased information does however also increase the time resource required for processing.

4 BALLISTIC MODELLING OF THE 27 APRIL 2016 PHREATIC ERUPTION AT WHAKAARI

4.1 Introduction

Ballistic numerical modelling is primarily used for inverse modelling, to shed light on eruptive conditions or to inform ballistic hazard assessments beyond what can be derived from basic field data (Fitzgerald et al., 2014; Biass et al., 2016; Tsunematsu et al., 2016; Strehlow et al., 2017; Bertin, 2017). This chapter presents the results from handheld photography mapping from systematic $1m^2$ field photos of ballistics and application of the numerical model Ballista to better understand the 27 April 2016 Whakaari eruption dynamics and hazard to tourists. High volcanic risk following the eruption limited the time available for field mapping and focussed mapping on delineating the maximum extent of the ballistic field and on 27 individual square metres within the ballistic field. Two scenarios were modelled to investigate feasible eruption conditions and investigate the possible minimum and maximum kinetic energy released by ballistic ejection. The resulting characterisation of the intensity of the hazard posed, in terms of the spatial distribution, impact energy and impact upon the tourism path, provides useful hazard metrics critical for effective ballistic hazard assessments.

This chapter addresses objective 4 of this thesis in applying an appropriate numerical model, as determined by the field mapping methodology, to inversely model a phreatic ballistic field. It also addresses objective 4 by examining the reasoning and choice of a single numerical model at a volcano at risk of further eruption. With careful description and collection of samples, combined with numerical and analogue models, the emplacement dynamics of an eruption through time can be recreated and a time variable hazard footprint can be created (Maneo et al. 2016, Kilgour et al., in review). This chapter creates a time variable ballistic hazard footprint at Whakaari for small phreatic eruptions, while work by Kilgour et al. (in review) seeks to delineate the time variable pyroclastic surge hazard from the same eruption.

Whakaari/White Island (Figure 4.1) is New Zealand's most frequently active volcano over the last 150 years with 27 phreatic eruptions since 1826 (Mayer et al., 2015; Kilgour, unpublished fieldwork, Kilgour et al., in review). Daily tours, weather permitting, take ~18,000 visitors per year within the ballistic hazard footprint of previous eruptions, as well as pyroclastic flow and ashfall hazard footprints (Kilgour and Bower, 2015). As such, the poorly constrained hazard at Whakaari is an ideal case study

to examine ballistic hazard in an area frequented by tourists. The 27 April 2016 eruption of Whakaari provides data to examine the potential and limitations of numerical modelling based on a rapid field handheld photo assessment and subsequent analysis, seismo-acoustic, and UAV data to elucidate the eruption dynamics and hazard footprint of a small phreatic eruption at a popular tourist destination

4.1.1. 27 April 2016 Eruption of Whakaari Volcano

Whakaari erupted phreatically on 27 April 2016, at 9.35pm (NZST) in an event that lasted ~40 minutes (Walsh et al., in review). There were 6 variably sized eruptive bursts, each 1-2 minutes long, from ~3 vents, based on seismo-acoustic data (Walsh et al., in review) which produced a composite ballistic field, pyroclastic surge and ashfall deposit (Kilgour et al., in review) (Figure 4.2 and 4.3). The ~9.30pm timing of the eruption meant it was not witnessed directly or recorded on GNS web cameras due to the poor light conditions. Observational flights were made by GNS science within 24 hours (Figure 4.2), but due to the risk of further eruptive activity (Deligne et al, 2018) scientists did not spend time within the hazard zones until the risk was deemed acceptable by GNS Science.

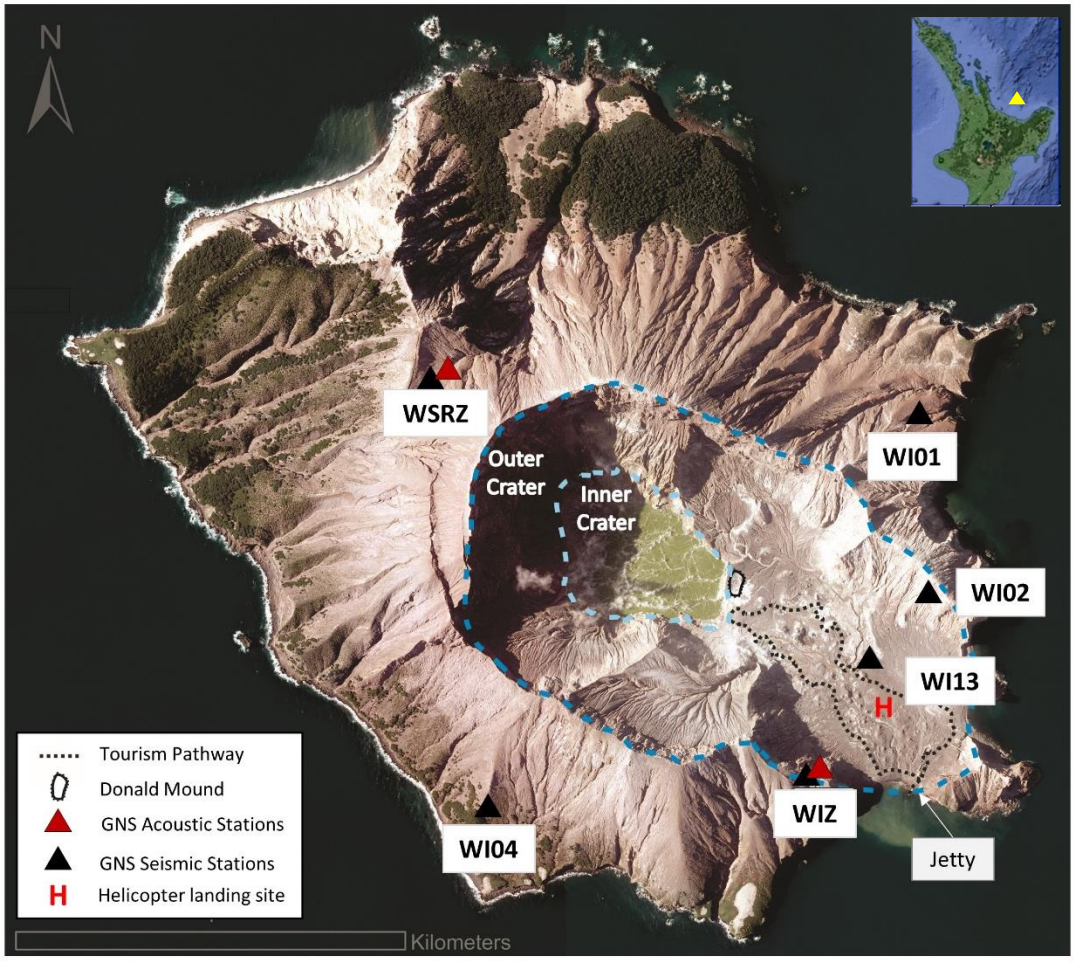

Figure 4.1 Whakaari map showing outer crater and inner crater with crater lake. GNS seismographs stations from Walsh et al. (in review).

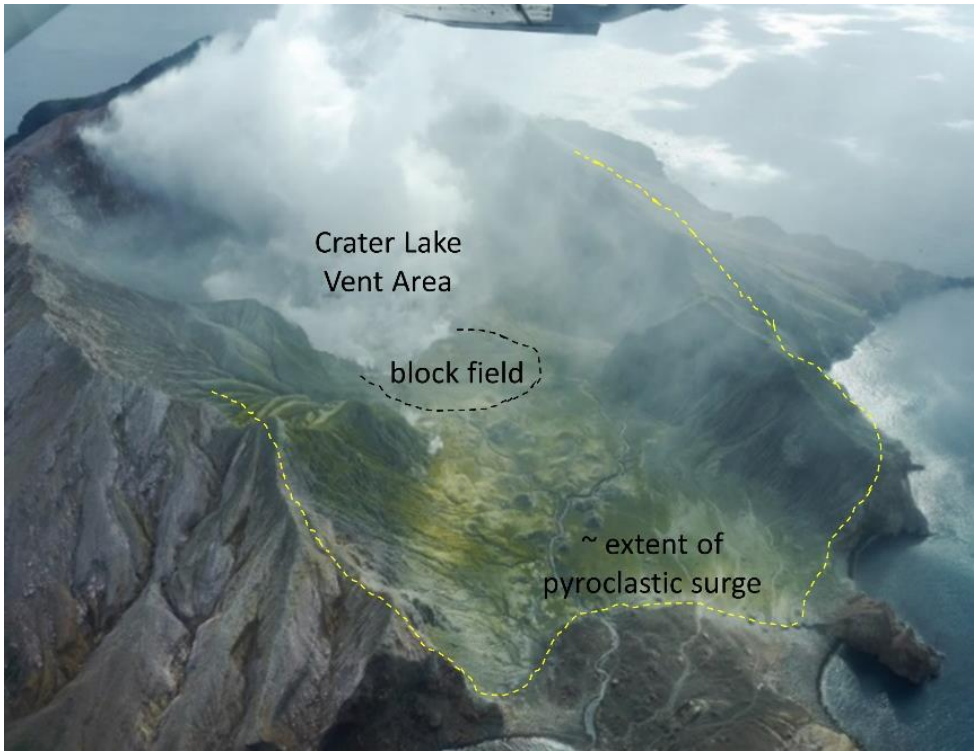

Figure 4.2 Photo taken the day following the eruption. Facing NW Photo credit: GNS Science

A rapid, handheld photography field assessment method was used by GNS staff on 19 May 2016 to assess the extent of the eruption deposits. Because of the risk of another non-forecasted eruption to the GNS staff mapping the eruption (Deligne et al., 2018), time inside the outer crater was restricted to 2 hours to collect data on the extent and magnitude of eruptive products. The vent area was observed to be vigorously steaming with more than one area showing activity (Kilgour et al., in review). A weak ash plume was generated which deposited ash over the northern outer crater wall, pyroclastic surge was emplaced across most of the crater floor and ballistic blocks landed up to ~310m from the vent. Distinct yellowy-brown alteration colours of the ash and surge deposit, caused by oxidation of sulfur rich fluids, coated the outer crater floor to a distance of ~700m (Kilgour et al., in review, Figure 3.2). During the eruption, the crater lake area enlarged as part of Donalds Mound collapsed into the main crater and the lake floor lowered by at least 13m (GeoNet Volcanic Alert Bulletin, 2016).

A further visit by GNS staff on the 2 June 2016, just over a month after the eruption, was specifically aimed at ballistic sampling. Near the inner crater wall impact craters were common to the south and east of Donald Mound. Only about half of the impact craters contained ballistic clasts and two pits were dug to find the ballistics responsible for crater formation which were located at a depth of approximately 200 mm (Kilgour et al., in review).

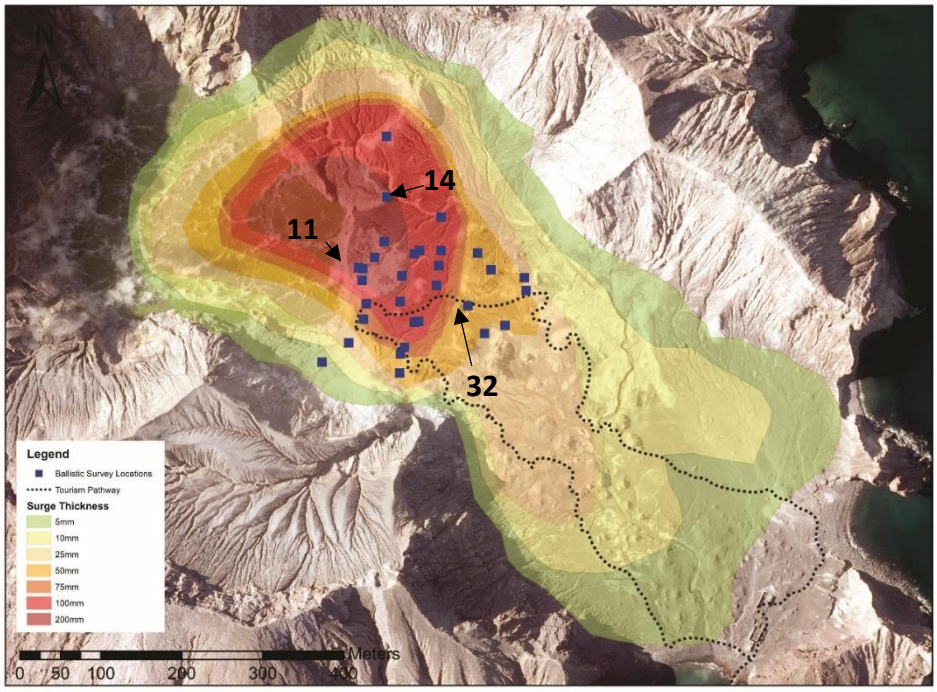

Figure 4.3 Eruption deposit map showing basic ballistic field outline and sample locations, approximate surge isopach thickness'. Selected field locations numbered for Figure 4- Modified from Kilgour et al. in review

4.2 Methodology

4.2.1 Ballistic Mapping at Whakaari

During the June visit by GNS Staff to map the eruption deposit a 1m^2 metal frame (Figure 4.4) was used to map the ballistic field at 27 locations spaced between 5m and 75m apart, with sampling focused on transecting the axis and width of the strew field and outlining the edge. This method was subsequently applied at Red Crater (Chapter 3) and compared to ground-truthed field data to quantify approximate errors, as time restraints at Whakaari meant no ground-truthing occurred. The frame was placed on the ground and photographs taken, as orthogonal as possible, to the deposit (Figure 4.4A). Using the frame allowed scaled images to be obtained rapidly reducing the time workers spent within the hazard footprint. The spatial density of blocks and size distribution at each sample location was then determined by handheld photography analysis.

Larger blocks were generally observed closer to and within ~100m the inner crater wall. Ballistic ejecta was trimodal, with a sulphate dominated breccia that oxidised to a bright yellow (Figure 4.4D), and weakly altered lava and sediment ballistic types (Kilgour et al., in review). A wide range of impact density was observed, from high near the crater (Figure 4.4B) to low densities near the edges (Figure 4.4C) and distal areas (Figure 4.4D).

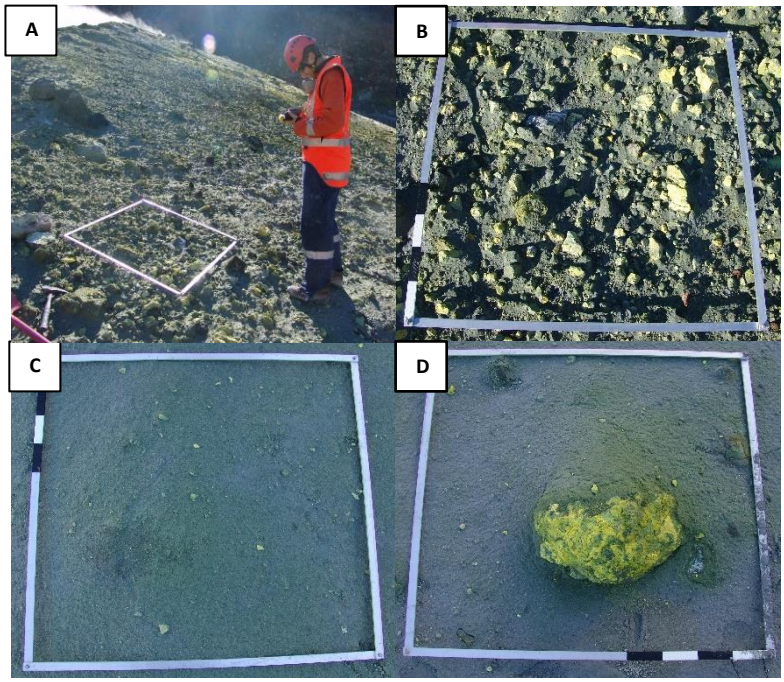

Figure 4.4 A) 1 m square frame is laid on the ground within the ballistic strew field (images courtesy Geoff Kilgour). B)-D) Example mapping sites with 1m2 frame for reference. B = Site 11, C= Site 14 - behind Donald Mound, note lack of clasts, D = Site 32 – note mantling of block with directional surge cover, bottom right of frame is easterly direction. Frame locations labelled in Figure 3.

Using field photographs, blocks were identified and outlined in ImageJ and the size distribution of the field was found by translating the area of each block to a calculated average diameter, similar to the approach of Gurioli et al. (2013). Blocks were mapped from photographs within CorelDRAW using the free hand drawing tool once the image was rectified to make frame sides, and therefore the image, as orthogonal as possible (Figure 4.5A). Once all blocks in the image were traced (Figure 4.5B) the file was exported into ImageJ where the $1m^2$ frame was used to set a scale and ImageJ "Particle Analysis' was used to determine the area of each clast.

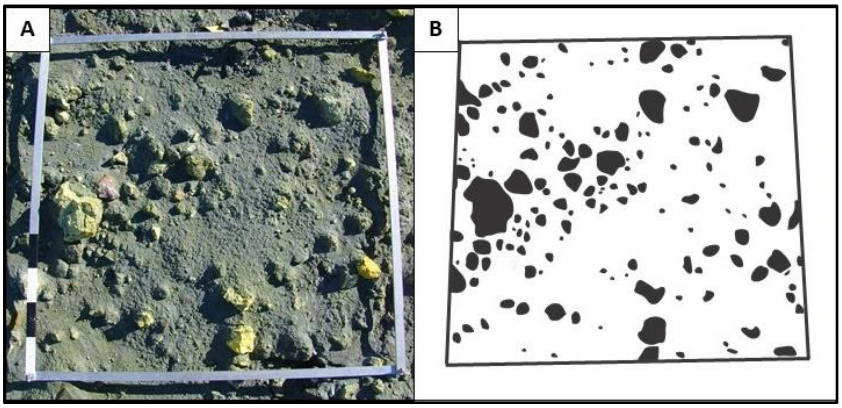

Figure 4.5 Handheld photography mapping approach A) orthorectified image and B) traced image from Corel Draw, ready for particle analysis within ImageJ.

The area of each clast was translated to a diameter for use within the model Ballista which calculates trajectory and drag forces based on spherical particles:

$$r = \sqrt{(\frac{A}{\pi})}$$

where *r* = radius and *A* = cross-sectional area.

The diameter was found by relating the area of a circle:

$$d = 2r$$

This rapid field mapping is not without limitations such as lack of ground-truthing (Fitzgerald et al., 2014). Chapter 3 showed the average ballistic diameter gained from handheld photography can be up to 15% different in diameter from that ground-truthed, even without the complication of syn-eruptive deposits. Lack of impact craters can cause misidentification of ballistics, or incorrect association of ballistics to particular eruptions (Biass et al., 2016, Alattore-Ibarguengoitia et al., 2016; Kaneko et al., 2016). The handheld photography limited field time and assumptions had to be made that all the clasts mapped were a result of the last eruption. Ash and surge deposits buried most previous deposits, however, the deposits and subsequent erosion also meant that impact craters and debris aprons were rarely available to verify that every block was indeed a ballistic.

The photographic mapping assumes that the 2D image is representative of the blocks a and b axis, however some of the ballistics were confirmed to be partially buried by surge deposits (Figure 4.4D). The size of blocks may therefore be under-represented. In In cases where most of a clast was outside the frame, it was not included in the sampling as this increased the area sampled to more than 1m^2.

In summary, the photo mapping of 31 locations spaced 5-75m apart was converted into a size distribution of clasts from 1.07 cm to 42.3. The size distribution of clasts is an important parameter, indicative of eruption type and energetics (e.g. Waitt et al., 2015) and crucial for multiparticle modelling approaches.

4.2.2. 3D volcanic ballistic trajectory modelling

Geoscience models are designed to replicate natural systems and provide insight into variables that remain uncertain. 3D numerical modelling has been applied at many volcanoes around the world, as discussed in Chapter 2 (e.g. Tsunematsu et al., 2016; Biass et al., 2016; Bertin 2017; Fitzgerald et al., 2014). To elucidate the dynamics of the eruption, as well as the hazard posed by small phreatic eruptions at the volcano, Tsunematsu's (2016) Ballista model was applied. Two scenarios were developed to investigate energetic end members; a higher energy single burst event which emplaced the whole ballistic field and a multi-burst event in which the ballistic field is composed of blocks from three separate explosive events.

Ballista calculates the velocity of particles using a finite difference method to solve Alatorre-Ibargüengoitia and Delgado-Granados' (2006) equation for each particle, location, direction and time step:

$$m\frac{D\boldsymbol{v}}{Dt} = \frac{AC_d\rho a(\boldsymbol{v}-\boldsymbol{u})|\boldsymbol{v}-\boldsymbol{u}|}{2} - mg$$

Where, m is the particle mass, *v = (vx, vy, vz*) is particle velocity, *t* is time, *u* is the wind or ambient gas flow velocity*, t* is time, *A* is the cross-sectional area of a block perpendicular to the flow direction, C_d is the drag coefficient, *ρa* is the air density, *m* is the particle mass, and *g* is the gravitational acceleration.

The transport of ballistic particles is then calculated using a Lagrangian method:

$$\boldsymbol{r} = \boldsymbol{r}_0 + \boldsymbol{v}\cdot\Delta t$$

Where *r* is the location of each block and Δt is the time step, which is constant throughout the simulation.

Ballista was chosen for several reasons; firstly, field mapping suggested that topographic shielding had occurred due to the lack of blocks behind Donald mound (Figure 4.4C) and Ballista includes topography when calculating flight paths and distribution of blocks through inputting a DEM of the study location. Through the use of a multi-particle model which is sensitive to topography, parameters such as ejection and inclination angles can be better refined. Secondly, the field approach (see field methods) provided detailed information on the spatial density variation of blocks at specific locations and field shape. Most ballistic models calculate the trajectory of individual blocks using the greatest distance reached by clasts (e.g. Fagents & Wilsons, 1993; Mastin, 2001; Bower & Woods, 1996). Ballista is multiparticle and considers 3 dimensions, capable of modelling the spatial distribution and overall shape of a ballistic strew field including local variations in distribution, allowing validation with field data. Following validation of field data this also allows for the total ballistic mass erupted to be estimated; a critical component when determining an eruption's energy budget in field areas with crater lakes or other mapping barriers. Thirdly, Ballista's strength as a model lies in its ability to sample eruption source parameters probabilistically, based on average values and standard deviations derived through field observations, improving upon traditional purely deterministic modelling approaches (Minakami 1942; Fudali & Melson 1972; Wilson 1972; Steinberg and Lorenz 1983; Fagents and Wilson 1993; Bower and Woods 1996; Mastin 2001; Alatorre-Ibargüengoitia and Delgado-Granados 2006; Alatorre-Ibargüengoitia et al. 2012). Finally, the success of Ballista in modelling the

phreatic eruptions of Ontake 2014 (Tsunematsu et al., 2016) and Tongariro, 2012 (Fitzgerald et al., 2014) made it the appropriate choice.

4.2.2.1. Model parameters

Ballista requires the input of parameters including; vent location, number of eruption pulses and number of particles in each pulse, azimuth direction of eruption, ejection angle from vertical and standard deviation (Figure 4.6), particle density and diameter, initial particle velocity and displacement of ejection points from vent centre, gas flow velocity and region of reduced drag and the drag co-efficient. These parameters are deduced through a combination of fieldwork, literature and iterative modelling to find the best fit.

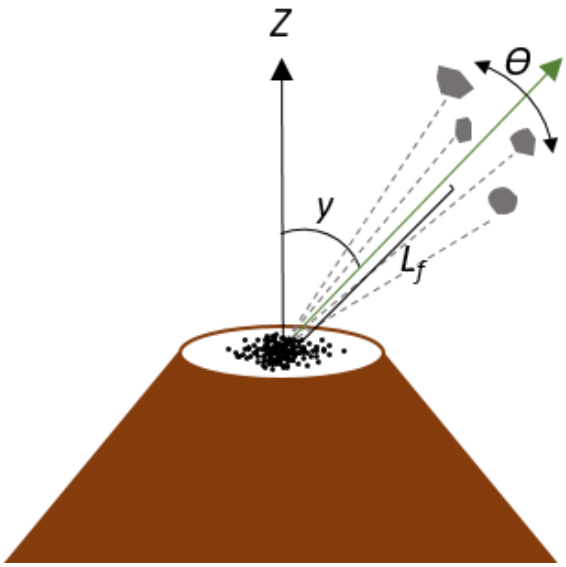

Figure 4.6 Selected Ballista input parameters: Angle of ejection (Y) and standard deviation (Θ), Region of reduced drag (Lf). (modified from Tsunematsu et al., 2016)

4.2.1.1. Number of eruption pulses, vent location and direction of particle deposition

As the eruption was not witnessed, the number of eruptive pulses that contributed to the ballistic field was determined on seismic and acoustic signals. Whakaari hosts two permanent Geonet seismometers with acoustic sensors (Figure 4.1) and due to the ongoing higher activity level since 2000, four additional temporary seismometers were on the island at the time of eruption. The acoustic sensors on Whakaari recorded at least 6 separate pressure pulses which are presumed to occur at the onset of an eruptive pulse (Table 4.1).

Table 4.1 Seismoacoustic characterisation of the eruption sequence. Acoustic average from stations WIZ and WSRZ. Seismic energy average from permanent and temporary seismic stations WIZ, WSRZ, WI01, WI02, WI04, WI13 (Figure 4.1 with seismograph stations) from Walsh et al., (in review).

Pulse No.	Start	End	Vent Location	Average Acoustic energy (J)	Rank	Average Seismic energy (J)	Rank
P1	21:35.3	21:37.3	Eastern	3.99E+06	5	6.91E+07	5
P2	21:40.5	21:42.4	Northern	3.05E+06	6	4.08E+07	6
P3	21:48.3	21:49.4	Centre	8.48E+06	4	2.96E+08	**2**
P4	21:54.1	21:56.0	Eastern	2.15E+07	**3**	2.67E+08	**3**
P5	22:03.4	22:04.3	Eastern	6.76E+07	**2**	1.88E+09	**1**
P6	22:11.3	22:13.1	Northern	1.84E+08	**1**	1.33E+08	4

Only the three pulses with the largest acoustic signature of the six pulses were modelled for scenario 2 (Pulses 4, 5 and 6). Based on previous acoustic signals at Whakaari (Jolly et al., 2016) the smallest three bursts detected were judged unlikely to produce ballistics that would exit the ~30m high inner crater wall and travel the 100m horizontal distance to the mappable ballistic field. The acoustic signature was used in favour of the seismic signature as the strength of the acoustic energy is more related to surficial energy release (Jolly et al., 2016). When the average acoustic energy is normalised to the largest burst, the smallest bursts make up less than 9% of the acoustic energy combined. The single burst scenario modelled only pulse 6 as contributing to the ballistic field.

The high spatial density of seismometers, 6, and two acoustic stations (Walsh et al., in review) on Whakaari at the time of the eruption allowed eruption locations to be determined. The general position of each eruptive burst was initially located through seismo-acoustic interpolation by Walsh et al. (in review) on a 50m grid (Figure 4.7). This information was paired with a 59mm DEM collected following the eruption, when the crater lake was emptied, which provides information on the crater floor structure (Kilgour et al., in review). The final modelled vent locations (Figure 4.7) and their dimensions were based on morphological depressions close to the seismo-acoustic locations inferred to be likely vents. The complexity of the vent locations fits well with the number of bursts interpolated from each, i.e. the 'Central' vent location associated with a single burst is close to a single explosion crater, the 'Eastern' location associated with three bursts is close to a complex area of multiple explosion craters. Although it is worth noting a complex explosion crater morphology that was likely highly modified by crater floor subsidence during the eruption.

The width of the vent affects the dynamics and flight path of the particles being ejected (de' Michieli Vitturi et al., 2010). Ballista models this in terms of the average displacement of particles from the vent centre, standard deviation of particles from the centre and the maximum displacement, in meters. The width of the morphological depressions chosen as vent locations were measured, with

the radius representing the maximum displacement from the vent centre and average displacement taken as half way between the centre of the vent and the edge.

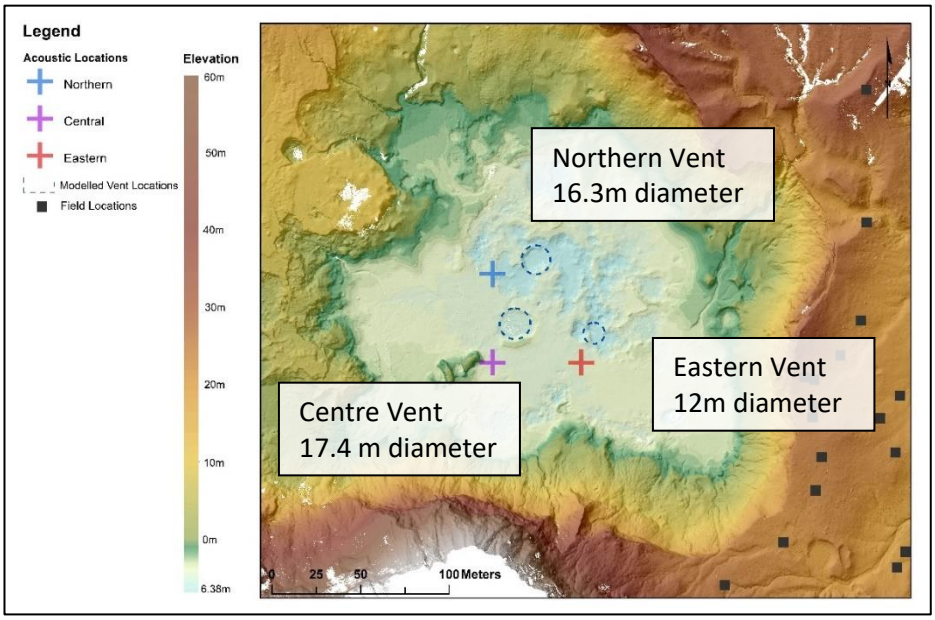

Figure 4.7 Modelled vent locations in Whakaari's inner crater. Crosses mark locations found by B. Walsh through seismo-acoustic interpolation. Post eruption 59mm DEM by C. Asher with modelled vent locations in blue hatched circles.

A vertical, axis-symmetric eruption generally creates circular ballistic field distribution (de Michiele Vitturi et al., 2010, Taddeucci et al., 2017). At Whakaari the furthest blocks reached was towards the east-southeast with the field shape elongated in an east-southeast direction. The east-southeast directionality of surge deposits and apparent directivity shown in the strength of seismic and acoustic signals reaching station WIZ to the east (Figures 4.1 and 4.8) suggests this directionality is authentic (Walsh et al. in review). The acoustic signal for all pulses, apart from pulse 1, is stronger towards the east, indicated by the data points position below the 1:1 line (Figure 4.8). The modelled bearing of

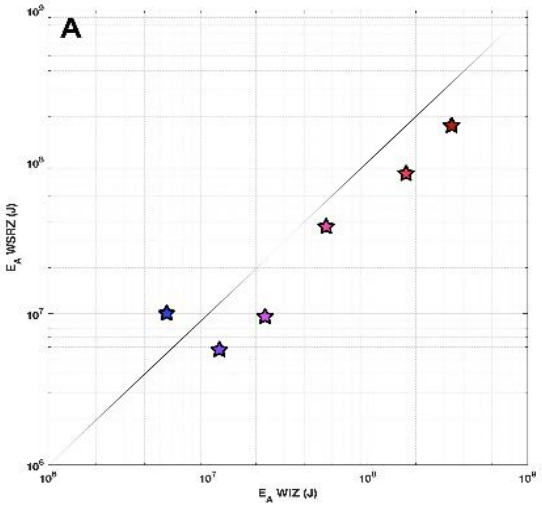

Figure 4.8 Acoustic signals at WIZ (SE end of island) and WSRZ (NW) stations. Stronger signals are shown towards WIZ, in the SE of the island. Modified from B. Walsh (in review).

each pulse for the multi-pulse scenario was chosen through best fitting the modelled distribution to the spatial variation, based on the east-southeast directivity suggested. The greatest number of clasts per m^2 was at the craters edge towards the east-southeast. Therefore, the directionality of the 3 eruptive pulses in the multi-burst scenario was determined to provide overlap in the crater edge and southern part of the field, while being elongated to the east-southeast. The bearing for Scenario 1 was iteratively chosen to best create the elongation to the east-southeast and general field shape.

4.2.1.2 Number of erupted particles

The number of particles erupted is an important parameter in determining the spatial density of a block field. The nature of the field mapping, providing only localised, detailed spatial density information at spread out locations, meant an estimation of the total number of blocks was not possible from the field data alone. Similarly, the pattern of deposition indicated a shallow ejection angle (See section 4.3.1.4.) indicating a proportion of the blocks would not have exited the inner crater and as such the number of ejected particles and number of mapped particles would be distinct. Therefore, the total number of blocks ejected in each scenario was chosen based on the best fit.

The acoustic energy of each pulse determined the relative number of particles in each eruptive pulse in this model (Table 4.2). It is assumed that the relative acoustic energy of each pulse is proportional to the kinetic energy release of each eruption, ignoring the energy partitioning into any accompanying eruption surge. Kinetic energy (E_k) of each burst is calculated based on the mass of particles ejection and the velocity at which they are ejected.

$$E_k = \frac{1}{2}mv^2$$

Table 4.2 Relative kinetic energy of eruption bursts and consequent number of blocks modelled in the multiburst and single burst scenarios.

Triple Pulse	Average Acoustic energy (J)	Normalised to largest	No. Particles	Average Velocity (m/s)	Average block mass (kg)	K energy (J)	Normalised
P4	2.15E+07	11.68	53300	50	0.026	1757038.83	11.68
P5	6.76E+07	36.74	124500	58	0.026	5522547.75	36.71
P6	1.84E+08	100	270000	65	0.026	154041966.54	100.00
					Total	22321553.11	
Single Pulse	Average Acoustic energy (J)	Normalised to largest	No. Particles	Average Velocity (m/s)	Average block mass (kg)	K energy (J)	Normalised
Northern Vent	1.84E+08	100	561000	65	0.026	31253863.81	100.00

4.2.1.3. Particle Density and Diameter

The density and size distribution of particles ejected from a volcanic vent are crucial in the transport and spatial distribution of ejected blocks. Three lithologies were sampled in the field; altered lava, cemented vent breccia and altered ash tuff. Farquhar (2018) and Christenson et al. (in review) measured the bulk density of 23 samples, with 92 measurements taken through precision mass measurements and volumetric measurement using callipers. An average bulk density of the 23 samples was calculated (1691 kg/m^3), and standard deviation (311 kg/m^3) used for modelling particle density. Density calculations were not weighted by occurrence as would be ideal (Fitzgerald et al., 2014) as the restricted field time and consequent photograph mapping impeded lithological identification.

The size distribution and subsequent diameter of the 27th April erupted blocks was derived through handheld photography mapping as described in section 4.2.1. A minimum clast size of 5 cm was used in the modelling consistent with minimum appropriate sizes for ballistic motion, as per Chapter 3 (Self et al., 1980; Waitt, et al. 1995; Spark et al., 1997; de' Michieli Vitturi, 2010). Ballista requires normal distribution of diameters for particle size. As such a normal distribution was calculated based on clast diameter mapped >5 cm. However, the ejected particle size was not normally distributed, but skewed towards smaller clast sizes. Future work with Ballista would be improved through editing the size distribution input function to suit the distribution found in the field.

4.2.1.4. Ejection Angle

The maximum ejection distance of a particle is dependent on the initial angle of ejection (Minakami, 1942; Steinberg & Lorenz, 1983). Ejection angles starting at 45° were iteratively changed until best fits were achieved for all pulses. Behind Donald Mound (Figure 4.9) there was a relatively low concentration of ballistics, despite the proximity to the vents. This suggests a shadow depositional

Figure 4.9 A distinct lack of blocks and yellow erupted material within the red outlined "shadow zone".

zone due to the topographic barrier (Kilgour et al., 2010; Tsunematsu et al., 2014). Model iterations were unable to reproduce this shadow effect at ejection angles > 30° from horizontal for each vent, therefore an ejection angle of 30° was chosen for each burst. The standard deviation of particles from the ejection angle (Figure 4.6), previously referred to as inclination or rotation angle (Tsunematsu et al., 2016, Fitzgerald et al., 2014), determines the spread of particle paths and eventual deposition. A smaller standard deviation will create a focussed ejection lobe (in this case where the eruption is non-vertical) along the ejection axis, whilst a larger standard deviation will create a wider deposition pattern. The spread of particle deposition was determined iteratively for the best fit, paying particular attention to the outer limit of the ballistic field

4.2.1.5. Initial Particle Velocity

The speed at which the clasts were ejected was based on best fit, starting with ejection speeds of <100m/s due to the significantly smaller distances reached by clasts at Whakaari as compared to other phreatic eruptions modelled in the literature. The phreatic eruption of Mt Ontake 2014, ejected clasts to ~950m at speeds of 111-185m/s (Kaneko et al., 2016; Oikawa et al., 2016; Tsunematsu et al., 2016); while the August 2012 Te Maari eruptions ejected clasts up to 2.3 km from the vent with velocities modelled at 165-200 m/s (Fitzgerald et al., 2014; Bread et al., 2014). As the clasts at Whakaari reached only ~310m from the active vents and were ejected at a low angle increasing their travel distance, model iterations started at 100m/s and decreased with successive iterations until the distances clasts reached matched the field distribution.

4.2.1.6. Gas flow velocity and distance over which this effects particle transport

Particles ejected during volcanic eruptions are initially supported by the eruption gas stream, until they decouple from the gas phase and travel on essentially ballistic trajectories as function of their velocity and ejection angle (Lorenz, 1970). The area in which the gas influences particle transport is an important, but poorly understood, influence on the distribution of particles.

It is assumed in Ballista that at ejection point, the speed of the particles and the gas phase is equal, and the particles are completely coupled with the gas phase. Soon after, the gas velocity decreases while ballistics continue to travel faster than the expanding gas due to inertial effects on the blocks, thereby increasing the relative drag force on the particles over time. At some distance from the vent the blocks decouple from the eruption jet completely and travel on essentially parabolic paths.

The total size distribution of the clasts ejected at Whakaari show an overall decrease in diameter with distance from the vent, a distribution common with ballistics from phreatomagmatic eruptions which have significant influence from a gas jet phase (Lorenz, 1970; Self et al., 1980; Waitt et al., 1995).

The eruption occurred at night, so the webcams on the island were unable to provide any information as to the speed of the gas jet, or the distance to which it influenced the block trajectories. The rarity of studies pertaining to gas flow regions in phreatic eruptions averages a combination of previous modelling publications and best fit has been used to derive a value for this scenario. Tsunematsu et al. (2016) used a gas flow region of 100m when modelling the 2014 Mt Ontake eruption, based on the size of a pyroclastic cone built around the vent, the radius of which was inferred to be a result of the end of the gas flow region. They derived ejection speeds of 145-185m/s-1. The eruption at Whakaari was smaller, with lower ejection speeds hence smaller gas flow regions were used (30m for single burst scenario, 30m, 25m and 20m for single burst) and varied with eruption burst size, i.e. smaller bursts have smaller gas flow regions.

4.2.1.7. Drag Co-efficient

The drag co-efficient, C_d, is a dimensionless number that quantifies the amount of drag force exerted on a particle travelling through air. Alatorre-Iberguengoitia & Delgado-Granados (2006) experimentally found that C_d values depend mainly on shape and texture of the ballistic block. C_d realistically changes as a block decelerates (Fudali & Melson, 1971) so an average value is applied for modelling purposes. Fitzgerald et al. (2014) set the drag coefficient to 0.7 based on Alatorre-Ibargüengoitia & Delgado-Granados (2006) experimental results as well as fieldwork which found the majority of clasts were sub-angular and smoothed. Tsunematsu used a Cd of 0.8 for remodelling of Fitzgerald's Te Maari data (Tsunematsu et al., 2017). The closest description of sample types to Whakaari from Alatorre-Iberguengoitia & Delgado-Granados (2006) criteria was "angular shape, "smooth surface" hence the Cd value attributed to that sample type was used, 0.7.

4.2.2.2. Model output processing

Ballista's design creates two results files per inputted parameter file, a deposition .txt file with an x, y, z co-ordinate of each block and a trajectory .txt file with the calculated trajectory of each block's x, y, z coordinates at each timestamp. The deposition file was added to ArcMap with a $1m^2$ grid overlay and the Spatial Join tool used to determine the modelled number of blocks per metre square. With the computational power available, a maximum of 30000 blocks could be computed per run and as such multiple initial files and outputs we run for each model scenario to calculate the total number of blocks per eruptive pulse. The generation of multiple results files and their merger required the creation of multiple basic codes created by Dale Cusack, University of Canterbury and Alec Wilde, Auckland University of Technology, in Python language, compatible with ArcGIS, to lighten the temporal load of the modelling process. The workflow developed in this study is attached in Appendix 1B.

4.2.2.2.1 Fitting modelled data to mapped

Comparison of modelled and mapped data was undertaken by iteratively comparing the modelled ballistics per m^2 at each sampled location and matching the ballistic field outline. The mapped ballistic density was matched to the modelled density within the adjacent $25m^2$ area (Figure 4.10). A comparison with the 25 m^2 area around the sample location was chosen due to the high local variability in modelled spatial density making comparison with the $1m^2$ the mapping site inappropriate. For computational efficiency the merged DEM resolution was reduced to 5m. As a result, the landing locations of the blocks has a 5m grid-like artefact (Figure 4.16), which contributed to the variable spatial density and necessitated comparison with the greater area for cases where the GPS field location was impacted by the 5m artefact. Additionally, Chapter 3 demonstrated the challenge of comparing small field areas ($1m^2$) with other datasets based only on GPS locations.

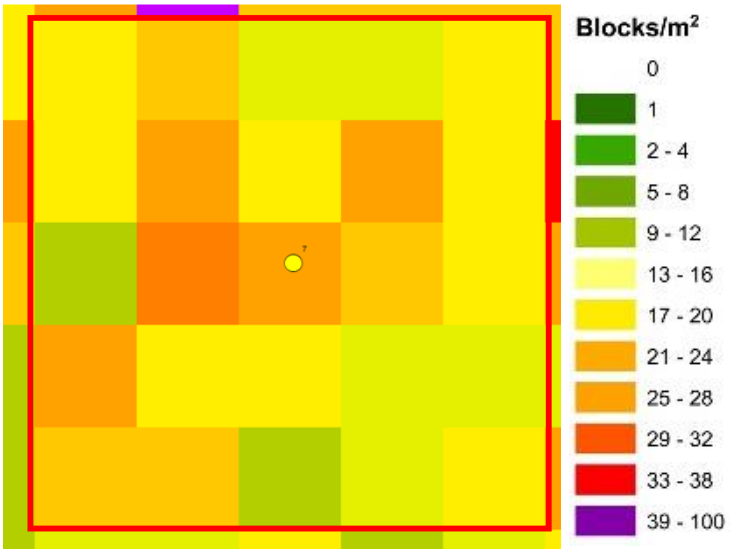

Figure 4.10 Fitting approach. Central circle is the GPS location of site 7, colour scale the same as the background. Each coloured square is $1m^2$ spatial density as modelled. Red Square is the $25m^2$ area sampled for comparison with handheld photography data.

4.4 Results

4.4.1. Orthomapping Results

27 of the 35 sites photographed were used to assess the spatial distribution of blocks ejected during the eruption. Site 35 was excluded from analysis due to the unusual size distribution of the site with more large clasts than expected and the lithological character, orange weathered surfaces, which appeared similar to the overlying cliff indicating at least some of the clasts in this area were emplaced through rock fall. Seven other sites photographed did not have the $1m^2$ reference frame required for handheld photography mapping.

A total of 4773 clasts that could be identified through photographs were traced and diameters calculated leading to a total size distribution of particles from 1.07 cm to 42.2 cm with an average diameter of 2.14 cm. The size distribution is strongly skewed to small clast sizes which dominate the deposit both when all clasts are mapped (Figure 4.11A) and when those below 5 cm are excluded (Figure 4.11B).

4.4.1.1. Size and spatial distribution of mapped blocks within field.

When all clasts are considered the average diameter tends to decrease with distance from the vent however, size does not show a convincing decrease with distance as predicted by purely ballistic models (Figure 12). Sites close to the crater edge in the south, sites 4, 6 and 7, have high average diameters ranging from 4 to 8 cm's, while sites 3, 21-24, ~60m further away, have average diameters from ~1- 4cm.

The relationship between the average diameter of clasts greater than 5 cm and distance is subtler than when all clasts sizes are included (Figure 12A). However, the sampling sites on the periphery of

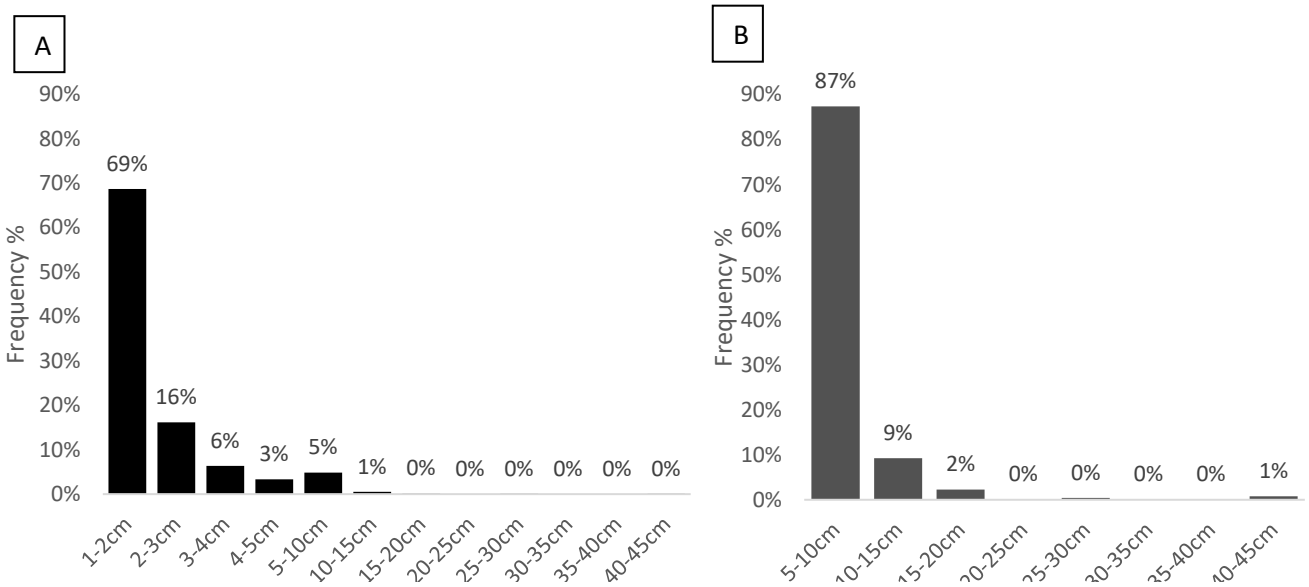

Figure 4.11 A) Handheld photography mapped diameters all clast sizes. calculated from the area of clast mapped, assuming a circular area. B) Total size distribution for clasts >5cm as per the modelled lower clast diameter.

the field (14, 28-34, 21 and 4) have no clasts above 5 centimetres indicating that at the fields extremities a smaller grain sizes dominate.

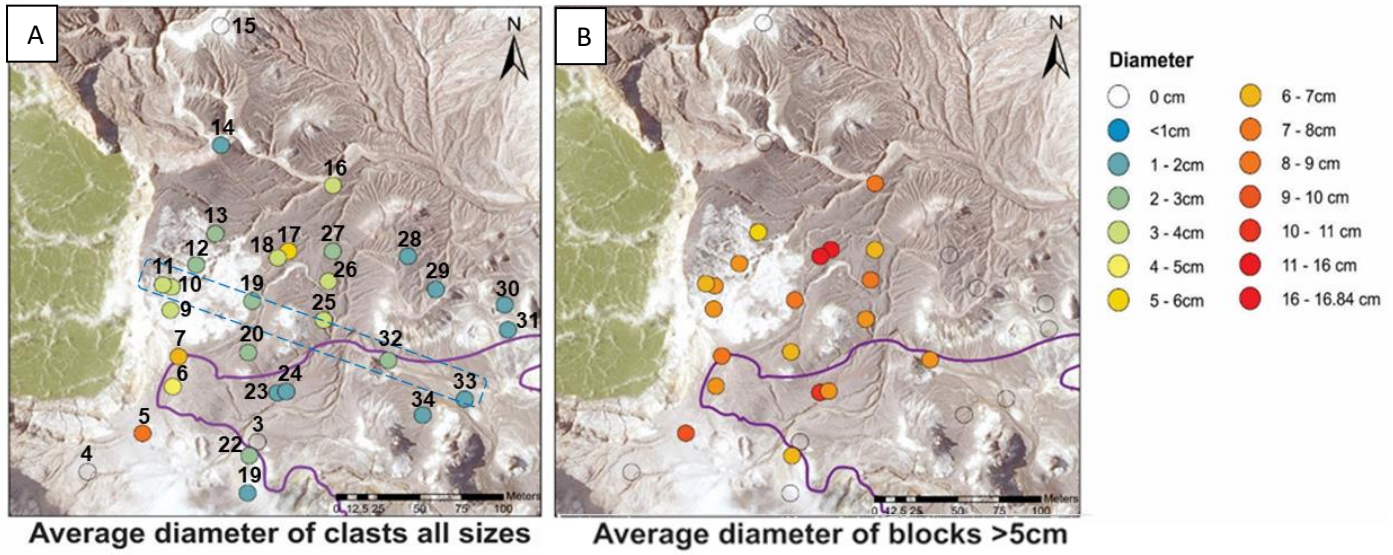

Figure 4.12 Maps illustrating the distribution of clasts. A): the average diameter of clasts >5cm at all surveyed sites, site numbers shown and B) the average diameter of all clasts at all surveyed sites.

The transect from Figure 4.12A was used to investigate how size distribution relates to distance from the closest vent. Figure 4.13 shows that the proportion of small clasts generally increases with distance. Just under 50% of the clasts at Site 33, 315 m from the closest vent, are less than two centimetres as opposed to the closest site, 121m from the vent at which less than 10% of clasts are less than 2 centimetres

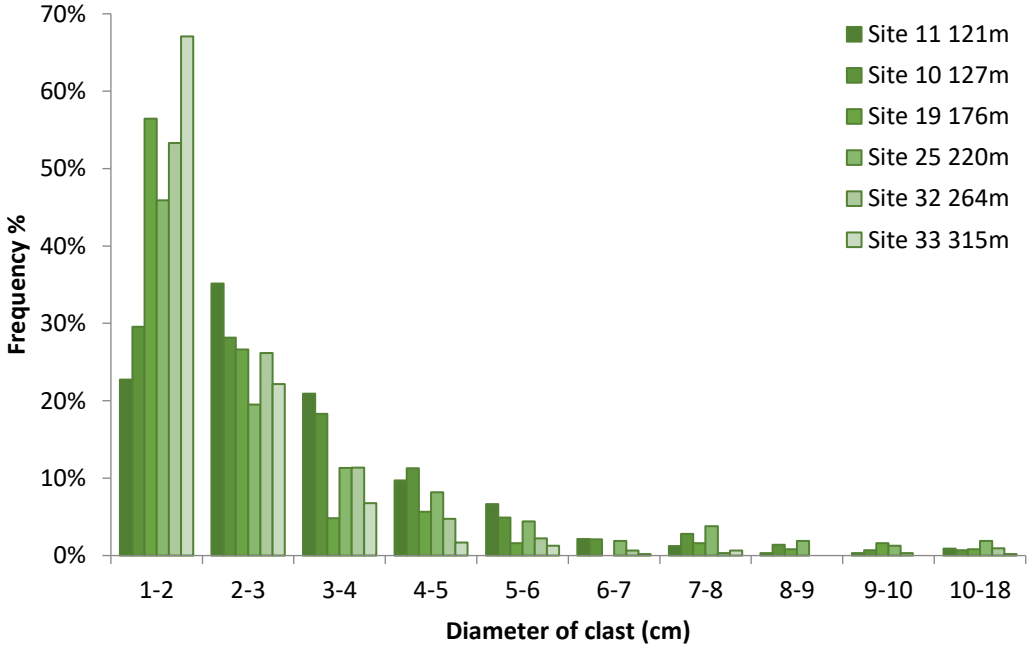

Figure 4.13 Proportion of mapped clasts in size category with distance, based on transect in Figure 11A. Lighter columns are for sites at greater distance from vents.

The number of blocks per metre square has a complex spatial distribution (Figure 4.14). The northern area of the map has fewer ballistics ranging from 1-16 blocks/m^2 while the southern and central area have relatively high spatial densities of blocks from 9 to 38 blocks/m^2. The small number of clasts in the northern area sites 14, 16, 13, may be a result of Donald Mound acting as a barrier between these sites and the vent locations. The complex spatial pattern supports the ballistic field being composite in nature, contributed to by multiple eruption pulses.

High spatial variation within small areas is evident from site locations such as site 11 and 10 which are the closest locations to the crater edge and situated only 5.5m apart (Figure 4.14A, Figure 4.12 for site numbers). Despite the proximity of the sites, the density of clasts varies by 20 blocks/m^2 (site 10 has 38 blocks/m^2 whilst site 11 has 18 blocks/m^2).

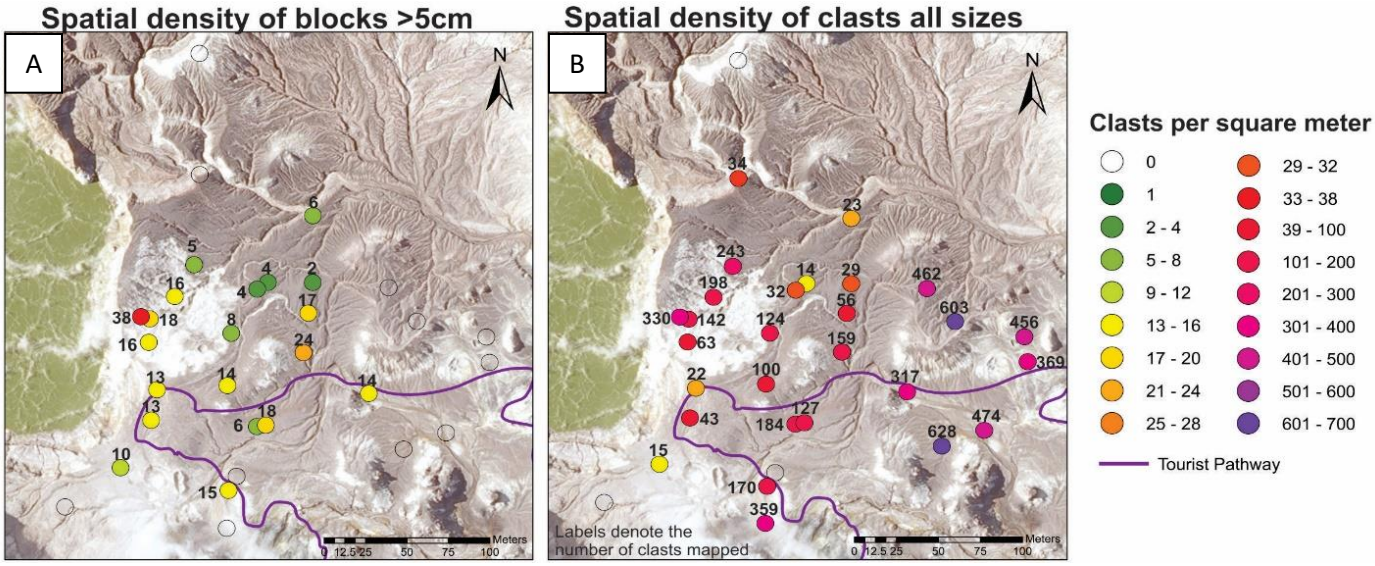

Figure 4.14 Variation in spatial density in strew field of April 27th Whakaari eruption with number of clasts mapped at each site shown. A) Spatial density of blocks greater than 5cm, B) Spatial density of all clasts mapped.

4.4.2 Modelling Results

A total of 119 model iterations were undertaken before the final best fit scenario was selected. 35 runs investigated the influence of parameters such as gas flow radius, gas flow speed, bearing, and ejection speed on block deposition patterns. 33 model runs were undertaken for scenario 1 – investigating the potential for the ballistic field to be emplaced in one large burst from the furthest vent. This scenario was developed to investigate the maximum E_k release and discern if a single burst could be responsible for the observed block field. 51 runs were completed of scenario 2, the multi-burst scenario indicated by seismo-acoustic signals and the variable burial of blocks by the pyroclastic surge. Input parameters of model runs were systematically varied until a sufficient fit was found. The greater number of runs in the multi-burst scenario reflects the increased complexity of modelling three bursts.

4.4.2.1. Eruption Parameters and Results

Scenario 1 – Single Pulse

Table 4.3 Final eruption parameters for best fit single burst model scenario

Vent	No. of particles	Particle Density (kg/m3)	Density s.d	Bearing	Drag coefficient	Gas flow velocity (m/s)		Flow range (m)	
Northern	561000	1691	311	110	0.7	65		30	
Particle Diameter (m)			Displacement from vent centre (m)			Initial Velocity (m/s)		Ejection Angle (from vertical)	
Average	s.d.	Range	Average	s.d.	max	Average	s.d.	Average	s.d.
0.0791	0.042	0.05 -0.422	4	3	8.138	65	5	60	10

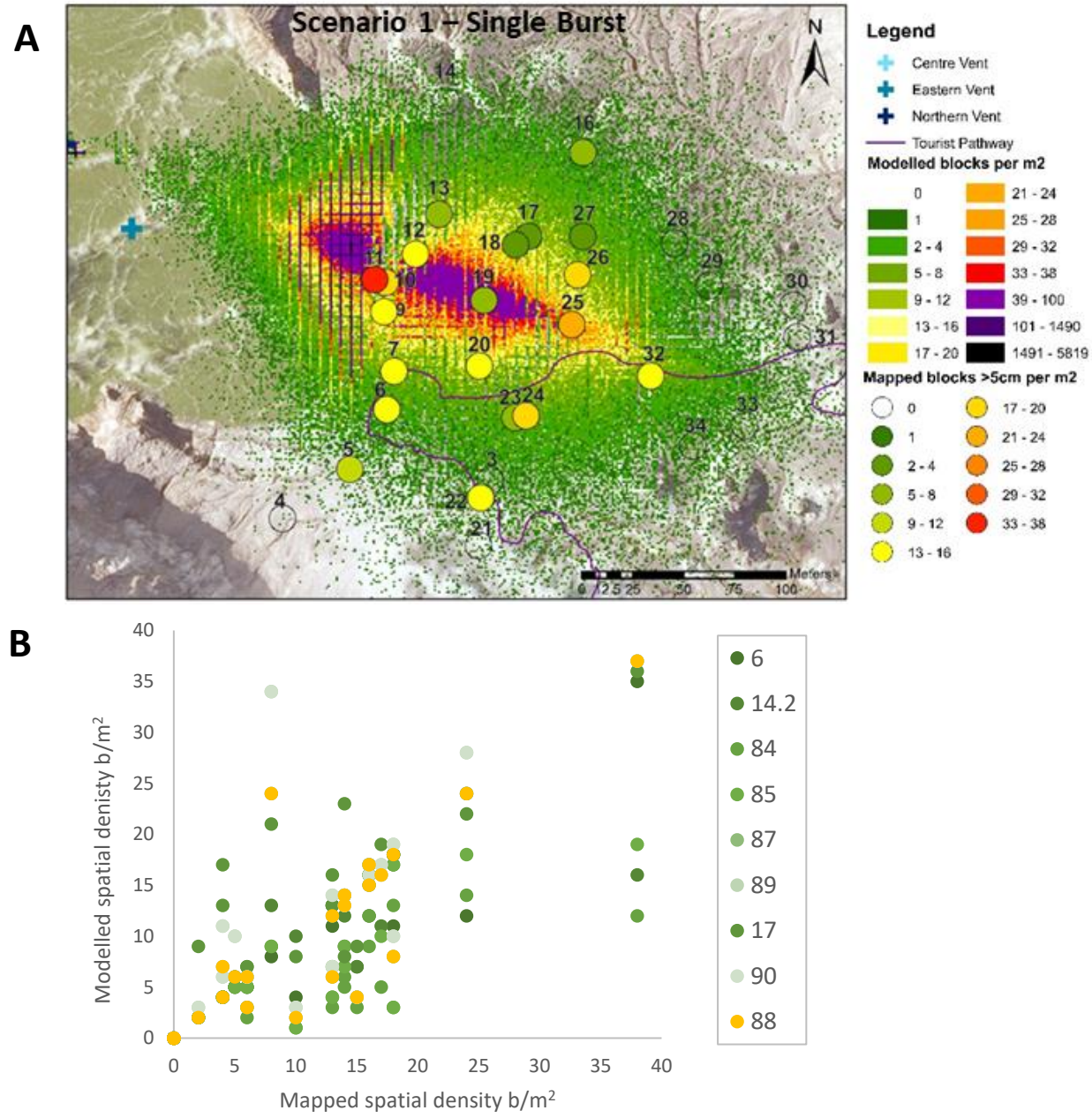

Figure 4.15 ***a) The mapped results from the best fit runs with one eruption pulse showing the number of ballistics per m², the number of mapped ballistics >5cm from figure 4.14A are also shown for comparison with the corresponding site number b) the best fit graph for scenario 1 plotting the modelled spatial densities against the mapped blocks/m².***

Scenario 2 – Multiburst

Table 4.4 Final eruption parameters for best fit muti- burst model scenario

Vent	No. of particles	Particle Density (kg/m3)	Density s.d.	Bearing	Drag coefficient	Gas flow velocity (m/s)		Flow range (m)	
Northern	270000	1691	311	110	0.7	65		30	
Eastern	124500	1691	311	114	0.7	58		25	
Eastern	53300	1691	311	114	0.7	50		20	
Particle Diameter (m)			Displacement from vent centre (m)			Initial Velocity (m/s)		Ejection Angle (from vertical)	
Average	s.d.	Range	Average	s.d.	max	Average	s.d.	Average	s.d.
0.0791	0.042	0.05-0.422	4	3	8.138	65	5	60	10
0.0791	0.042	0.05- 0.422	3	2	6	58	5	60	10
0.0791	0.042	0.05- 0.422	3	2	6	50	5	60	10

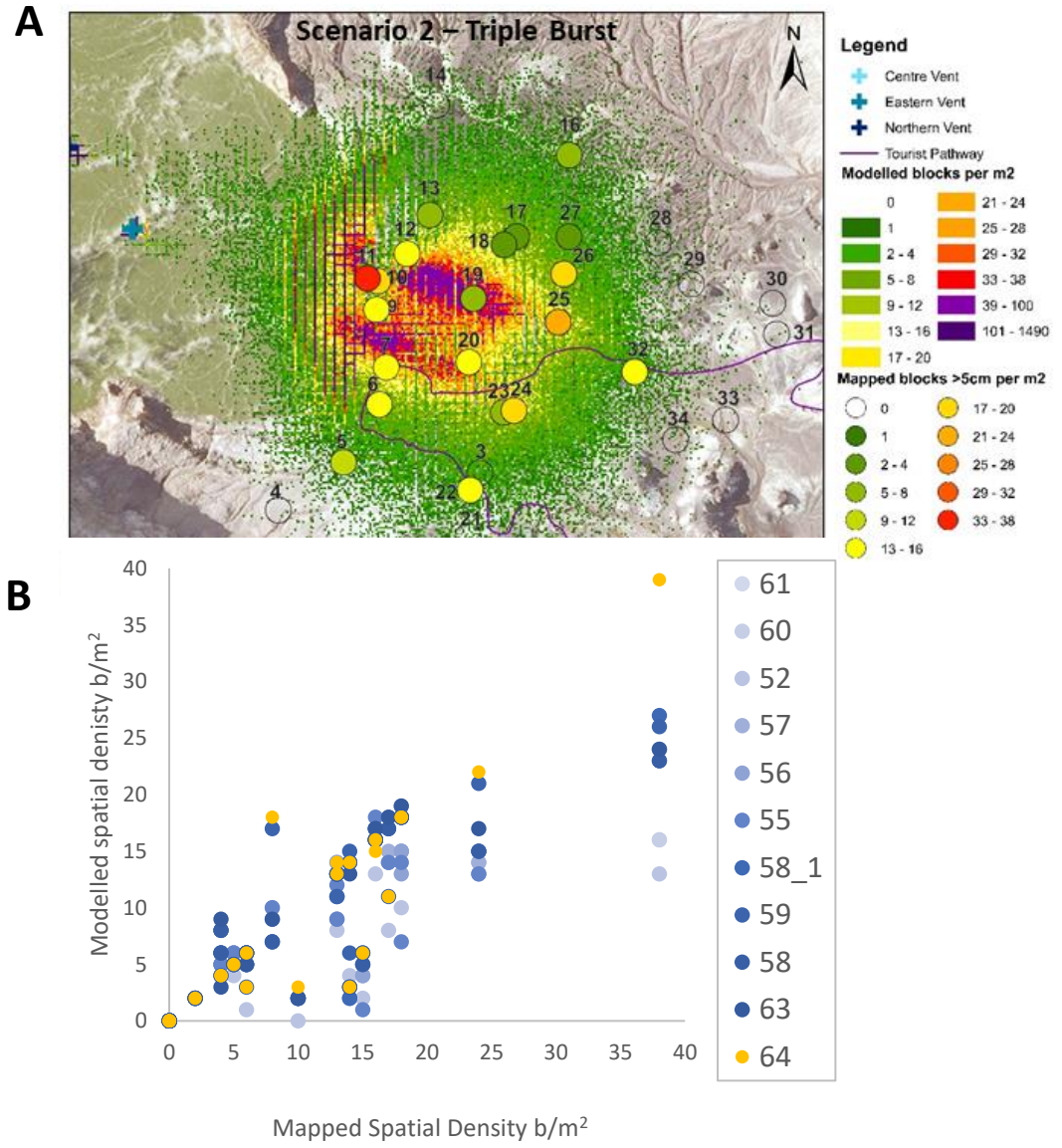

Figure 4.16 A) The mapped results from the best fit runs of the triple pulse eruption showing the number of ballistics per m² B) the best fit graph for the multipulse scenario.

While both scenarios had strengths, the multi-burst, scenario 2 was chosen over the single burst scenario 1 for the following reasons:

- Geophysical data suggested that multiple eruptive bursts occurred and field data supported this with variable coating of clasts by surge deposits. Some blocks were clearly emplaced on the top of surge deposits, while others were partially buried suggesting they were ejected as pulses spread either side of the pyroclastic surge (Kilgour et al., in review).
- Scenario 1 required many more blocks to fit field data points, the best model run ejected 561000 particles in one eruption. This resulted a central strip of extremely high spatial density (Figure 4.15), up to 73 blocks >5cm per m^2 within the mapping area and did not reproduce the high local variability mapped.
- Scenario 1 did fit the furthest extent location, site 33, and general elongated field shape better than scenario 2, however the field was described as having a sharp edge with few ballistics beyond it, and scenario 1 consistently had many blocks beyond mapped outline.
- Scenario 2 has better fit to spatial density data, a single burst scenario could not reproduce the high localised variability (Figure 4.16).

Run 64 for scenario 2 was chosen as the best fit scenario as the model data deviated the least from the mapped data (Fitting 4.16B). 79.3% of the maps of the site locations were within 2 ballistics per metre squared from that mapped with 65.5% exactly matching the number of ballistics per meter squared in the mapped data. Additionally, run 64 fit the outline of the field the best of all runs however it is limited as it does not replicate the full extent of elongation to the east as mapped. Further model runs were attempted to rectify this, however an elongated field shape was not able to be produced within timeframe of this study without negatively impacting the fit of all other points in the model. The decision making processes for selecting best fit is demonstrated in Table 4.5.

Table 4.5 Decision making table for selected model

	Scenario 1 – Single Burst							
Run No.	**52/61**	**62/72**	**84**	**85**	**86**	**87**	**88**	**89**
% sites within 2 blocks/m²	58.62068966	62.06896552	51.72413793	62.06896552	68.96551724	65.51724138	75.86207	75.86207
% sites match mapped	48.27586207	48.27586207	44.82758621	48.27586207	51.72413793	55.17241379	48.27586	51.72414
Fit to field outline	Poor	Poor	Poor	Moderate	Good/Moderate	Poor/Moderate	**Best** Good/Moderate	Good/Moderate
Reasoning	Too much spread, south and north field edge completely overshot, blocks hitting outer crater wall, too far. Good distance reached in centre of field.		Thin, elongated shape to field, edge sample locations not being covered.	Not many beyond field boundaries, too few blocks overall	Blocks overshooting mapped area, south and outer aspects of field under catered, shadowing behind DM evident.	many block overshooting - not "sharp edge" of field as described by Geoff. Poor fit to southern area.	Blocks overshooting mapped area, south of field under catered, shadowing behind DM evident. Run 89 has one more site with zero difference where run 88 underestimated this site by 1 block and 89 over estimates site 19 by 26 blocks - run 88 overestimates by 16.	
	Scenario 2 – Multiburst							
Run No.	**57**	**58**	**59**	**60**	**61**	**62**	**63**	**64**
% sites within 2 blocks/m²	75.86206897	68.96551724	62.06896552	75.86206897	75.86206897	79.31034483	37.93103	79.31034
% sites match mapped	41.37931034	51.72413793	48.27586207	62.06896552	58.62068966	51.72413793	27.58621	65.51724
Fit to field outline	Poor/Moderate	Poor/Moderate	Poor/Moderate	Moderate	Moderate	Moderate	Moderate	**Best** Good/Moderate
Reasoning	Circular field, not elongated. Good fit to northern edge and almost no blocks overshooting end of field.			Circular field, not elongated. Good fit to northern edge and almost no blocks overshooting end of field.		Good shadowing behind Donald Mound, more circular field than mapped, few blocks overshooting mapped field edge.		circularish shape, more elongated towards furthest site. Best fit for scenario 2

4.4.2.2. Modelled size distribution with distance

The relationship between block diameter and distance from vent from the best model iteration was compared to the mapped distribution. The modelled data shows the average block diameter increases with distance (Figure 4.17, yellow points). The diameter of blocks >5cm from handheld photography, however, shows no systematic decrease with distance (Figure 4.17 "Mapped"). When all photo identified clasts were included the average diameter decreases with distance. The implications of this are discussed below.

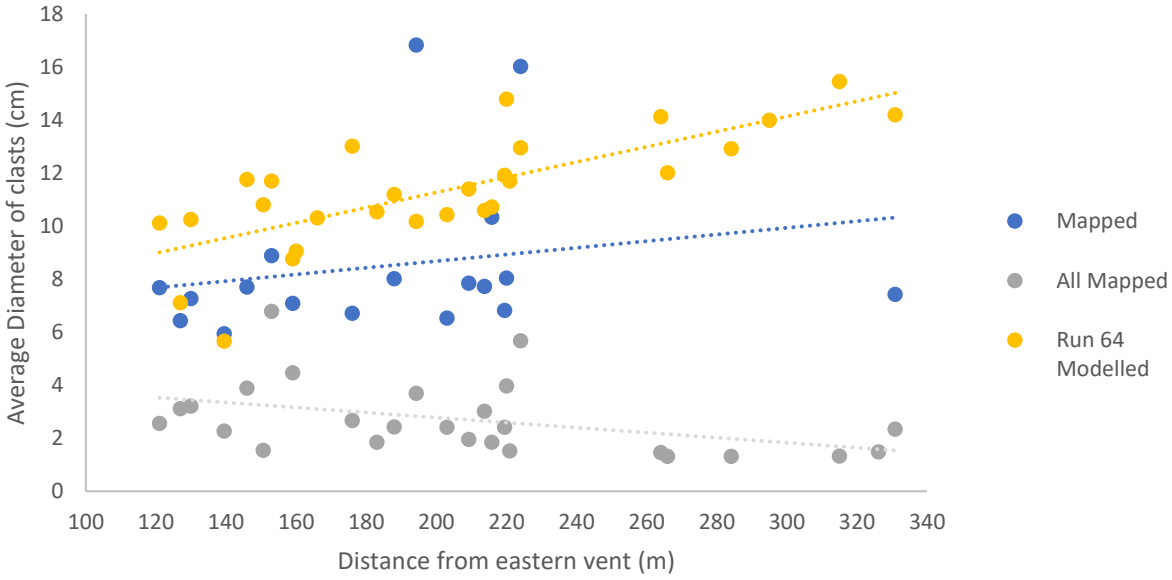

Figure 4.17 Average clast diameter with distance

4.4.3. Limitations

Whilst modelling is often the only way in which to estimate eruption parameters, they are limited by the quality of the inputted data and the quality of model design. Two parameters which can be included in Ballista but were excluded are wind speed and collisions between particles. Collisions between particles have been demonstrated by Vanderkluysen et al. (2012) as a potentially important parameter to include in modelling as it was shown to increase the travel distance of approximately 12% of ballistics observed in the studied Strombolian activity. Following this Ballista was originally developed to investigate the potential of modelling collisions between particles and their effect on deposition (Tsunematsu et al., 2014). Collisions are thought to be most applicable to ongoing eruptive activity with multiple bursts in which particles are continuously ejected, such as Strombolian, large Vulcanian or Plinian eruption styles (Tsunematsu et al., 2014; Bertin, 2017). Particles from a subsequent burst hitting those already in flight has the greatest impact on increasing travel distance (Tsunematsu et al., 2014). Ballista, as used in this study, assumes that all particles are ejected at once.

However, acoustics indicate bursts lasted for ~2 minutes each, therefore ballistics were potentially ejected over this time, not instantaneously. As such, collisions between particles may be occurring and impacting flight paths and deposition. Ballista models multi-burst eruptions by the user determining the time separation of each burst, i.e. 5 bursts 4 seconds apart, which may be compatible if the 2 minutes of acoustic signal comprised of multiple individual bursts. However, the small eruption size, resulting resolution of the acoustic data and the lack of visual observations for the Whakaari eruption mean the involvement of collision was unconstrained and computationally heavy and therefore not included in this study.

Wind speed is also not included, although it is known to be an important factor in the trajectories of ballistic particles (Bertin, 2017). This was due to the poor constraints on wind vectors within the crater. The influence of wind speed is greatest upon small clasts (Bower & Woods, 1996), and Alatorre-Iberguenoitia et al. (2016) found that maximum distance a clast travelled was increased by 15% when wind speed of 20m/s were included in modelling, however they were considering ballistic ranges of 4.8 - 8.4km, many times the size of the Whakaari eruption. The small distance that the vast majority of clasts at Whakaari travelled, >300m, would minimise the influence of wind. Within the purposes of this study, namely inversely modelling an unobserved small phreatic eruption to gain insight into reasonable eruption parameters and the hazard posed, emphasis was put on completing a high number of model runs. Despite the limitations of the modelling, a set of reasonable eruptions parameters has been derived which are useful as the first study on the initial conditions and velocities of clasts ejected during Whakaari's frequent small phreatic eruptions.

The presence of water in a crater lake and eruption plume is currently not accounted for in any known ballistic models (GBF (Biass et al., 2016), Fagents & Wilson (1993); Ballista (Tsunematsu et al., 2016)). The presence of water would increase drag on the particles, decreasing travel distance and distributed area. As such, initial ejection velocities may be underestimated without taking water drag into account. At Whakaari the crater lake was empty by the end of the eruption sequence so the influence of this is not certain – this may suggest that pulse 6, which contributed most significantly to the E_k and ballistic field, may have had less water over-burden and drag than earlier eruptions.

The whole island DEM used for the modelling was sourced from a 2008 flight, processed in 2011. The bathymetry of the lake was included following a high-resolution run creating a 59mm bathymetric DEM. Whakaari's crater lake edge is a changeable feature and as such the two DEM lake edges did not match. A composite DEM was created to take advantage of the high-resolution lake data, however

the compilation of the two has introduced some error to the lake edge position, and created a more gradual slope than is true, however the upper edge of the inner crater, the most important aspect that could impede ballistic flight paths, was from the DEM closest in time to the eruption, therefore the most accurate.

The deterministic scenario modelled is not a unique solution, being one of many possible eruption scenarios, however it is reasonable based on literature values for small phreatic eruptions and fits the field data well. Modelling unwitnessed eruptions will consistently have this issue as there will remain uncertainties with eruption parameters. Future work in which this scenario is modelled probabilistically, with particular focus of varying the ejection direction and inclination angle, would enable the production of a rigorous ballistic hazard map with less dependence on vent geometry.
With a significant increase in computing power the study would be able to include all parameters such as wind speed and collisions and the resulting best fit scenario could also be developed probabilistically.

4.4.4. Results Summary

The 27 April Whakaari ballistic field was mapped using the handheld photography mapping method and inversely modelled using two scenarios to gain insight into the dynamics of an unwitnessed eruption. 4773 clasts were mapped showing the field was dominated by small clasts, ranging from 1.07cm to 42.2 cm in diameter with an average diameter of 2.14cm. The spatial and size distribution were complexly distributed, average clast size decreased from the vent when all sizes were considered but showed no distinct pattern when clasts <5cm were excluded from analysis. As the smallest clasts were unlikely to have travelled by ballistic motion, their spatial distribution was considered separately, and they were excluded from modelling. The spatial distribution of mapped blocks was also complex, with high variation within small areas.

The best single burst scenario ejected 561,000 blocks at 65± 5 m/s, a total kinetic energy release of ~3.13×10^7 J. The best multi-burst scenario ejected a total of 447,800 blocks in three eruptive bursts at speeds of 50, 58 and 65± 5 m/s, an energy release of ~2.07×10^7 J. Both scenarios discerned highlight directed, low angled eruptions. The multi-burst scenario fit the mapped distribution better than a single burst scenario when both spatial density, the field outline were considered, seismo-acoustics and variable coating of blocks by surge material was considered.

4.5. Discussion

4.5.1. Eruption Dynamics

4.5.1.1 Size Distribution

The size distribution of the mapped clasts and blocks from the 27 April 2016 Whakaari eruption provides insight into the dynamics of the eruption and highlights the importance of using mapping methods that can obtain information on small clasts. The average clast size measured using a handheld photography mapping method was very small, an average size of 2.14 cm. 95% of clasts measured were less than 5 cm in diameter (4474/4735). This portion of the deposit was not included in ballistic modelling as the transport mechanisms of these smaller clasts, which are likely transported by both the combination of lofting and ballistic motion, is currently not well understood (Self 1980, Taddeucci et al., 2017). Even when clasts less than 5 cm in diameter removed, 87% of the remaining deposit is between 5 cm and 10 cm in diameter. The eruption at Ontake in 2014 demonstrated that even small, cm sized clasts have the potential to main or kill (Oikawa et al., 2016). While there has been progress into development of combined ballistic/convective modelling (Saunderson et al., 2008) there is none currently available for use in ballistics hazard modelling. The dominance of small clasts at Whakaari and their proven potential for harm highlights the need for greater appreciation of their significance when mapping and developing ballistic models.

The mapped average clast size decreases with distance when the whole deposit is considered and increases slightly with distance when only clasts >5cm are considered, however the relationship is weak. Block size is expected to increase with distance due to the greater momentum of larger massed objects, when blocks are ejected at a similar velocity (Nairn &Self, 1978; Bertin et al., 2017). However, decreasing particle size with distance has been suggested in phreatomagmatic eruptions due a gas flow region, reducing the drag upon the ejected particles (Lorenz et al., 1970; Self et al., 1980; Taddeucci et al., 2017). Field observations and the modelled scenario suggests that blocks were ejected at a very low ejection angle (30°), with at least two syn-eruptive surges (Kilgour et al., in review). The syn-eruptive surges may have acted in a similar manner to the reduced gas region in a gas-rich phreatomagmatic eruption and reduced the drag on the small clast, buoying them to greater distances than can be explained by ballistic transport alone. The multiple hazards posed by synchronous ballistic fall and pyroclastic surge is common during phreatic eruptions (Breard et al., 2014; Oikawa et al., 2016; Kilgour et al., 2010) and an important consideration for comprehensive hazard assessments.

4.5.1.2 Ballistic Mass of the 27 April 2016 Whakaari Eruption

For the April 27th Whakaari eruption, the total ballistic mass ejected was quantitatively estimated based on the total number of blocks and their modelled mass. Between 404,000kg (multiburst scenario) and 507,623kg (single burst scenario) of ballistic mass was erupted, excluding small, semi ballistic clasts discussed earlier. Uneven ballistic distributions are common, due to influences such as zoning between plume jets, multiple eruption deposits overlapping, and as such isopleth maps are an inaccurate manner of determining the total ballistic mass ejected (Gurioli et al., 2013). As such, modelled scenarios fitted using internal spatial distribution variation and the field outline provides the best estimate for ballistic mass.

While a small number of phreatic and hydrothermal eruptions have been described in recent years (Kilgour et al., 2010; Fitzgerald et al., 2014; Kaneko et al., 2016), they are all larger than the Whakaari eruption. The most comparable eruption by ballistic range and size distribution is the 14 September 2015 phreatomagmatic eruption of Nakadake first crater, Aso Volcano, Japan (Miyabushi et al., 2018). Unfortunately, quantification of ballistic mass erupted is rare, omitted by Miyabushi et al., (2018) and the only other phreatic study reporting total ballistic mass found is that of Te Maari, 2012 (Fitzgerald et al., 2014). The value in modelling end members, a single and multi-burst scenario, is that it allows comparison of potential outcomes depending on scenario development. If seismo-acoustic data did not provide evidence of multiple bursts a single burst would potentially be used to provide quantitative insight into the eruption. Comparing each scenario to the August 2012 Te Maari eruption, the mass ejected during the Whakaari eruption was small, between ~404,000kg and ~507,623kg, multiburst and single burst respectively, ~33.4 - ~42.3% of Te Maari's ballistic mass (Fitzgerald et al., 2014).

A large proportion of the modelled eruptive ballistic mass did not exit the crater lake due to the low ejection angle. For the best fitted single burst scenario, 35% of modelled trajectories ended in the crater lake, 31% of the total mass. Similarly, 34% of blocks and 30% the ballistic mass did not exit the crater lake in the multi-burst scenario. This is due to the low ejection angle of the eruptions and the steep inner crater wall at Whakaari impeding ballistic flight, shown in Figure 4.18. This mass could not be quantified by mapping, even if field time was unlimited. ~ 12% of the 700 active volcanoes in the world have crater lakes (Rowe et al., 1992) with barriers to clast ejection and mapping accessibility (crater walls, water) which emphasizes the importance of modelling when reconstructing eruption conditions and determining erupted mass.

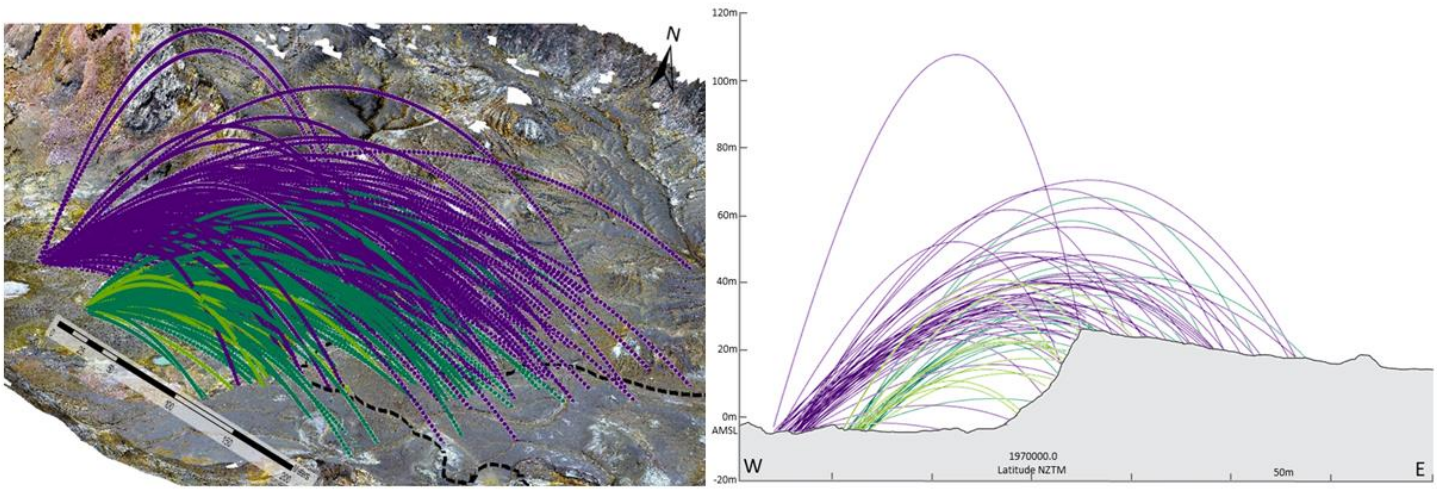

Figure 4.18 Particle trajectory figures. Dark purple represents Pulse 6, Dark Green Pulse 5 and Light Green Pulse 4. Reduced number of particles for figure clarity, number remains proportional to that modelled. Left: 3D trajectories, 100 particles P6, 46 for Pulse 5, 20 for Pulse 4. Created in ArcScene. Right: 2D trajectory figure showing 50 particles for Pulse 6, 23 for Pulse 5, 10 for Pulse 4. Created by Dale Cusack, edited by myself.

4.5.1.3. Kinetic energy of ballistics

Two scenarios were developed and modelled to estimate the reasonable range of kinetic energy released by ballistics during the April eruption. A single burst eruption where all blocks were emplaced at once to determine the maximum Kinetic energy (E_k), and a multi-burst eruption based on the three largest acoustic signatures for a minimum E_k. The calculated kinetic energy, based on the average ejection speed and ballistic mass ranged from ~3.13×10^7J - ~2.07×10^7J (Table 4.2). When compared to the calculated E_k of Te Maari's 2012 eruption from Ballista modelling, ~1.7×10^{10} J, the energy released from ballistics during the Whakaari eruption was 3 magnitudes smaller, less than 0.2% of Te Maari's energy. This is consistent with the comparatively small size of the Whakaari ballistic field (<400m travel distances vs 2.3km distance at Te Maari), and the higher initial velocities at which the Te Maari clasts were ejected (<70m/s at Whakaari, 200m/s at Te Maari). Had the kinetic energy release from erupted blocks been determined solely on the deposits mapped, the erupted blocks that did not overtop the inner crater wall would have been used for calculations, significantly underestimating the ballistic contribution to the overall energetics of the April Whakaari eruption. This further emphasizes the need for modelling to estimate the unmappable portions of the ballistic deposit, e.g. inside the crater, for eruption dynamic studies.

4.5.2 Ballistic Hazard

4.5.2.1. Hazard Footprint

The ballistic hazard footprint of the 27 April eruption was small compared to other phreatic eruptions in the literature, however consistent with small Whakaari eruptions in the past. The edge of the field was mapped as a maximum of ~380m from the furthest vent, with blocks up to 5cm in diameter

mapped to ~320m (Figure 5.12 A, B). The single burst scenario modelled blocks landing up to 513m away (most impacted within 450m from the vent) covering a total area of 137,988m^2 while the multiburst model ejected blocks to ~390m (majority within 320m) covering between 60670 m^2, 61146 m^2 and 95230m^2 for pulses 4, 5 and 6 respectively. The distance blocks reached is under half that of other phreatic eruptions in the literature; maximum distance clasts reached at Ontake (2014) was 1km, Te Maari (2012) 2.3km, Ruapehu (2007) ~2km (Kilgour et al., 2010; Fitzgerald et al., 2014, Kaneko et al. 2016). This indicates the ballistic study at Whakaari to be an important dataset for informing reasonable small phreatic eruption parameters.

Phreatic eruptions from Whakaari have erupted small muddy blocks in bubble burst style eruptions to 32.5m (Edwards et al., 2016) and eruptions in 2013 ejected clasts "onto the crater floor" (Global Volcanism Program, 2014). A phreatic eruption in 1989 ejected blocks to a minimum of ~150m (Global Volcanism Program, 1989) and a sketch map of a block field from the 19 October 1993 eruption at Whakaari shows blocks reaching ~500m (Figure 4.19) (Global Volcanism Program, 1993). These previous examples demonstrate that small phreatic eruptions of a similar magnitude to the 27 April eruption are common at Whakaari and should be included in ballistic hazard and risk assessments. The eruption parameters derived from this study are therefore of use to future workers creating probabilistic background ballistic hazards assessments.

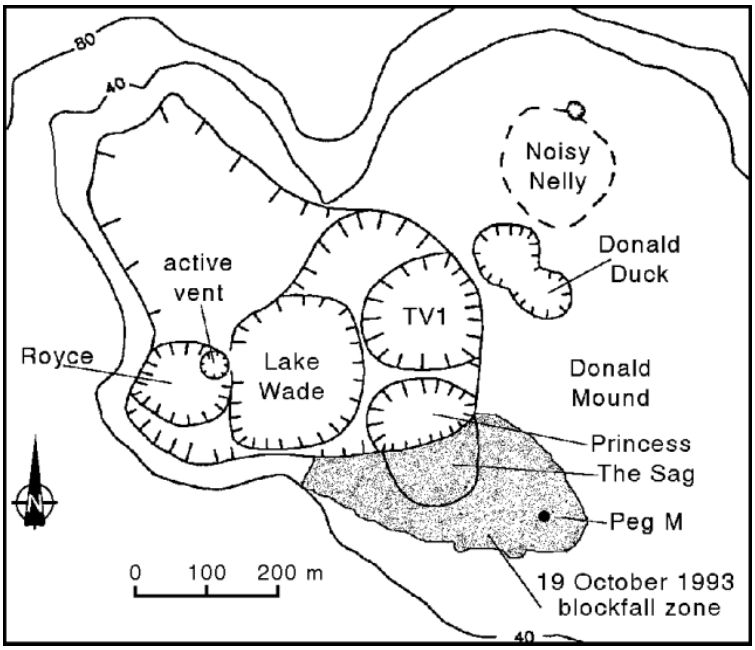

Figure 4.19 Sketch map of the 1978/90 crater complex of Whakaari showing block field. The modern crater lake is larger than in 1993 due to progressive crater rim collapse, but the block field can still be viewed in relation to Donald Mound. Image from IGNS,sourced ,sourced from Global Volcanism Programme (1993).

4.5.2.2. Ballistic Hazard Intensity

When undertaking modelling for hazard assessment purposes, the output needs to determine the spatial extent of the hazard and the intensity of the hazard within that space, specifically in terms of relevant hazards intensity measures and ideally probabilities of impact (Fitzgerald et al., 2017). For ballistic hazard the most important metric is impact energy (Tsunematsu et al., 2016). Williams (2017) found impact energy to be the most relevant metric for assessing risk to buildings and infrastructure. For life safety calculations a lethality threshold of missiles to humans of >80 J (Baxter & Gresham, 1997) is currently used within best practice to calculate likelihood of casualty from ballistic impact (Fitzgerald et al., 2017). A 2m width track was used to assess impact of eruption on the pathway used by visitors, due to possible divergence of tourists from this path the 2m width is likely a conservative area. The pathway mapped was obtained from Google street viewer and validity of track placement was judged by two colleagues who had travelled to the island to be approximately correct.

The total ballistic hazard footprint from the single burst model scenario was 137,988m^2 with 1114m^2 of the track impacted by 5642 ballistics with E_k ranging from 53-6925 J (Figure 4.20). Blocks up to 16cm in diameter with masses up to 4.9kg hit the pathway at an average velocity of 40.4m/s and impact energy of 1350 J (average). 21% of the track (817m/3948m) is within the area of hazard, and using the 80J human lethality threshold, 42% of the pathway is lethal within the hazard area

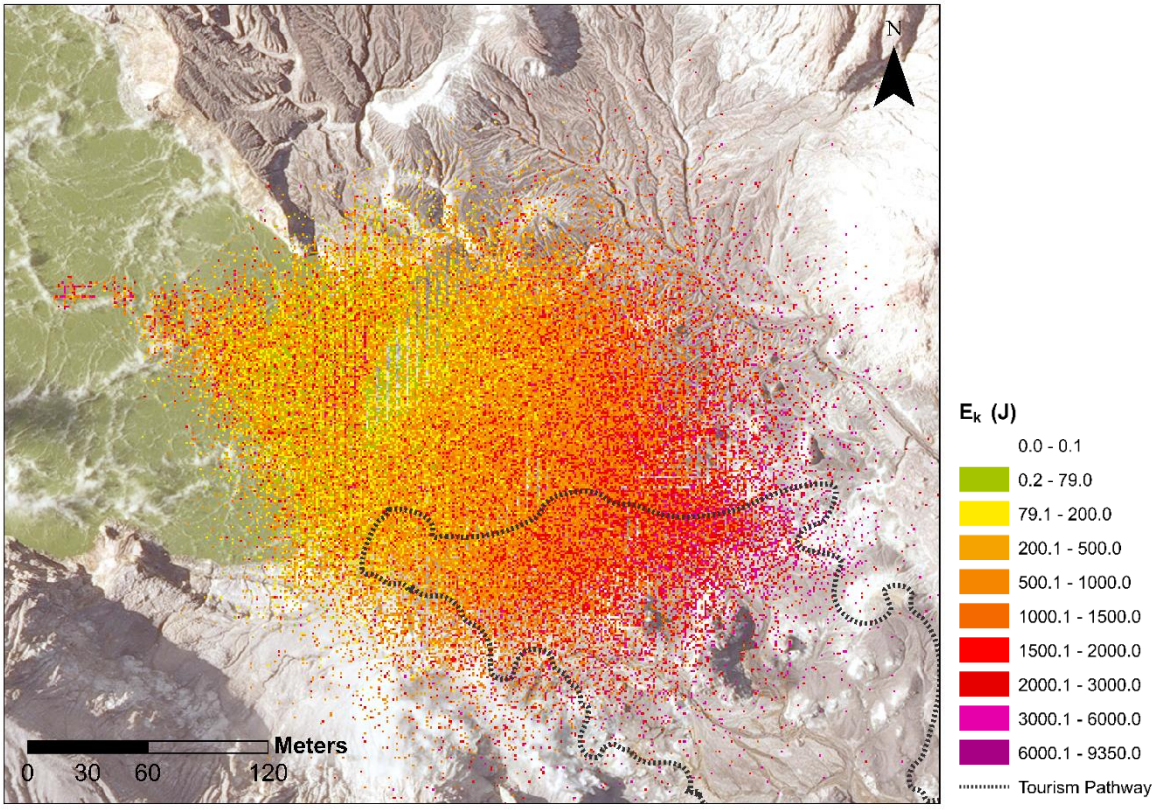

Figure 4.20 Single burst scenario hazard intensity. Average impact energy per m2 modelled. For spatial intensity, (blocks/m^2) see figure 15A.

(1101m^2/2597m^2). The single burst scenario demonstrates the hazard intensity that may have been

derived from modelling without seismo-acoustic data or recognition of the significance of variable coating of blocks by surge material, to support a three-pulse eruption. The better fitting multi-burst scenario, when coupled with timing based on acoustic signals allows the development of a four-dimensional hazard scenario with varying hazard intensity through time.

The modelled hazard scenario is as follows. Using seismo-acoustic data from Walsh et al. (in review) our eruption scenario consists of 6 separate pulses (Table 4.1). The first three eruptive pulses may have ejected blocks, which did not overcome the inner crater wall, therefore not posing a hazard nor contributing to the ballistic field (Figure 4.21).

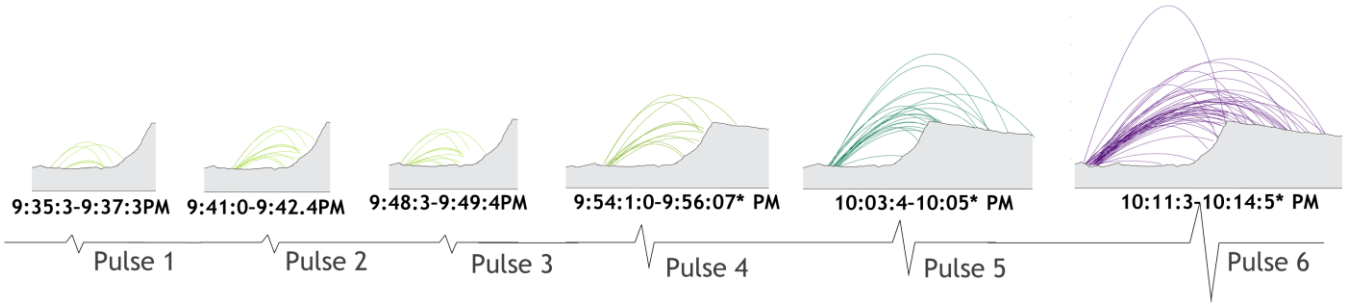

Figure 4.21 Modelled eruption sequence. Pulses 1,2,3 omitted from modelling as blocks did not leave the inner crater duration of pulse from seismo-acoustics. Pulses 4,5,6 modelled, with eruption duration based on initiation of acoustic signal, to ~ time of last ballistic impact (see Appendix 1B for timing calculations).

Pulse 4 occurred at ~9:54pm NZST erupting blocks at initial speeds of 50 ±5m/s, the last of which hit the ground at ~9:56pm (see appendix 1B for timing). 576 blocks hit the pathway over ~2 minutes with up to 7blocks/m^2 at an average velocity of 34.16m/s (Figure 4.22A). 8% of the pathway was hit with blocks >80J (Baxter & Gresham (1997) fatality threshold), and 27% of the pathway within the area of hazard impacted by blocks >80J energy (Figure 4.22B).

At 10:03pm Pulse 5 erupted with 4316 blocks hitting the pathway, up to 29b/m^2, over the ~1 minute ballistic shower (Figure 4.22C) at average impact speeds of 35.8m/s. The area of pathway hit with blocks >80J more than doubled from Pulse 4 to 19% of the total pathway, and 66% of the path within the area of hazard (Figure 4.22D). The intersection of the eruption lobe axis with the pathway leads to high hazard intensity.

At 10:11pm the largest pulse, 6, ejected blocks over ~3 minutes. Pulse 6 erupted the greatest number of blocks, however almost the same impact on the tourism pathway as Pulse 5 as the bearing of Pulse 6 is orientated 4° northward, so the eruption axis does not intersect with the pathway as significantly.

A total of 2582 blocks hit the pathway, a maximum of 13b/m^2 (Figure 4.22E). 19% of the pathway was hit with blocks >80J, also 65% of the area of hazard (Figure 4.22F).

The modelled scenario demonstrates how hazardous small phreatic eruptions are at Whakaari due to the high spatial density of impacts and high impact energy of blocks. Inverse modelling which can provide detailed information on the changing hazard footprint and intensity over time, could be powerful tool for risk managers. Combined with agent-based modelling (e.g. Mas et al., 2015), datasets like this may provide information for risk managers to consider when providing life safety advice.

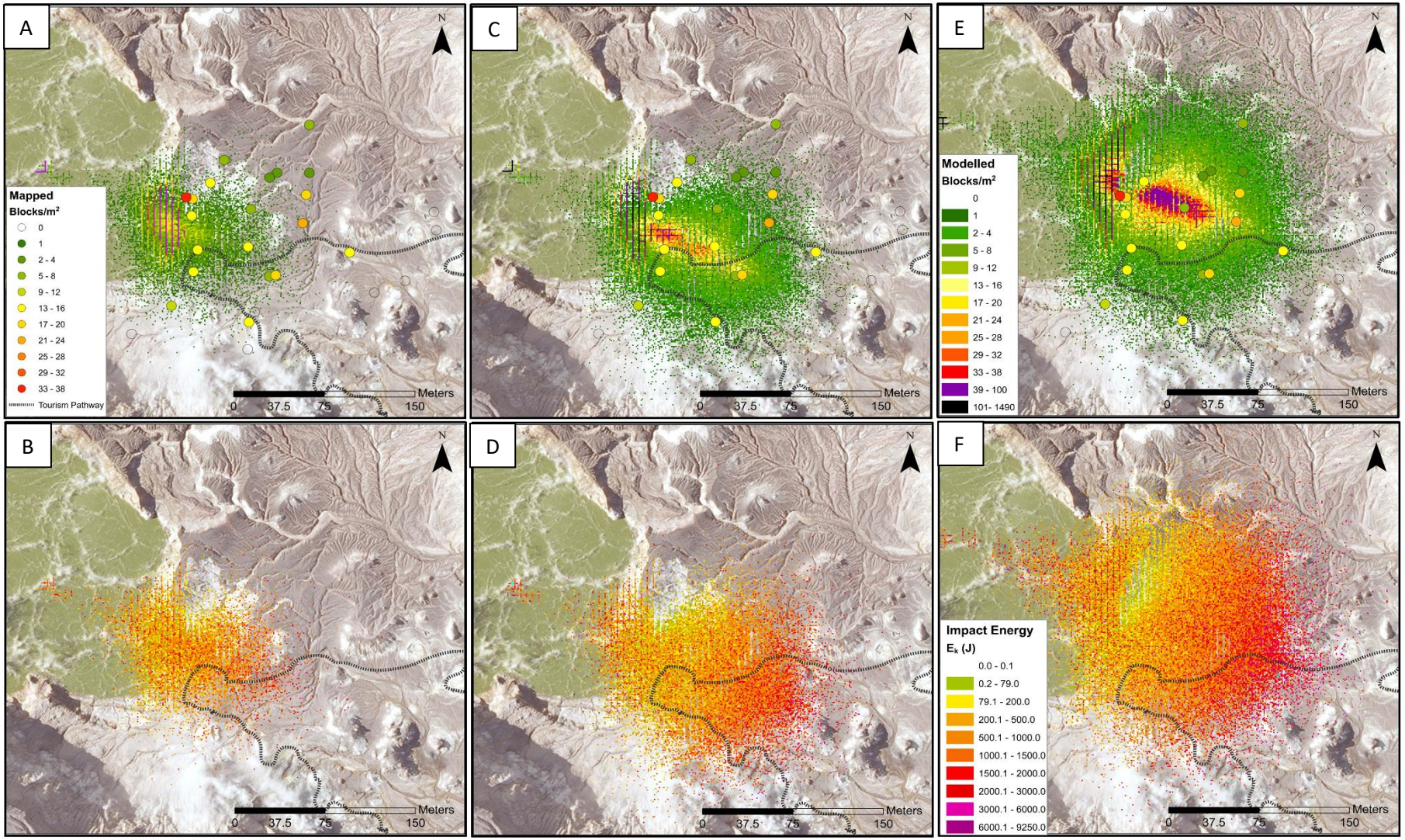

Figure 4.22 Ballistic hazard scenario through time, spatial intensity shown in upper panels, impacted blocks/m2. Impact intensity, average impact energy per m2 shown in lower panels. A) & B) Pulse 4, C) & D) Pulse 5, E) & F) Pulse 6.

4.5.2.3. Vertical ballistic hazard

The hazard posed to aircraft by airborne ash is well known (e.g. Bonasia et al., 2012) however ballistics are also a risk to aircrafts close to a volcano during an eruption (Alatorre-Iberguenoitia et al. 2010, 2012, 2016; Bertin, 2017) and relevant to Whakaari due to the daily helicopter tours that frequent the crater. The computational load of exporting trajectory files for 447800 particles is prohibitive, therefore the vertical ballistic hazard was determined based on simulations of 3000 particles for each eruptive burst. As Figure 4.18 shows, most clasts modelled did not reach heights greater than 80 m. The maximum height ballistics reached per pulse, from smallest to largest was: 82.5m, 85m and 111.4m for Pulses 4, 5, 6 respectively. As shown in Figure 4.18, clasts with eruption source parameters sampled from the edges of the probability distribution may pose a hazard outside of the primary ballistic hazard zone. This was also found from the 2012 Te Maari eruption, where a single ballistic penetrated the ice at Blue Lake, Tongariro, significantly outside of the main mapped ballistic hazard area (Fitzgerald et al., 2014; Bread et al., 2014; B Christenson, Personal communications 2018). The integration of the vertical ballistic hazard into a ballistic hazard assessment at Whakaari is important for fully informing tour operators of the hazard to aircraft.

4.5.3. Discussion summary paragraph

This work has shown how careful coupling of mapped ballistic distribution data, seismo-acoustics and 3D numerical modelling can provide a plethora of information on the eruption dynamics and ballistic hazard through time. The poor relationship between distance from vent and clast size supports a syn-eruptive surge and the dominance of small clast sizes emphasises the importance of a mapping approach that is capable of measuring clasts down to ~2cm in diameter. Through developing two end member scenarios a range of reasonable eruption characteristics have been found. The range of total ballistic mass and kinetic energy release from ballistics has been informed by modelling and shown the importance of modelling when field areas such as inner craters restrict the data available from mapping. A 4D ballistic hazard assessment shows how the ballistic hazard changed throughout the Whakaari eruption and the pathway was variably impacted with both the directionality and size of the eruptive burst influencing the impact on the tourism pathway. Small phreatic eruptions at Whakaari therefore pose a notable hazard to visitors.

4.6. Conclusions

The 27 April 2016 eruption at Whakaari was successfully inversely modelled based on detailed spatial density mapping, integration of seismo-acoustic data and end member scenario development. The eruption was found to consist of three ballistic producing, highly directed, pulses with low ejection angles of 30° from horizontal. Bursts ejected blocks at speeds between 45 and 65m/s (s.d. 5m/s), with blocks impacting up to 395m from the vent. The mapped size distribution with distance supports field

evidence for at least one syn-eruptive surge and indicates the multiple concurrent hazards present during the eruption. The area where the >18,000 annual tourists, guides and monitoring scientists frequent was impacted by high energy blocks with up to 21% of the tourism pathway hit by blocks with sufficient impact energies to cause serious injury or death. The modelling results suggest that even small eruptions at Whakaari pose a potentially lethal hazard.

This is the first known occasion in which detailed mapping of the spatial density within a ballistic field as well as the field outline has been used to validate the eruption source conditions of a phreatic eruption through multiparticle, 3D numerical modelling (Figure 4.23). The ability of a rapid handheld photography mapping approach coupled with an appropriate 3D numerical model to inversely model a multi eruption scenario has been demonstrated through; 1) mapping indicating pyroclastic surges were synchronous with ballistic ejection; 2) end member scenarios providing a range of reasonable eruptive parameters; 3) ~30% of modelled ballistic mass not being preserved/mappable because of the presence of a crater lake suggesting the importance of a combined mapping and modelling approach; 4) the development of a time variable ballistic hazard footprint and intensity assessment which is directly useable in risk assessments.

Despite the limitations of the time restricted mapping and modelling this work has made several important findings for future comprehensive ballistic and multi-phenomenon hazards assessments at Whakaari and provides crucial data for assessing the risk to visitors. Had modelling been excluded and field data alone informed the hazard footprint, only the spatial extent and small areas of hazard intensity would be known. Modelling has produced important hazard metrics, such as impact energy, spatial variation throughout the whole field and how these vary through time. This is important information for risk assessors for potential use in agent-based modelling when evaluating risk to persons and potential shelters or other mitigative action (Mas et al., 2015). Finally, this study provides much needed additional data on phreatic eruption conditions.

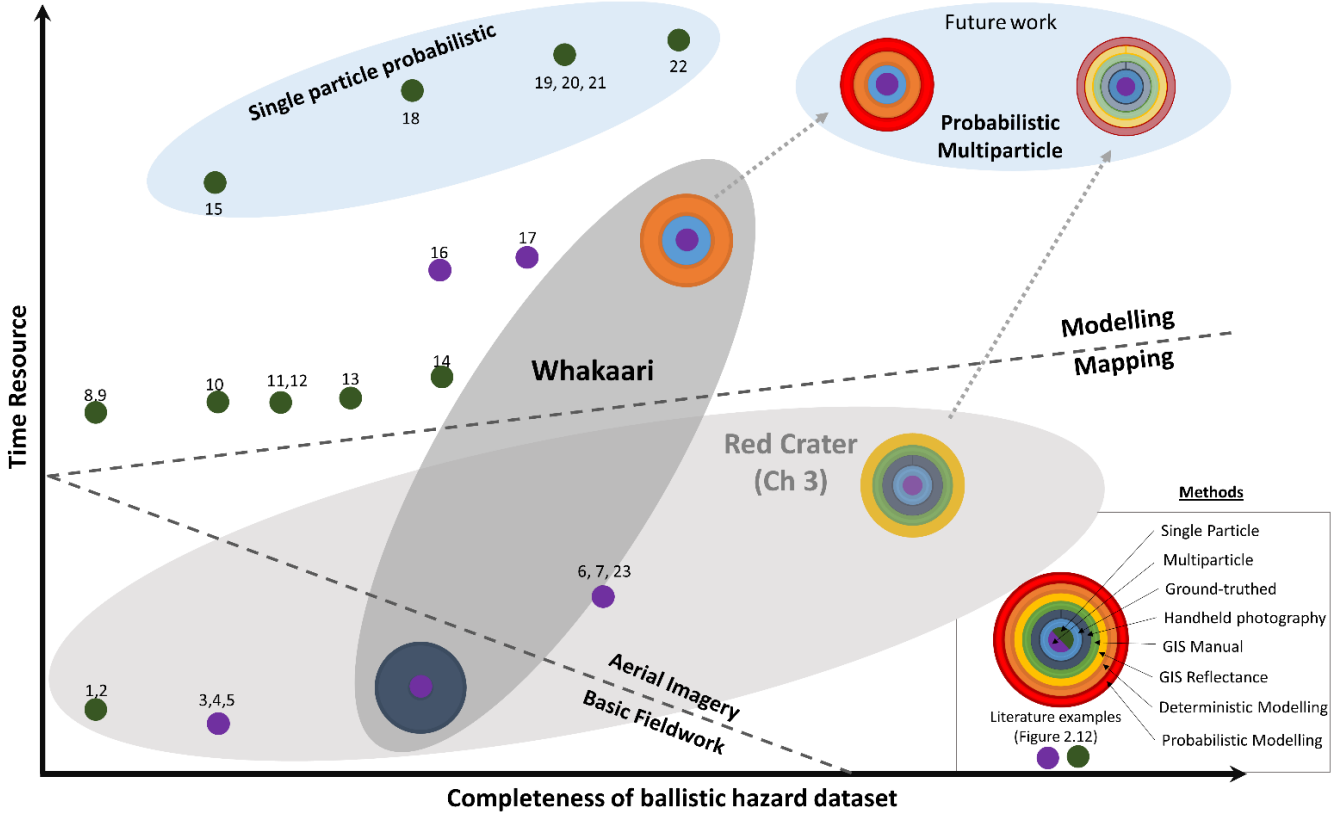

Figure 4.1 Conceptual diagram relating the ballistic study of the April Whakaari eruption to literature studies. This study is located as a more complete ballistic hazard dataset than previous multiparticle model studies (16 – Te Maari (Fitzgerald et al., 2014) and 17 – Ontake (Tsunematsu et al., 2014)) as at Te Maari only the ballistic field edge was used to fit the models and at Ontake only blocks of 20cm diameter were modelled. This study has used both the field outline and spatial density to find the best fit.

5 SUMMARY DISCUSSION AND CONCLUSIONS

5.1 Introduction

The most pressing use of ballistic distribution information, at volcano-tourism destinations prone to phreatic eruptions, is for risk assessment to calculate the likelihood of impact, casualty or death and structural penetration (Fitzgerald et al., 2014; Biass et al., 2016; Williams et al., 2017). For this purpose, hazard assessments must provide ballistic distribution information; the distance ballistics reach, the number of blocks impacting the ground, impact energy and spatial density of blocks. The aim of this thesis has been to work towards better ballistic hazard assessments for improved assessment of ballistic risk by improving characterisation of mapped ballistic distribution information (spatial distribution, extent, size distribution) and modelled ballistic hazard intensity (impact energy, spatial density of ballistic impact, evolution of hazard intensity through time). To achieve the thesis objectives gaps have been identified in current methods of ballistic hazard assessment through a comprehensive literature review (Chapter 2) and used phreatic case studies to demonstrate that careful combination of datasets can improve both completeness of ballistic mapping and detail of deterministic modelling (Chapters 3 and 4). Additionally, the case studies have demonstrated the power of handheld photography for measuring small clasts which make up a significant portion of ballistic deposits, particularly phreatic eruptions, and pose a substantial hazard, yet are frequently excluded from mapped ballistic size distributions. This chapter summarises the main findings of the thesis and demonstrates how the methods developed can produce exceptionally detailed ballistic attribute datasets for integration into comprehensive multiparticle modelling. This chapter addresses the final objective of this thesis by developing a guide for location appropriate ballistic mapping techniques and application of ballistic modelling, to assist future ballistic hazard assessments.

Firstly, a review of the major findings of chapters 3 and 4 will demonstrate how the techniques developed have improved the ballistic hazard information available to risk managers. Then a discussion of field attributes, resources and study intention are used to frame a simple guide for consideration when embarking on a ballistic hazard study.

5.2 Improving ballistic hazard information

To date, ballistic hazard assessments have been limited by incomplete mapping methods through field and resource constraints, leading to a reliance on probabilistic modelling techniques for useful ballistic hazard information for risk management (Figure 5.1). Multiparticle, probabilistic modelling of ballistic distribution is ideal, but has so far been limited by the time taken to fit multiparticle scenarios to

mapped distributions (Fitzgerald et al., 2014; Tsunematsu et al., 2016). This section demonstrates how this study has made the goal of probabilistic, multiparticle modelling more accessible.

Chapter 3 considered four ballistic particle mapping methods and identified two, handheld photography or GIS Reflectance, which, when calibrated with ground-truthed field data, can create detailed ballistic distribution maps. Most importantly, the techniques cover large portions of the total ballistic field, relative to other methods, and sample both the total size distribution and spatial variation of ballistics. While these techniques may be applied to any type of ballistic field, the identification of clasts down to 5cm in diameter particularly enhances the mapping of phreatic block fields, in which the majority of the ballistics are <10cm in diameter. Compared to previous studies (Figure 5.1), these techniques allow a more complete ballistic hazard dataset has been obtained through sampling both the size distribution and spatial distribution. By comparing a variety of methods at a single field location, the benefits and limitations of each have contributed to a mapping guide (Section 5.3) for recommended methods based on field site, decision making context (crisis vs background) and resource limitations.

The combination of methods undertaken at Whakaari (Chapter 4) maximised the potential of a limited dataset. All the field data available was utilised; the sharpness of the field edge, the shadow zone behind Donald Mound and the highly variable spatial densities within the field. The addition of geophysical data and an inner crater digital elevation model supported field evidence and further constrained the number of eruptive bursts, vent locations and directivity. A single particle modelling approach would have been able to consider some of these variables; the topographic shadowing, the maximum distance blocks reached and directivity, but not the spatial density variations within the field, or to separate out the three eruptive burst scenarios which combined to fit the total field distribution. Thus, the use of a multiparticle ballistic hazard model constrained the possible combination of eruption parameters in a way that a single particle model could not, creating a more complete ballistic hazard dataset.

Ballistic hazard assessments which seek to inform risk assessments should ideally provide data on the maximum distance ballistics reach, the number of ballistic impacts, impact energy and spatial density, to allow risk to persons, buildings and infrastructure to be fully quantified (Fitzgerald et al., 2017). A single particle model can provide information on some of these variables, but only using a probabilistic approach which requires a large number of iterations to obtain results (e.g. 10^6 Biass et al., 2016 & Bertin 2017). Crucially, they do not provide the number and spatial density of blocks impacting the

ground from a single eruption. Recent ballistic risk assessment studies have identified the utility of evaluating the risk to life safety considering a realistic scenario of multiple ballistic impacts within specific spatial and temporal domains, and to consider both direct impact and secondary impact from shrapnel or cratering debris (Pistolesi et al., 2008; Fitzgerald et al., 2016). Multiparticle approaches are much better suited to producing this dataset than single particle models. Additionally, multiparticle scenarios informed by geophysical data allow the creation of a 4D hazard footprint, which provide insight into how the hazard changes through time. This modelling has the potential to greatly assist risk management planning, such as informing evacuation route selection – particularly if combined with human behavioural models (e.g. agent based models, Mas et al., 2015) and protective shelters design and siting (Tsunematsu et al., 2016). As such, probabilistic, multi-particle models, combined with robust input parameters, potentially offer the most comprehensive hazard assessments which this study has bought closer (Figure 5.1).

A challenge of ballistic hazard assessments, like many natural hazard assessments, is there tends to be a trade-off as the more accurate, complex and complete the hazard assessment, the greater the resources, time and expertise required. An attempt to summarise this for ballistic hazard assessment methodologies from previous studies has been presented in Figure 1. Ideally, the time and effort used in a ballistic hazard assessment should be optimised for the need, yet there is little guidance for this when it comes to ballistic hazard assessments. For example, in times of volcanic unrest or post eruption, access to an area may be restricted, but economic drivers may pressure reopening (Jolly et al., 2014) and therefore rapid hazard assessment methods are crucial for risk managers calculating if risk is acceptable. This thesis has demonstrated that handheld photography is a valid way of rapidly collecting field data and, if available, UAV imagery and basic GIS tools can substantially decrease mapping time required while obtaining large, accurate datasets. Additionally, the compatibility of GIS based multiparticle mapping and multiparticle modelling techniques can be easily coupled and rapidly analysed. Additionally, inverse multiparticle modelling of ballistic distributions has to date been largely completed by qualitative judgement or based on very limited data (e.g. Tsunematsu et al., 2016) and without variation in spatial densities considered (Fitzgerald et al., 2014). This is both time intensive and subjective. The developed reflectance method within this thesis has been shown to allow much more rapid comparison and fitting of multiparticle ballistic models outputs with measured ballistic deposit distributions. The subsequent reduction in computational time can allow a greater number

of model iterations to be completed and/or more rapid hazard assessments for informing risk management decisions.

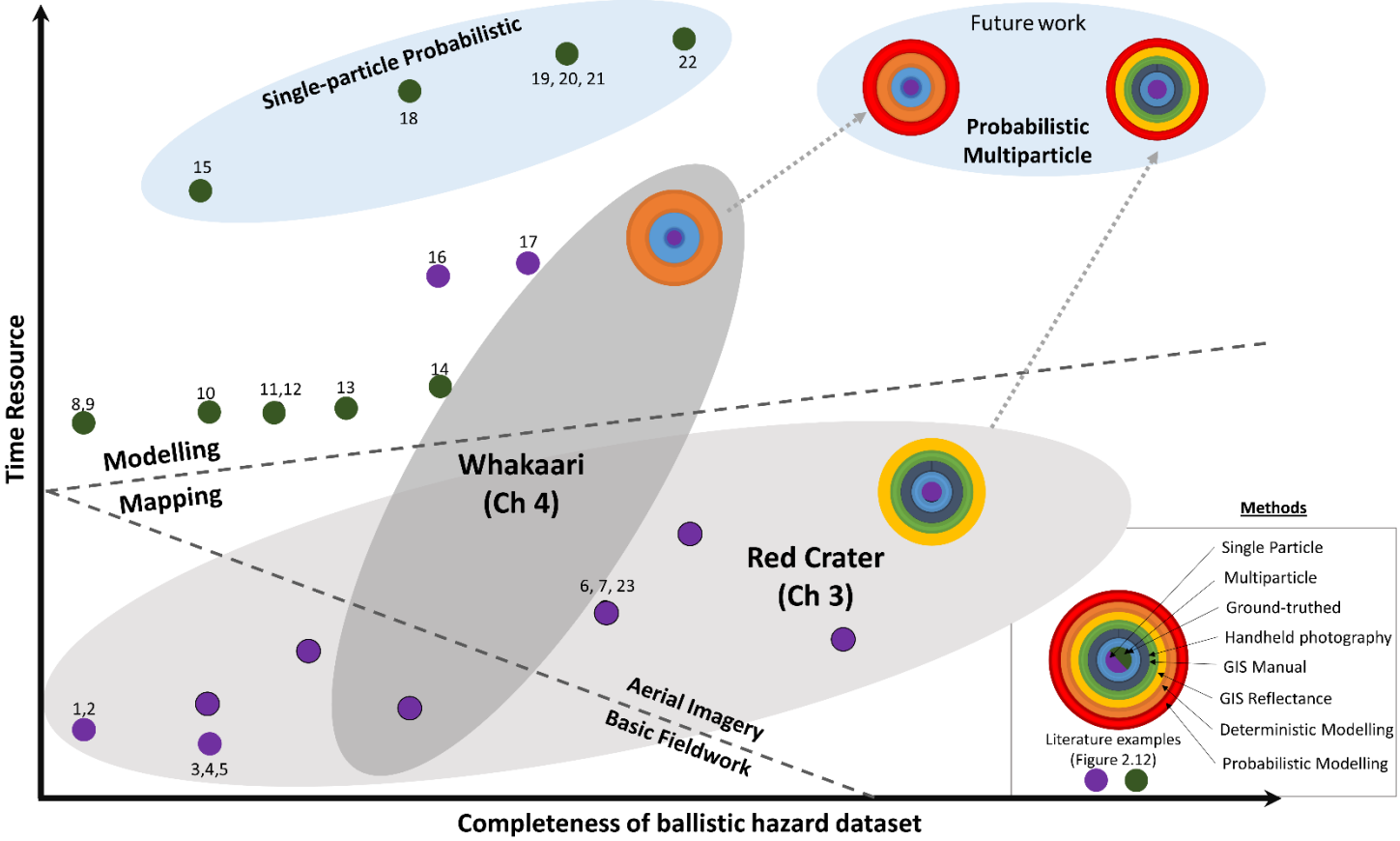

Figure 5.1 Ballistic mapping and modelling methods used in this thesis, compared to literature examples, sorted based on time resource and completeness of ballistic hazard information. This body of work has increased the completeness of the ballistic mapping with a relatively small increase in time resource, and has increased the detail of information gained through scenario based modelling.

5.3 Guide for future ballistic hazard assessors

Considering different field characteristics and resources, a simple guide has been developed to help ballistic hazard assessors gain the most useful information possible using the smallest amount of resources in both crisis and non-crisis assessment environments (Figure 5.2). This guide considers variables including age of deposit, field time available (due to state of unrest, accessibility), access to UAV or high-resolution imagery, and visible contrast between erupted blocks and underlying lithology. Also of importance but not explicitly included is type of eruption and consequent total size of the field and average ballistic diameter.

On the left of the guide flow chart (Figure 5.2) is the suggested mapping approach for non-recent ballistic deposits, where the blocks or bombs are not on the present ground surface. Collecting complete ballistic datasets of non-recent deposits is challenging with less information freely available

due to frequent burial of ballistics from deposition of later eruptive products and erosion (Lorenz, 1970; Biass et al., 2016; Fudali & Melson, 1971). As such, a focus on finding the most distal clasts possible will provide some information for single particle modelling. The high uncertainty due to the small sample number necessitates probabilistic modelling (Alatorre-Iberguenoitia et al., 2006, 2012, 2016; Biass et al., 2016; Bertin, 2017). If the field outline is mapped, a multiparticle model can then be applied (e.g. Fitzgerald et al., 2014) although this entails high uncertainty on ballistic size distribution. If field time allows, and if the ballistics are accessible, a few locations where the ballistic stratigraphic layer can be uncovered and an estimate for the spatial density and total size distribution can inform multi-particle modelling.

For recent eruptions where the ballistic field is on the ground surface, mapping is considerably simpler and more complete datasets are limited mainly by resourcing constraints (right and central Figure 5.2). Ideally fieldwork would be unlimited in time or have many people involved allowing extensive ground-truthed field sampling and handheld photography. Additionally, high-resolution imagery would be available for either GIS Reflectance, if applicable, or GIS Manual mapping of the field. Realistically, field time is always limited and a combination of carefully selected ground-truthed locations and either handheld photography or a GIS mapping method is the best way to ensure the field area is representatively sampled (Figure 5.2). Ground-truthed locations should be selected based on: variable distances and directions from vent/s, changes in underlying lithology, and changes in burial from syn-eruptive material (e.g. Whakaari, Chapter 4; Kaneko et al., 2016), to ensure errors based on different field variables/locations are reduced or quantified.

It is crucial to carefully consider, (1) the field site in question, (2) the time, for both field and desktop analysis, and (3) the technological resources available, when choosing methodologies for ballistic hazard assessments. The purpose of the study, eruption dynamics or risk assessment, will also determine the level of detail and if full probabilistic modelling is required.

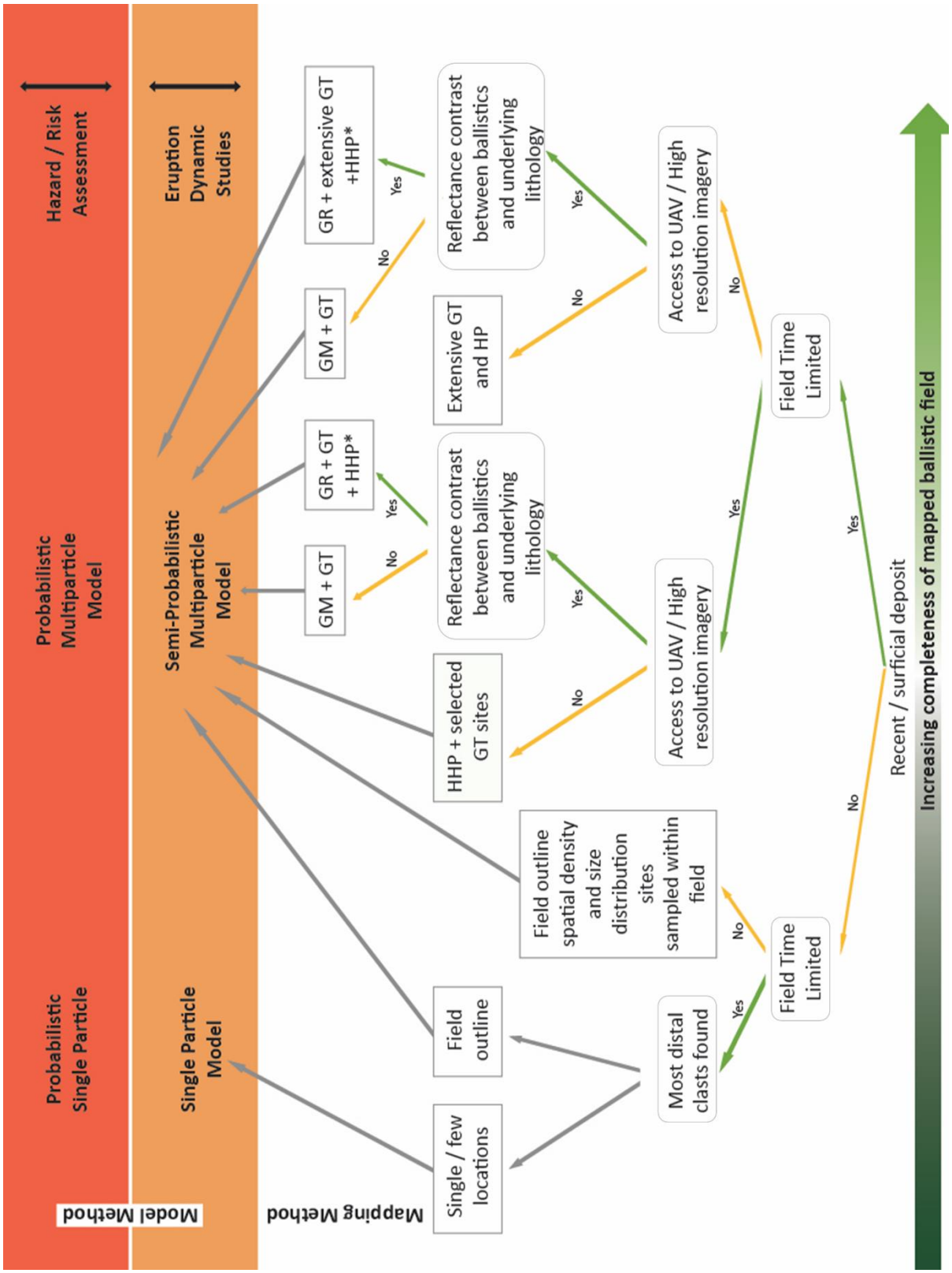

Figure 5.2 A flowchart guide for ballistic mapping methods. Abbreviations as follows: GT = Ground-truthed, HHP = Handheld Photography, GM = GIS Manual, GR = GIS Reflectance, HHP* = collection of handheld photography which may be used to extend dataset, or as a backup if GIS Reflectance is not successful.

5.4 Conclusions

The aim of this thesis was to evaluate current best practice for ballistic mapping and modelling, to inform appropriate hazard assessment choices at two phreatic ballistic fields in New Zealand and work towards more informative/risk applicable ballistic hazard assessments. This aim has been achieved by completing the objectives stated in Chapter 1. Best methodological practice for ballistic hazard assessments and knowledge gaps in the literature were reviewed (Chapter 2). A comparison of four different mapping techniques at Red Crater, Tongariro, including the development of a new method, was used to assess the efficacy and efficiency of ballistic data collection at a phreatic block field (Chapter 3). Chapter 3 provided support for the handheld Whakaari mapping method and an identification of the specific sources of uncertainty. The lack of previous comparative ballistic mapping studies for the April 2016 Whakaari phreatic block field led to some spatial uncertainty interpreting directly from the handheld photography mapping (Chapter 4). A 3D numerical model, was chosen to compliment the mapping method, and inversely modelled the Whakaari eruption using photographed spatial densities, geophysical and digital elevation datasets. The modelled scenario produced a 4D ballistic hazard footprint and provided constrains on unknown eruptive parameters (Chapter 4). Chapter 5 has presented a guide for use in future ballistic hazard assessments. This research has improved aspects of both ballistic hazard mapping and modelling using phreatic eruption examples and the main conclusions of the research are outlined below.

- A review of the ballistic hazard assessments around the world showed that ballistic hazard assessments are limited from incomplete mapping methods which do not obtain complete size or spatial distribution data.
- Fieldwork and remote mapping comparisons showed handheld photography to be an effective, rapid mapping method which can be highly accurate in obtaining spatial density information. The error associated with using 2D images to measure ballistic size has been quantified with a 9% overestimation of block size at Red Crater, when the highest resolution handheld photography was used to map clasts.
- Remote mapping methods using UAV's are applicable to phreatic block fields, despite the small grain size and high spatial density, provided adequate ground-truthing has occurred to compensate for the underestimation of total block number.
- A simple, accessible and relatively rapid method using basic UAV imagery has been developed and has the potential to obtain complete ballistic hazard datasets with accurate spatial density and size distribution.

- The 27 April 2016 Whakaari eruption scenario shows a highly directed, 3 pulse eruption where clasts were ejected at speeds of 45 - 65m/s^{-1} at low ejection angles of 30° from horizontal.
- A total of 447,800 blocks were erupted in the best fit scenario, with 30% of the modelled ballistic mass not exiting the crater lake at Whakaari. This highlights the importance of modelling when estimating erupted ballistic mass at volcanoes with crater lakes and other impediments to complete mapping.
- Each burst erupted blocks which impacted between 8 - 19% of the tourism pathway with sufficient kinetic energy to cause casualties indicating even small phreatic eruptions pose a risk to life safety.
- A 4D ballistic hazard model produced a time varying hazard map for the Whakaari eruption, demonstrating the strength of multiparticle modelling combined with geophysical datasets to further inform development of appropriate life safety advice.
- The eruption at Whakaari is smaller than any other modelled ballistic field in the literature, and the first in which detailed spatial density variation as well as the field outline is used to validate eruption sources conditions, thus providing essential data in our understanding of the dynamics and hazard of small explosive eruptions.
- The best ballistic mapping method for a study area depends on both field attributes and resourcing availability. Both require consideration when designing a ballistic mapping campaign, for either hazard assessment or eruption dynamic studies, and Figure 5.2 provides a tool to help guide future workers based on the findings from the case studies of Red Crater and Whakaari.

5.5 Limitations Summary

- A full systematic review of mapping methodologies was limited by the resolution and sample size variations between mapping methods. A full discussion of the limitations associated with the mapping methodology is contained in Chapter 3.
- Inverse modelling of volcanic events is always limited by what data is available as well as the ability of the model to replicate complex natural phenomenon. Similarly, deterministic modelling will always produce one possibility out of many. As such, probabilistic modelling is required for a deterministic scenario to be useful for risk managers. Modelling an unwitnessed eruption, with no visual recordings is therefore particularly challenging and the full limitations of data availability are addressed in Chapter 4.

5.6 Summary

Ballistic producing phreatic eruptions are a major hazard to visitors to two of New Zealand's most frequented volcanoes, Tongariro and Whakaari. Recent unheralded, hydrothermal and phreatic

eruptions at these volcanic centres have ejected high velocity ballistics onto tourism pathways. As these eruption types are hazardous but without warning, ballistic hazard assessments are useful for individuals to assess if the risk posed is personally acceptable and for risk managers in decision making(Jolly and Taig et al., 2012). Ballistic distribution mapping and numerical modelling are two crucial aspects of ballistic hazard assessments, however, both have significant limitations which this work has shown to be manageable when complimentary datasets are combined.

Overall, this research has demonstrated that careful consideration of field characteristics and resource availability can allow highly accurate, extensive ballistic mapping and detailed modelling for use in eruption dynamic studies and hazard and risk assessments. This thesis has focussed on phreatic eruptions due to their relevance in the New Zealand volcano-tourism context and the knowledge gap in the literature, however these lessons can be applied to hazard assessments at any type of ballistic field.

5.7 Future work

This study has developed a potentially beneficial mapping method, with which comprehensive ballistic size distributions and spatial distributions can be obtained from aerial imagery, a valuable tool for studies with access to imagery but with limited field time due to risk or accessibility constraints. Further application of the reflectance method to other lithologies and a full exploration of variables such as image wavelength and light conditions is required to fully constrain the methods use.

The time restraints of a MSc thesis, and major uncertainties due to gaps in the eruptive history at Red Crater mean the phreatic block field was used for a methodological mapping comparative study. However, the ballistic hazard in the area and the risk posed to the >140,000 annual users of the Tongariro Alpine Crossing is still not well understood. Future work should include a full probabilistic assessment of ballistic hazard and subsequent a risk assessment to better inform DoC's risk management of the popular walking track.

The scenario developed for modelling Whakaari's 27 April eruption represents a small eruption, and while having the benefit of being a semi-probabilistic modelling method, is not a unique solution and does not contain an associated probability. For this information to be useful for risk assessment, a full probabilistic ballistic assessment, which incorporates the impacts and likelihood of larger eruptions is needed. Future work focussing on the ballistic hazard posed by larger phreatic and magmatic eruptions at Whakaari is needed for integration into a full probabilistic hazard assessment.

The development of a multiparticle mapping method and a technique to compare modelled and mapped spatial densities, provides a new combined approach which may allow rapid processing of modelling results. Both mapping and modelling approach have compatible outputs, allowing the potential for semiautomated comparison and therefore reducing the subjectivity best fit modelling. Further work at other ballistic fields in which a full GIS reflectance to multiparticle modelling process is applied would demonstrate if this can increase the number model iterations and create better deterministic modelling outcomes.

6 REFERENCES

Alatorre-Ibargüengoitia MA, Delgado-Granados H 2006 Experimental determination of drag coefficient for volcanic materials: Calibration and application of a model to Popocatépetl volcano (Mexico) ballistic projectiles. Geophysical Research Letters 33(11): L11302.

Alatorre-Ibargüengoitia MA, Delgado-Granados H, and Farraz Montes IA 2006. Hazard zoning for ballistic impact during volcanic explosions at Volcan de Fuego de Colima (Mexico). GSA Special Papers 402: 209 – 216.

Alatorre-Ibargüengoitia MA, Delgado-Granados H, Dingwell DB 2012. Hazard map for volcanic ballistic impacts at Popocatépetl volcano (Mexico). Bulletin of Volcanology 74(9): 2155–2169.

Artunduaga, A. D. H., Jimenez, G. P. C. 1997. Third version of the hazard map of Galeras Volcano, Colombia. *Journal of Volcanology and Geothermal Research*, *77*(1–4), 89–100. http://doi.org/10.1016/S0377-0273(96)00088-1

Australian/New Zealand Standards (AS/NZS) ISO 31000 2009. Risk Management – Principles and guidelines. Jt Australian New Zealand Standard, superseding AS/NZS 4360: 2004, 37p

Barberi, F., Bertagnini, A., Landi, P., & Principe, C. 1992. A review on phreatic eruptions and their precursors, *52*, 231–246.

Bardsley C 2004. The physical volcanology of red crater. Unpublished thesis. University of Waikato, Hamilton, New Zealand

Baxter P, Gresham A 1997. Deaths and injuries in the eruption of Galeras Volcano, Colombia, 14 January 1993. Journal of Volcanology and Geothermal Research 77: 325– 338.

Bernard, B. 2018 Rapid hazard assessment of volcanic ballistic projectiles using long-exposure photographs: insights from the 2010 eruptions at Tungurahua volcano, Ecuador, *Volcanica*, 1.1 49-61 p

Bertin, D. 2017. 3D ballistic transport of ellipsoidal volcanic projectiles considering horizontal wind field and variable shape-dependent drag coefficients. *Journal of Geophysical Research: Solid Earth*, 1–26. http://doi.org/10.1002/2016JB013320

Berryman K, Villamor P 1999. Spatial and temporal patterns of active faulting in the Taupo Volcanic Zone, New Zealand. Geological Society of New Zealand Miscellaneous Publication 107A: 15.

Bonasia, R., Cosa, A., Folch, A., Macedonio, G., & Capra, L (2012). Numerical simulations of tephra transport and deposition of the 982 El Chichon eruption and implications for haza rd

assessment, Journal of Volcanology and Geothermal Research, 231-323, 39-49, doi:101016/j.jvolgeores.2012.05.006

Biass S, Falcone JL, Bonadonna C, Di Traglia F, Pistolesi M, Rosi M, Lestuzzi P. 2016. Great Balls of Fire: A probabilistic approach to quantify the hazard related to ballistics – A probabilistic approach to quantify the hazard related to ballistics - A case study at La Fossa volcano, Vulcano Island, Italy. J Volcanol Geoth Res. 2016;325:1–14.

Bibby HM, Caldwell TG, Davey FJ 1995. Geophysical evidence on the structure of the Taupo Volcanic Zone and its hydrothermal circulation. Journal of Volcanology and Geothermal Research 68: 29–58.

Birkmann J 2013. Exposure to natural hazards. In: Bobrowsky, PT (ed.) Encyclopedia of Natural Hazards. Springer Netherlands: 305-306.

Black, E., 2001. 27 January, NZ Herald "Eruption leaves 12 meter crater in Rotorua Park" retrieved from https://www.nzherald.co.nz/nz/news/article.cfm?c_id=1&objectid=169944

Blong R J 1984. Volcanic hazards: A sourcebook on the effects of eruptions. Orlando: Academic Press. 424 p.

Blong R 1996. Volcanic hazards risk assessment. In: Scarpa R, Tilling RI eds. Monitoring and mitigationof volcano hazards. New York, USA, Springer: 675-698.

Bower S, Woods A 1996. On the dispersal of clasts from volcanic craters during small explosive eruptions. Journal of Volcanology and Geothermal Research 73: 19–32.

Breard ECP, Lube G, Cronin SJ, Fitzgerald R, Kennedy B, Scheu B, Montanaro C, White JDL, Tost M, Procter JN, Moebis A 2014. Using the spatial distribution and lithology of ballistic blocks to interpret eruption sequence and dynamics: August 6 2012 Upper Te Maari eruption, New Zealand. Journal of Volcanology and Geothermal Research. DOI: 10.1016/j.jvolgeores.2014.03.006.

Brown, S. K., Jenkins, S. F., Sparks, R. S. J., Odbert, H., & Auker, M. R. 2017. Volcanic fatalities database: analysis of volcanic threat with distance and victim classification. *Journal of Applied Volcanology*, *6*(1), 15. http://doi.org/10.1186/s13617-017-0067-4

Browne, P.R.L., Lawless, J.V., 2001. Characteristics of hydrothermal eruptions, with examples from New Zealand and elsewhere. Earth-Sci. Rev. 52, 299–331.

Burby RJ, Wagner F 1996. Protecting tourists from death and injury in coastal storms. Disasters 20(1):49–60

Calder ES, Cole PD, Dade WB, Druitt TH, Hoblitt RP, Huppert HE, Ritchie L, Sparks RSJ, Young SR 1999. Mobility of pyroclastic flows and surges at the Soufriere Hills Volcano, Montserrat. Geophysical Research Letters 26(5): 537 – 540.

Carter L 1980. NZ regional bathymetry 1:6,000,000 (2nd ed.). NZ Oceanographic Institute Chart. Misc. Series 15. Department of Scientific and Industrial Research, Wellington, New Zealand.

CDEM Act, 2002. Civil Defence Emergency Management Act. http://www.legislation.govt. nz/ (accessed 8 August 2017).

Chardot, L., Jolly, A. D., Kennedy, B. M., Fournier, N., & Sherburn, S. 2015. Using volcanic tremor for eruption forecasting at White Island volcano (Whakaari), New Zealand. *Journal of Volcanology and Geothermal Research*, *302*, 11–23. http://doi.org/10.1016/j.jvolgeores.2015.06.001

Christenson BW, Britten K, Mazot A, Fitzgerald J 2013. The 2012 eruption of Te Maari: Pre- and post-eruption gas signatures from the magmatic-hydrothermal system. Taupo District Council Offices, Turangi, New Zealand: Te Maari day - a workshop to discuss scientific advances from the 2012 Te Maari eruptions, 22 Mar 2013. In: GNS Miscellaneous Series 66.

Christenson, B., White, S., Britten, K., Scott, B., (2017), Hydrological evolution and chemical structure of a hyper-acidic spring-lake system on Whakaari/White Island, NZ, *J. Volcanol. Geotherm. Res*., 346:180--211.

Civil Defence 1995. Volcanic Hazards in New Zealand, *Tephra* 14.2 retreived on 05/05/2018 https://www.civildefence.govt.nz/assets/Uploads/publications/tephra-october-1995.pdf

Cole, J. W. 1970. Structure and eruptive history of the Tarawere Volcanic Complex. New Zealand Journal of Geology and Geophysics, 13(4), 879-902, doi:10.1080/00288306.1970.10418208

Cole JW, Lewis KB 1981. Evolution of the Taupo-Hikurangi subduction system. Tectonophysics 72:1-21.

Cole JW, Nairn IA 1975. Catalogue of the active volcanoes and solfatara fields of New Zealand. International Association of Volcanology and Chemistry of the Earth's Interior, Rome, Italy: Catalogue of the active volcanoes of the world including solfatara fields, 22: pp. 156.

Cole JW 1978. Andesites of the Tongariro volcanic centre, North Island, New Zealand. Journal of Volcanology and Geothermal Research 3: 121- 153.

Cole JW, Graham IJ, Hackett WR, Houghton BF, 1986. Volcanology and petrology of the Quaternary composite volcanoes of Tongariro Volcanic Centre, Taupo Volcanic Zone. Bulletin - Royal Society of New Zealand 23: 224 – 250.

Cole, J.W.; Nairn, I.A.; Houghton, B.F.; 1996 Volcanic hazards at White Island. 2nd ed. [Palmerston North, NZ]: Ministry of Civil Defence. *Volcanic hazards information series 3.* 27 p

Cole, J. W., Thordarson, T., & Burt, R. M. 2000. Magma Origin and Evolution of White Island (Whakaari) Volcano, Bay of Plenty, New Zealand. *Journal of Petrology*, *41*(6), 867–895. http://doi.org/10.1093/petrology/41.6.867

Cole JW 1990. Structural control and origin of volcanism in the Taupo volcanic zone, New Zealand. Bulletin of Volcanology, 52: 445–459.

Coombs, M. L., McGimsey, R. G., & Browne, B. L. 2008. Preliminary Volcano-Hazard Assessment for Gareloi Volcano , Gareloi Island , Alaska. *Scientific Investigations Report*, *5159*, 5159.

Cowan J 1927. The Tongariro National Park, New Zealand. Tongariro National Park Board, Wellington. 156 p.

Crozier MJ, Glade T 2005. Landslide hazard and risk: issues, concepts and approach. In: Glade, T, Anderson, MG, Crozier, MJ, eds. Landslide hazard and risk. Chichester, England, Wiley. 802 p.

Crouch J, Pardo P, Miller CA 2014. Dual Polarisation C-Band Weather Radar Imagery of the 6 August 2012 Te Maari Eruption, Mount Tongariro, New Zealand. Journal of Volcanology and Geothermal Research. DOI: 10.1016/j.jvolgeores.2014.05.003.

Cutter SL 2013. Vulnerability. In: Bobrowsky, PT ed. Encyclopedia of Natural Hazards. Springer Netherlands: 1088-1090.

Delgado-Granados H, Cardenas Gonzalez L, Piedad Sanchez N 2001. Sulfur dioxide emissions from Popocatepetl volcano (Mexico): case study of a high-emission rate, passively degassing erupting volcano. Journal of Volcanology and Geothermal Research 108: 107–120.

Deligne, N. I., Jolly, G. E., Taig, T., & Webb, T. H. 201. Evaluating life-safety risk for fieldwork on active volcanoes : the volcano life risk estimator (VoLREst), a volcano observatory ' s decision-support tool, 1–19.

DeMets C, Gordon RG, Argus DF, Stein S 1994. Effect of recent revisions to the geomagnetic reversal time scale on estimates of current plate motions. Geophysical Research Letters 21: 2191–2194.

de' Michieli Vitturi M, Neri A, Esposti Ongaro T, Lo Savio S, Boschi E 2010. Lagrangian modeling of large volcaanic particles: Application to Vulcanian explosions. Journal of Geophysical Research 115(B8), B08206.

Dominguez-Cuesta MJ 2013. Susceptibility. In: Bobrowsky PT ed. Encyclopedia of Natural Hazards. Springer Netherlands: 988.

Douglas, J., 2007. Physical vulnerability modelling in natural hazard risk assessment. Nat. Hazards Earth Syst. Sci. 7, 283–288

Druitt TH, Kokelaar BP 2002. The eruption of Soufriere Hills Volcano, Montserrat, from 1995 – 1999. Geological Society, London, Memoirs 21: 281 – 306.

Duncan, A.R. 1970. The petrology and petrochemistry of andesite volcanoes in Eastern Bay of Plenty, New Zealand. Ph.D. Thesis, Victoria University of Wellington, New Zealand

Erfurt-Cooper, P. 2011. Geotourism in volcanic and geothermal environments: Playing with fire? *Geoheritage*, *3*(3), 187–193. http://doi.org/10.1007/s12371-010-0025-6

Eruption at Kairau Park. 7 November 2003. Daily Post Rotorua. Retrieved from https://www.nzherald.co.nz/nz/news/article.cfm?c_id=1&objectid=3533007 04/05/2018.

Edwards, M., Kennedy, B., Jolly, A., & Scheu, B. 2017. Evolution of a small hydrothermal eruption episode through a mud pool of varying depth and rheology, White Island, NZ. *Bulletin Of*. http://doi.org/10.1007/s00445-017-1100-5

Eriksen, A. 2006, 12 December, Rotorua Daily Post, "Kairau Park Erupts" retrieved from https://www.nzherald.co.nz/rotorua-dailypost/news/article.cfm?c_id=1503438&objectid=10949028

Fagents SA, Wilson L 1993. Explosive volcanic eruptions—VII. The ranges of pyroclasts ejected in transient volcanic explosions. Geophysical Journal International 113: 359– 370.

Fink, J. 1995. Exploding volcanic myths. *Nature, 373*(6516), 660-661. doi:10.1038/373660a0

Fitzgerald, R., Tsunematsu, K., Kennedy, B., Breard, E., Lube, G., Wilson, T., Jolly, A., Pawson, J., Rosenberg, M., Cronin, S., 2014. The application ofa calibrated 3D ballistic trajectory model to ballistic hazard assessments at Upper Te Maari, Tongariro. J. Volcanol. Geotherm. Res. 286, 248–262.

Fitzgerald, R. H., Kennedy, B. M., Wilson, T. M., Leonard, G. S., Tsunematsu, K., & Keys, H. 2017. The Communication and Risk Management of Volcanic Ballistic Hazards Volcanic risk. http://doi.org/10.1007/11157

Fleming CA 1953. The geology of Wanganui subdivision. New Zealand Geological Survey bulletin, 52: 362 p.

Foster, H, and Corwin, G. 195). Iwo Jima maars, Corwin and Foster.pdf. *American Journal of Science*, *257*.

Friedlaender B 1898. Some notes on the volcanoes of the Taupo District. Transactions of the New Zealand Institute 31: 498-310.

Fudali RF, Melson WG 1972. Ejecta velocities, magma chamber pressure and kinetic energy associated with the 1968 eruption of Arenal volcano. Bulletin of Volcanology 35: 383 – 401.

Gamble JA, Wood P, Price RC, Smith IEM, Waight TE 1999. A fifty year perspective of magmatic evolution on Ruapehu volcano, New Zealand: verification of open system behaviour in an arc volcano. Earth and Planetary Science Letters 170: 301–314

Gamble,J.A., Price, R. C., Smith,I.E.M., McIntosh, W.C.& Dunbar, N.W. 2003. 40Ar/39Ar geochronology ofmagmatic activ- ity, magma flux and hazards at RuapehuVolcano, Taupo volcanic zone, New Zealand. Journal of Volcanology and Geothermal Research 120, 271^287.

Ganci, G., Cappello, A., Bilotta, G., Herault, A., Zago, V., & Del Negro, C. 2018. Mapping Volcanic Deposits of the 2011–2015 Etna Eruptive Events Using Satellite Remote Sensing. *Frontiers in Earth Science*, *6*(June), 1–12. http://doi.org/10.3389/feart.2018.00083

Gaudin, D., M. Moroni, J. Taddeucci, P. Scarlato, and L. Shindler 2014, Pyroclast tracking velocimetry: A particle tracking velocimetry-based tool for the study of strombolian explosive eruptions, J. Geophys. Res. Solid Earth, doi:10.1002/2014JB011095

GeoNet Volcanic Alert Bulletin, 2016 https://www.geonet.org.nz/vabs/T7GDhGjrkkicUmuUqmOuA

Giggenbach, W.F., Shinohara, H., Kusakabe, M., Ohba, T., 2003. Formation of acid volcanic brines through interaction of magmatic gases, seawater and rock within the White Island volcanic–hydrothermal system, New Zealand. Soc. Econ. Geol. Spec. Publ. 10, 19–40.

Gurioli, L., Harris, A. J. L., Colò, L., Bernard, J., Favalli, M., Ripepe, M., & Andronico, D. 2013. Classification, landing distribution, and associated flight parameters for a bomb field emplaced during a single major explosion at Stromboli, Italy. *Geology*, *41*(5), 559–562. http://doi.org/10.1130/G33967.1

Graham IJ, Cole JW, Briggs RM, Gamble JA, Smith IEM 1995. Petrology and petrogenesis of volcanic rocks from the Taupo Volcanic Zone: a review. Journal of Volcanology and Geothermal Research 68: 59–87.

Graham IJ, Hackett WR 1987. Petrology of calc-alkaline lavas from Ruapehu volcano and related vents, Taupo Volcanic Zone, New Zealand. Journal of Petrology 28: 531-657.

Gregg DR 1960. The geology of Tongariro subdivision. N.Z. Geological Survey Bulletin 40: 152 p.

Gregg DR 1961. Volcanoes of Tongariro National Park. In: N.Z. Department of Scientific and Industrial Research (eds). New Zealand Geological Survey Handbook, Information Series 28

Greve, A., Turner, G. M., Conway, C. E., Townsend, D. B., Gamble, J. A., & Leonard, G. S. 2016. Palaeomagnetic refinement of the eruption ages of Holocene lava flows, and implications for the eruptive history of the Tongariro Volcanic Centre, New Zealand. *Geophysical Journal International*, *207*(2), 702–718. http://doi.org/10.1093/gji/ggw296

Global Volcanism Program, 2014. Report on White Island (New Zealand). In: Wunderman, R (ed.), Bulletin of the Global Volcanism Network, 39:2. Smithsonian Institution. https://doi.org/10.5479/si.GVP.BGVN201402-241040.

Global Volcanism Program, 1989. Report on White Island (New Zealand). In: McClelland, L (ed.), Scientific Event Alert Network Bulletin, 14:10. Smithsonian Institution. https://doi.org/10.5479/si.GVP.SEAN198910-241040.

Global Volcanism Program, 1993. Report on White Island (New Zealand). In: Venzke, E (ed.), Bulletin of the Global Volcanism Network, 18:10. Smithsonian Institution. https://doi.org/10.5479/si.GVP.BGVN199310-241040.

GNS Science (compiler), 2007a. Volcanic Hazards at Tongariro. http://info.geonet.org.nz/download/attachments/8585571/Tongariro_Poster_A4.pdf (accessed July 2014).

GNS Science (compiler), 2008. Volcanic Hazards at Ruapehu. http://info.geonet.org.nz/download/attachments/8585571/Ruapehu_Hazards_poster_A3.pdf (accessed July 2014).

GNS Science (compiler), 2012. Te Maari Erupion Phenomena. http://info.geonet.org.nz/download/attachments/8585571/Northern_Tongariro_eruption_phenomena.pdf (Accessed July 2014

Gurioli L, Harris AJL, Colo L, Bernard J, Favalli M, Ripepe M, Andronico D 2013. Classification, landing distribution, and associated flight parameters for a bomb field emplaced during a single major explosion at Stromboli, Italy. Geology 41(5): 559–562.

Hadisantono RD, Andreastuti MCHSD, Abdurachman EK, Sayudi DS, Nursusanto I, Martono A, Sumpena AD, Muzani M 2002. Peta Kawasan Rawan Bencana Gung Api Merapi, Jawa Tengah dan Daerah Istimewa Yogyakarta scale 1:50 000 Direktorat Vulkanologi dan Mitigasi Bencana Geologic

Hamilton, W.M., & Baumgart, I.L. (Eds.) 1959., White Island. N.Z. Dep. Sci. & Indust. Res. Bull. 127, 9–24.

Haynes K, Barclay J, Pidgeon N 2007 Volcanic hazard communication using maps: an evaluation of their effectiveness. Bull Volc 70:123–138

Hobden BJ, Houghton BF, Lanphere MA, Nairn IA 1996. Growth of the Tongariro volcanic complex: New evidence from K-Ar age determinations. New Zealand Journal of Geology and Geophysics, 39(1): 151–154.

Hobden BJ, Houghton BF, Davidson JP, Weaver SD 1999. Small and short-lived magma batches at composite volcanoes: time windows at Tongariro volcano, New Zealand. Journal of the Geological Society, London 156: 865–868.

Houghton BF, Swanson DA, Carey RJ, Rausch J, Sutton AJ 2011. Pigeonholing pyroclasts: Insights from the 19 March 2008 explosive eruption of Kilauea volcano. Geology 39(3): 263–266.

Houghton, B. F., & Nairn, I. A. 1989. The phreatomagmatic and Strombolian eruption events at White Island volcano 1976-82: eruption narrative. NZ Geol Surv Bull, 103, 13-23.

Houghton, B. F., & Nairn, I. A. 1991. The 1976–1982 Strombolian and phreatomagmatic eruptions of White Island, New Zealand: eruptive and depositional mechanisms at a ‘wet’volcano. Bulletin of Volcanology, 54(1), 25-49.

Hurst, A. W., Rickerby, P. C., Scott, B. J., & Hashimoto, T. 2004. Magnetic field changes on White Island, New Zealand, and the value of magnetic changes for eruption forecasting. Journal of Volcanology and Geothermal Research, 136(1), 53-70.

James, M.R., Robson, S., 2012. Straightforward reconstruction of 3D surfaces and topography with a camera: accuracy and geoscience application. J. Geophys. Res. 117, F3017.

Jenkins SF, Spence RJS, Fonseca JFBD, Solidum RU, Wilson TM 2014. Volcanic risk assessment: Quantifying physical vulnerability in the built environment. Journal of Volcanology and Geothermal Research 276: 105–120.

Jolly AD, Jousset P, Lyons JJ, Carniel R, Fournier N, Fry B, Miller C 2014a. Seismo-acoustic evidence for an avalanche driven phreatic eruption through a beheaded hydrothermal system: An example from the 2012 Tongariro eruption. Journal of Volcanology and Geothermal Research. DOI: 10.1016/j.jvolgeores.2014.04.007.

Jolly GE, Taig T 2012. Risk assessment for Department of Conservation staff working on the Tongariro Alpine Crossing Track near Ketetahi and for visitors walking on the Tongariro Alpine Crossing Track. GNS Science Consultancy Report 2012/310. 24 p.

Jolly, A.D., Sherburn, S., Jousset, P., Kilgour, P., 2010. Eruption source processes derived from seismic and acoustic observations of the 25 September 2007 Ruapehu eruption–North Island, New Zealand. J. Volcanol. Geotherm. Res. 191, 33–45.

Jolly GE, Taig T 2013. Update of risk assessment for visitors walking on the Tongariro Alpine Crossing, February 2013. GNS Science Letter Report. 10 p.

Jolly GE, Keys HJR, Procter JN, Deligne N. 2014 Overview of the co-ordinated risk-based approach to science and management response and recovery for the 2012 eruptions of Tongariro volcano, New Zealand. Journal of Volcanology and Geothermal Research.

Kaneko, T., Maeno, F., & Nakada, S. 2016. 2014 Mount Ontake eruption: characteristics of the phreatic eruption as inferred from aerial observations. *Earth, Planets and Space*, *68*(1), 72. http://doi.org/10.1186/s40623-016-0452-y

Kereszturia, G., Schaefer, L.N., Schleiffarth, W. K., Procter, J., Pullannagari, R. R. Mead, S., Kennedt, B. 2018. Integrating airborne hyperspectral imagery and LiDAR for volcano mappingand monitoring through image classification International Journal of Applied Earth Observation and Geoinformation 73, 323-339

Kato A, Terakawa T, Yamanaka Y, Maeda Y, Horikawa S, Matsuhiro K, Okuda T 2015. Preparatory and precursory processes leading up to the 2014 phreatic eruption of Mount Ontake, Japan. Earth Planet Space 67:111. https ://doi.org/10.1186/s4062 3-015-0288-x

Keys, H., Williams 2014. Volcanoes of the Tongariro National Park, New Zealand In Erfurt-Cooper, P. (2014). *Volcanic tourist destinations* (1st;2014; ed.). Heidelberg: Springer. doi:10.1007/978-3-642-16191-9

Kilgour GN, Bowyer E (2015) Recent eruption at White Island: Quantifying the amount of material lost to the geological record. In: Holt, K. A. (ed.). Abstract Volume, GeoSciences 2014 Conference, 24th – 27th November 2014, Pukekura Raceway and Function Centre, New Plymouth, New Zealand. Geoscience Society of New Zealand Miscellaneous Publication 139A.

Kilgour G, Manville V, Della Pasqua F, Graettinger A, Hodgson KA, Jolly GE 2010. The 25 September 2007 eruption of Mount Ruapehu, New Zealand: Directed ballistics, surtseyan jets, and ice-slurry lahars. Journal of Volcanology and Geothermal Research 191: 1–14.

Kilgour G, Blundy J, Cashman K, Mader HM 2013. Small volume andesite magmas and melt– mush interactions at Ruapehu, New Zealand: evidence from melt inclusions. Contributions to Mineralogy and Petrology 166(2): 371–392.

Kilgour, G., Gates, S., Kennedy, B., Farquhar, A, McSporran, A., Asher, C. (in review) Phreatic eruption dynamics derived from deposit analysis: A case study from a small, phreatic eruption from Whakaari/White Island, New Zealand. *Earth, Planets and Space*

Lauta, K. C. (2014). New fault lines? on responsibility and disasters. *European Journal of Risk Regulation, 5*(2), 137-145. doi:10.1017/S1867299X0000355X

Leonard, G. S., Stewart, C., Wilson, T. M., Procter, J. N., Scott, B. J., Keys, H. J., … McBride, S. K. 2014. Integrating multidisciplinary science, modelling and impact data into evolving, syn-event volcanic hazard mapping and communication: A case study from the 2012 Tongariro eruption crisis, New Zealand. *Journal of Volcanology and Geothermal Research*, *286*(2014), 208–232. http://doi.org/10.1016/j.jvolgeores.2014.08.018

Letham-Brake, M. 2013. Geological constraints on fluid flow at Whakaari volcano (White Island). M.Sc. Thesis. Department of Geological Sciences, University of Canterbury, Christchurch, New Zealand.

Lorenz, V. 1970. Some aspects of the eruption mechanism of the big hole maar, central oregon. *Bulletin of the Geological Society of America*, *81*(6), 1823–1830. http://doi.org/10.1130/0016-7606(1970)81[1823:SAOTEM]2.0.CO;2

Lube G, Breard ECP, Cronin SJ, Procter JN, Brenna M, Moebis A, Pardo N, Stewart RB, Jolly A, Fournier N 2014. Dynamics of surges generated by hydrothermal blasts during the 6 August 2012 Te Maari eruption, Mt. Tongariro, New Zealand. Journal of Volcanology and Geothermal Research. DOI: 10.1016/j.jvolgeores.2014.05.010.

Maeno F, Nakada S, Nagai M, Kozono T 2013. Ballistic ejecta and eruption condition of the vulcanian explosion of Shinmoedake volcano, Kyushu, Japan on 1 February, 2011. Earth, Planets and Space 65(6): 609–621.

Maeda, Y., Kumagai, H., Lacson, R., Figueroa, M. S., Yamashina, T., Ohkura, T., & Baloloy, A. V. 2015. A phreatic explosion model inferred from a very long period seismic event at Mayon Volcano, Philippines. *Journal of Geophysical Research: Solid Earth*, *120*(1), 226–242. http://doi.org/10.1002/2014JB011440

Marzocchi, W., Sandri, L., Selva, J., 2008. BET_EF: a probabilistic tool for long- and short- term eruption forecasting. Bull. Volcanol. 70, 623–632.

Mas, E., Koshimura, S., Imamura, F., Suppasri, A., Muhari, A., & Adriano, B. 2015. Recent advances in agent-based tsunami evacuation simulations: Case studies in Indonesia, Thailand, Japan and Peru. *Pure and Applied Geophysics, 172*(12), 3409-3424. doi:10.1007/s00024-015-1105-y

Mastin LG 2001. A simple calculator of ballistic trajectories for blocks ejected during volcanic eruptions. US Department of the Interior. US Geological Survey Open File Rep: 01-45.

Matthews, W.H., 1967. A contribution to the geology of the Mount Tongariro Massif, North Island, New Zealand. N.Z.J. Geol. Geophys., 10 (4): 1027--1038.

Marzano, F. S., Lamantea, M., Montopoli, M., Herzog, M., Graf, H., & Cimini, D. 2013. Microwave remote sensing of the 2011 Plinian eruption of the Grímsvötn Icelandic volcano. *Remote Sensing of Environment*, *129*, 168–184. http://doi.org/10.1016/j.rse.2012.11.005

Mayer K, Scheu B, Gilg HA, Heap MJ, Kennedy BK, Lavalle Y, Letham-Brake M, Dingwell DB 2015 Experimental constraints on phreatic eruption processes at Whakaari (White Island volcano). J Volcanol Geotherm Res 302:150–16

Minakami T 1942. 5. On the distribution of volcanic ejecta (Part I.): The distributions of volcanic bombs ejected by the recent explosions of Asama. Bulletin of Earthquake Research Institute 20: 65 – 92.

Moebis A, Cronin SJ, Neall VE, Smith IE 2011. Unravelling a complex volcanic history from fine-grained, intricate Holocene ash sequences at the Tongariro Volcanic Centre, New Zealand. Quaternary International 246(1-2): 352–363.

Mongillo, M. A., & Wood, C. P. 1995. Thermal infrared mapping of White Island volcano, New Zealand. *Journal of Volcanology and Geothermal Research*, *69*(1–2), 59–71. http://doi.org/10.1016/0377-0273(95)00016-X

Moon, V., Bradshaw, J., Smith, R., de Lange, W., 2005. Geotechnical characterisation of stratocone crater wall sequences, White Island Volcano, New Zealand. Eng. Geol. 81, 146–178. http://dx.doi.org/10.1016/j.enggeo.2005.07.014.

Migon, P., & Pijet-Migon, E. 2017. Interpreting geoheritage at new zealand's geothermal tourist sites-systematic explanation versus storytelling.*Geoheritage, 9*(1), 83-95. doi:10.1007/s12371-016-0185-0

Miller, C.A., Jolly, A.D., 2014. A model for developing best practice volcano monitoring: a combined threat assessment, consultation and network effectiveness approach. Nat. Hazards 71, 493–522.

Miller, C. A., & Williams-Jones, G. 2016. Internal structure and volcanic hazard potential of Mt Tongariro, New Zealand, from 3D gravity and magnetic models. *Journal of Volcanology and Geothermal Research*, *319*, 12–28. http://doi.org/10.1016/j.jvolgeores.2016.03.012

Miyabuchi, Y., Iizuka, Y., Hara, C., Yokoo, A., & Ohkura, T. 2018. The September 14, 2015 phreatomagmatic eruption of Nakadake first crater, Aso Volcano, Japan: Eruption sequence inferred from ballistic, pyroclastic density current and fallout deposits. *Journal of Volcanology and Geothermal Research*, *351*, 41–56. http://doi.org/10.1016/j.jvolgeores.2017.12.009

Murphy, S., Wright, R., & Rouwet, D. 2018. Color and temperature of the crater lakes at Kelimutu volcano through time. *Bulletin of Volcanology, 80*(1), 1-12. doi:10.1007/s00445-017-1172-2

Nairn, I.A.; Houghton, B.F.; Cole, J.W. 1996 Volcanic hazards at White Island. 2nd ed. [Palmerston North, NZ]: Ministry of Civil Defence. *Volcanic hazards information series 3.* 27 p

Nairn, I. A. 1976. Atmospheric shock waves and condensation clouds from ngauruhoe explosive eruptions. *Nature, 259*(5540), 190-192. doi:10.1038/259190a0

Nairn IA, Self S 1978. Explosive eruptions and pyroclastic avalanches from Ngauruhoe in February 1975. Journal of Volcanology and Geothermal Research 3: 36–60.

Neall, V.E.; Alloway, B.V. 1993 Volcanic hazards at Egmont volcano. 2nd ed. [Palmerston North, NZ]: Ministry of Civil Defence. *Volcanic hazards information series 1.* 31 p.

Neal CA, McGimsey RG, Miller TP, Riehle JR, Waythomas CF 2001. Preliminary volcano-hazard assessment forAniakchakVolcano, Alaska.United States Geological Survey Open File Report 00-519, Plate 1

Nishi, Y., Sherburn, S., Scott, B.J., Sugihara, M., 1996. High-frequency earthquakes atWhite Island volcano, New Zealand: insights into the shallow structure of a volcano– hydrothermal system. J. Volcanol. Geotherm. Res. 72 (3–4), 183–197.

Nurmawati, A., & Konstantinou, K. I. 2018. Hazard assessment of volcanic ballistic impacts at Mt Chihshin, Tatun Volcano Group, northern Taiwan. *Natural Hazards*, *92*(1), 77–92. http://doi.org/10.1007/s11069-018-3192-4

ISO 2009. 31000: 2009 Risk management–Principles and Guidelines. International Organization for Standardization, Geneva, Switzerland.

Oikawa, T., Yoshimoto, M., Nakada, S., Maeno, F., Komori, J., & Shimano, T. 2016. Reconstruction of the 2014 eruption sequence of Ontake Volcano from recorded images and interviews. *Earth, Planets and Space*. http://doi.org/10.1186/s40623-016-0458-5

Pallister, J. S., Schneider, D. J., Griswold, J. P., Keeler, R. H., Burton, W. C., Noyles, C., … Ratdomopurbo, A. 2013. Merapi 2010 eruption-Chronology and extrusion rates monitored with satellite radar and used in eruption forecasting. *Journal of Volcanology and Geothermal Research*, *261*, 144–152. http://doi.org/10.1016/j.jvolgeores.2012.07.012

Pistolesi M, Rosi M, Pioli L, Renzulli A, Bertagnini A, Andronico D 2008. The paroxysmal event and its deposits. The Stromboli Volcano: An Integrated Study of the 2002 - 2003 Eruption. Geophysica 317–330.

Price RC, Gamble JA, Smith IEM, Stewart RB, Eggins S, Wright IC 2005. An integrated model for the temporal evolution of andesites and rhyolites and crustal development in New Zealand's North Island. Journal of Volcanology and Geothermal Research Res 140: 1– 24.

Reyners M 2010. Stress and strain from earthquakes at the southern termination of the Taupo Volcanic Zone, New Zealand. Journal of Volcanology and Geothermal Research 190: 82–88.

Rich, Motoko. 10 October 2017. Japan and Utility are found negligent again in Fukushima Meltdowns. The New York Time, retrieved 20/08/2018 https://www.nytimes.com/2017/10/10/world/asia/japan-fukushima-lawsuit.html

Robertson R, Cole P, Sparks RSJ, Harford C, Lejeune AM, McGuire WJ, Miller AD, Murphy MD, Norton G, Stevens NF, Young SR 1998. The explosive eruption of Soufriere Hills Volcano, Montserrat, West Indies, 17 September, 1996. Geophysical Research Letters 25(18): 3429–3432.

Rowe, G.L., Ohsawa, S., Takano, B., Brantley, S., Fernandez, J.F., Baurquero, J., 1992. Using Crater Lake chemistry to predict volcanic activity at Poás Volcano, Costa Rica. Bull. Volcanol. 54, 494–503

Saunderson, H. C. (2008). Equations of motion and ballistic paths of volcanic ejecta. *Computers and Geosciences*, *34*(7), 802–814. http://doi.org/10.1016/j.cageo.2007.10.004

Schaefer, L., Lu, Z., & Oommen, T. (2016). Post-eruption deformation processes measured using ALOS-1 and UAVSAR InSAR at pacaya volcano, guatemala. *Remote Sensing, 8*(1), 73. doi:10.3390/rs8010073

Scott BJ, Potter SH 2014. Aspects of historical eruptive activity and volcanic unrest at Mt. Tongariro, New Zealand: 1846-2013. Journal of Volcanology and Geothermal Research. DOI: 10.1016/j.jvolgeores.2014.04.003.

Self S, Kienle J, Huot J 1980. Ukinrek Maars, Alaska, II. Deposits and formation of the 1977 craters. Journal of Volcanology and Geothermal Research 7: 39–65.

Shane, P., Maas, R., & Lindsay, J. 2017. History of Red Crater volcano, Tongariro Volcanic Centre (New Zealand): Abrupt shift in magmatism following recharge and contrasting evolution between neighboring volcanoes. *Journal of Volcanology and Geothermal Research*, *340*, 1–15. http://doi.org/10.1016/j.jvolgeores.2017.04.008

Sherwood, a. E. 1967. Effect of air drag on particles ejected during explosive cratering. *Journal of Geophysical Research*, *72*(6), 1783. http://doi.org/10.1029/JZ072i006p01783

Shiroko, T. 2016. An experience of trauma cases: patients hit by rocks during the Mt Ontake volcanic eruption in Japan. *Journal of Japanese Association for Acute Medicine*, *27*(12), 770–775. http://doi.org/10.1002/jja2.12127

Simons, B.C., 2014. Volcanic History and Eruption Processes of Blue Lake Crater, Tongariro Ph.D. thesis University of Waikato.

Sparks, Z., 2018, 22 July. Rare mud eruption south of Rotorua at Wai-O-Tapu. The Daily Post. Retrieved from https://www.nzherald.co.nz/nz/news/article.cfm?c_id=1&objectid=12093013

Spinetti, C., Mazzarini, F., Casacchia, R., Colini, L., Neri, M., Behncke, B., … Pareschi, M. T. 2009. Spectral properties of volcanic materials from hyperspectral field and satellite data compared with LiDAR data at Mt. Etna. *International Journal of Applied Earth Observation and Geoinformation*, *11*(2), 142–155. http://doi.org/10.1016/j.jag.2009.01.001

Steinberg GS, Lorenz V 1983. External ballistic of volcanic explosions. Bulletin volcanologique 46(4): 333-348.

Steinberg, 1975, On the Determination of the Energy and Depth of Origin of Volcanic Explosions. Geologiya i Geofizika, no. 7, (in Russian).

Stowell, L. 2017, 27 February. Crowds cause crossing concern Tongariro Alpine. Wanganui Chronicle. Retrieved from https://www.nzherald.co.nz/thecountry/news/article.cfm?c_id=16&objectid=11808432

Strehlow, K., Sandri, L., Gottsmann, J. H., Kilgour, G., Rust, A. C., & Tonini, R. 2017. Phreatic eruptions at crater lakes: occurrence statistics and probabilistic hazard forecast. *Journal of Applied Volcanology*, *6*(1), 4. http://doi.org/10.1186/s13617-016-0053-2

Swanson, D. A., Zolkos, S. P., & Haravitch, B. 2012. Ballistic blocks around Kilauea Caldera: Their vent locations and number of eruptions in the late 18th century. *Journal of Volcanology and Geothermal Research*, *231–232*, 1–11. http://doi.org/10.1016/j.jvolgeores.2012.04.008

Taddeucci J, Scarlato P, Capponi A, Del Bello E, Cimarelli C, Palladino DM, Kueppers U 2012. High-speed imaging of Strombolian explosions: The ejection velocity of pyroclasts. Geophysical Research Letters 39(2): L02301.

Taddeucci, J., Palldino, D. M., Camaldo, C., & Scarlato, P. 2015. High-speed imaging of Strombolian eruptions reveals gas-pyroclast interactions in volcanic jets, *14*, 9132. http://doi.org/10.1002/2015GL064874.Received

Taddeucci, J., Alatorre-Ibargüengoitia, M. A., Cruz-Vázquez, O., Bello, E. Del, Scarlato, P., & Ricci, T. 2017. In-flight dynamics of Volcanic Ballistic Projectiles. *Reviews of Geophysics*. http://doi.org/10.1002/2017RG000564

Thouret JC, Lavigne F, Kelfoun K, Bronto S 2000. Toward a revised hazard assessment at Merapi volcano, Central Java. Journal of Volcanology and Geothermal Research 100: 479-502.

Topping WW 1974. Some aspects of Quaternary history of Tongariro Volcanic Centre. Unpublished PhD Thesis. Victoria University of Wellington, New Zealand.

Tsunematsu, K., Chopard, B., Falcone, J. L., & Bonadonna, C. 2014. A numerical model of ballistic transport with collisions in a volcanic setting. *Computers and Geosciences*, *63*, 62–69. http://doi.org/10.1016/j.cageo.2013.10.016

Tsunematsu, K., Ishimine, Y., Kaneko, T., Yoshimoto, M., Fujii, T., & Yamaoka, K. 2016. Estimation of ballistic block landing energy during 2014 Mount Ontake eruption. *Earth, Planets and Space*, *68*(1), 1–11. http://doi.org/10.1186/s40623-016-0463-8

United Nations Office for Disaster Risk Reduction (2017) 2016-17 Biennium Work Programme Final Report. Retrieved from https://www.unisdr.org/files/58158_unisdr2017annualreport.pdf/ 4/05/2018

Vanderkluysen L, Harris AJL, Kelfoun K, Bonadonna C, Ripepe M 2012. Bombs behaving badly: unexpected trajectories and cooling of volcanic projectiles. Bulletin of Volcanology 74(8): 1849–1858.

van der Meer, F. D., van der Werff, H. M. A., van Ruitenbeek, F. J. A., Hecker, C. A., Bakker, W. H., Noomen, M. F., … Woldai, T. 2012. Multi- and hyperspectral geologic remote sensing: A review. *International Journal of Applied Earth Observation and Geoinformation*, *14*(1), 112–128. http://doi.org/10.1016/j.jag.2011.08.002

Vougioukalakis, G. E., & Fytikas, M. 2005. Volcanic hazards in the Aegean area, relative risk evaluation, monitoring and present state of the active volcanic centers. *Developments in Volcanology*, *7*(C), 161–183. http://doi.org/10.1016/S1871-644X(05)80037-3

Wadsworth, F. B., Kennedy, B. M., Branney, M. J., von Aulock, F. W., Lavall??e, Y., & Menendez, A. 2015. Exhumed conduit records magma ascent and drain-back during a Strombolian eruption at Tongariro volcano, New Zealand. *Bulletin of Volcanology*, *77*(9). http://doi.org/10.1007/s00445-015-0962-7

Waitt, R., Mastin, L. G., & Miller, T. 1995. Ballistic showers during Crater Peak eruptions of Mount Spurr volcano, Summer 1992. *The 1992 Eruptions of Crater Peak Vent, Mount Spurr Volcano, Alaska*, 86–106.

Wallace LM, Beavan J, McCaffrey R, Darby D 2004. Subduction zone coupling and tectonic block rotations in the North Island, New Zealand. Journal of Volcanology and Geothermal Research 109, B12406.

Walker, G. P. L., L. Wilson, and E. L. G. Bowell (1971), Explosive volcanic eruptions I. The rate of fall of pyroclasts, Geophys. J. R. Astron. Soc., 22, 377–383.

Walker, G. P. L., Self, S., & Wilson, L. 1984. Tarawera 1886, new zealand — A basaltic plinian fissure eruption. *Journal of Volcanology and Geothermal Research, 21*(1), 61-78. doi:10.1016/0377-0273(84)90016-7

Walsh, B., Procter, J., Lokmer, I., Thun, J., Jolly, A., Hurst, T., Christenson, B., (in review), Geophysical examination of the 27 April 2016 Whakaari/White Island, New Zealand eruption and its implications for vent physiognomies and eruptive dynamics, *Manuscript in review, EPS, Special Issue.*

Watson, M. 2012, March 31, Dominion Post, “Injured mountaineer to return to Ruapehu” Retrieved on 04/05/2018 http://www.stuff.co.nz/dominion-post/news/6670258/Injured-mountaineer-to-return-to-Ruapehu

Wardman J, Sword-Daniels V, Stewart C, Wilson T 2012. Impact assessment of the May 2010 eruption of Pacaya volcano, Guatemala. GNS Science Report 2012/09. 90 p.

Werner, C., Hurst, T., Scott, B., Sherburn, S., Christenson, B. W., Britten, K., Cole-Baker, J., & Mullan, B. 2008. Variability of passive gas emissions, seismicity, and deformation during crater lake growth at White Island Volcano, New Zealand, 2002–2006. Journal of Geophysical Research: Solid Earth (1978–2012), 113(B1).

White, B. R., & Chambefort, I. 2016. Geothermal development history of the Taupo Volcanic Zone/ Geothermics, 59,148-167. DOI:10.1016/j.geothermics.2015.10.001

White Island Tours, April 2018, personal communication.

Williams, G. T., Kennedy, B. M., Wilson, T. M., Fitzgerald, R. H., Tsunematsu, K., & Teissier, A. 2017. Buildings vs. ballistics: Quantifying the vulnerability of buildings to volcanic ballistic impacts using field studies and pneumatic cannon experiments. *Journal of Volcanology and Geothermal Research*, *343*, 171–180. http://doi.org/10.1016/j.jvolgeores.2017.06.026

Wilson L 1972. Explosive volcanic eruptions II. The atmospheric trajectories of pyroclasts. Geophysical Journal of the Royal Astronomical Society 30(4): 381 – 392.

Wilson, L. 1980. Relationships between pressure, volatile content and ejecta velocity in three types of volcanic explosion. *Journal of Volcanology and Geothermal Research*, *8*(2–4), 297–313. http://doi.org/10.1016/0377-0273(80)90110-9

Wilson CJN, Houghton BF, McWilliams MO, Lanphere MA, Weaver SD, Briggs RM 1995. Volcanic and structural evolution of Taupo Volcanic Zone, New Zealand: a review. Journal of Volcanology and Geothermal Research 68: 1–28.

Wood, C. P. 1994. Mineralogy at the magma-hydrothermal system interface in Andesite Volcanoes, New Zealand, *Geology*, *22*(1), 75–78.

Yamagishi H, Feebrey C 1994. Ballistic ejecta from the 1988–1989 andesitic Vulcanian eruptions of Tokachidake volcano, Japan: morphological features and genesis. Journal of Volcanology and Geothermal Research 59(4): 269–278.

Yamaoka,K. Geshi, N., Hashimoto, T., Ingebritsen, S, E., & Oikawa, T. (2016). Special issue “the phreatic eruption of Mt Ontake in 2014”. Earth, Planets and Space (online), 68 (1), 1. DOI:10.1186/s40623-016-0548-4

Zobin VM, Luhr JF, Taran YA, Breton M, Corte A, De La Cruz-Reyna S, Dominguez T, Galindo I, Gavilanes JC, Muniz JJ, Navarro C, Ramirez JJ, Reyes GA, Ursua M, Velasco J, Alatorre E, Santiago H 2002. Overview of the 1997–2000 activity of Volcán de Colima, México. Journal of Volcanology and Geothermal Research 117: 1–19.

APPENDIX 1: ELECTRONIC APPENDIX

A – Red Crater

- (a) Field (handheld) Photos
- (b) GIS Reflectance Spectrum
- (c) Size Distribution – all methods
- (d) Conversion Factors

B – Whakaari

- (a) Handheld field Photos
- (b) Mapping locations
- (c) Size Distribution
- (d) Ballista Processing Workflow
- (e) Model fits
- (f) Multiburst Scenario
- (g) Single Burst Scenario
- (h) Multiburst Trajectories
- (i) Hazard scenario timings